

UNIVERSITÀ DEGLI STUDI DELL'INSUBRIA
Facoltà di Scienze Matematiche Fisiche e Naturali
Corso di Laurea in Matematica



Tesi di Laurea Magistrale

Isogeometric Analysis for reduced Fluid-Structure Interaction models in Haemodynamic applications

Relatore interno: Prof. Stefano Serra Capizzano
Relatore esterno: Prof. Alfio Quarteroni
Correlatore: Dr.Ing. Luca Dedè

Tesi di Laurea di:
Tagliabue Anna
Matr. 705658

ANNO ACCADEMICO 2011-2012

To Einstein.

Abstract

Isogeometric analysis (IGA) is a computational methodology recently developed to numerically approximate Partial Differential Equation (PDEs). It is based on the *isogeometric paradigm*, for which the same basis functions used to represent the geometry are then used to approximate the unknown solution of the PDEs. In the case in which Non-Uniform Rational B-Splines (NURBS) are used as basis functions, their mathematical properties lead to appreciable benefits for the numerical approximation of PDEs, especially for high order PDEs in the standard Galerkin formulation. In this framework, we propose an a priori error estimate, extending existing results limited to second order PDEs.

The improvements in both accuracy and efficiency of IGA compared to Finite Element Analysis (FEA), encourage the use of this methodology in the haemodynamic applications. In fact, the simulation of blood flow in arteries requires the numerical approximation of Fluid-Structure Interaction (FSI) problems. In order to account for the deformability of the vessel, the Navier-Stokes equations representing the blood flows, are coupled with structural models describing the mechanical response of the arterial wall. However, the FSI models are complex from both the mathematical and the numerical points of view, leading to high computational costs during the simulations.

With the aim of reducing the complexity of the problem and the computational costs of the simulations, reduced FSI models can be considered. A first simplification, based on the assumption of a thin arterial wall structure, consists in considering shell models to describe the mechanical properties of the arterial walls. Moreover, by means of the additional kinematic condition (continuity of velocities) and dynamic condition (balance of contact forces), the structural problem can be rewritten as generalized boundary condition for the fluid problem. This results in a generalized Navier-Stokes problem which can be expressed only in terms of the primitive variables of the fluid equations (velocity and pressure) and in a fixed computational domain. As a consequence, the computational costs of the numerical simulations are significantly reduced. On the other side, the generalized boundary conditions associated to the reduced FSI model could involve high order derivatives, which need to be suitably approximated. With this respect, IGA allows an accurate, *straightforward* and efficient numerical approximation of the generalized Navier-Stokes equations characterizing the reduced FSI problem.

In this work we consider the numerical approximation of reduced FSI models by means of IGA, for which we discuss the numerical results obtained in haemodynamic applications.

Contents

1	Isogeometric Analysis	1
1.1	Geometrical representation: B-Splines and NURBS	2
1.1.1	The knot vector	2
1.1.2	Univariate B-Splines basis	3
1.1.3	Multivariate B-Splines basis	5
1.1.4	B-Splines geometries	6
1.1.5	Uni- and multivariate NURBS basis	7
1.1.6	NURBS geometries	9
1.1.7	h -, p - and k -refinements	12
1.2	Galerkin method for IGA	16
1.2.1	High order scalar elliptic PDEs: variational formulation	17
1.2.2	Galerkin method for IGA applied to high order scalar elliptic PDEs	20
1.3	A priori error estimate for elliptic PDEs	23
1.3.1	Preliminaries and interpolation estimate for NURBS	24
1.3.2	A priori error estimate	25
1.4	Numerical examples	28
1.4.1	The Poisson problem (Example 1.11): a comparison of IGA and FEA	28
1.4.2	The advection-diffusion problem (Example 1.12): SUPG stabilization with IGA	31
1.4.3	High order PDEs (Examples 1.13 and 1.14)	33
2	An Introduction to the Cardiovascular System	37
2.1	Cardiovascular anatomy and physiology	37
2.2	Cardiovascular pathologies	40
3	Blood Flows in Arteries: Rigid Wall Models	43
3.1	Mathematical modeling of blood flows	44
3.1.1	The Navier-Stokes equations	44
3.1.2	The Navier-Stokes equations in dimensionless form	46
3.1.3	The Navier-Stokes equations in variational formulation	47
3.2	Boundary conditions for physiological flows	48
3.2.1	The inlet condition: pulsatile flow	48
3.2.2	The outlet condition: the resistance condition	50
3.3	The numerical approximation of the Navier-Stokes equations	51
3.3.1	Spatial approximation by means of IGA	51

3.3.2	The Variational Multiscale method: stabilization and Large Eddy Simulation	52
3.3.3	Time discretization: the generalized- α method	58
3.4	Numerical results	61
3.4.1	Asymmetric and axisymmetric stenosis: a comparison between VMS stabilizations	61
3.4.2	Symmetric stenosis: a comparison between boundary conditions	67
3.4.3	Artery with an Aneurysm	70
4	Isogeometric Analysis for Reduced Fluid-Structure Interaction Models	73
4.1	Mathematical modeling of artery walls	74
4.1.1	Differential geometry: preliminaries	75
4.1.2	The linear Koiter shell model	77
4.2	The reduced Fluid-Structure Interaction model	81
4.2.1	The Coupled Momentum method	81
4.2.2	The reduced FSI problem: variational formulation and dimensionless form	83
4.2.3	Numerical approximation: IGA and generalized- α method	88
4.3	Numerical results	88
4.3.1	A comparison between rigid wall and reduced FSI models	89
4.3.2	The reference configuration	91
4.3.3	A comparison between different parameters	98
4.3.4	Numerical simulation with the linear Koiter shell model with radial displacement	102
	Conclusions	105
A	Isogeometric Analysis for Navier-Stokes Equations in Stream Function Formulation	109
A.1	The Navier-Stokes equations in stream function formulation	109
A.1.1	Numerical approximation: Isogeometric Analysis	111
A.2	Numerical results: the Lid-driven cavity problem	112
B	Imposition of Essential Boundary Conditions for High Order PDEs	121
B.1	Strong imposition for fourth order PDEs	121

List of Tables

1.1	Poisson problem <i>case 1</i> : comparison of the errors in L^2 and H^1 norms	30
1.2	Poisson problem <i>case 2</i> : comparison of the errors in L^2 and H^1 norms	30
4.1	Fluid and structural physical and geometrical parameters for the axisymmetric cylindrical artery.	89
A.1	Vortex centers: numerical results compared with [GGS82].	114
A.2	Values for the contour lines of the stream-function and the vorticity.	115

List of Figures

1.1	Isoparametric and Isogeometric paradigms	2
1.2	Example of quadratic B-Splines basis functions for open knot vector	4
1.3	Variation diminishing property vs Lagrange polynomial interpolation	6
1.4	NURBS as projection of B-Splines	9
1.5	Arc with angle size $\theta < \pi/2$	11
1.6	NURBS Curve	11
1.7	NURBS Surfaces	12
1.8	NURBS Solid	12
1.9	Refinements: <i>knot insertion</i> and <i>order elevation</i>	14
1.10	Refinements: <i>k-refinement</i>	15
1.11	NURBS Solid and <i>k-refinement</i>	16
1.12	Poisson problem: computational domain Ω defined by a quarter of an annulus.	29
1.13	Poisson problem <i>case 1</i> : exact solution and meshes	30
1.14	Poisson problem <i>case 2</i> : exact solution and meshes	31
1.15	Advection-diffusion problems: problems settings and data	31
1.16	Advection-diffusion problem <i>case 1</i> : numerical solutions	32
1.17	Advection-diffusion problem <i>case 2</i> : numerical solutions	32
1.18	High order problems: computational domain	33
1.19	Bilaplacian problem <i>case 1</i> : solution and plot of the errors	34
1.20	Bilaplacian problem <i>case 2</i> : solution and plot of the errors	35
1.21	Trilaplacian problem: plot of the errors	36
2.1	Heart anatomy and physiology: qualitative description of the cardiac cycle	38
2.2	Schematic description of the systemic circulation and pulmonary circulation; description of the artery wall	39
2.3	Schematic example of a stenosis and aneurysms	41
3.1	Two dimensional computational domain Ω for a vessel section of cylindrical shape	48
3.2	Physiological flow profile	49
3.3	Degeneration of stabilization parameters	57
3.4	Streamlines for the asymmetric stenosis at different times in the cardiac cycle	63
3.5	Velocity magnitude for the asymmetric stenosis	64
3.6	Velocity magnitude for the asymmetric stenosis: comparison between stabiliza- tions	65
3.7	Vorticity magnitude for the asymmetric stenosis: comparison between stabi- lizations	65

3.8	Vorticity magnitude for the axisymmetric stenosis: comparison between stabilizations	66
3.9	Streamlines for the axisymmetric stenosis	67
3.10	Streamlines for the axisymmetric stenosis	68
3.11	Comparison between homogeneous Neumann boundary conditions and resistance boundary conditions	69
3.12	Evolution of the pressure in time sampled in three points at the inlet and outlet boundaries and corresponding to the aneurysm region	70
3.13	Streamlines for the aneurysm at different times in the cardiac cycle	71
4.1	Example 4.1: shell of thickness h_s and middle surface represented by a cylindrical ring with $R = R(z)$	76
4.2	Comparison between rigid and reduced FSI models: pressure and flow vs. time	90
4.3	Comparison between rigid and FSI models: streamlines of the velocity field	90
4.4	Comparison between implicit and explicit method	93
4.5	Analysis of the displacement field during an heartbeat period for the reference configuration at the sections S_1 (red), S_2 (cyan) and at a section distal 10cm from the inlet interface (green).	94
4.6	Solutions for the reference configuration at time $t = 0.011625$	95
4.7	Solutions for the reference configuration at the peak systole.	96
4.8	Solutions for the reference configuration in the mean diastolic phase.	97
4.9	Comparison between $C_{\text{out}} = 5300 \text{dyn} \cdot \text{s}/\text{cm}^5$ and $C_{\text{out}} = 2500 \text{dyn} \cdot \text{s}/\text{cm}^5$	99
4.10	Comparison between $C_{\text{out}} = 5300 \text{dyn} \cdot \text{s}/\text{cm}^5$ and $C_{\text{out}} = 10000 \text{dyn} \cdot \text{s}/\text{cm}^5$	100
4.11	Comparison between $E = 4 \cdot 10^6 \text{dyn}/\text{cm}^2$ and $E = 2 \cdot 10^6 \text{dyn}/\text{cm}^2$	101
4.12	Comparison between simplified linear Koiter shell model with respect to the full model: pressure and flow vs. time	102
4.13	Comparison between simplified linear Koiter shell model with respect to the full model: displacement	103
A.1	Lid-driven cavity problem: problem setting and data. $\Omega = (0, 1)^2$, $\Gamma_D = \partial\Omega$	113

Introduction

In this work we numerically simulate blood flows in the cardiovascular system. Specifically, we focus on the haemodynamics of large human arteries by using Isogeometric Analysis as numerical method to approximate reduced Fluid-Structure Interaction problems.

In the last years, several efforts have been made in Mathematics and Engineering to provide suitable mathematical models and numerical methods for the study of the cardiovascular system [FQV⁺09, WSN05]. The attention to this subject of research is also motivated by the fact that, at the present time, one of the primary cause of human disease and mortality is related to the cardiovascular system. Therefore, a deep understanding and a rigorous investigation of the complex bio-mechanical processes of the human circulatory system is stimulated from the medical and life sciences communities for both the physiological and pathological conditions. Numerical simulations represent a powerful mean and recently became an effective tool to describe quantitatively and in an accurate manner some aspects of the cardiovascular system. Moreover, among the applications of computational haemodynamics there are the surgical planning and the optimization of medical devices [BGH⁺09], especially in the patient specific contexts.

The computational approach still presents some limitations with respect to in-vivo studies, even if not invasive, and less physiological in vitro experiments. Indeed, the study of the cardiovascular system in its whole complex variety is beyond the current computational resources; to couple different levels of details in the description of the phenomena. Moreover, when performing local investigations, mathematical models need a proper set of patient specific data in order to formulate a well-posed problem. Nowadays, the geometrical data, which define the computational domain, can be obtained by means of non-invasive investigations, such as magnetic resonance or Doppler anemometry. Nevertheless, when considering a section of the cardiovascular system, we introduce *artificial boundaries*, meaning that they do not represent physical interfaces between the vascular domain and the exterior. In this part of the boundary only average data are provided by in-vivo measurements [HNF⁺99, RMP⁺09] and they are not sufficient to describe the problem from the mathematical point of view. For this reason, starting from the analysis of the physical principles governing the fluid flow and taking into account available data, different formulations have been proposed in literature to overcome this inconveniences which is till now an important issue in fluid-dynamic computation [VdVS11, THZ98, BGH⁺09, VCFJT06]. In similar manner, the parameters characterizing the blood flows, vary from an individual to another, for this reason the large part of the studies have been performed in idealized geometries and average data, even if there is an increasing interest towards the possibility of considering specific-patient configurations.

The complexity of the anatomy and physiology of the cardiovascular system leads to consider several assumptions on the physical properties and principles that regulate blood flows. Specifically, for the haemodynamic of large and medium arteries, it is a common practice

to describe the blood flow dynamics by means of the classical laws of mass and momentum conservation for a Newtonian viscous fluid with constant density, namely the Navier-Stokes equations [FQ⁺02]. These are set in terms of the variables describing the fluid velocity and the pressure. An additional unknown, represented by the wall displacement, needs to be considered when accounting for the deformability of the vessels. This is an important feature that largely influences the blood velocity and pressure fields in pathological conditions and in large arteries, for which there is a significant wall displacement (up to the 10% of their radius). Nevertheless, in this case, it is required to solve a complex strongly coupled and computationally expensive Fluid-Structure Interaction problem, which describes the mechanical interaction between the walls and the flowing blood [FQV⁺09]. However, this leads to considerable computational costs when solving the problem numerically.

In order to overcome the difficulty of solving the coupled Fluid-Structure Interaction problem and to cope with the computational costs, a rigid-wall approximation can be considered. Moreover, with the same goals, reduced Fluid-Structure Interaction models can be introduced to limit the complexity and the computational costs when describing the complex physiology of the arterial wall [Hol06]. In this context, shell models [NV09, BW97, BvG⁺12], based on the assumption of a thin structure, are largely used to describe the wall mechanics. Besides the fact that they reduce a three-dimensional problem to a two-dimensional one, shell models allow to embed the solid problem into the fluid one at a variational level by using a coupled momentum method. [FVCJT06, NV09, BvG⁺12]. This follows from the correspondence between the fluid boundary and the approximated thin wall together with a strong coupling of the corresponding degrees of freedom. Moreover, they proceed in the assumption of the kinematic condition, which imposes the continuity of the velocities of the wall and the fluid, and the dynamic condition, requiring the balance of the contact forces at the surface level [vTG⁺06]. The resulting fluid-structure coupling leads to the formulation of a generalized Navier-Stokes problem, which includes the simplified structural model as a generalized boundary condition. Depending on the model adopted for the structure, this kind of boundary condition can eventually involve high order derivatives. By using classical Finite Element Analysis [Qua09], the approximation of the solution of high order Partial Differential Equations can lead to accuracy problems, including when approximating the geometry. Moreover, mixed formulations of the problem may be required in order to supply the low regularity of the basis functions, which are only globally continuous.

Isogeometric Analysis is a computational methodology recently developed and initiated with the work of Hughes et al. in [CHB05]. It has been introduced to facilitate the interaction of Computed Aided Design (CAD) and Finite Element Analysis technologies [CHB09]. Based on the computational geometry technologies such as Non Uniform Rational B-Splines [PT97] for the CAD, Isogeometric Analysis is based on the isogeometric paradigm, for which the same basis functions used to represent the known geometry are then used to form a basis in the approximation of Partial Differential Equations. Isogeometric Analysis offers several possibilities which are prevented or which constitute a non trivial task in the context of classical Finite Element Analysis; namely, exact geometrical representation, simplified refinement procedures [CHR07] and smooth basis functions, eventually globally \mathcal{C}^k -continuous with $k \geq 0$. In such a way, the generalized Navier-Stokes equations, representing the reduced Fluid-Structure Interaction model, can be suitably approximated by using Isogeometric Analysis with a standard Galerkin formulation [CHB09], especially the high order terms of the generalized boundary condition derived from the structural problem. Compared to the standard Finite Element Method, the combination of this property and the capability of facilitating the exact repre-

sensation of smooth geometries, as for patient-specific configurations of arterial vessels, lead to improvements in both the accuracy and the efficiency in the solution of the haemodynamic Fluid-Structure Interaction problems [BCHZ08].

With this motivation, we consider Isogeometric Analysis for solving high order Partial Differential Equations. In particular, we deal with elliptic boundary value problems considering Isogeometric Analysis in the framework of the Galerkin method, for which we provide an a priori error estimate in lower order norms for high order Partial Differential Equations, which extends existing results limited to second order Partial Differential Equations [BBadVC⁺06]. Successively, we simulate blood flows in two-dimensional models of arterial vessels, by considering rigid wall models. Then, we consider Isogeometric Analysis for the numerical approximation of reduced Fluid-Structure Interaction models. In this context, a complete membrane-bending model for the structure is considered by means of the linear elastic Koiter shell model for the arterial walls [Cia05]. The strongly coupling between the fluid and the structural problems results in generalized Navier-Stokes equations formulated only in terms of the primitive variables, i.e. the velocity and the pressure fields.

The outline of this work is as it follows:

- Chapter 1 We introduce Isogeometric Analysis by recalling the main properties of NURBS basis functions and the geometrical representation by means of NURBS. Then, we consider the numerical solution of high order elliptic Partial Differential Equations by means of Isogeometric Analysis in the framework of the Galerkin method. Several examples are presented. Moreover, we provide the a priori error estimate for NURBS-based IGA for the case of high order partial differential operators, extending the results for second order operators of [BBadVC⁺06]; in particular, we address the case of lower order norms.
- Chapter 2 In this chapter we briefly discuss the physiological and pathological aspects of the cardiovascular system.
- Chapter 3 We consider a rigid wall model for blood flows in arteries in two-dimensional domains. We recall the Navier-Stokes equations, and we report their dimensionless form, highlighting the dependency of the solution on the Reynolds number. In the following, we discuss the choice of a proper set of boundary conditions accounting for the pulsatile nature of blood flow and the presence of the downstream circulation (resistance boundary condition). Then, we present the numerical approximation of the problem by means of Isogeometric Analysis and the generalized- α method [JWH00] used as time discretization scheme. Specifically, we consider the stabilization of the Galerkin approximation of the Navier-Stokes equations, by means of a variational multiscale method for large eddy simulation [BCC⁺07].
- Chapter 4 We deal with a reduced Fluid-Structure Interaction problem in haemodynamics. We adopt a reduced model in the framework of the Coupled Momentum Method proposed by Figueroa et al. in [FVCJT06], which by means of a strong coupling of the degrees of freedom of the fluid and the structure, embeds the structural problem into the fluid problem as a generalized boundary condition at a variational level. The resulting problem is expressed only in terms of the primitive variables of the fluid, velocity and pressure, and, above all, defined in a fixed computational domain. The model chosen for the structure is a full linear elastic Koiter shell model [Cia05], which involves high order derivatives. By considering NURBS-based Isogeometric Analysis for its numerical approximation, we can take advantage of the efficacy and accuracy allowed by the method

in the solution of high order Partial Differential Equations and in the exact geometrical representation.

Conclusions We draw some conclusion on this work and we suggest some further extensions.

Appendix A We consider the numerical approximation of the two-dimensional time-dependent Navier-Stokes equations in stream function formulation. We recast the Navier-Stokes equations formulated in primitive variables in the fourth order nonlinear problem in terms of the scalar stream function. By using NURBS-based Isogeometric Analysis a standard Galerkin formulation is used to solve the benchmark Lid-driven cavity problem.

Appendix B We consider the strong imposition of essential boundary conditions for high order Partial Differential Equations; in particular, we propose a technique to enforce the boundary condition on the normal gradient of the solution stemming from a fourth order partial differential operators.

The numerical simulations were performed by means of a C++ IGA library, developed by the author. GeopPDEs (<http://geopdes.sourceforge.net>) [dFRV11], and MATLAB (<http://www.mathworks.com>) have been used as support tools. The visualizations were performed by means of ParaView (<http://www.paraview.org/>).

Chapter 1

Isogeometric Analysis

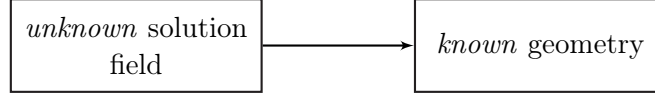
Isogeometric Analysis (IGA) is a computational methodology for the numerical approximation of Partial Differential Equations (PDEs), initiated with the work of Hughes et al. in [CHB05]. The aim of the methodology is to close the existing gap in current Computed Aided Design (CAD) and Finite Element Analysis (FEA), basically determined by the need of generating a computational mesh. In fact, the geometrical models provided by CAD technology need to be modified in order to obtain analysis suitable geometries, which are compatible with the Finite Element approximation. Indeed, FEA requires the generation of a Finite Element mesh, usually a piecewise approximation of the actual computational domain (geometry) obtained by mapping of reference elements via polynomial bases. As a result, the construction of a Finite Element geometry is one of the more time consuming steps in the FEA, in addition to the fact that the geometrical approximation may lead to significant accuracy issues [CHB05, CHB09]. An additional problem may occur when performing mesh refinement, for which the geometrical approximation generally does not improve, since direct communications between CAD systems and the Finite Element solvers are not available in general.

These factors led to the development of a computational methodology based on a unique geometrical representation under the *isoparametric paradigm*, for which the same basis functions are used to represent the geometry and the unknown solution fields. Nevertheless, the isoparametric paradigm occurs in IGA with a significant difference with respect to FEA and it is indeed referred to as *isogeometric paradigm*. In fact, in FEA, a basis approximating the unknown solution field of the PDEs is firstly chosen and then used to represent and approximate the known geometry; on the contrary, IGA firstly introduces the basis field representing the known geometry which is later used to approximate the unknown solution (see Figure 1.1).

Different computational geometry technologies could be adopted to represent the geometries. We choose to refer to Non Uniform Rational B-Splines (NURBS) due to their large use and development in CAD, but also for their mathematical properties in view of the numerical approximation of PDEs. In particular, NURBS can exactly represent some common geometries in engineering design, e.g. conic sections, provide globally smooth basis functions, eventually C^k -continuous with $k \geq 0$, and offer new refinements possibilities beside standard h - and p -refinements of the FEA [CHB09]. In this work, we consider only NURBS-based IGA, although recently improvements have been done in the direction of IGA based on *T-Splines*, a generalization of NURBS technology [BCC⁺10].

This chapter is devoted to the description of the main properties and features of Isogeometric Analysis, starting from the geometric point of view, based on NURBS, and then moving

Finite Element Analysis: Isoparametric paradigm



Isogeometric Analysis: Isogeometric paradigm

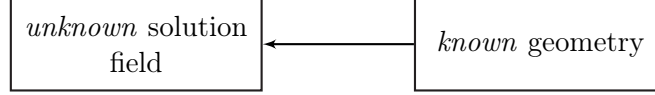


Figure 1.1: Isoparametric and Isogeometric paradigms.

to the use of NURBS as a basis for analysis. We specifically consider IGA in the framework of the *Galerkin method* to solve elliptic PDEs, although different numerical methods can be used, such as collocation or least square methods [CHB09]. We present IGA in the framework of the Galerkin method for approximating high order PDEs and we provide a general a priori error estimate under h -refinement by extending the result of [BBadVC⁺06] for second order PDEs.

In Section 1.1 we discuss the geometrical representation by means of NURBS and B-Splines. In Section 1.2 we consider IGA based on the Galerkin method for solving second order and high order elliptic boundary value problems. In Section 1.3 we provide the a priori error estimate for high order PDEs. Finally, in Section 1.4, we report and discuss some numerical results.

1.1 Geometrical representation: B-Splines and NURBS

In view of the description of NURBS-based IGA, we recall the geometrical representation by means of B-Splines and NURBS, since the computational domains, in which the PDEs are defined, are parametrized as NURBS entities. We consider the case of geometries that can be modeled as a single *patch*, i.e. a “large” domain topologically representable by geometrical mapping of a rectangular or a cuboid reference domain. A large number of geometries can be modeled with a single NURBS patch, even if sometimes, it is useful or necessary to represent a geometry as a collection of multiple patches, e.g. when the geometry differs topologically from a square or a cube or when local refinement is required. The NURBS parameter space is local to individual patches for which a unique geometrical mapping from the parameter space into the physical one is defined for the entire patch.

In this section we describe the mathematical construction and the properties of B-Splines and NURBS basis and geometries and we report some examples. For more details, we refer the interested reader to e.g. [CHB09, PT97, CHB05, CHR07].

1.1.1 The knot vector

In one dimension a *knot vector* is a set of non-decreasing real numbers, representing coordinates in the *parameter space*. By convention, we define a parameter domain $\hat{\Omega} = [0, 1] \subseteq \mathbb{R}$. The

knot vector can be written as $\Xi = \{\xi_1, \xi_2, \dots, \xi_{n+p+1}\}$, where ξ_i is the i -th knot, with the knot index $i \in \{1, \dots, n+p+1\}$ characterized by p and n , i.e., the polynomial degree and the number of basis functions representing the B-Splines basis, respectively. By convention, we assume that $\xi_1 = 0$ and $\xi_{n+p+1} = 1$, in such a way the parameter domain is $\hat{\Omega} = [\xi_1, \xi_{n+p+1}]$. A knot vector is said to be *uniform*, if the knots are equally spaced in the parameter domain and *non-uniform* otherwise. Knots may be repeated and the number of times in which the knot is repeated is indicated as the *multiplicity* of the knot value. A knot vector is said to be *open* if its first and last knots appear $p+1$ times, with each knot different from the first and the last ones called *internal knot*. Specifically, we consider the case of open knot vectors.

We can collect all the r distinct ordered knots of Ξ into a vector $\mathcal{Z} = \{\zeta_1, \dots, \zeta_r\}$ and define in a straightforward way the partition into *elements* induced by the knots on the parameter domain. In particular, the j -th element of the *mesh* over $\hat{\Omega} = [0, 1]$ is defined as the subdomain $Q_j := (\zeta_j, \zeta_{j+1})$, for $j = 1, \dots, r$, bounded by two distinct knots, while we will refer to the subdomain bounded by two consecutive knots (ξ_i, ξ_{i+1}) , for $i = 1, \dots, n+p$, as a *knot span*, noticing that it can have null size. It holds that $n = p + n_{ks}$, where n_{ks} stands for the total number of *internal knot spans*, i.e. knots spans delimited by at least an internal knot.

The multiplicity of the knots has important implications in the properties of the basis functions, in particular for their regularity. Therefore, an additional auxiliary vector, say \mathcal{M} , is defined in relation with \mathcal{Z} in order to gather the multiplicities of the distinct knots; specifically, $\mathcal{M} := \{m_1, \dots, m_r\}$, with $m_j \geq 1$ representing the multiplicity of the knot value ζ_j , for $j = 1, \dots, r$.

Example 1.1. For the open knot vector $\Xi = \{0, 0, 0, 1/4, 1/2, 3/4, 3/4, 1, 1, 1\}$, we have $\mathcal{Z} = \{0, 1/4, 1/2, 3/4, 1\}$ and $\mathcal{M} = \{3, 1, 1, 2, 3\}$. Graphically, we can represent \mathcal{Z} as:

$$\begin{array}{ccccccccc} | & | & | & | & | & | & | & | & | \\ \hline \zeta_1 & \zeta_2 & \zeta_3 & \zeta_4 & \zeta_5 \end{array}$$

and the *index space*, which identifies the knots as separated entities, independently of their actual values, as:

$$\begin{array}{ccccccccccccccc} | & | & | & | & | & | & | & | & | & | & | & | & | & | \\ \hline \xi_1 & \xi_2 & \xi_3 & \xi_4 & \xi_5 & \xi_6 & \xi_7 & \xi_8 & \xi_9 & \xi_{10} \end{array}$$

◇

1.1.2 Univariate B-Splines basis

Given a knot vector $\Xi = \{\xi_1, \dots, \xi_{n+p+1}\}$, the *univariate* B-Splines basis functions $N_{i,p} : \hat{\Omega} \rightarrow \mathbb{R}$, for $i = 1, \dots, n$, are piecewise polynomials of degree p , built by means of the *Cox-de Boor recursion formula*. For $N_{i,p}(\eta)$, with $\eta \in \hat{\Omega}$ and for $i = 1, \dots, n$, we have:

$$\begin{aligned} \text{for } p = 0 : N_{i,0}(\eta) &= \begin{cases} 1 & \text{if } \xi_i \leq \eta < \xi_{i+1}, \\ 0 & \text{otherwise,} \end{cases} \\ \text{for } p \geq 1 : N_{i,p}(\eta) &= \frac{\eta - \xi_i}{\xi_{i+p} - \xi_i} N_{i,p-1}(\eta) + \frac{\xi_{i+p+1} - \eta}{\xi_{i+p+1} - \xi_{i+1}} N_{i+1,p-1}(\eta). \end{aligned} \quad (1.1)$$

By convention we assume that $\frac{0}{0} = 0$, as it occurs when the knots are repeated.

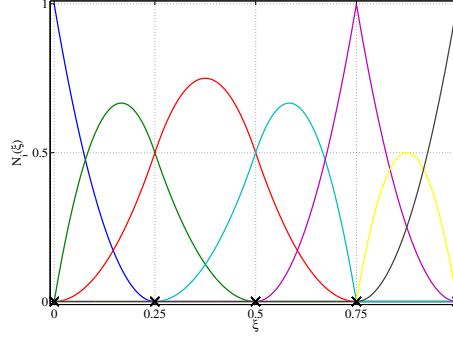


Figure 1.2: Quadratic B-Splines basis functions for the open knot vector $\Xi = \{0, 0, 0, 1/4, 1/2, 3/4, 1, 1, 1\}$.

The properties characterizing a B-Splines basis $\{N_{i,p}\}_{i=1}^n$ can be directly deduced from the knot vector Ξ , as for the number of basis functions n and their degree p ; moreover, the regularity of each basis function can be deduced by Ξ (specifically from \mathcal{Z}, \mathcal{M}). Basis functions of order $p+1$ and degree p , are \mathcal{C}^∞ -continuous in the domain $\hat{\Omega}$, except in knots ζ_j , where they are only \mathcal{C}^{p-m_j} -continuous. In particular, if m_j equals the degree p , the basis function is interpolatory in the correspondent knot. This implies that a basis function defined from an open knot vector possesses the so-called *end-point interpolation property*, for which $N_{1,p}(0) = N_{n,p}(1) = 1$; since the multiplicities of the first and last knots equal $p+1$, the basis becomes discontinuous, thus defining the *patch* boundary. The smoothness integer indexes $k_j = p+1-m_j \in [0, p]$, for all $j = 1, \dots, r$, are collected in a vector $\mathbf{k} = \{k_1, \dots, k_r\}$, for which we define $k_{\min} := \min_{j=2, \dots, r-1} \{k_j\}$ and $k_{\max} := \max_{j=2, \dots, r-1} \{k_j\}$. We observe that in the knot ζ_j the basis functions are \mathcal{C}^{k_j-1} -continuous, according to the definition of the smoothness integer k_j , for $j = 1, \dots, n$.

Additional properties of the B-Splines basis can be inferred by the formula (1.0). Firstly, the basis functions constitute a *partition of unity*, i.e. $\sum_{i=1}^n N_{i,p}(\eta) = 1$ for all $\eta \in \hat{\Omega}$; then, each basis function is pointwise non-negative, i.e. for all $i = 1, \dots, n$ we have $N_{i,p}(\eta) \geq 0$ for all $\eta \in \hat{\Omega}$. We can deduce that each basis function has compact support in $p+1$ knot spans, in particular $\text{supp}(N_{i,p}) \subseteq [\xi_i, \xi_{i+p+1}]$ for all $i = 1, \dots, n$; moreover, we point out that $p+1$ basis functions have support in each knot span.

In term of computational costs, the recursive construction of B-Splines basis functions can be expensive. However, efficient algorithms have been developed for the evaluation of basis functions and their derivatives, see [PT97]. By supposing that in $\eta \in \hat{\Omega}$ the basis function $N_{i,p}$ is sufficiently regular, the general form of its l -th derivative can be recursively expressed in terms of basis function of inferior order. For $p \geq 1$, we have:

$$\frac{d^l}{d\eta^l} N_{i,p}(\eta) = \frac{p}{\xi_{i+p} - \xi_i} \left(\frac{d^{l-1}}{d\eta^{l-1}} N_{i,p-1}(\eta) \right) - \frac{p}{\xi_{i+p+1} - \xi_{i+1}} \left(\frac{d^{l-1}}{d\eta^{l-1}} N_{i+1,p-1}(\eta) \right). \quad (1.2)$$

Remark 1.1. For the sake of simplicity, we will omit henceforth the subscript p , referred to the degree of basis functions $N_{i,p}$, which will read as N_i .

The B-Splines space built by the B-Splines basis functions is denoted as:

$$\mathcal{S}^h := \text{Span}(\{N_i\}_{i=1}^n), \quad (1.3)$$

where the parameter h indicates its finite dimension and it is reminiscent of the definition of the mesh over the parameter domain, say \mathcal{Q}_h ; i.e. setting for each element $Q_j \in \mathcal{Q}_h$, with $j = 1, \dots, r$, the size $h_{Q_j} := |\zeta_{j+1} - \zeta_j|$, we define $h := \max\{h_{Q_j} : Q_j \in \mathcal{Q}_h\}$.

Example 1.2. In Figure 1.2 an example of quadratic B-Splines basis is provided. The basis is defined starting from the open knot vector of Example 1.1, for which we notice the end-point interpolation property. In this case, $n = 7$, $p = 2$, $\mathbf{k} = \{0, 2, 2, 1, 0\}$ with the 4th, 5th and 6th basis functions only continuous and interpolatory in knot value $\zeta_4 = 3/4$. Each function has support contained in $p + 1$ knot spans, some of them with have null size, due to the presence of repeated knots. \diamond

1.1.3 Multivariate B-Splines basis

The definition of B-Splines spaces, introduced in Section 1.1.2, can be extended to the κ -dimensional case by using a tensor product structure, where $\kappa \geq 1$.

For $\alpha = 1, \dots, \kappa$, we provide κ knot vectors $\Xi_\alpha = \{\xi_1^\alpha, \xi_2^\alpha, \dots, \xi_{n_\alpha+p_\alpha+1}^\alpha\}$ and the corresponding vectors $\mathcal{Z}_\alpha = \{\zeta_1^\alpha, \dots, \zeta_{r_\alpha}^\alpha\}$ and $\mathcal{M}_\alpha = \{m_1^\alpha, \dots, m_{r_\alpha}^\alpha\}$. A *mesh* \mathcal{Q}_h over the parametric domain $\hat{\Omega} = [0, 1]^\kappa$ is defined by its partition into κ -dimensional *elements*:

$$\mathcal{Q}_h := \{Q_{(j_1, \dots, j_\kappa)} := \otimes_{\alpha=1}^\kappa (\zeta_{j_\alpha}^\alpha, \zeta_{j_\alpha+1}^\alpha), 1 \leq j_\alpha \leq r_\alpha - 1\}. \quad (1.4)$$

For the sake of simplicity, we refer to an element of the mesh \mathcal{Q}_h by omitting its index (j_1, \dots, j_κ) . Moreover, having set the element size to $h_Q := \text{diam}(Q)$ for all $Q \in \mathcal{Q}_h$, the parameter $h := \max\{h_Q : Q \in \mathcal{Q}_h\}$ will be referred to as the *global mesh size*.

We define, for each $i_\alpha = 1, \dots, n_\alpha$ with $\alpha = 1, \dots, \kappa$, the *multivariate* B-Splines basis function as:

$$N_{(i_1, \dots, i_\kappa)} : \hat{\Omega} \rightarrow \mathbb{R}, \quad N_{(i_1, \dots, i_\kappa)}(\boldsymbol{\eta}) := \prod_{\alpha=1}^\kappa N_{i_\alpha}^\alpha(\eta_\alpha). \quad (1.5)$$

Remark 1.2. In order to simplify the notation, we introduce a multi-index \mathbf{i} in the set $I = \{\mathbf{i} = (i_1, \dots, i_\kappa) : 0 \leq i_\alpha \leq n_\alpha, 1 \leq \alpha \leq \kappa\}$.

Due to the tensor product structure of multivariate B-Splines, several properties satisfied by univariate B-Splines basis functions still hold for multivariate B-Splines basis functions. In particular, the basis functions are piecewise polynomials, pointwise non-negative and constitute a partition of unity. As for their supports, they are the tensor product of the relative univariate supports, being still compact. Moreover, the (directional) regularity of each basis function $N_{\mathbf{i}}$ can be deduced by the one of the univariate functions used in the tensor product. In all the elements $\overset{\circ}{Q} \in \mathcal{Q}_h$ the basis functions are \mathcal{C}^∞ -continuous; while, across each internal $\kappa - 1$ dimensional face, separating the elements Q^+ and Q^- , it reaches a regularity of the order equals to the maximum order of continuity of the derivatives across this face. We can still refer to smoothness parameters and define for each parametric direction the vectors $\mathbf{k}_\alpha = \{k_1^\alpha, \dots, k_{r_\alpha}^\alpha\}$. The minimum and maximum regularity in each α -direction are $k_{\min}^\alpha := \min_{j_\alpha=2, \dots, r_\alpha-1} \{k_{j_\alpha}^\alpha\}$ and $k_{\max}^\alpha := \max_{j_\alpha=2, \dots, r_\alpha-1} \{k_{j_\alpha}^\alpha\}$; while the global ones are $k_{\min} := \min\{k_{\min}^\alpha : \alpha = 1, \dots, \kappa\}$ and $k_{\max} := \max\{k_{\max}^\alpha : \alpha = 1, \dots, \kappa\}$.

The tensor product B-Splines space, spanned by these basis functions, is defined with a notation similar to the one of the univariate case as:

$$\mathcal{S}^h := \text{Span}(\{N_{\mathbf{i}}\}_{\mathbf{i} \in I}). \quad (1.6)$$

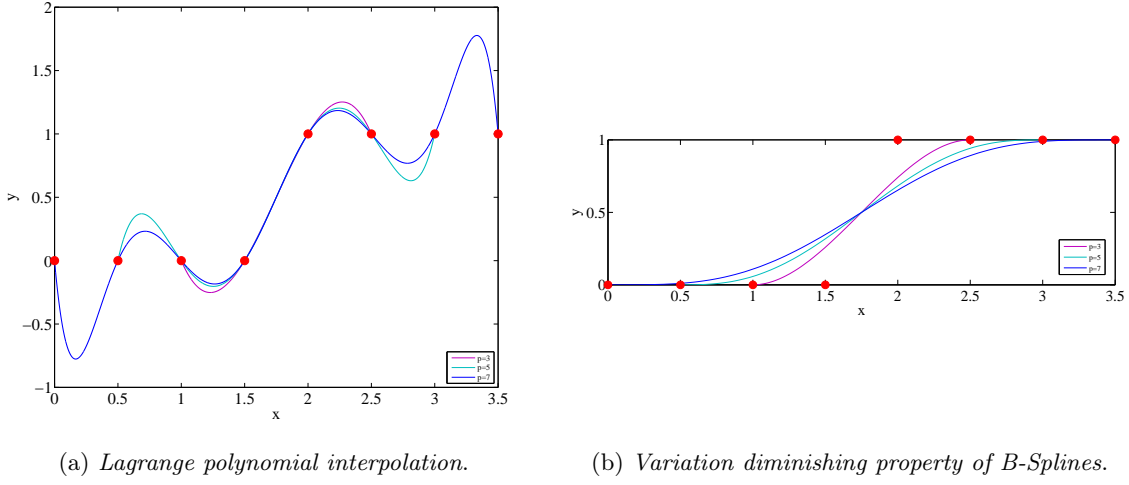


Figure 1.3: Interpolation of discontinuous data with Lagrange polynomials for a set of discontinuous data and variation diminishing property for the corresponding B-Splines curves.

1.1.4 B-Splines geometries

By means of uni- and multivariate B-Splines bases, we can construct geometries in \mathbb{R}^d , e.g. curves, surfaces and solids.

Definition 1.1. Given the univariate B-Splines space $\mathcal{S}^h := \text{Span}(\{N_i\}_{i=1}^n)$ over the parametric domain $\hat{\Omega} = [0, 1]$, and a set of points $\{\mathbf{P}_i\}_{i=1}^n \subseteq \mathbb{R}^d$, called control points, a B-Splines curve in \mathbb{R}^d is defined as the linear combination of B-Splines basis functions with the control points assumed as coefficients; i.e.

$$\mathbf{C} : \hat{\Omega} \rightarrow \Omega \subseteq \mathbb{R}^d, \quad \mathbf{C}(\eta) = \sum_{i=1}^n N_i(\eta) \mathbf{P}_i, \quad (1.7)$$

where Ω indicates the curve in \mathbb{R}^d .

We remark that a B-Splines curve is defined on the parameter domain $\hat{\Omega}$ and with values in the physical domain $\Omega \subseteq \mathbb{R}^d$, where the control points are defined. The properties of B-Splines curves follow directly from the properties of the basis functions, particularly, concerning the regularity and *locality*. The latter is related to the support of the basis functions and determines the fact that changing the position of a single control point may affect the geometry of the curve in at most $p + 1$ elements. Because of the non-interpolatory nature of the basis, the control points do not generally lie on the geometry. This leads to a lack of an immediate interpretation of their role in the physical space, contrarily to the use of Lagrangian interpolatory basis functions in FEA. Moreover, we have the so called *convex hull property*, for which a B-Splines curve is contained in the union of the convex hulls defined by $p + 1$ consecutive control points. Then, by Definition 1.7, it follows the property known as *affine covariance*, for which, applying an affine transformation $\mathcal{A} : \mathbb{R}^d \rightarrow \mathbb{R}^d$ to a B-Splines curve is equivalent to apply it to the control points $\{\mathcal{A}(\mathbf{P}_i)\}_i$, without changes to the basis functions. Lastly, considering the piecewise linear interpolation of the control points, named *control polygon*, we

deduce that no plane has more intersections with the B-Splines curve than it has with the control polygon. We refer to this last property as to the *variation diminishing property*, which is peculiar to B-splines curves and implies a monotone nature of them. As shown in Figure 1.3, given a set of discontinuous data, the standard Lagrange polynomial interpolation provides curves whose oscillating behavior increases when increasing the degree of the basis functions. Instead, by considering the same data set as control points, the corresponding B-splines curves are monotone, accordingly to the variation diminishing property.

By exploiting the tensor product nature of the multivariate B-Splines basis functions, it is possible to define geometrical entities of dimension $\kappa \geq 1$ in the physical space \mathbb{R}^d , where $1 \leq \kappa \leq d$.

Definition 1.2. Given an integer κ with $1 \leq \kappa \leq d$ and knot vectors $\Xi_\alpha = \{\xi_1^\alpha, \xi_2^\alpha, \dots, \xi_{n_\alpha+p_\alpha+1}^\alpha\}$ for $\alpha = 1, \dots, \kappa$, let us consider the multivariate B-Splines space \mathcal{S}^h of Definition 1.6, whose multivariate basis functions $\{N_i\}_{i \in I}$ are defined over the parametric domain $\hat{\Omega} = [0, 1]^\kappa$, and a set of $\prod_{\alpha=1}^\kappa n_\alpha$ control points $\{\mathbf{P}_i\}_{i \in I} \subseteq \mathbb{R}^d$. A κ -dimensional B-Splines geometrical entity in \mathbb{R}^d is defined by the geometrical mapping:

$$\mathbf{x} : \hat{\Omega} \rightarrow \Omega \subseteq \mathbb{R}^d, \quad \mathbf{x}(\boldsymbol{\eta}) = \sum_{i \in I} N_i(\boldsymbol{\eta}) \mathbf{P}_i, \quad (1.8)$$

where Ω indicates the geometry in \mathbb{R}^d . Two-dimensional B-splines entities ($\kappa = 2$) represent B-Splines surfaces in \mathbb{R}^d , $d = 2, 3$, while three-dimensional ones ($\kappa = 3$) B-Splines solids, in \mathbb{R}^3 .

As for the univariate case, due to the tensor product nature of κ -dimensional B-Splines entities, several of their properties are directly inherited from the ones of the B-Splines curves and analogously, they follow from the properties of the related multivariate basis. In particular, the regularity and locality properties still hold, as well as the affine covariance and convex hull properties.

In the multivariate case, we refer to the piecewise multilinear interpolant of the control points \mathbf{P}_i as the *control mesh* in the physical space \mathbb{R}^d , which does not necessary lay in the geometry Ω . The latter does not coincide with the *physical mesh* in the physical domain Ω induced by the geometrical mapping \mathbf{x} of the mesh defined in the parameter space. In particular, the *elements* in the physical domain are obtained from Eq. (1.8) as the image of the elements in the parametric domain:

$$\mathcal{K}_h := \{K = \mathbf{x}(Q) : Q \in \mathcal{Q}_h\}. \quad (1.9)$$

1.1.5 Uni- and multivariate NURBS basis

Since B-Splines are polynomial functions, a large category of geometries used in engineering design, as conic sections, cannot still be exactly represented. In order to close this gap, Non-Uniform Rational B-Splines (NURBS) have been introduced and are typically used in CAD system [PT97].

Given a knot vector $\Xi = \{\xi_1, \xi_2, \dots, \xi_{n+p+1}\}$, a *univariate NURBS basis* is provided on the parametric domain $\hat{\Omega} = [0, 1]$ by introducing a set of real numbers $\{\omega_i\}_{i=1}^n$ called *weights* and the univariate B-Splines basis $\{N_i\}_{i=1}^n$, defined through the knot vector Ξ . We assume that the weights are positive; this hypothesis is not necessary, but it is common in literature

and in most applications of engineering interest. We introduce a scalar (positive) piecewise polynomial function, called *weighting function*, as:

$$W : \hat{\Omega} \rightarrow \mathbb{R}, \quad W(\eta) = \sum_{i=1}^n N_i(\eta) \omega_i. \quad (1.10)$$

Through it, we can define for all $i = 1 \dots, n$, the i -th *NURBS basis function* as:

$$R_i : \hat{\Omega} \rightarrow \mathbb{R}, \quad R_i(\eta) = \frac{N_i(\eta) \omega_i}{W(\eta)} = \frac{N_i(\eta) \omega_i}{\sum_{j=1}^n N_j(\eta) \omega_j}. \quad (1.11)$$

Each basis function is a piecewise rational function defined in the parameter domain $\hat{\Omega}$. Despite its not-polynomial nature, it is a convention to refer to the *degree* of the NURBS basis functions as to the degree of the B-splines basis $\{N_i\}_{i=1}^n$, introduced in Eq. (1.11).

Analogously to univariate B-Splines basis function, the most of the properties can be directly deduced taking into account the knot vector Ξ , e.g. the number of basis function n and the degree p . As for the regularity, the basis functions are \mathcal{C}^∞ -continuous in the interior of each element Q of the mesh \mathcal{Q}_h , while in the knots they are \mathcal{C}^{p-m_j} -continuous, with m_j the multiplicity of the knot value $\zeta_j \in \mathcal{Z}$, for $j = 1, \dots, r$. The basis $\{R_i\}_{i=1}^n$ still constitutes a *partition of unity*, i.e. $\sum_{i=1}^n R_i(\eta) = 1$ for all $\eta \in \hat{\Omega}$, and, if defined from an open knot vector,

it possesses the *end-point interpolation property*, i.e. $R_1(\xi_1) = R_n(\xi_{n+p+1}) = 1$. Each basis function is everywhere pointwise non-negative and has compact support in $p + 1$ knot spans, i.e. $\text{supp}(R_i) \subseteq [\xi_i, \xi_{i+p+1}]$ for $i = 1, \dots, n$; moreover, $p + 1$ basis functions have support in each knot span.

By assuming that the basis functions R_i , for $i = 1, \dots, n$, are sufficiently regular in $\eta \in \hat{\Omega}$, an explicit formula for the l -th derivative of univariate NURBS basis functions can be provided, applying the quotient rule. In particular, from Eq. (1.2) we have that:

$$\frac{d^l}{d\eta^l} R_i(\eta) = \frac{\omega_i \frac{d^l}{d\eta^l} N_i(\eta) - \sum_{j=1}^l \binom{l}{j} \frac{d^j}{d\eta^j} W(\eta) \frac{d^{l-j}}{d\eta^{l-j}} R_i(\eta)}{W(\eta)}. \quad (1.12)$$

The univariate NURBS space on the parametric domain $\hat{\Omega}$, spanned by the NURBS basis functions previously described, is denoted as:

$$\mathcal{N}^h := \text{Span}(\{R_i\}_{i=1}^n), \quad (1.13)$$

where, as before, the parameter h indicates the global mesh size.

These arguments can be easily generalized to define *multivariate NURBS basis functions* and related *multivariate NURBS spaces*. For $\alpha = 1, \dots, \kappa$, given κ knot vectors $\Xi_\alpha = \{\xi_1^\alpha, \xi_2^\alpha, \dots, \xi_{n_\alpha+p_\alpha+1}^\alpha\}$ and their associated multivariate B-Splines basis $\{N_i\}_{i \in I}$, as given in Eq. (1.5). Assigned a set of weights $\omega = \{\omega_i\}_{i \in I}$, where, as previously, $I = \{\mathbf{i} = (i_1, \dots, i_\kappa) : 0 \leq i_\alpha \leq n_\alpha, 1 \leq \alpha \leq \kappa\}$, a *weighting function* is defined over the parametric domain $\hat{\Omega} = [0, 1]^\kappa$ as:

$$W : \hat{\Omega} \rightarrow \mathbb{R}, \quad W(\boldsymbol{\eta}) := \sum_{\mathbf{i} \in I} \omega_{\mathbf{i}} N_{\mathbf{i}}(\boldsymbol{\eta}). \quad (1.14)$$

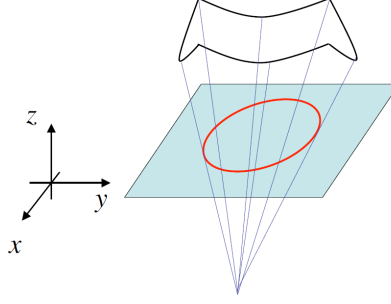


Figure 1.4: Projection of a piecewise quadratic B-Splines curve in \mathbb{R}^3 into a plane. The resulting object (red) is a NURBS curve.

This leads to the definition of the i -th multivariate NURBS basis function:

$$R_i : \hat{\Omega} \rightarrow \mathbb{R}, \quad R_i(\boldsymbol{\eta}) = \frac{N_i(\boldsymbol{\eta})\omega_i}{W(\boldsymbol{\eta})} \quad \forall i \in I, \quad (1.15)$$

whose properties can be deduced by the ones of the related multivariate B-Splines basis $\{N_i\}_{i \in I}$ and the tensor product structure. Moreover, the resulting NURBS space over the parametric domain $\hat{\Omega}$ reads:

$$\mathcal{N}^h := \text{Span}(\{R_i\}_{i \in I}). \quad (1.16)$$

Remark 1.3. If for all $i \in I$, the weights are unitary, i.e. $\omega_i = 1$ (or constant), we obtain that $R_i \equiv N_i$ for all i ; indeed, B-Splines represents a particular case of NURBS.

1.1.6 NURBS geometries

NURBS geometrical entities can be described from two different perspectives: the geometrical and algebraical points of view.

From the geometrical point of view, a NURBS geometry in \mathbb{R}^d is obtained by projecting a B-Splines geometry in \mathbb{R}^{d+1} onto an hypersurface in \mathbb{R}^d . The resulting object is, then, identified with the corresponding physical domain $\Omega \subseteq \mathbb{R}^d$. In particular, conic sections can be exactly represented by the projective transformation of piecewise quadratic B-Splines, as shown in Figure 1.4.

Given a B-Splines curve C^ω called in this context *projective curve* and defined through basis functions the $\{N_i\}_{i=1}^n$ in the domain $\hat{\Omega} = [0, 1]$ and control points $\{\mathbf{P}_i^\omega\}_{i=1}^n \subseteq \mathbb{R}^{d+1}$, which we call *projective control points* (we assume that these lie in the positive semi-space $\{\mathbf{x} \in \mathbb{R}^{d+1} : x_{d+1} > 0\}$), with $\omega_i = (\mathbf{P}_i^\omega)_{d+1}$. The projection of the B-Splines curve into the plane $\{\mathbf{x} \in \mathbb{R}^{d+1} : x_{d+1} = 1\}$ is the ratio of two piecewise polynomials and defines a *NURBS curve*. In particular, we can apply this transformation to the set of projective control points $\{\mathbf{P}_i^\omega\}_{i=1}^n$ to obtain the *control points* associated to the NURBS curve, which are given by $(\mathbf{P}_i)_j = \frac{(\mathbf{P}_i^\omega)_j}{\omega_i}$ for all $j = 1, \dots, d$, where $(\mathbf{P}_i)_j$ indicates the j -th component of the i -th control point $\mathbf{P}_i \in \mathbb{R}^d$. We can interpret ω_i as the *weights* for $i = 1, \dots, n$ defining the *weighting function* W of Eq. (1.10). In this manner, the NURBS curve $\mathbf{C} : \hat{\Omega} \rightarrow \mathbb{R}^d$ is given component-wise by:

$$\mathbf{C} : \hat{\Omega} \rightarrow \Omega \subseteq \mathbb{R}^d, \quad (\mathbf{C}(\boldsymbol{\eta}))_j = \frac{(\mathbf{C}^\omega(\boldsymbol{\eta}))_j}{W(\boldsymbol{\eta})} \quad \forall j = 1, \dots, d. \quad (1.17)$$

By adopting an algebraic perspective, we define the NURBS geometries through *control points* and the uni- and multivariate NURBS bases defined in Section 1.1.5.

Definition 1.3. *By means of a NURBS basis $\{R_i\}_{i \in I}$, whose basis functions defined in $\hat{\Omega} = [0, 1]^\kappa$ are given in Eq. (1.15), and a set of $\Pi_{\alpha=1}^\kappa n_\alpha$ control points $\{\mathbf{P}_i\}_{i \in I} \subseteq \mathbb{R}^d$, a NURBS geometry in \mathbb{R}^d is represented by the geometrical mapping:*

$$\mathbf{x} : \hat{\Omega} \rightarrow \Omega \subseteq \mathbb{R}^d, \quad \mathbf{x}(\boldsymbol{\eta}) = \sum_{i \in I} R_i(\boldsymbol{\eta}) \mathbf{P}_i. \quad (1.18)$$

As for B-Splines, it is important to underline that a NURBS geometry is defined as a map from the parametric domain $\hat{\Omega} = [0, 1]^\kappa$ into the physical space \mathbb{R}^d , to which the control points belong. The properties of NURBS geometries derive from the ones of the NURBS basis functions. In particular, the regularity and locality properties (referring, as for B-Splines geometries, to each parametric direction) still hold, as well as the affine covariance, convex hull and end-point (corner-point) interpolation properties. Moreover, the variation diminishing property, for which no plane has more intersections with the curve than with the control polygon, is valid also for NURBS curves.

In view of Isogeometric Analysis, for which we consider NURBS as the basis used for the analysis, other than for the representation of the physical domain Ω by means of the geometrical mapping \mathbf{x} of Eq. (1.18), we restrict hereafter to the case in which the dimension κ of the parametric space \mathbb{R}^κ equals the one relative to the physical space \mathbb{R}^d , i.e. $\kappa = d$ and $\hat{\Omega}, \Omega \subseteq \mathbb{R}^d$. Moreover, we introduce the *deformation tensor* and *Jacobian* of the map.

Definition 1.4. *We define the deformation tensor of the geometrical mapping (1.18) as:*

$$T : \hat{\Omega} \rightarrow \mathbb{R}^{d \times d}, \quad T_{ij}(\boldsymbol{\eta}) := \frac{\partial \mathbf{x}_i}{\partial \eta_j}(\boldsymbol{\eta}), \quad \forall i, j = 1, \dots, d, \quad (1.19)$$

and Jacobian of the mapping:

$$J : \hat{\Omega} \rightarrow \mathbb{R}, \quad J(\boldsymbol{\eta}) := \det(T(\boldsymbol{\eta})). \quad (1.20)$$

From the geometrical point of view, there will be no impediment in considering NURBS geometries defined by maps with non-constant sign Jacobian. We will call them *degenerate geometries* and an example of them is represented by geometries characterized by *crossing* control points. However, we assume that the following necessary condition must be satisfied by the geometries considered:

$$J(\boldsymbol{\eta}) > 0 \text{ a.e. in } \hat{\Omega} \text{ with } |\hat{\Omega}_{J_0}| = 0, \quad (1.21)$$

where $\hat{\Omega}_{J_0} := \{\boldsymbol{\eta} \in \hat{\Omega} : J(\boldsymbol{\eta}) = 0\}$ and $|\cdot|$ is the measure with respect to the topology of the parameter space. Degenerate geometries are studied in [LEB⁺10]. Moreover, the geometrical mapping given in Eq. (1.18) is assumed to be invertible, with smooth inverse on each element K of the *physical mesh* \mathcal{K}_h introduced in Eq. (1.9).

In virtue of the geometrical mapping (1.18), we define the space of NURBS in the domain Ω as the push-forward of the space $\mathcal{N}^h = \text{Span}(\{R_i\}_{i \in I})$ of Eq. (1.16), for which:

$$\mathcal{V}^h := \text{Span}(\{R_i \circ \mathbf{x}^{-1}\}_{i \in I}) = \text{Span}(\{\mathcal{R}_i\}_{i \in I}), \quad (1.22)$$

We denote with $\{\mathcal{R}_i\}_{i \in I}$ the NURBS basis in the physical domain, with $\mathcal{R}_i := R_i \circ \mathbf{x}^{-1}$ for all $i \in I = \{i = (i_1, \dots, i_\kappa) : 0 \leq i_\alpha \leq n_\alpha, 1 \leq \alpha \leq \kappa\}$.

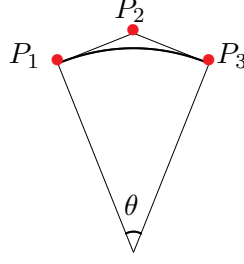


Figure 1.5: Example 1.3: Arc obtained with NURBS basis of degree $p = 2$ and control points (•) P_i , for $i = 1, \dots, 3$.

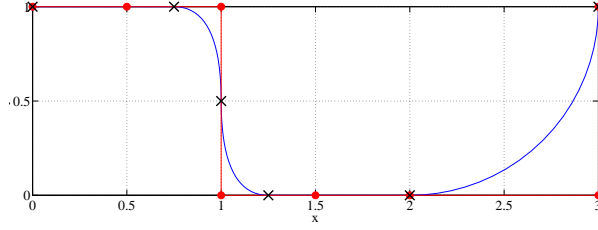
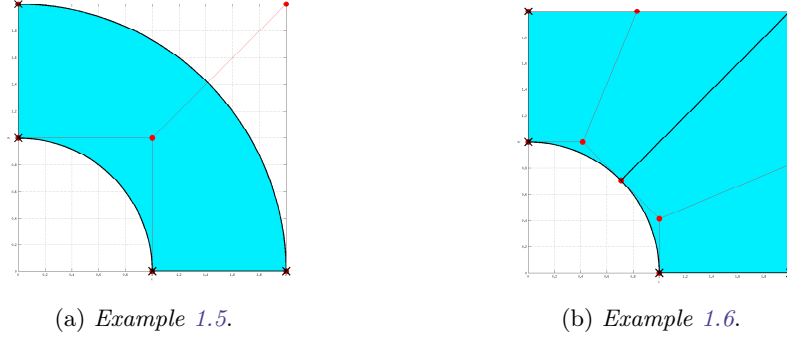
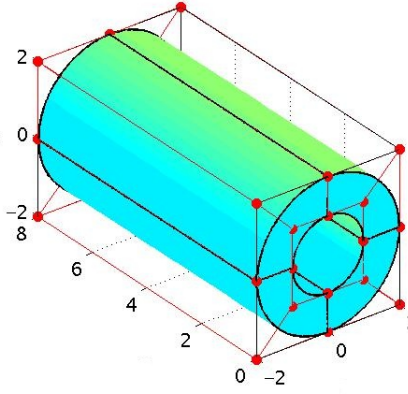


Figure 1.6: Example 1.4: NURBS curve built considering the open knot vector $\Xi = \{0, 0, 0, 1/6, 2/6, 3/6, 4/6, 5/6, 5/6, 1, 1, 1\}$ and control points marked by •. The geometrical mapping of the knots in the physical domain, denoted by ×, defines the boundaries of elements K in the physical mesh \mathcal{K}^h .

Example 1.3 (NURBS curve). We represent an arc of circumference, corresponding to an angle of size $\theta \leq \pi/2$. We consider a NURBS basis function of degree $p = 2$, defined by the open knot vector $\Xi = \{0, 0, 0, 1, 1, 1\}$ and weights $\omega_1 = \omega_3 = 1$, while $\omega_2 = \cos(\theta/2)$. Then, the control points are located as shown in Figure 1.5, i.e. P_1 and P_3 represent the arc terminal points (due to the end-points interpolation property), while P_2 is located at the intersection of the tangent lines to the curve in P_1 and P_3 . \diamond

Example 1.4 (NURBS curve). We build the NURBS curve \mathbf{C} given in Figure 1.6 with the following requirements on its regularity: $\frac{d\mathbf{C}}{d\eta}(0) = \frac{d^2\mathbf{C}}{d\eta^2}(0) = 0$, $\frac{d\mathbf{C}}{d\eta}(1/3^-) = \frac{d^2\mathbf{C}}{d\eta^2}(1/3^-) = 0$, $\frac{d\mathbf{C}}{d\eta}(1/3^+) = 0$ and $\frac{d^2\mathbf{C}}{d\eta^2}(1/3^+) \neq 0$. The univariate NURBS basis is defined by means of the open knot vector $\Xi = \{0, 0, 0, 1/6, 2/6, 3/6, 4/6, 5/6, 5/6, 1, 1, 1\}$, degree of basis functions $p = 2$ and weights $\omega_i = 1$ for all $i = 1, \dots, 6$, while $\omega_7 = \omega_9 = 1$ and $\omega_8 = \sqrt{2}/2$. Control points are located as in Figure 1.6, i.e. $P_1 = [0, 1]^T$, $P_2 = [1/2, 1]^T$, $P_3 = [1, 1]^T$, $P_4 = [1, 0]^T$, $P_5 = [3/2, 0]^T$, $P_6 = [2, 0]^T$, $P_7 = [2, 0]^T$, $P_8 = [3, 0]^T$ and $P_9 = [3, 1]^T$. \diamond

Example 1.5 (NURBS surface). By using the tensor product structure, a quarter of an annulus can be easily constructed by building univariate NURBS in the radial and angular directions. The bivariate NURBS basis is defined by means of the knot vectors $\Xi_1 = \{0, 0, 1, 1\}$ (for the radial direction) and $\Xi_2 = \{0, 0, 0, 1, 1, 1\}$ (for the angular component) and weights $\omega_{1,1} = \omega_{1,3} = 1$, $\omega_{1,2} = \sqrt{2}/2$, $\omega_{2,1} = \omega_{2,3} = 1$, $\omega_{2,2} = \sqrt{2}/2$, where the subscripts refers to the parametric directions. Then, the NURBS surface shown in Figure 1.7a is obtained by choosing control points as $P_{1,1} = [1, 0]^T$, $P_{1,2} = [1, 1]^T$, $P_{1,3} = [0, 1]^T$, $P_{2,1} = [2, 0]^T$, $P_{2,2} = [2, 2]^T$, $P_{2,3} = [0, 2]^T$. \diamond

Figure 1.7: Examples 1.5 and 1.6: control points denoted by \bullet .Figure 1.8: Example 1.7: NURBS solid generated from the knot vectors $\Xi_1 = \{0, 0, 1, 1\}$ (radial component), $\Xi_2 = \{0, 0, 0, 1/4, 1/4, 1/2, 1/2, 3/4, 3/4, 1, 1, 1\}$ (angular component) and $\Xi_3 = \{0, 0, 1, 1\}$ (depth). Control points are \bullet .

Example 1.6 (NURBS surface). In Figure 1.7b it is shown a NURBS surface built by means of the open knot vectors $\Xi_1 = \{0, 0, 1, 1\}$ (radial component) and $\Xi_2 = \{0, 0, 0, 1/2, 1/2, 1, 1, 1\}$ (angular component). Control points are located as in Figure 1.7b. \diamond

Example 1.7 (NURBS solid). We want to construct a linear tube, with length L , inner radius r , and outer radius R . The geometry is defined by means of open knot vectors $\Xi_1 = \{0, 0, 1, 1\}$ (radial component), $\Xi_2 = \{0, 0, 0, 1/4, 1/4, 1/2, 1/2, 3/4, 3/4, 1, 1, 1\}$ (angular component) and $\Xi_3 = \{0, 0, 1, 1\}$ (depth), and weights: $\omega_{(i_1, i_2, i_3)} = \sqrt{2}/2$ for $i_1, i_3 = 1, 2$ and $i_2 = 2, 4, 6, 8$, otherwise $\omega_{(i_1, i_2, i_3)} = 1$. Control points are located as in Figure 1.8. \diamond

1.1.7 h -, p - and k -refinements

In order to build more detailed geometries, but also in view of the enrichment of the NURBS space \mathcal{N}^h of Eq. (1.13), we recall the refinement procedures that can be performed within the B-Splines and NURBS frameworks. In particular, two kind of refinement, called h - and p -refinement, are affine with those used in FEA with the Lagrangian globally \mathcal{C}^0 -continuous basis. However, a third possibility, referred as k -refinement is peculiar to the NURBS and B-splines basis. We will briefly describe them for an univariate B-Splines basis. For a detailed description of refinements, we refer to [CHB09, CHR07].

h -refinement (knot insertion). Let $\Xi = \{\xi_1, \xi_2, \dots, \xi_{n+p+1}\}$ be the knot vector which defines a B-Splines basis and consider a knot to be inserted in Ξ , $\bar{\xi} \in [\xi_l, \xi_{l+1})$. By applying the recursive formula in (1.0) to the *extended* knot vector $\bar{\Xi} = \{\bar{\xi}_1, \bar{\xi}_2, \dots, \bar{\xi}_{n+p+1+1}\} := \{\xi_1, \xi_2, \dots, \xi_l, \bar{\xi}, \xi_{l+1}, \dots, \xi_{n+p+1}\}$, a new set of $n+1$ basis functions is obtained and their span, $\bar{\mathcal{S}}^h := \text{Span}(\{\bar{N}_i\}_{i=1}^n + 1)$ is nested in $\mathcal{S}^h := \text{Span}(\{N_i\}_{i=1}^n)$. Thus, for a curve in \mathbb{R}^d a new set of control points should be defined for the new basis in order to obtain a curve which is geometrically and parametrically equivalent to the original one. Moreover, h -refinement allows to increase the number of elements of a mesh by adding new knots, but also to reduce the regularity of the basis functions when inserting new knot $\bar{\xi}$ already present in Ξ . Through this kind of refinement, the number of elements increases, as well as the number of basis functions and, consequently, the number of control points.

Example 1.8 (h -refinement). An example of knot insertion is given in Figure 1.9b, where we perform a single knot insertion, adding a new knot value. Taking into account the relation $n = n_{\text{ks}} + p$, the number of basis functions increases by one and they are \mathcal{C}^1 -continuous in the new knot $\zeta_2 = 1/2$, which defines $\bar{\Xi} = \{0, 0, 1/2, 1, 1\}$; nevertheless, the regularity of the curve is preserved by suitably choosing the new set of control points $\{\bar{P}_i\}_{i=1}^{n+1}$. The physical mesh $\bar{\mathcal{K}}^h$ on the curve has two elements whose size is an half of the single element constituting the original physical mesh \mathcal{K}^h . \diamond

p -refinement (order elevation). Analogously with the p -refinement procedure of FEA, we can elevate the polynomial order of the basis functions; we refer to this process as *order elevation* or *p -refinement*. As for knot insertion, it is performed in such a manner that both the parametrization and the geometry of the original curve are preserved. Since we want to preserve also the regularity of the basis in the whole domain, it follows that, when performing an order elevation, the multiplicity of each existing knot in Ξ has to be increased by one, without inserting any additional knots. The implementation of this kind of refinement is, in general, less straightforward than knot insertion. We refer to [PT97] for suitable algorithms. As for h -refinement, the p -refined procedure leads to the generation of nested function spaces, i.e. $\bar{\mathcal{S}}^h \subseteq \mathcal{S}^h$.

Example 1.9 (p -refinement). In Figure 1.9c we illustrate an example of p -refinement for the same curve shown in Figure 1.9a and already used in the Example 1.8. We obtain $\bar{\Xi} = \{0, 0, 0, 1, 1, 1\}$. We notice that the position of the control points and the basis functions are different for the two procedures, but the curve is left unchanged. \diamond

k-refinement. The fact that order elevation and knot insertion procedures do not commute, introduces the possibility of a new refinement strategy, called *k -refinement*, which has not analogue in FEA, [CHB09].

Let us consider a B-Splines basis of degree p . If a knot insertion is performed, when adding a new knot $\bar{\xi}$, the basis functions in $\bar{\xi}$ are \mathcal{C}^{p-1} -continuous. This regularity in $\bar{\xi}$ is preserved if we subsequently elevate the degree to $q \geq p$ with the multiplicity of each knot, including $\bar{\xi}$, increased accordingly. On the other hand, we can first perform order elevation, until the polynomial degree is q and then insert a new knot value $\bar{\xi}$. In this case the number of non-zero knot spans is still the same as before, but the basis functions are now \mathcal{C}^{q-1} -continuous in $\bar{\xi}$, instead of only \mathcal{C}^{p-1} -continuous, the regularity attained according to the previous procedure. The latter procedure is referred to as *k -refinement*.

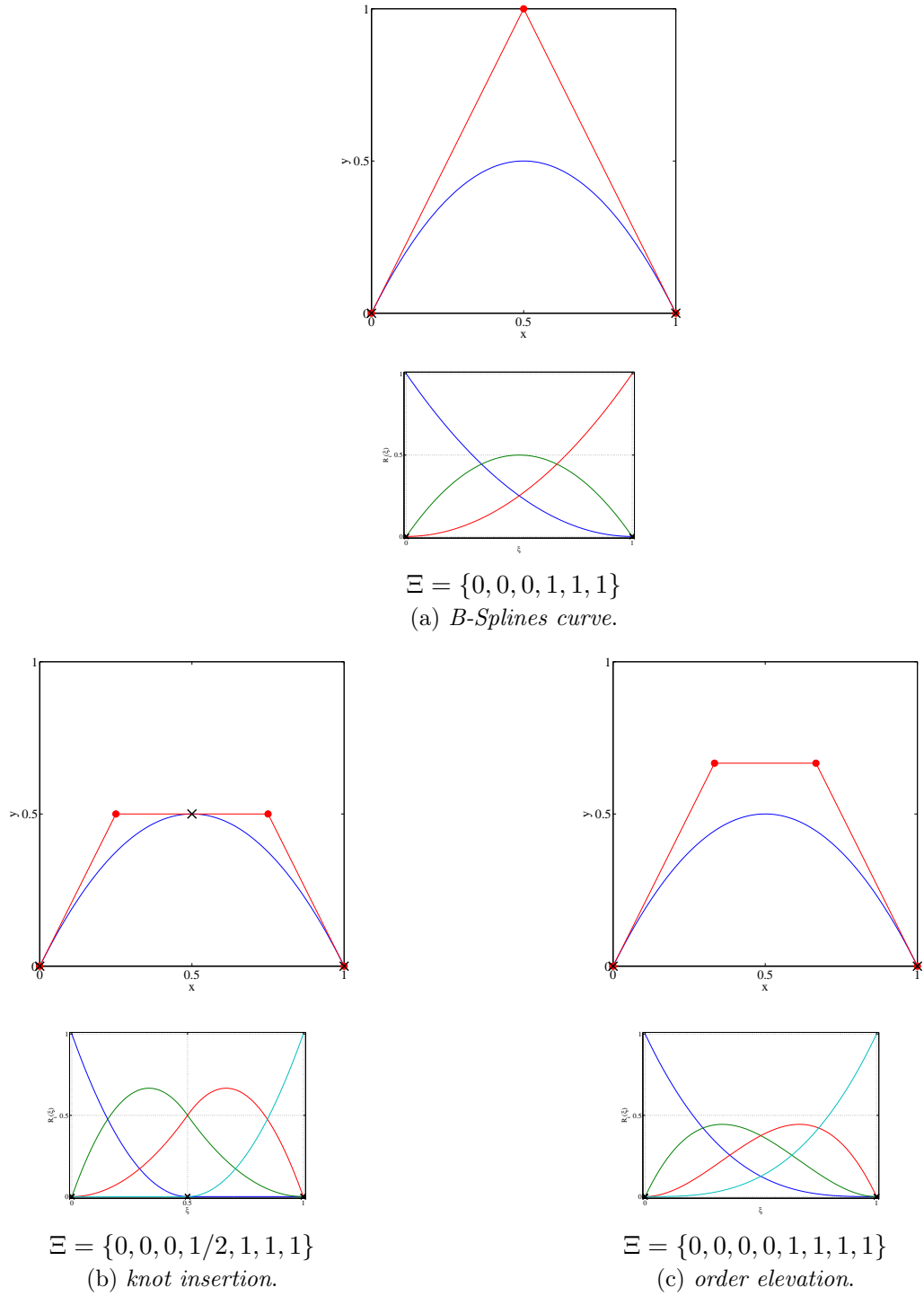


Figure 1.9: Refinements: comparison between *knot insertion* (b) and *order elevation* (c) starting from the same B-Splines curve shown in (a); control points (\bullet), and knots in the physical mesh (\times). The corresponding basis functions and the knot vectors are reported.

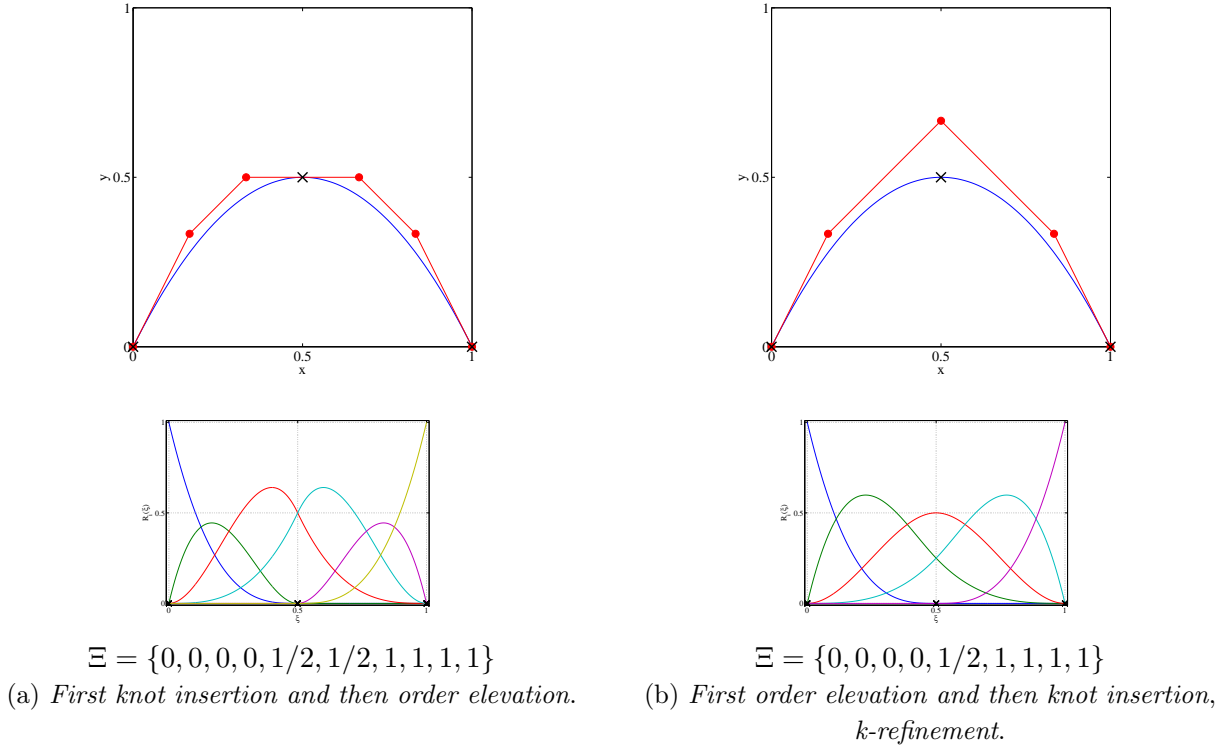


Figure 1.10: Refinements: comparison between performing firstly *knot insertion*, then *order elevation* (a), and performing firstly *order elevation*, then *knot insertion* (b), starting from the same B-Splines curve of Figure 1.9a; control points (•), and knots in the physical domain (×). The corresponding basis functions and the knot vectors are reported.

Example 1.10. We show that the order elevation and knot insertion procedures do not commute in Figure 1.10. We start from the same curve of Figure 1.9a and we perform a single knot insertion and order elevation in different orders. As we can see, we obtain bases with different regularity and number of basis functions; as a result, also the number and the locations of control points is different for a curve parametrized in the new spaces. The knot vector associated to the k -refinement is $\bar{\Xi} = \{0, 0, 0, 0, 1/2, 1, 1, 1, 1\}$, starting from $\Xi = \{0, 0, 0, 1, 1, 1\}$. \diamond

Simply considering the regularity of the new set of basis functions, obtained through k -refinement, it is straightforward to observe that the procedure does not lead to sequences of nested spaces, $\bar{\mathcal{S}}^h \not\subseteq \mathcal{S}^h$. Because of this, k -refinement cannot be referred as a refinement in the classical sense. Nevertheless, there is an important advantage associated to k -refinement, since it allows to increase the regularity of the basis functions by limiting their number.

Remark 1.4. The h -, p - and k -refinement procedures can be extended to multivariate B-Splines basis and geometries, in virtue of the tensor product structure. Moreover, they can be performed as well as for NURBS. We observe that after refinement, the weights defining the NURBS basis functions will change, similarly to the control points. Nevertheless, both the weighting function W of Eq. (1.14) and the geometrical mapping \mathbf{x} of Eq. (1.18), which define the NURBS geometries, are preserved under refinement.

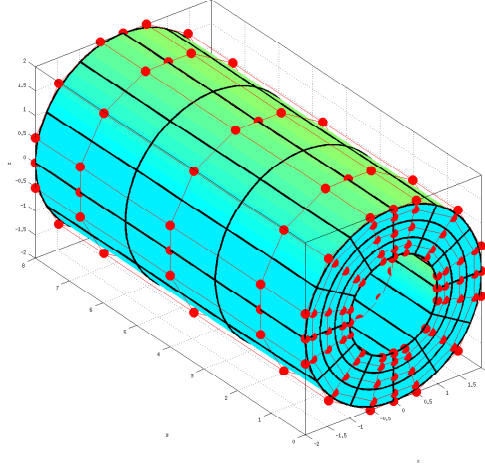


Figure 1.11: Example 1.7: k -refinement of the NURBS solid reported in Figure 1.8. Resulting control points are located in \bullet and the knot vectors are: $\Xi_1 = \{0, 0, 0, 1/3, 2/3, 1, 1, 1\}$, $\Xi_2 = \{0, 0, 0, 1/12, 2/12, 3/12, 4/12, 5/12, 6/12, 6/12, 7/12, 8/12, 9/12, 9/12, 10/12, 11/12, 1, 1, 1\}$ and $\Xi_3 = \{0, 0, 0, 1/3, 2/3, 1, 1, 1\}$.

Example. 1.7 (NURBS solid and k -refinement). For the NURBS solid defined in Example 1.7, we perform k -refinement in order to achieve in each parametric direction the same degree $p = 3$ and a number of basis functions equal to $3 \times 12 \times 3$. The knot vectors obtained and the location of control points are reported in Figure 1.11. \diamond

1.2 Galerkin method for IGA

In this section we consider NURBS as a basis for analysis and we present the IGA-Galerkin method based on NURBS for the approximation of PDEs. Specifically, we consider the general case of high order PDEs.

Given a NURBS basis $\{R_i\}_{i \in I}$ in the parameter domain $\hat{\Omega} \subseteq \mathbb{R}^d$, a real valued function \hat{u}_h can be represented in $\hat{\Omega}$ as:

$$\hat{u}_h : \hat{\Omega} \rightarrow \mathbb{R}, \quad \hat{u}_h(\boldsymbol{\eta}) := \sum_{i \in I} R_i(\boldsymbol{\eta}) d_i, \quad (1.23)$$

where $\{d_i\}_{i \in I} \subseteq \mathbb{R}$ are the *control variables*. We have already use the subscript $_h$ referring to the global mesh size, to remark that we are defining functions over the finite dimensional NURBS space \mathcal{N}^h of Eq. (1.16).

By considering a composition with the inverse of the geometrical mapping (1.18), a function defined in the physical domain Ω can be expressed as an element of the space \mathcal{V}^h (1.22) as:

$$u_h : \Omega \rightarrow \mathbb{R}, \quad u_h(\mathbf{x}) = \hat{u}_h \circ \mathbf{x}^{-1}(\mathbf{x}) = \sum_{i \in I} R_i(\mathbf{x}^{-1}(\mathbf{x})) d_i = \sum_{i \in I} \mathcal{R}_i(\mathbf{x}) d_i. \quad (1.24)$$

Given a well posed boundary value problem, we look for an approximate solution in the form (1.24) by means of suitable *numerical methods*. In particular, we refer to the *Galerkin method* [SF73, Qua09], for which, after providing the variational formulation of the problem,

the approximate solution is sought in a suitable finite dimensional space, which we assume to be the NURBS space \mathcal{V}^h . In this section we describe the IGA-Galerkin method for the solution of general high order scalar elliptic boundary value problems.

Remark 1.5. *Usually, the geometry, i.e. the computational domain Ω , is represented at the coarsest level of discretization and h -, p -, k -refinement, as described in Section 1.1.7, are performed according to accuracy requirements to enrich the NURBS spaces \mathcal{N}^h and \mathcal{V}^h . We will denote by \mathcal{Q}_{h_0} the coarsest mesh of the family of meshes $\{\mathcal{Q}_h\}_h$, obtained by performing h -refinement. The weighting function W in Eq. (1.14), and the geometrical mapping \mathbf{x} in Eq. (1.18), are maintained fixed at the coarsest level of discretization; see Remark 1.4.*

1.2.1 High order scalar elliptic PDEs: variational formulation

Let us consider a domain $\Omega \subseteq \mathbb{R}^d$, i.e. a connected open subset of the finite dimensional space \mathbb{R}^d , whose boundary $\partial\Omega$ is sufficiently regular. An *elliptic boundary value problem* of order $2m$ is defined once provided an elliptic linear partial differential operator \mathcal{L} of order $2m$ and a normal set of boundary operators $\{\mathcal{B}_j\}_{j=1}^m$. The problem in *strong form* reads:

$$\text{find } u : \Omega \rightarrow \mathbb{R} \quad : \quad \begin{cases} \mathcal{L}u = f & \text{in } \Omega, \\ \mathcal{B}_j u = g_j & \text{on } \partial\Omega \quad \forall j = 1, \dots, m, \end{cases} \quad (1.25a)$$

for given functions f and g_j for $j = 1, \dots, m$ which must satisfy suitable regularity hypotheses, for which we refer to [Ode00].

The *weak formulation* of problem (1.25a) is obtained by multiplying the partial differential equation (1.25a) governing the problem, by a *test function* $v \in V$, with V a suitable function space depending on the order of the operator \mathcal{L} and on the set of boundary conditions (1.25b), and then integrating over the domain Ω . This yields:

$$\text{find } u : \Omega \rightarrow \mathbb{R} \quad : \quad (\mathcal{L}u, v)_{L^2(\Omega)} = (f, v)_{L^2(\Omega)} \quad \forall v \in V. \quad (1.26)$$

Specifically, V is defined as the subspace of $H^m(\Omega)$ whose functions satisfy the homogeneous counterpart of the *essential boundary conditions*, say $\{\mathcal{B}_{\tilde{j}}^{Ess} u = g_{\tilde{j}}\}_{\tilde{j}=1}^{\tilde{m}} \subseteq \{\mathcal{B}_j u = g_j\}_{j=1}^m$, with $\tilde{m} \leq m$ defining the problem (1.25a), i.e.:

$$V := \{v \in H^m(\Omega) : \mathcal{B}_{\tilde{j}}^{Ess} v = 0 \text{ for } \tilde{j} = 1, \dots, \tilde{m}\}. \quad (1.27)$$

Let us assume for the moment to consider the case in which the essential boundary conditions are homogeneous, i.e. $g_{\tilde{j}} = 0$ for all $\tilde{j} = 1, \dots, \tilde{m}$, then, by setting $u = u_0$, we can provide the so called *variational formulation* of problem (1.25a) which seeks for a solution in the space V and for which the problem reads:

$$\text{find } u_0 \in V \quad : \quad a(u_0, v) = F(v) \quad \forall v \in V, \quad (1.28)$$

where $a : V \times V \rightarrow \mathbb{R}$ is a bilinear form related to the the differential operator \mathcal{L} and $F : V \rightarrow \mathbb{R}$ is a linear functional depending on the source term f and on the *natural boundary conditions*, that are naturally embedded in the weak form of the problem. We observe that in the case of non homogeneous boundary conditions, the problem can be recast in the form (1.28) by introducing a suitable *lifting function*, say \bar{g} , such that $u = u_0 + \bar{g}$. We will discuss in Example 1.11 this case for the Poisson problem.

The equivalence between the problem in strong form (1.25a) and its variational formulation (1.28) is satisfied in the sense of distributions; moreover, the well posedness of problems in the form (1.28) is established in the *Lax-Milgram Lemma* (see for instance [Qua09, Ode00]).

Theorem 1.1 (Lax-Milgram Lemma).

Given the problem (1.28) defined on the Hilbert space endowed with norm $\|\cdot\|_V$. If the following hypotheses are satisfied:

- i) $a(\cdot, \cdot)$ is continuous, i.e. there exists $M > 0$ such that $|a(w, v)| \leq M\|w\|_V\|v\|_V$ for all $w, v \in V$,
- ii) $a(\cdot, \cdot)$ is strongly coercive, i.e. there exists $\alpha > 0$ such that $a(v, v) \geq \alpha\|v\|_V^2$ for all $v \in V$,
- iii) $F \in V'$, i.e. $F(\cdot)$ is a linear and continuous functional,

then, there exists a unique solution $u_0 \in V$ of problem (1.28) and $\|u_0\|_V \leq \frac{1}{\alpha}\|F\|_{V'}$.

We consider now some examples of elliptic PDEs with operators \mathcal{L} of order $m \geq 1$ in order to provide their variational formulation. We characterize the space of admissible solutions V , explaining the choice made in the definition (1.27), and we explicit the dependence of the bilinear form $a(\cdot, \cdot)$ and of the linear functional $F(\cdot)$ on the data defining the problem (1.25a) in its strong form.

Example 1.11 (Poisson problem). Let $\Omega \subseteq \mathbb{R}^2$ a domain whose boundary is partitioned in $\Gamma_D, \Gamma_N \subseteq \partial\Omega$ such that $\overline{\Gamma_D \cup \Gamma_N} = \partial\Omega$ and $\overset{\circ}{\Gamma}_D \cap \overset{\circ}{\Gamma}_N = \emptyset$. The known functions $f : \Omega \rightarrow \mathbb{R}$ with $f \in L^2(\Omega)$, $\mu : \Omega \rightarrow \mathbb{R}$ with $\mu \in L^\infty(\Omega)$ and $\mu(\mathbf{x}) \geq \mu_0 > 0$ a.e. in Ω , are assigned. Moreover, we assume $g : \Gamma_D \rightarrow \mathbb{R}$ with $g \in H^{1/2}(\Gamma_D)$ and $h : \Gamma_N \rightarrow \mathbb{R}$ with $h \in L^2(\Gamma_N)$. The problem reads:

$$\text{find } u : \Omega \rightarrow \mathbb{R} \quad : \quad \begin{cases} -\nabla \cdot (\mu \nabla u) = f & \text{in } \Omega, \\ u = g & \text{on } \Gamma_D, \\ \mu \nabla u \cdot \mathbf{n} = h & \text{on } \Gamma_N, \end{cases} \quad \begin{array}{l} (1.29a) \\ (1.29b) \\ (1.29c) \end{array}$$

To reduce the problem to the variational formulation (1.28), firstly, we multiply Eq. (1.29a) by an arbitrary test function $v \in V$, with V to be defined, and then we apply the Green's formula, to obtain the relation:

$$\int_{\Omega} \mu \nabla u \cdot \nabla v \, d\Omega - \int_{\Gamma_D} \mu \nabla u \cdot \mathbf{n} v \, d\Gamma = \int_{\Omega} f v \, d\Omega + \int_{\Gamma_N} v h \, d\Gamma. \quad (1.30)$$

By defining the *test space* V as the space of functions satisfying homogeneous essential boundary conditions in the sense of the trace, i.e.:

$$V := \{v \in H^1(\Omega) : v|_{\Gamma_D} = 0\}, \quad (1.31)$$

we obtain that for $v \in V$ the second integral in the left hand side of Eq. (1.30) is zero. Since the solution u satisfies essential boundary conditions which are not homogeneous (the data g is not necessary zero), we introduce the so called, *lifting function* \bar{g} such that $\bar{g} \in H^1(\Omega)$ and $\bar{g}|_{\Gamma_D} = g$. In this way, for the solution u belonging to the *trial space* defined as:

$$V_g := \{u \in H^1(\Omega) : u|_{\Gamma_D} = g\}, \quad (1.32)$$

there exists a unique $u_0 \in V$ such that $u = \bar{g} + u_0$.

The problem in variational formulation reads as in Eq. (1.28) with $a(u_0, v) := \int_{\Omega} \mu \nabla u_0 \cdot \nabla v \, d\Omega$ and $F(v) := \int_{\Omega} f v \, d\Omega + \int_{\Gamma_N} v h \, d\Gamma - \int_{\Omega} \mu \nabla \bar{g} \cdot \nabla v \, d\Omega$. \diamond

Remark 1.6. Often the weak formulation of a boundary value problem can be expressed by considering the following formulation, for which we look for a solution in a function space different from the test space, i.e.:

$$\text{find } u \in V_g \quad : \quad a(u, v) = \bar{F}(v) \quad \forall v \in V, \quad (1.33)$$

where the linear functional $\bar{F} : V \rightarrow \mathbb{R}$ reads $\bar{F}(v) := \int_{\Omega} f v \, d\Omega + \int_{\Gamma_N} v h \, d\Gamma$ for all $v \in V$.

Example 1.12. (Advection-diffusion problem) We consider an advection-diffusion equation, for which the operator \mathcal{L} is not self-adjoint and the bilinear form $a(\cdot, \cdot)$ is not symmetric. The problem reads:

$$\text{find } u : \Omega \rightarrow \mathbb{R} \quad : \quad \begin{cases} -\nabla \cdot (\mu \nabla u) + \mathbf{b} \cdot \nabla u = f & \text{in } \Omega, \\ u = g & \text{on } \partial\Omega, \end{cases} \quad (1.34a)$$

$$(1.34b)$$

where, in addition to hypotheses of Example 1.11, we assume that $\mathbf{b} \in [L^\infty(\Omega)]^d$ with $\nabla \cdot \mathbf{b} = 0$ a.e. in Ω ; moreover $\Gamma_D \equiv \partial\Omega$. Following the same steps as in Example 1.11, we recast problem (1.34a) in the weak form (1.33) considering as trial and test function spaces, respectively:

$$V_g = \{v \in H^1(\Omega) : v|_{\partial\Omega} = g\}, \quad (1.35a)$$

$$V = \{v \in H^1(\Omega) : v|_{\partial\Omega} = 0\}, \quad (1.35b)$$

and $a(u, v) := \int_{\Omega} \mu \nabla u \cdot \nabla v \, d\Omega + \int_{\Omega} v \mathbf{b} \cdot \nabla u \, d\Omega$ and $F(v) := \int_{\Omega} f v \, d\Omega$. Since the bilinear form $a(\cdot, \cdot)$ is no more symmetric, when the convection term dominates the diffusion one, we may obtain solutions highlighting internal and boundary layers. \diamond

Example 1.13 (Biharmonic problem). The biharmonic problem defined in a domain $\Omega \subseteq \mathbb{R}^2$ is governed by a fourth order partial differential operator $\mathcal{L} = \Delta^2$, often called *bilaplacian*, which applied to a sufficiently regular function u reads:

$$\Delta^2 u := \frac{\partial^4 u}{\partial x^4} + 2 \frac{\partial^4 u}{\partial x^2 \partial y^2} + \frac{\partial^4 u}{\partial y^4}. \quad (1.36)$$

We restrict to the case of essential boundary conditions on $\partial\Omega$. The problem in strong form reads:

$$\text{find } u : \Omega \rightarrow \mathbb{R} \quad : \quad \begin{cases} \Delta^2 u = f & \text{in } \Omega, \\ u = g_1 & \text{on } \partial\Omega, \\ \nabla u \cdot \mathbf{n} = g_2 & \text{on } \partial\Omega. \end{cases} \quad (1.37a)$$

$$(1.37b)$$

$$(1.37c)$$

To provide the weak form, we multiply Eq. (1.37a) by a sufficiently smooth test function v and integrate over the domain: $\int_{\Omega} \Delta^2 u v \, d\Omega = \int_{\Omega} f v \, d\Omega$. Then, we apply the Green's formula to the left hand side, to obtain $\int_{\Omega} \Delta^2 u v \, d\Omega = \int_{\Omega} \nabla \cdot (\nabla (\Delta u)) v \, d\Omega = \int_{\Omega} \nabla \cdot (\nabla (\Delta u) v) \, d\Omega - \int_{\Omega} \nabla (\Delta u) \cdot \nabla v \, d\Omega = \oint_{\partial\Omega} \nabla (\Delta u) \cdot \mathbf{n} v \, d\Gamma - \oint_{\partial\Omega} \Delta u \nabla v \cdot \mathbf{n} \, d\Gamma + \int_{\Omega} \Delta u \Delta v \, d\Omega$. This yields:

$$\int_{\Omega} \Delta u \Delta v \, d\Omega + \oint_{\partial\Omega} \nabla (\Delta u) \cdot \mathbf{n} v \, d\Gamma - \oint_{\partial\Omega} \Delta u (\nabla v \cdot \mathbf{n}) \, d\Gamma = \int_{\Omega} f v \, d\Omega. \quad (1.38)$$

We define the trial and test function spaces, respectively:

$$V_g = \{v \in H^2(\Omega) : v|_{\partial\Omega} = g_1, \quad (\nabla v \cdot \mathbf{n})|_{\partial\Omega} = g_2\}, \quad (1.39a)$$

$$V = \{v \in H^2(\Omega) : v|_{\partial\Omega} = 0, \quad (\nabla v \cdot \mathbf{n})|_{\partial\Omega} = 0\}, \quad (1.39b)$$

for which we recast the problem (1.34a) in the weak form (1.33) with the bilinear form $a(u, v) := \int_{\Omega} \Delta u \Delta v \, d\Omega$ and the linear functional $F(v) := \int_{\Omega} f v \, d\Omega$. \diamond

Example 1.14 (Trilaplacian problem). We consider a problem defined in the domain $\Omega \subseteq \mathbb{R}^2$ governed by the sixth order partial differential operator $\mathcal{L} = \Delta^3$, called *trilaplacian*, which, applied to a sufficiently smooth function u , reads:

$$\Delta^3 u := \Delta(\Delta^2 u) = \frac{\partial^6 u}{\partial x^6} + 3 \frac{\partial^6 u}{\partial x^4 \partial y^2} + 3 \frac{\partial^6 u}{\partial x^2 \partial y^4} + \frac{\partial^6 u}{\partial y^6}. \quad (1.40)$$

In such a way, the trilaplacian problem complemented by essential boundary conditions reads:

$$\text{find } u : \Omega \rightarrow \mathbb{R} \quad : \quad \begin{cases} -\Delta^3 u = f & \text{in } \Omega, \\ u = g_1 & \text{on } \partial\Omega, \\ \nabla u \cdot \mathbf{n} = g_2 & \text{on } \partial\Omega, \\ \Delta u = g_3 & \text{on } \partial\Omega. \end{cases} \quad \begin{array}{l} (1.41a) \\ (1.41b) \\ (1.41c) \\ (1.41d) \end{array}$$

In order to provide the variational formulation, as usual, we multiply the governing Eq. (1.41a) by a suitable test function v and then apply the Green's formula. Thus, defining the trial and test function spaces as, respectively:

$$V_g = \{v \in H^3(\Omega) : v|_{\partial\Omega} = g_1, \quad (\nabla v \cdot \mathbf{n})|_{\partial\Omega} = g_2, \quad \Delta v|_{\partial\Omega} = g_3\}, \quad (1.42a)$$

$$V = \{v \in H^3(\Omega) : v|_{\partial\Omega} = 0, \quad (\nabla v \cdot \mathbf{n})|_{\partial\Omega} = 0, \quad \Delta v|_{\partial\Omega} = 0\}, \quad (1.42b)$$

the weak form (1.33) is obtained with $a(u, v) := \int_{\Omega} \nabla(\Delta u) \cdot \nabla(\Delta v) \, d\Omega$ and $F(v) := \int_{\Omega} f v \, d\Omega$. \diamond

1.2.2 Galerkin method for IGA applied to high order scalar elliptic PDEs

We consider the approximation of the problem (1.28) by means of the (*Bubnov*-) *Galerkin* method [CHB09]. We consider a nontrivial and close subspace $V^h \subseteq V$ for which the variational boundary values problem (1.28) reads:

$$\text{find } u_{0h} \in V^h \quad : \quad a(u_{0h}, v_h) = F(v_h) \quad \forall v_h \in V^h. \quad (1.43)$$

where the bilinear form $a(\cdot, \cdot)$ and the linear functional $F(\cdot)$ in (1.43) are defined in Section 1.2.2 and $u_{0h} \in V^h$ represents the approximation of $u_0 \in V$, given in Eq. (1.28).

Remark 1.7. A generalization of the Galerkin method is the so called Petrov-Galerkin method, in which the finite dimensional space of test functions, say W^h , is different from the trial space V^h . Thus, the problem reads:

$$\text{find } u_{0h} \in V^h \quad : \quad a(u_{0h}, v_h) = F(v_h) \quad \forall v_h \in W^h. \quad (1.44)$$

The well-posedness of problem (1.43) is determined in the following approximation theorem; see for instance [Qua09, Ode00].

Theorem 1.2 (Approximation Theorem). *With the hypotheses of Lax-Milgram Lemma 1.1 satisfied, for the problem (1.43) there exists a unique solution $u_{0h} \in V_h$, for which the following stability estimate holds:*

$$\|u_{0h}\|_V \leq \frac{1}{\alpha} \|F\|_{V'}. \quad (1.45)$$

Moreover, the approximation error $e_h := u_0 - u_{0h}$, with u_0 the unique solution of problem (1.28), satisfies the optimal error estimate:

$$\|u_0 - u_{0h}\|_V \leq \frac{M}{\alpha} \inf_{v_h \in V^h} \|u_0 - v_h\|_V. \quad (1.46)$$

Remark 1.8. *In virtue of the optimal error estimate (1.46), in order to obtain the convergence of the method, it is sufficient to choose the family of nested spaces, say $\{V^h\}_h$, such that the following density property is satisfied:*

$$\lim_{h \rightarrow 0} \inf_{v_h \in V^h} \|v - v_h\|_V = 0 \quad \forall v \in V. \quad (1.47)$$

When considering NURBS-based IGA, the function space V^h is chosen as a finite dimensional subspace of the space \mathcal{V}^h of NURBS defined in the computational domain Ω , given in Eq. (1.22), i.e. $V^h := V \cap \mathcal{V}^h$.

Remark 1.9. *The parameter h associated to V^h corresponds the one characterizing \mathcal{V}^h and it indicates the global mesh size used for the parametrization of the physical domain as a NURBS geometry.*

By exploiting the locality of the supports of NURBS basis functions, we can identify n_{eq} basis functions that identically satisfy the homogeneous essential boundary conditions and by reordering the indexes, we assume: $\mathcal{R}_A|_{\Gamma_D} = 0$ for all $A = 1, \dots, n_{eq}$. In such a way, a basis for the finite dimensional space is provided, $V^h := \text{Span}\{\mathcal{R}_A\}_{A=1}^{n_{eq}}$, and, due to the linearity of $F(\cdot)$ and bilinearity of the form $a(\cdot, \cdot)$, it is sufficient for problem (1.43) to be verified for each basis function. Moreover, since $u_{0h} \in V^h$, we have:

$$u_{0h} = \sum_{B=1}^{n_{eq}} \mathcal{R}_B d_B, \quad (1.48)$$

with $\{d_B\}_{B=1}^{n_{eq}}$ set of unknown *control variables*. Reconsidering problem (1.43) and exploiting once more the bilinearity of the form $a(\cdot, \cdot)$, we obtain the following, equivalent discrete problem:

$$\text{find } \{d_B\}_{B=1}^{n_{eq}} \quad : \quad \sum_{B=1}^{n_{eq}} d_B a(\mathcal{R}_B, \mathcal{R}_A) = F(\mathcal{R}_A) \quad \forall A = 1, \dots, n_{eq}. \quad (1.49)$$

The finite dimensional linear system (1.49) can be rewritten in matrix form as:

$$\mathbf{A} \mathbf{d} = \mathbf{F}, \quad (1.50)$$

where $\mathbf{A} \in \mathbb{R}^{n_{eq} \times n_{eq}}$ is the *stiffness matrix*, reading component-wise $\mathbf{A}_{AB} = a(\mathcal{R}_B, \mathcal{R}_A)$, $\mathbf{d} \in \mathbb{R}^{n_{eq}}$ is the vector of unknown coefficients d_A and $\mathbf{F} \in \mathbb{R}^{n_{eq}}$ is such that $\mathbf{F}_A = F(\mathcal{R}_A)$.

Remark 1.10. Due to the locality of the supports of NURBS basis functions, \mathbf{A} is a sparse matrix, which is assembled at the element level with a connectivity array, linking every local function index to its global index; see for instance [CHB09]. Numerical integration is performed by means of suitable gaussian quadrature formula applied in the parametric domain $\hat{\Omega}$. We refer the reader to [dFRV11, Hug00] for a detailed presentation of this process; moreover, a study of efficient quadrature rules for NURBS-based isogeometric analysis has been initiated in [HRS10].

We briefly discuss the case of non homogeneous essential boundary conditions. With this aim, we consider as example the Poisson problem of Example 1.11.

Example. 1.11 (Poisson problem). The non homogeneous essential boundary condition (1.29b) is embedded in the variational formulation (1.28) in the linear functional F , by means of the lifting function \bar{g} , such that for all functions $u \in V_g$ there exists a unique $u_0 \in V$ for which $u = \bar{g} + u_0$. Regarding its discrete counterpart, the solution u_h belongs to the finite dimensional NURBS affine space $V_g^h := V_g \cap \mathcal{V}^h$, for which, if $\bar{g} \in V_g^h$, then there exists a unique $u_{0h} \in V^h$ yielding $u_h = \bar{g} + u_{0h}$. Nevertheless, not every function \bar{g} belongs to the NURBS space; in this case, we have to resort to a \bar{g}_h extension of the boundary datum g , which is only an approximation of \bar{g} , i.e. such that $\bar{g}_h \approx \bar{g}$. Thus, the finite dimensional affine space V_g^h is characterized by functions $u_h \in V_g^h$ such that $u_h|_{\Gamma_D} = \bar{g}_h|_{\Gamma_D} \approx g$. In this case the functional F of the weak form (1.43) is replaced by the following one, say F_h :

$$F_h(v) := \int_{\Omega} f v \, d\Omega + \int_{\Gamma_N} v h \, d\Gamma - \int_{\Omega} \mu \nabla \bar{g}_h \cdot \nabla v \, d\Omega. \quad (1.51)$$

In practice, by means of a suitable ordering of the degrees of freedom, \bar{g}_h can be expressed as:

$$\bar{g}_h = \sum_{A=1}^{n_{eq}} \mathcal{R}_A \bar{g}_A + \sum_{A=n_{eq}+1}^n \mathcal{R}_A \bar{g}_A; \quad (1.52)$$

in virtue of the condition $\mathcal{R}_A|_{\Gamma_D} = 0$ for all $A = 1, \dots, n_{eq}$, we can assume that $\bar{g}_A = 0$ for all $A = 1, \dots, n_{eq}$; thus, the solution u_h reads:

$$u_h = u_{0h} + \bar{g}_h = \sum_{A=1}^{n_{eq}} \mathcal{R}_A d_A + \sum_{A=n_{eq}+1}^n \mathcal{R}_A g_A. \quad (1.53)$$

Different approaches can be chosen to determine the values of the coefficients g_A . Specifically, we consider an L^2 projection of the function g on Γ_D . \diamond

Remark 1.11. In analogy with Remark 1.6, the approximation by means of the Galerkin method of the variational counterpart of problem (1.25a) reads:

$$\text{find } u_h \in V_g^h \quad : \quad a(u_h, v_h) = \bar{F}(v_h) \quad \forall v_h \in V^h, \quad (1.54)$$

with the functional $\bar{F}(\cdot)$ as in Eq. (1.33).

Example. 1.12 (Advection-diffusion problem). When approximating the solution of the advection-diffusion equation, it is well-known that the Galerkin method can provide *unstable* results when the diffusion term is largely dominated by the convection term and h is not

small enough. This can be explained considering the optimal error estimate (1.46) since, up to constants dependent on the shape of the domain Ω , the upper bound is determined by $\frac{M}{\alpha} = \frac{\|\mu\|_{L^\infty(\Omega)} + \|\mathbf{b}\|_{L^\infty(\Omega)}}{\mu_0}$, which grows with the ratio $\frac{\|\mathbf{b}\|_{L^\infty(\Omega)}}{\|\mu\|_{L^\infty(\Omega)}}$. A parameter, which measures the extent of the domination of the diffusion term over the convection term at the discrete level, is the *local Péclet number*, defined locally as $\mathbb{P}e_K := \frac{\|\mathbf{b}\|_{L^\infty(\Omega)} h_K}{2\|\mu\|_{L^\infty(\Omega)}}$, where $h_K = \text{diam}(K)$ is the element dimension in the physical mesh, defined for each $K \in \mathcal{K}_h$. When $\mathbb{P}e_K \gg 1$, the standard Galerkin formulation produces an unstable discretization of the differential non-symmetric operator; several strategies have been proposed in order to overcome this issue in the context of FEA [Qua09, SF73]. A common remedy, which increases stability within strongly consistent formulations, is the *Streamline Upwind Petrov-Galerkin (SUPG) method*. An extensive literature is devoted to its analysis in the FEA framework; see for instance [Qua09, BF91]. The SUPG method can be suitably used in the framework of IGA by augmenting the weak form (1.28) or (1.43) with the following term on the left hand side:

$$\mathcal{L}_h(u_h, f; v_h) := \sum_{K \in \mathcal{K}_h} \tau_K (-\nabla \cdot (\mu \nabla u_h) + \mathbf{b} \cdot \nabla u_h - f, \mathbf{b} \cdot \nabla v_h)_{L^2(K)}, \quad (1.55)$$

where the stabilization parameter τ_K , computed element wise, controls the amount of *artificial viscosity* introduced. In particular, we define the stabilization parameter τ_K as in [BH07]:

$$\tau_K = \frac{h_K}{2\|\mathbf{b}\|_{L^\infty(K)}} \min \left\{ 1, \frac{1}{3p^2} \mathbb{P}e_K \right\}, \quad (1.56)$$

where h_K is element size for all $K \in \mathcal{K}_h$ and p indicates the degree of the basis functions. \diamond

Remark 1.12. When considering high order PDEs, specifically of order $2m$ with $m > 1$, the weak form of the problem exhibits derivatives of the solution and test functions of order m . The numerical approximation of the problem by means of the Galerkin method requires that the basis functions are at least globally C^{m-1} -continuous in Ω . When considering the standard FEA, the Lagrangian basis functions are only globally C^0 -continuous and, in order to solve high order PDEs, we need to resort to mixed formulations or weak penalization across the mesh elements. On the contrary, NURBS-based IGA, for which we can build basis functions with the required regularity, allows the use of the standard Galerkin formulation. This leads to efficient numerical approximations in the framework of the Galerkin method formulations without the need to increase the number of variables as it is the case of mixed formulations.

1.3 A priori error estimate for elliptic PDEs

In this section we provide the *a priori error estimate* for the errors corresponding to the NURBS-based IGA approximation of scalar elliptic PDEs defined by differential operators of order $2m$, as in Eq. (1.25a). The result generalizes the a priori error estimate provided in [BBadVC⁺06] and in [BadVBRS10] for second order elliptic operators and it is based on the use of the *Aubin-Nietsche's argument* for the derivation of the error in lower order norms, see for instance [Ode00, SF73]. We consider the case of high order ($2m$) scalar elliptic PDEs, see Eq. (1.25a), with homogeneous essential boundary conditions, for which the variational formulation reads as in Eq. (1.28):

$$\text{find } u \in V \quad : \quad a(u, v) = F(v) \quad \forall v \in V, \quad (1.57)$$

since $u_0 \equiv u$. The case of non homogeneous boundary conditions can be deduced by the previous one.

Remark 1.13. *In the following, we will denote by C a positive constant independent of the mesh size h and the unknown function u , which may change at each occurrence.*

1.3.1 Preliminaries and interpolation estimate for NURBS

In order to provide the a priori error estimate of the approximation error of the Galerkin method for NURBS-based IGA, we firstly need to recall some results concerning the interpolation theory of NURBS. The first interpolation result for the NURBS spaces is given in [BBadVC⁺06], which we briefly recall here. In this work, the family of meshes over the parameter domain $\{\mathcal{Q}_h\}_h$, is assumed to undergo only h -refinement, being the degree p fixed. The interpolation result is based on the introduction of a *support extension* \bar{Q} of an element Q in the mesh \mathcal{Q}_h over the parametric domain, as the union of the supports of basis functions whose support intersect the element itself. This last induces naturally the definition of a *physical support extension* of K , an element of the physical mesh \mathcal{K}_h (1.9) image of the element $Q \in \mathcal{Q}_h$ by means of the geometrical mapping \mathbf{x} of Eq. (1.18), i.e. $K = \mathbf{x}(Q)$, as $\bar{K} := \mathbf{x}(\bar{Q})$. Moreover, in order to take into account the regularity across the common $(d-1)$ -dimensional face between two adjacent elements $Q^+, Q^- \in \{\mathcal{Q}_h\}_h$, the authors define the so called *bent Sobolev spaces* of order $l \in \mathbb{N}$, see for reference [BBadVC⁺06].

Given a function \hat{v} integrable over the parameter domain $\hat{\Omega}$, $\hat{v} \in L^2(\hat{\Omega})$, we introduce a standard projective operator over the B-Splines space \mathcal{S}^h , say $\Pi_{\mathcal{S}^h}$, given by:

$$\Pi_{\mathcal{S}^h} : L^2(\hat{\Omega}) \rightarrow \mathcal{S}^h, \quad \Pi_{\mathcal{S}^h} \hat{v} := \sum_{\mathbf{i} \in I} \langle \lambda_{\mathbf{i}}, \hat{v} \rangle_{L^2(\hat{\Omega})', L^2(\hat{\Omega})} N_{\mathbf{i}}, \quad (1.58)$$

where the linear functional $\lambda_{\mathbf{j}} \in L^2(\hat{\Omega})'$ is defined as $\langle \lambda_{\mathbf{j}}, N_{\mathbf{i}} \rangle_{L^2(\hat{\Omega})', L^2(\hat{\Omega})} := \delta_{\mathbf{j}, \mathbf{i}}$ for $\mathbf{i}, \mathbf{j} \in I$. The corresponding projective operator over \mathcal{N}^h , the NURBS space on the parametric domain of Eq. (1.16), is defined by means of the previous one and the definition of the NURBS basis functions in Eq. (1.15) through the weighting function W of Eq. (1.14). In particular, $\Pi_{\mathcal{N}^h}$ is given by:

$$\Pi_{\mathcal{N}^h} : L^2(\hat{\Omega}) \rightarrow \mathcal{N}^h, \quad \Pi_{\mathcal{N}^h} \hat{v} := \frac{\Pi_{\mathcal{S}^h}(W \hat{v})}{W}, \quad (1.59)$$

for $\hat{v} \in L^2(\hat{\Omega})$. In such a way the projection map over \mathcal{V}^h , the NURBS space in the physical domain Ω defined in Eq. (1.22) as the push-forward of the space \mathcal{N}^h , is given by:

$$\Pi_{\mathcal{V}^h} : L^2(\Omega) \rightarrow \mathcal{V}^h, \quad \Pi_{\mathcal{V}^h} v := (\Pi_{\mathcal{N}^h}(v \circ \mathbf{x})) \circ \mathbf{x}^{-1}. \quad (1.60)$$

Firstly, we consider the provided local estimate for the interpolation error. Then, a global estimate can be provided taking into account the minimum global regularity of the basis functions, k_{\min} , see Section 1.1.3.

Theorem 1.3 (Local error estimate). *Let \mathcal{V}^h be the NURBS space in the physical domain Ω defined by NURBS basis functions of degree $p_\alpha = p$ for all $\alpha = 1, \dots, d$. Given the integers l and r such that $0 \leq l \leq r \leq p+1$ and $r \geq m$; for a function $u \in L^2(\Omega) \cup H^r(\bar{K})$, the local estimate for the interpolation error is:*

$$|u - \Pi_{\mathcal{V}^h} u|_{H^l(K)} \leq Ch_K^{r-l} \sum_{i=0}^r \|\nabla \mathbf{x}\|_{L^\infty(\bar{Q})}^{i-r} |u|_{H^i(\bar{K})}^2, \quad (1.61)$$

where h_K is the element size of $K \in \mathcal{K}_h$.

Proposition 1.1 (Global error estimate). *Given the integers l and r such that $0 \leq l \leq r \leq p+1$, $r \geq m$ and a function $u \in H^r(\Omega)$, then:*

$$\begin{aligned} \sum_{K \in \mathcal{K}_h} |u - \Pi_{\mathcal{V}^h} u|_{H^l(K)}^2 &\leq C \sum_{K \in \mathcal{K}_h} h_K^{2(r-l)} \sum_{i=0}^r \|\nabla \mathbf{x}\|_{L^\infty(\mathbf{x}^{-1}(K))}^{2(i-r)} |u|_{H^i(K)}^2, \\ &\leq Ch^{2(r-l)} \|u\|_{H^r(\Omega)}^2. \end{aligned} \quad (1.62)$$

Moreover, if $l \leq k_{\min}$, we have:

$$|u - \Pi_{\mathcal{V}^h} u|_{H^l(\Omega)} \leq Ch^{r-l} \|u\|_{H^r(\Omega)}. \quad (1.63)$$

The constants C are dimensionless and depend on the shape of the domain Ω ; moreover, they also include the contribution of the gradient of the geometrical mapping \mathbf{x} over the mesh elements, where non explicit.

Corollary 1.1. *Let $u \in H^r(\Omega)$ be a function defined in the physical domain Ω . Given an integer l such that $0 \leq l \leq p+1$, $l \leq r$ and $l \leq k_{\min}$; then*

$$|u - \Pi_{\mathcal{V}^h} u|_{H^l(\Omega)} \leq Ch^{\delta-l} \|u\|_{H^r(\Omega)}. \quad (1.64)$$

where $\delta = \min\{r, p+1\}$.

Remark 1.14. *The approximation result given in Proposition 1.1 and Corollary 1.1 only highlights the dependence of the error on the mesh size h , considering the family of meshes undergone only h -refinement. However, the potentiality of high order and global regularity of NURBS higher than \mathcal{C}^0 is pointed out in [BadVBRs10], where the explicit dependences of the interpolation error on the order $p+1$ and the global regularity \mathbf{k} of the basis is provided.*

1.3.2 A priori error estimate

The Galerkin method provides an approximated solution for the scalar elliptic PDEs in Eq. (1.57), for which we incur in approximation errors due to the fact that the space $V^h \subseteq V$, in which we seek the solution, is finite dimensional. We present the following result for the IGA-Galerkin method in the framework of high order scalar elliptic PDEs, extending the one provided in [BBadVC⁺06] for second order PDEs.

Theorem 1.4. *Let $u \in H^r(\Omega)$ be the exact solution of problem (1.57) and $u_h \in V^h$ the approximated solution obtained with the IGA-Galerkin method, which considers basis functions of degree p_α , with $p_\alpha = p$ for all $\alpha = 1, \dots, d$ and with global regularity $k_{\min} \geq m$. Then, the following a priori error estimate holds:*

$$\|u - u_h\|_{H^m(\Omega)} \leq Ch^\gamma \|u\|_{H^r(\Omega)}, \quad (1.65)$$

where $\gamma = \min\{p+1-m, r-m\}$, and C is a positive constant independent of u and h , the global mesh size.

Proof. By means of the optimal error estimate (1.46) given in Theorem 1.2 and the approximation result (1.64) in Corollary 1.1, we have:

$$\begin{aligned} \|u - u_h\|_{H^m(\Omega)} &\leq \frac{M}{\alpha} \inf_{v_h \in V_h} \|u - v_h\|_{H^m(\Omega)} \leq C \|u - \Pi_{V_h} u\|_{H^m(\Omega)} \\ &\leq C \|u - \Pi_{V_h} u\|_{H^m(\Omega)} \leq Ch^{\delta-m} \|u\|_{H^r(\Omega)}, \end{aligned} \quad (1.66)$$

where $\delta = \min\{r, p+1\}$. The third inequality is the generalization of *Poincaré inequality*, valid since the domain Ω is a bounded with regular boundary, see for reference Corollary 6.31 in [AF07]. \square

In order to derive lower order error estimate of the Galerkin-IGA approximation, we use similar arguments to those applied for the FEA, see for reference [Ode00, SF73, Hug00]. In particular, we consider the Aubin-Nietsche's argument introducing the adjoint problem and we resort to a generalized form of the *Lax-Milgram Lemma* 1.1 (the interested reader can refer to, e.g., [Ode00, SF73]), which we recall in the following.

Theorem 1.5 (Nečas-Babuška Theorem).

Let V and W be two Hilbert spaces, endowed with norms $\|\cdot\|_V$ and $\|\cdot\|_W$, and V' and W' be their respective dual spaces. A boundary value problem in variational form can be formulated as follows:

$$\text{find } u \in V \quad : \quad a(u, w) = F(w) \quad \forall w \in W, \quad (1.67)$$

with $a : V \times W \rightarrow \mathbb{R}$ a bilinear form and $F : W \rightarrow \mathbb{R}$ a linear functional. If the following hypotheses are satisfied:

- i) $a(\cdot, \cdot)$ is continuous, i.e. there exists $M > 0$ such that $|a(v, w)| \leq M \|v\|_V \|w\|_W$ for all $v \in V, w \in W$,
- ii) there exists $\beta > 0$ such that $\inf_{v \in V \setminus \{0\}} \sup_{w \in W \setminus \{0\}} \frac{a(v, w)}{\|v\|_V \|w\|_W} \geq \beta$,
- iii) $\inf_{w \in W \setminus \{0\}} \sup_{v \in V \setminus \{0\}} \frac{a(v, w)}{\|v\|_V \|w\|_W} > 0$,
- iv) $F \in W'$,

then, there exists a unique solution $u \in V$ of problem (1.67) and $\|u\|_V \leq \frac{1}{\beta} \|F\|_{W'}$.

Theorem 1.6. Given the elliptic boundary value problem of order $2m$ of Eq. (1.57), let σ be an integer such that $0 \leq \sigma \leq m$ and the linear functional $F \in H^{-\sigma}(\Omega)$. Let $u \in H^r(\Omega)$, with $r \geq m$, be the exact solution of problem (1.57) and u_h the approximated solution obtained with the IGA-Galerkin method, with NURBS basis functions of degree $p_\alpha = p$ for all $\alpha = 1, \dots, d$, and $k_{\min} \geq m$. Then, the following a priori error estimate holds:

$$\|u - u_h\|_{H^\sigma(\Omega)} \leq Ch^\beta \|u\|_{H^r(\Omega)}, \quad (1.68)$$

where $\beta = \min\{\delta - \sigma, 2(\delta - m)\}$ with $\delta = \min\{r, p+1\}$ and C is a constant independent of u and h , but depending on the shape of Ω .

Proof. The *adjoint problem* of problem (1.57) reads:

$$\text{find } \varphi_F \in V \quad : \quad a^*(\varphi_F, v) = F(v) \quad \forall v \in V, \quad (1.69)$$

where we define the bilinear form $a^* : V \times V \rightarrow \mathbb{R}$ as $a^*(v, w) := a(w, v)$ for all $w, v \in V$ (see for instance [Ode00, Hug00, Qua09]). Its elliptic regularity is inherited by problem (1.57). Moreover, by the space embedding rule $V \subseteq H^\sigma \subseteq H^{-\sigma} \subseteq V'$ and the hypothesis $F \in H^{-\sigma}(\Omega)$, problem (1.69) satisfies the hypotheses of the Nečas-Babuška Theorem 1.5; thus, there exists a unique solution $\varphi_F \in V$ of the adjoint problem (1.69) and $\|\varphi_F\|_{H^{2m-\sigma}(\Omega)} \leq C\|F\|_{H^{-\sigma}(\Omega)}$, for some constant C . By means of the generalized *Poincaré inequality* and the approximation result of Corollary 1.1, there exists a projective operator $\Pi_{\mathcal{V}^h}$ (1.60) onto the NURBS space \mathcal{V}^h , for which:

$$\|\varphi_F - \Pi_{\mathcal{V}^h} \varphi_F\|_{H^m(\Omega)} \leq Ch^\epsilon \|\varphi_F\|_{H^{2m-\sigma}(\Omega)}, \quad (1.70)$$

with $\epsilon = \min\{m - \sigma, p + 1 - m\}$ if $r \geq 2m - \sigma$ or $\epsilon = \min\{r - m, p + 1 - m\}$ if $r \leq 2m - \sigma$. Inequality (1.70) follows considering, as for the case $r \geq 2m - \sigma$, $\varphi_F \in H^r(\Omega)$ as an element of $H^{2m-\sigma}(\Omega)$ thanks to the inclusion $H^r(\Omega) \subseteq H^{2m-\sigma}(\Omega)$, while in the second case we only take into account $\|\cdot\|_{H^r(\Omega)} \leq \|\cdot\|_{H^{2m-\sigma}(\Omega)}$.

By definition of $\|\cdot\|_{H^\sigma(\Omega)}$, and choosing in Eq. (1.69) $v = u - u_h$, we have:

$$\|u - u_h\|_{H^\sigma(\Omega)} = \sup_{F \in H^{-\sigma}} (\Omega) \frac{|\langle F, u - u_h \rangle_{H^{-\sigma}(\Omega), H^\sigma(\Omega)}|}{\|F\|_{H^{-\sigma}(\Omega)}} = \sup_{F \in H^{-\sigma}} \frac{|a^*(\varphi_F, u - u_h)|}{\|F\|_{H^{-\sigma}(\Omega)}}.$$

By the Galerkin orthogonality of the error with respect to \mathcal{V}^h and the continuity of the bilinear form $a^*(\cdot, \cdot)$, we obtain:

$$\begin{aligned} \|u - u_h\|_{H^\sigma(\Omega)} &= \sup_{F \in H^{-\sigma}(\Omega)} \frac{|a^*(\varphi_F - \Pi_{\mathcal{V}^h} \varphi_F, u - u_h)|}{\|F\|_{H^{-\sigma}(\Omega)}} \\ &\leq M \|u - u_h\|_{H^m(\Omega)} \sup_{F \in H^{-\sigma}(\Omega)} \frac{\|\varphi_F - \Pi_{\mathcal{V}^h} \varphi_F\|_{H^m(\Omega)}}{\|F\|_{H^{-\sigma}(\Omega)}}. \end{aligned} \quad (1.71)$$

Then, applying the error estimate provided in Theorem 1.4 and the upper bound of Eq. (1.70) we have:

$$\|u - u_h\|_{H^\sigma(\Omega)} \leq Ch^\gamma \|u\|_{H^r(\Omega)} \sup_{F \in H^{-\sigma}} \frac{h^\epsilon \|\varphi_F\|_{H^{2m-\sigma}(\Omega)}}{\|F\|_{H^{-\sigma}(\Omega)}},$$

where $\gamma := \min\{p + 1 - m, r - m\}$.

Finally, by considering the inequality $\|\varphi_F\|_{H^{2m-\sigma}(\Omega)} \leq \|F\|_{H^{-\sigma}(\Omega)}$ and adding the exponents of $h^{\gamma+\epsilon}$, we obtain the result (1.68). \square

Remark 1.15. The regularity r of the exact solution $u \in H^r(\Omega)$ and the degree p of the NURBS basis functions, used to obtain the approximated solution, determine the convergence rate of the error with respect to the global mesh size h . Moreover, the rate of convergence β depends on the order of the problem m , but also on the norm $\|\cdot\|_{H^\sigma}$ in which we want to determine the error $u - u_h$. It is straightforward to conclude that the smaller is σ the faster is the convergence of the error with the mesh size h . However, we observe that p has to be large enough with respect to m for $u \in H^r(\Omega)$, with $r \geq p + 1$, in order to achieve this result.

For example, for $m = 2$ and for $u \in H^r(\Omega)$, with $r \geq p + 1$, we obtain that:

$$\begin{aligned}\|u - u_h\|_{L^2(\Omega)} &\leq Ch^{\min\{p+1, 2p-2\}} \|u\|_{H^r(\Omega)}, \\ \|u - u_h\|_{H^1(\Omega)} &\leq Ch^{\min\{p, 2p-2\}} \|u\|_{H^r(\Omega)}, \\ \|u - u_h\|_{H^2(\Omega)} &\leq Ch^{\min\{p-1, 2p-2\}} \|u\|_{H^r(\Omega)},\end{aligned}$$

and, if $p = 2$, the convergence rate for the errors in norms $L^2(\Omega)$ and $H^1(\Omega)$ is coincident and equals 2.

The same considerations are more evident when considering the case $m = 3$ for $u \in H^r(\Omega)$, with $r \geq p + 1$, for which:

$$\begin{aligned}\|u - u_h\|_{L^2(\Omega)} &\leq Ch^{\min\{p+1, 2p-4\}} \|u\|_{H^r(\Omega)}, \\ \|u - u_h\|_{H^1(\Omega)} &\leq Ch^{\min\{p, 2p-4\}} \|u\|_{H^r(\Omega)}, \\ \|u - u_h\|_{H^2(\Omega)} &\leq Ch^{\min\{p-1, 2p-4\}} \|u\|_{H^r(\Omega)}, \\ \|u - u_h\|_{H^3(\Omega)} &\leq Ch^{\min\{p-2, 2p-4\}} \|u\|_{H^r(\Omega)}.\end{aligned}$$

In this case, the same rates of convergence of the errors in different norms is obtained up to the case $p = 5$; in fact, if $p = 3$, the convergence rates for the errors in norms $L^2(\Omega)$, $H^1(\Omega)$ and $H^2(\Omega)$ are the same and equal to 2, while if $p = 4$, the convergence rates in norms $L^2(\Omega)$ and $H^1(\Omega)$ are the same and equals 4.

1.4 Numerical examples

We show several numerical results in order to highlight the properties of IGA in the framework of the Galerkin method. We take into account the elliptic PDEs considered in the examples of Section 1.2 and defined in a domain $\Omega \subseteq \mathbb{R}^2$ described by NURBS. Firstly, we deal with second order PDEs, to compare IGA to FEA. Successively, we solve high order elliptic PDEs by using NURBS basis functions with high global regularity. In particular, we consider high order PDEs involving the bilaplacian and trilaplacian operators for which the exact solution is known, in order to show that the convergence rates predicted by the a priori error estimate Eq. (1.68) are confirmed both with homogeneous and nonhomogeneous boundary conditions.

We refer to Appendix B for a description of the implementation of non homogeneous essential boundary conditions for high order PDEs. Problems described by the Stokes and Navier-Stokes equations in stream function formulations represents another example of high order PDEs. We refer the reader to Appendix A for an insight into the topic.

1.4.1 The Poisson problem (Example 1.11): a comparison of IGA and FEA

Let us consider the Poisson problem described in Example 1.11 and defined in the domain Ω represented by a quarter of an annulus with inner radius $r_{\text{in}} = 4$ and outer radius $r_{\text{out}} = 5$, see Figure 1.12. The geometry can be exactly represented by NURBS; on the contrary, since the domain is not representable by polynomials, Finite Elements only allow an approximation of Ω with a polygonal shaped domain, Ω^h . This induces a geometric error, for whose analysis in the framework of FEA we refer to [SF73].

We consider two problems, whose analytical smooth solution is known, in order to compare the errors, in the L^2 and H^1 norms, obtained in solving them with IGA or FEA. For both

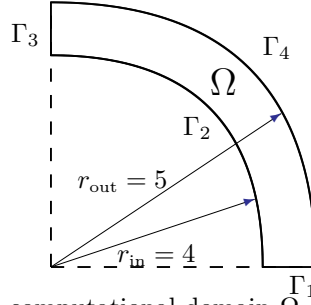


Figure 1.12: Poisson problem: computational domain Ω defined by a quarter of an annulus.

the problems, say *case 1* and *case 2*, we consider a constant diffusion coefficient $\mu = 1$ and homogeneous Dirichlet boundary conditions imposed on the whole boundary $\partial\Omega = \cup_{i=1}^4 \Gamma_i$. We assume that for:

case 1 the source term is given by:

$$f(x, y) = \frac{4}{(x^2 + y^2)^4} \left[12x^2y^2(x^2 + y^2)^2 - 2(x^2 + y^2)^4 + 2(r_{\text{in}} + r_{\text{out}})(x^2 + y^2)^{7/2} - 15(r_{\text{in}} + r_{\text{out}})x^2y^2(x^2 + y^2)^{3/2} - 2r_{\text{in}}r_{\text{out}}(x^6 - 5x^4y^2 - 5x^2y^4 + y^6) \right],$$

with the exact solution:

$$u(x, y) = \frac{4x^2y^2}{(x^2 + y^2)^2} \left[x^2 + y^2 - (r_{\text{in}} + r_{\text{out}})(x^2 + y^2)^{1/2} + r_{\text{in}}r_{\text{out}} \right];$$

case 2 the source term is given by:

$$f(x, y) = -\frac{1}{10r_{\text{in}}r_{\text{out}}}xy \left[32(x^2 + y^2) - 12(r_{\text{in}}^2 + r_{\text{out}}^2) \right],$$

with the exact solution:

$$u(x, y) = \frac{1}{10r_{\text{in}}r_{\text{out}}}xy \left[(x^2 + y^2)^2 - (r_{\text{in}}^2 + r_{\text{out}}^2)(x^2 + y^2) + r_{\text{in}}^2r_{\text{out}}^2 \right].$$

We represent the domain Ω of Figure 1.12 by means of NURBS of degree $p = 2$, with $N_{\text{el}} = (2^{N_{\text{ref}}})^2$ mesh elements, for $N_{\text{ref}} = 2, \dots, 5$, maintaining global \mathcal{C}^1 -continuity of the basis functions across the mesh elements in Ω . For the FEA we consider Lagrangian polynomial bases of degree 2 ($P2$ finite elements) on meshes composed by triangular elements.

In Figure 1.13 we plot the exact solution of the problem of *case 1* and the IGA and FEA meshes to obtain, approximatively, the same errors in the norms L^2 and H^1 of order, respectively, 10^{-5} and 10^{-3} . As we can see, the number of elements (N_{el}) is noticeable different in the two cases. The same comparison is performed in last line of Table 1.1 with respect to the degrees of freedom (N_{DoFs}) for errors in the norms L^2 and H^1 of order, respectively, 10^{-6} and 10^{-4} . We also compare the corresponding errors in the norms L^2 and H^1 when computing solutions with a similar number of degrees of freedom (N_{DoFs}) for several cases.

We perform the same analysis with the problem given of *case 2*, referring respectively to Figure 1.14 and Table 1.2. In this case, in Figures 1.14b and 1.14c meshes which lead to approximatively the same number of degrees of freedom ($N_{\text{DoFs}} = 580$) are shown. The same considerations made for *case 1* are still valid and once again we highlight the efficiency of the

Table 1.1: Poisson problem *case 1*: comparison of the errors in L^2 and H^1 norms corresponding to solutions obtained with IGA and FEA, with a similar number of degrees of freedom (N_{DoFs}).

IGA				FEA			
N_{el}	N_{DoFs}	$\ u - u_h\ _{L^2}$	$\ u - u_h\ _{H^1}$	N_{el}	N_{DoFs}	$\ u - u_h\ _{L^2}$	$\ u - u_h\ _{H^1}$
16	52	$6.17869 \cdot 10^{-3}$	$2.67170 \cdot 10^{-2}$	42	61	$9.92176 \cdot 10^{-3}$	$6.07732 \cdot 10^{-2}$
64	164	$4.77005 \cdot 10^{-4}$	$3.94278 \cdot 10^{-3}$	114	185	$2.39930 \cdot 10^{-3}$	$2.29175 \cdot 10^{-2}$
324	580	$5.13074 \cdot 10^{-5}$	$8.73335 \cdot 10^{-4}$	326	583	$8.53220 \cdot 10^{-4}$	$9.91611 \cdot 10^{-3}$
1,024	2,180	$6.15555 \cdot 10^{-6}$	$2.12188 \cdot 10^{-4}$	1,180	2,217	$2.11927 \cdot 10^{-4}$	$3.38785 \cdot 10^{-3}$
—	—	—	—	42,538	84,227	$6.15077 \cdot 10^{-6}$	$2.15786 \cdot 10^{-4}$

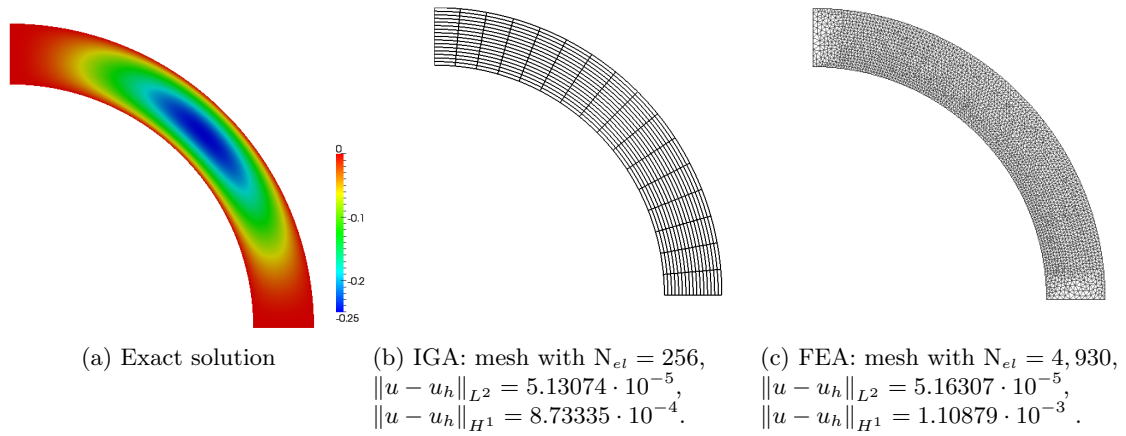


Figure 1.13: Poisson problem *case 1*: exact solution (a) and IGA (b) and FEA (c) meshes yielding approximatively the same errors in norms L^2 and H^1 (about 10^{-4} and 10^{-3}).

Table 1.2: Poisson problem *case 2*: comparison of the errors in L^2 and H^1 norms corresponding to solutions obtained with IGA and FEA, with a similar number of degrees of freedom (N_{DoFs}).

IGA				FEA			
N_{el}	N_{DoFs}	$\ u - u_h\ _{L^2}$	$\ u - u_h\ _{H^1}$	N_{el}	N_{DoFs}	$\ u - u_h\ _{L^2}$	$\ u - u_h\ _{H^1}$
16	52	$3.90103 \cdot 10^{-3}$	$7.84435 \cdot 10^{-2}$	42	61	$7.06703 \cdot 10^{-2}$	$4.05533 \cdot 10^{-1}$
64	164	$4.39159 \cdot 10^{-4}$	$1.93967 \cdot 10^{-2}$	114	185	$1.76357 \cdot 10^{-2}$	$1.74868 \cdot 10^{-1}$
324	580	$5.34384 \cdot 10^{-5}$	$4.83807 \cdot 10^{-3}$	326	583	$5.80311 \cdot 10^{-3}$	$7.28272 \cdot 10^{-2}$
1,024	2,180	$6.63574 \cdot 10^{-6}$	$1.20884 \cdot 10^{-3}$	1,180	2,217	$1.38576 \cdot 10^{-3}$	$2.31970 \cdot 10^{-2}$
—	—	—	—	308,044	613,795	$6.62414 \cdot 10^{-6}$	$2.66791 \cdot 10^{-4}$

IGA method versus FEA, in particular when comparing the performances in computing an error in norm L^2 of an order of magnitude of 10^{-6} . We deduce that the combination of the exact geometrical representation and the smoothness of the basis functions used in IGA allows to achieve similar errors of the FEA with a noticeable inferior number of degrees of freedom.

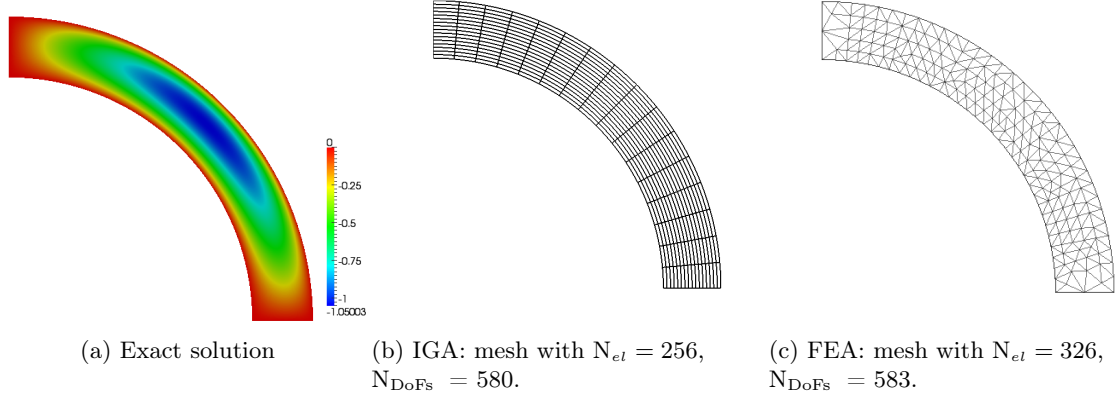


Figure 1.14: Poisson problem *case 2*: exact solution (a) and IGA (b) and FEA (c) meshes yielding approximatively equals number of degrees of freedom (N_{DoFs}).

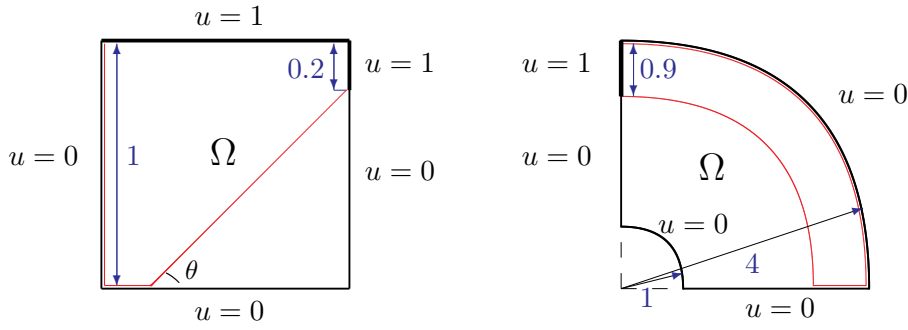


Figure 1.15: Advection-diffusion problems: problems settings and data; boundary and internal layers (red). Values imposed on the solution for the Dirichlet boundary conditions on $\Gamma_D = \partial\Omega$ are reported.

1.4.2 The advection-diffusion problem (Example 1.12): SUPG stabilization with IGA

We consider the advection-diffusion problem, introduced in Example 1.12. Two different configurations for this problem are taken into account and shown in Figure 1.15. In both of the cases the parameters of the problem are chosen in such a way that the global Péclet number is much greater than one, say $\mathbb{P}e \gg 1$, so that the diffusion term is dominated by the advection term. We solve these problems by means of IGA both with the standard Galerkin method and considering the SUPG stabilization presented in Section 1.2.2.

The first problem, say *case 1*, is defined by the data shown in Figure 1.15a and it represents a benchmark problem, whose solution is characterized by internal and boundary layers [Qua09]. Considering the given velocity field such that $\|\mathbf{b}\|_{L^\infty(\Omega)} = 1$ and the constant viscosity $\mu = 10^{-4}$ and choosing a uniform mesh of size $h = 1/20$, we are dealing with a very

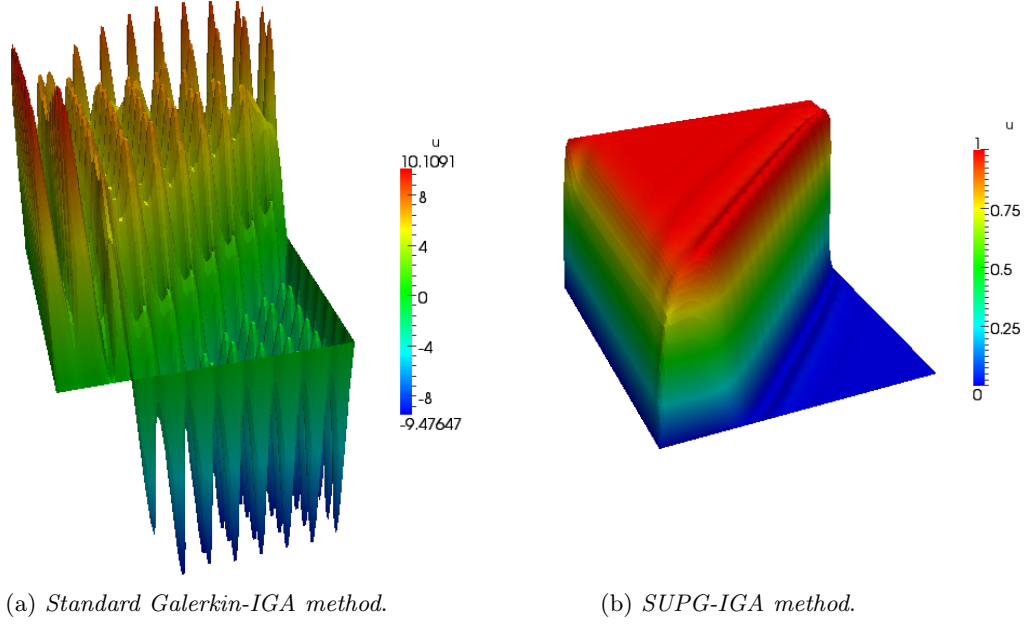


Figure 1.16: Advection-diffusion problem *case 1*: comparison between numerical solutions obtained with the standard Galerkin-IGA method (a) and SUPG-IGA method (b), with a local Péclet number $\mathbb{P}e_K = 25,000$.

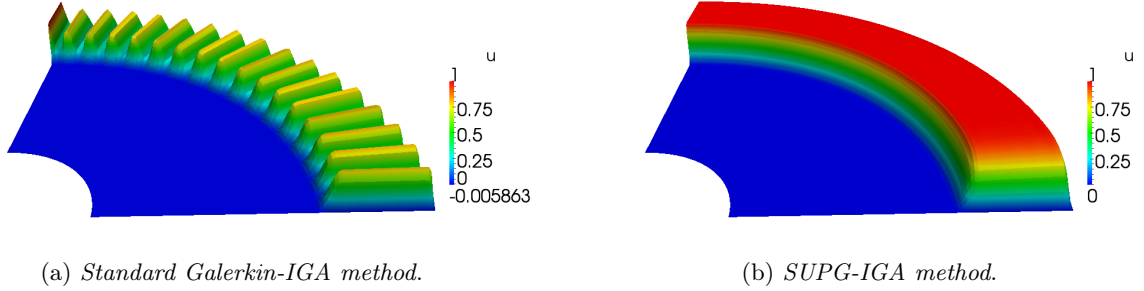


Figure 1.17: Advection-diffusion problem *case 2*: comparison between numerical solutions with the standard Galerkin-IGA method (a) and SUPG-IGA method (b), with a local Péclet number $\mathbb{P}e_K \approx 3,300$.

high local Péclet number, namely, $\mathbb{P}e_K = 25,000$ for all $K \in \mathcal{K}_h$. As expected, the solution provided by the standard Galerkin method, reported in Figure 1.16a presents instabilities, which completely dominate the numerical solution. On the contrary, when considering the SUPG formulation, the numerical solution is satisfactory, even if some limited under- and over-shooting phenomena appear near the layers, as reported in literature [SDS⁺12].

The second problem, say *case 2* is defined in Figure 1.15b and considers an advection field aligned along the circumferential direction. This gives rise to internal and boundary layers. The computational domain is exactly represented through NURBS basis functions of degree $p = 2$. We use a uniform mesh of $N_{el} = 32^2$ and, by the given velocity field such that $\|\mathbf{b}\|_{L^\infty(\Omega)} = 4$ and the constant viscosity $\mu = 10^{-4}$, we have a local Péclet number $\mathbb{P}e_K \approx 3,300$ sufficiently high to lead to oscillations, controlled by the SUPG stabilization, as shown in Figure 1.17.

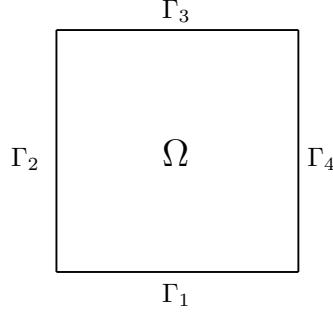


Figure 1.18: High order problems: computational domain $\Omega = (0, 1)^2$.

1.4.3 High order PDEs (Examples 1.13 and 1.14)

In order to validate the error estimate given in Theorem 1.6, we consider two examples for the biharmonic problem (1.37a) and one example for the trilaplacian problem (1.41a), for which the exact solution is known (see Examples 1.13 and 1.14). Both the problems are defined in the physical domain $\Omega = (0, 1)^2$ as described in Figure 1.18.

Example. 1.13 (Biharmonic problem). By referring to problem (1.37a) we consider two problems, say *case 1* and *case 2*, with different boundary conditions. For:

case 1: we set:

$$\begin{aligned} g_1(x, y) &= 0, \quad g_2(x, y) = 0, \\ f(x, y) &= 4\pi^4 (\cos(2\pi(x - y)) + \cos(2\pi(x + y))) \\ &\quad - 8\pi^4 (-4\sin^2(\pi x) \sin^2(\pi y) + \sin^2(\pi x) + \sin^2(\pi y)), \end{aligned}$$

yielding the exact solution:

$$u(x, y) = \sin^2(\pi x) \sin^2(\pi y).$$

case 2: we set:

$$g_1(x, y) = 0, \quad g_2(x, y)|_{\Gamma_j} = \chi_{\{1,3\}}(j)(-\hat{i})^{\hat{j}} \sin(\pi x) + \chi_{\{2,4\}}(j)(-\hat{i})^{\hat{j}-1} \sin(\pi y),$$

for all $j = 1, 2, 3, 4$ and with $\hat{i}^2 = -1$,

$$f(x, y) = 4\pi^4 \sin(\pi x) \sin(\pi y),$$

yielding the exact solution:

$$u(x, y) = \sin(\pi x) \sin(\pi y).$$

In both cases the exact solution u is smooth. In the latter case, the essential boundary condition involving the normal derivative of the solution is non homogeneous.

For both the problems we consider the domain Ω described by B-Splines on uniform meshes with number of elements $N_{el} = (2^{N_{ref}})^2$, for $N_{ref} = 2, \dots, 6$, for three different choices of degree of the basis, $p = 2, 3, 4$. Having performed k -refinement, different global regularities are achieved, respectively we have $\mathcal{C}^1, \mathcal{C}^2, \mathcal{C}^3$ -continuous basis functions. We observe that the hypotheses in Theorem 1.6 are satisfied for each degree p .

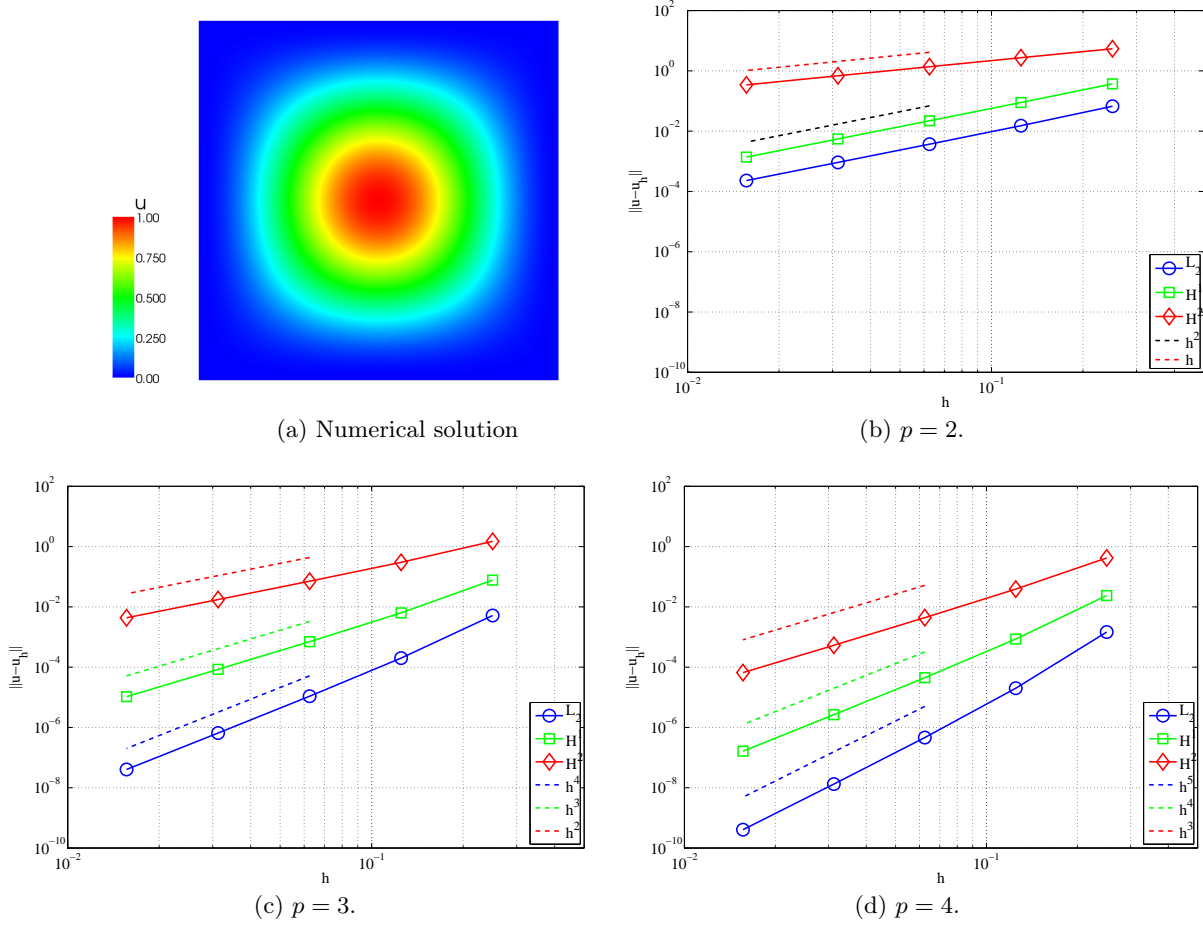
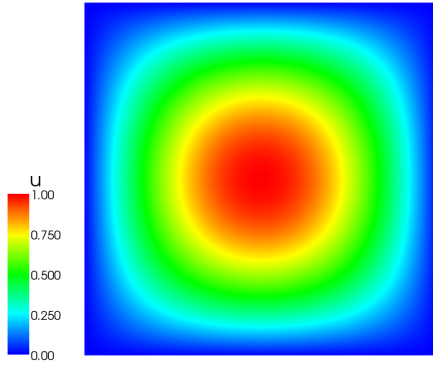


Figure 1.19: Bilaplacian problem *case 1*: (a) exact solution; plot of the errors in norm $L^2(\circ)$, $H^1(\square)$ and $H^2(\diamond)$ vs. the mesh size h for basis functions of degree p , $p = 2$ (b), $p = 3$ (c) and $p = 4$ (d); comparison with the theoretical convergence rate.

For *case 1*, in Figure 1.19 we show the exact solution u and the convergence rates of the errors in L^2 , H^1 and H^2 norms vs. the mesh size h . The results confirm the a priori error estimate provided in Theorem 1.6 and the considerations of Remark 1.15. Furthermore, we can easily see the benefit of a high order approach, which characterizes IGA. Let us consider, for example, the error in L^2 norm: for $p = 2$, the error is of order 10^{-4} using $N_{el} = (2^6)^2$, while the same order is already attained for $p = 3$ with a mesh of $N_{el} = (2^3)^2$, thus reducing significantly the number of degrees of freedom.

For *case 2*, we observe that the theoretical result (1.68) in Theorem 1.6 is valid also when non homogeneous essential boundary conditions are considered, as highlighted in Figure 1.20. \diamond



(a) Numerical solution

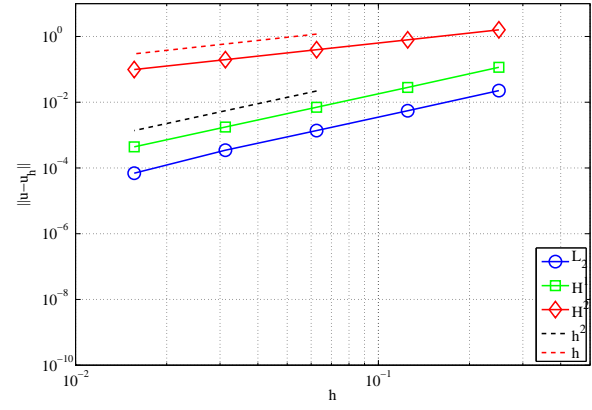
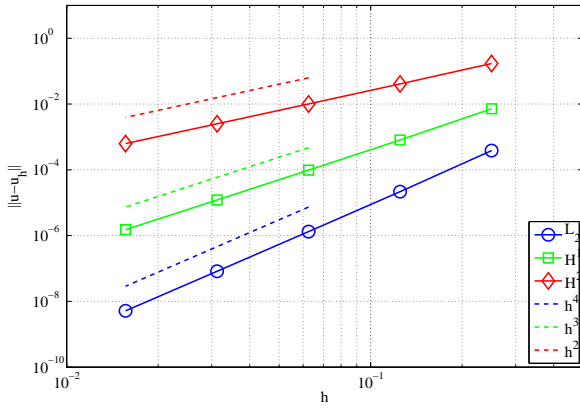
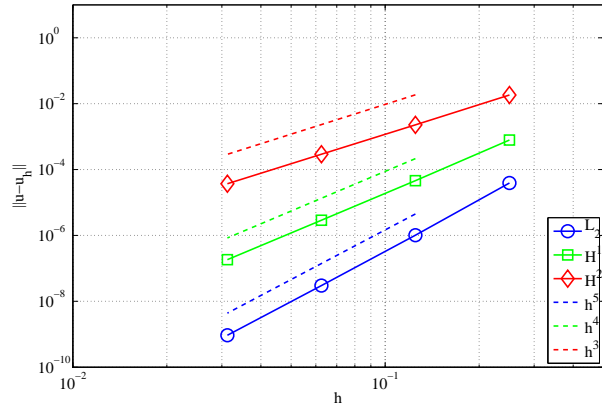
(b) $p = 2$.(c) $p = 3$.(d) $p = 4$.

Figure 1.20: Bilaplacian problem *case 2*: (a) exact solution u ; plot of the errors in norm $L^2(\circ)$, $H^1(\square)$ and $H^2(\diamond)$ vs. the mesh size h for basis functions of degree p , $p = 2$ (b), $p = 3$ (c) and $p = 4$ (d); comparison with the theoretical convergence rate.

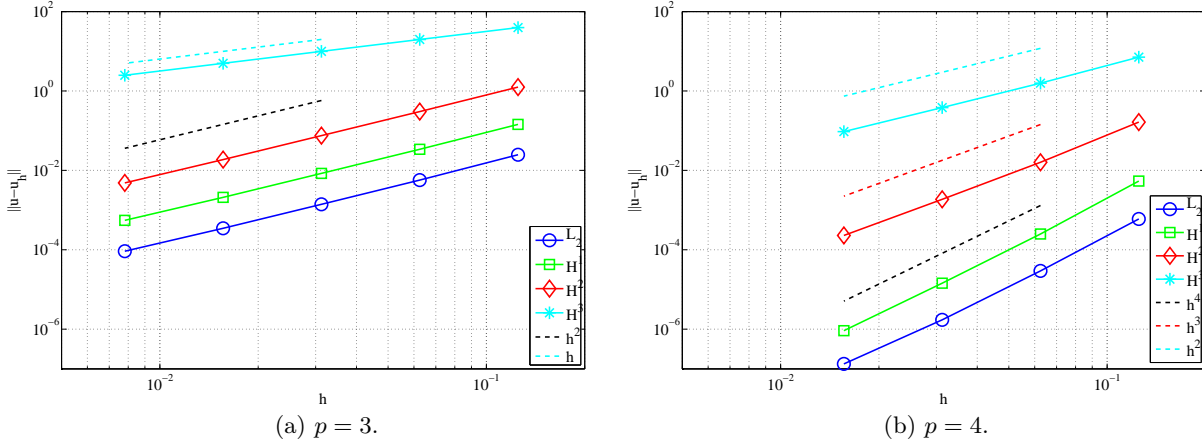


Figure 1.21: Trilaplacian problem: plot of the errors in norm $L^2(\circ)$, $H^1(\square)$, $H^2(\diamond)$ and $H^3(*)$ vs. the mesh size h for basis functions of degree p , with $p = 3$ (a), $p = 4$ (b). Comparison with the theoretical convergence rate.

Example. 1.14 (Trilaplacian problem). We consider the trilaplacian problem (1.41a), set in the physical domain $\Omega = (0, 1)^2$ as described in Figure 1.18, in order to validate, once more, the a priori error estimate provided in Theorem 1.6. We consider homogeneous essential boundary conditions imposed on the whole boundary $\partial\Omega$, while the source term together with the corresponding exact smooth solution are given by:

$$f(x, y) = -24\pi^6 \sin(\pi x) \sin(\pi y) [151 \sin^2(\pi x) - 243 \sin^2(\pi x) \sin^2(\pi y) + 151 \sin^2(\pi y) - 90],$$

$$u(x, y) = \sin^3(\pi x) \sin^3(\pi y).$$

This problem is solved on uniform k -refined meshes with number of elements $N_{el} = (2^{N_{ref}})^2$, for $N_{ref} = 3, \dots, 7$, for different choices of the degrees $p = 3, 4$ and thus different global regularity of the basis functions, which are globally \mathcal{C}^{p-1} -continuous. The hypotheses in Theorem 1.6 are satisfied and the plots of errors vs. the mesh size h in Figure 1.21 confirm the theoretical results provided in Eq. (1.68). As already discussed in Remark 1.15, we can observe that for $p = 3$ the convergence rates of the errors in norms $\|\cdot\|_{L^2}$, $\|\cdot\|_{H^1}$ and $\|\cdot\|_{H^2}$ are equal to 2. For $p = 4$ the convergence rates of the errors in norms $\|\cdot\|_{L^2}$ and $\|\cdot\|_{H^1}$ are equal to 4. \diamond

Chapter 2

An Introduction to the Cardiovascular System

The cardiovascular system is a complex and active organ system, that together with the lymphatic system constitutes the circulatory system. The human cardiovascular system supplies the human cells, tissues and organs with blood in order to maintain their functional needs. The cardiovascular system is constituted by the heart and an intricate network of vessels and it is regulated by complex mechanisms of nervous, biochemical and mechanical typology, that allow it to quickly adapt to changes in the environment of the human body. Both the complexity of the cardiovascular physiology and the variability of physical characteristics between individuals, make its study an hard task.

In this chapter we briefly describe the main components and features characterizing the cardiovascular system. Specifically, we focus on these aspects connected to the vascular flows, in particular in arteries, with a mention to the related diseases and pathologies, whose causes and cures are the primary reasons that move the research. For an extensive overview of the topic, we refer the interested reader to [Fio00, V⁺08] and to [FQV⁺09, FQ⁺02] for a description of the cardiovascular system in view of mathematical modeling.

2.1 Cardiovascular anatomy and physiology

The human cardiovascular system can be thought as an hydraulic system in which a pump leads a fluid flow in a closed system of pipes. The pump is represented by the heart, the fluid is the blood and the vascular network is constituted by a distribution net (the *arterial system*), an exchange system (the *microcirculation*) and a blood collector (the *venous system*). Moreover, the whole circulatory system can be divided into the *systemic circulation*, which includes the vessels that distribute the oxygenated blood from the heart to the various organs and then bring the oxygen-depleted blood back to the heart, and the *pulmonary circulation*, where the oxygen-depleted blood is sent to the lungs in order to be oxygenated and therefore returning to the heart.

Heart. The *heart* is a muscular organ that, contracting in a rhythmic and periodic way, maintains the blood circulation active. It is divided into four cavities, the upper *left* and *right atria* and the lower *left* and *right ventricles*. A thick wall of muscle, called the *septum*, separates the left side, involved in the systemic circulation, from the right side, being

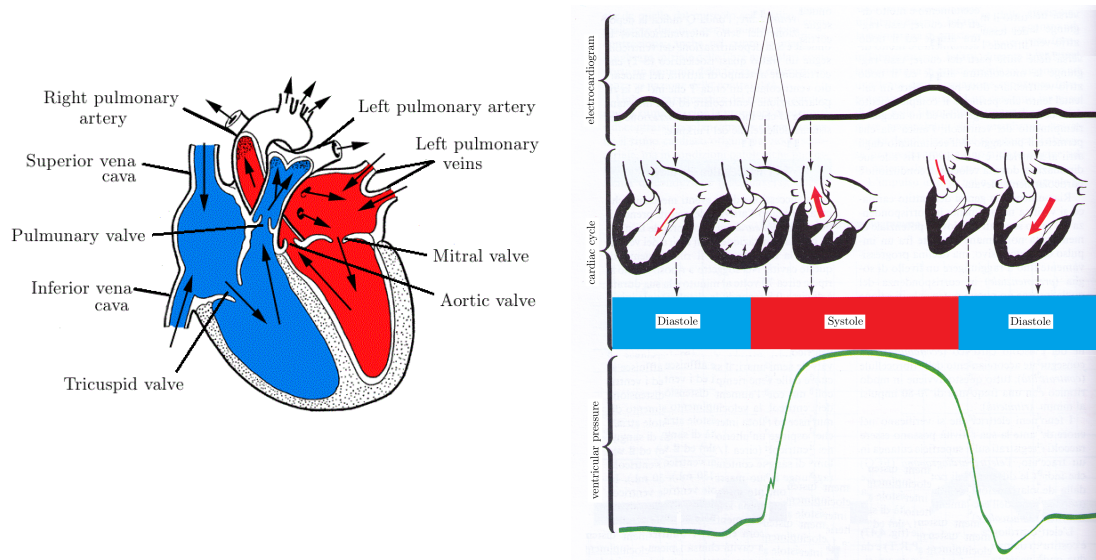


Figure 2.1: Heart anatomy and physiology: qualitative description of the cardiac cycle. Images from [V⁺08] and [Fio00].

part of the pulmonary circulation. Each atrium, which collects the blood from the veins, is connected to the correspondent ventricle, through a valve, which prevents blood from flowing back from the ventricle to the atrium during the contraction of the former. In particular, the one corresponding to the left atrium and ventricle is called *mitral valve*, the one to the right *tricuspid valve*. The same task is performed by the *aortic valve* and *pulmonary valve*, which avoid backflows from the arteries to the ventricles.

The mechanics of the heart is regulated by a complex and involuntary electro-chemical activation of the muscle cells. The sequence of contraction and relaxation phases which allows the heart to perform its pump functions is called *cardiac cycle* or *heartbeat* and it covers a period of about $T_{HB} = 1.1s$. It can be divided into two major stages, the *systole* and the *diastole* phases. The former covers the period in which the myocardium contracts and it is usually identified with the period between the closure of the mitral valve and that of the aortic valve, the latter corresponds to the complementary and relaxing phase. The total duration of each phase depends upon the state of the human body.

Blood. The blood is an inhomogeneous fluid constituted by a fluid part, called *plasma*, in which particles and cells are suspended, mainly: red cells (erythrocytes, responsible for the exchange of oxygen), white cells (leukocytes, part of the immune system) and platelets (thrombocytes, controlling blood coagulation). On the whole, the blood (plasma and cells) exhibits a non-Newtonian rheological behavior and its density is between $1.054g/cm^3$ and $1.06g/cm^3$. The primary function performed by the blood is the transport and the delivery of the substances needed to maintain the metabolic activity of the cells and the removal of the metabolic waste. Together with nutrients, blood transfers also respiratory gases and substances at the level of solution. Moreover, it covers also an important part in the thermo-regulation process and in preserving the chemical and physical characteristics of the tissues, e.g. by maintaining constant levels of Ph and osmotic pressure.

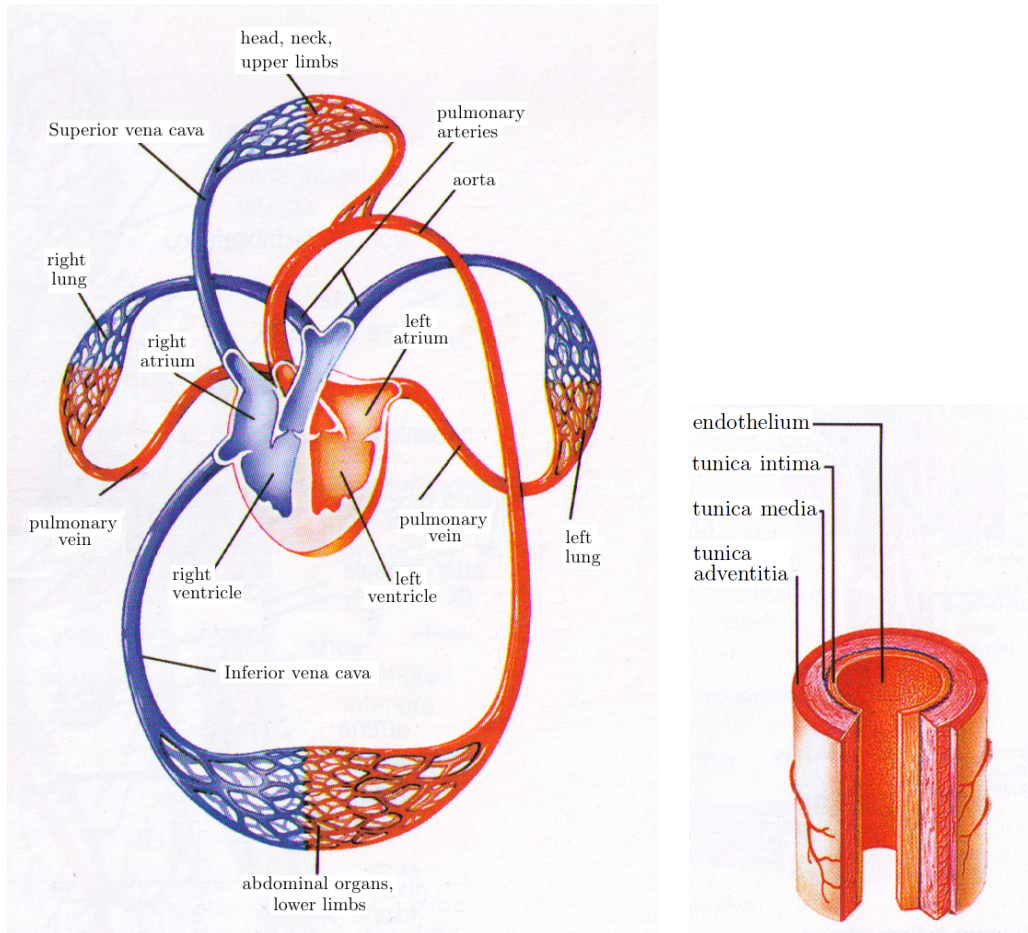


Figure 2.2: Schematic description of the systemic circulation and pulmonary circulation (left); description of the artery wall (right). Images from [V⁺08].

Vascular network. The circulatory system, in which the blood is flowing, is distributed in all the organs and tissues. Starting from the heart, it is constituted by a network of arteries which progressively branch, up to becoming a very thick network of thin wall capillaries; the latter converge into veins whose radius becomes larger and larger in proximity of the heart. There are also some direct interconnections, called anastomoses, between the arterial and venous systems; however, the arterial and venous systems can be considered primarily two distinct networks interconnected by means of the microcirculation. Typically, large vessels have a diameter between $1 - 3\text{cm}$, medium vessels are characterized by a diameter of $0.2\text{mm} - 1\text{cm}$. The small vessels (arterioles and venules) are considered to be part of the microcirculation, to which the capillaries belong. The latter possesses a diameter which can be as small as $5\mu\text{m}$.

On the other hand, blood flow in larger vessels is pulsatile and characterized by high values of the mean and maximum velocity. Moreover, the walls of the larger vessels respond primarily in an elastic way with respect to small vessels due to the different characterization of their complex stratified structure. Arterial walls are composed by three distinct concentric layers of muscular smooth tissue and/or of connective tissue: the tunica intima, tunica media and tunica adventitia. The tunica intima is constituted by a single layer of endothelial cells

which lies on a thin lamina of connective tissue, the basal lamina. This interface between the blood and the internal layer, called endothelium, is subject and react to the normal and shear stresses caused by the fluid pressure and flow. The tunica media is mainly constituted by fibromuscular tissue and it goes from the internal elastic membrane to the external elastic one. The mechanical properties of the walls are mainly characterized by this layer, depending on the prevalence of muscular or connectivity cells. The tunica adventitia, finally, is an outer covering, characterized by a connective nature, which does not essentially contribute to the compliance of the vessel, and fill with nerve fibers, lymphatic and blood vessels. The arterial wall thickness in the vascular network changes accordingly to the mean blood pressure. Moreover, the arteries and the veins near the heart are thicker because of the additional pressure effect determined by the gravity force. The chronic change in blood pressure, in conjunction with the flow rate, has also a crucial role in the remodeling of the vessels, which increases the luminal diameter during each cardiac systole.

The pressure is maximum during the systolic phase, with relatively high values also during the diastolic phase, due to the arterial walls elasticity. During the cardiac cycle, it is possible to observe high and nearly periodic fluctuations of the blood pressure in the circulatory system. Usually, we distinguish between a maximum or systolic pressure, whose value is $90 - 130\text{mmHg}$, and a minimum or diastolic pressure, whose value is $70 - 85\text{mmHg}$. The difference between the maximum pressure and the minimum pressure is called differential or pulse pressure and its value is about $30 - 45\text{mmHg}$. All these values refer to the arterial system, while the pressure in veins is smaller and lies in the range of $7.5 - 15\text{mmHg}$, but it is subdued to sensible changes depending on the state and the posture of the body. An additional difference is e.g. the fact that veins have thinner and less elastic walls, The irregularity and complexity of the venous flow has limited, till now, a deep understanding of the physical laws that regulate it. More attention has been paid to the study of the arterial system.

Blood flows in arteries in normal physiological conditions is laminar, but some local flow instabilities can occur during the cardiac systolic phase in proximity of the aortic valve, as well as in the presence of branching or pathological conditions. The flow and the pressure waves generated by the contraction of the heart propagate through the arterial tree because of the elasticity of the walls. Moreover, there is a noticeable phenomenon of reflection of waves in correspondence of discontinuities in the geometrical or elastic properties of the arteries. This gives rise to a superposition of traveling and reflected pressure waves which must be taken into account when studying the local pressure and velocity.

2.2 Cardiovascular pathologies

The cardiovascular system can be affected by several pathologies of different nature (congenital defects, inflammatory or degenerative processes) which can concern the heart or the vascular system. We briefly describe two largely diffused and degenerative pathologies of the arterial system.

Stenosis. It indicates all the pathological situations characterized by the reduction of the size of an orifice or a vessel, independently of the cause that has generated it, so much that it obstructs and prevents the normal and physiological transition of substances. Stenoses of the vascular type are seldom of congenital nature; more frequently they indicate advanced stages of atheroscleroses. In the latter case, the artery wall thickens as consequence of the

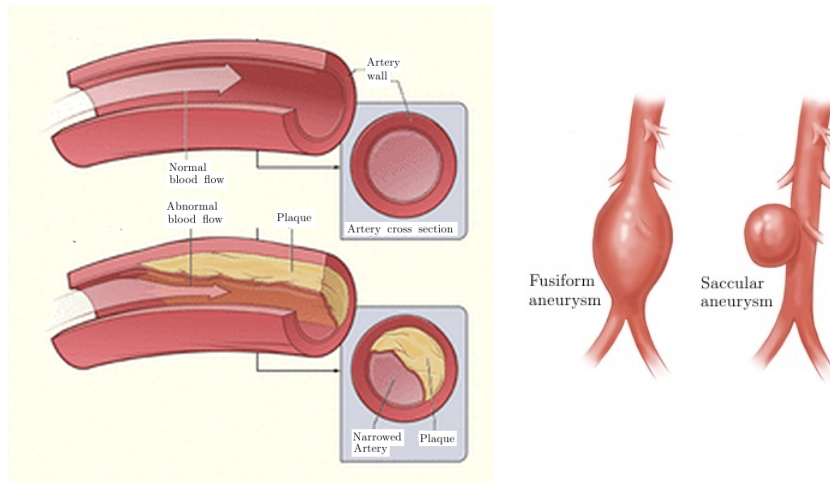


Figure 2.3: Schematic example of a stenosis (left) and aneurysms (right). *Images from [V⁺08].*

deposition of lipids and cholesterol. This disease may affect the whole artery tree, but above all the large, high-pressure vessels, e.g. the cerebral and coronary arteries. The narrowing of the lumen area is linked to an increase in the wall rigidity. The main surgical devices which can be adopted to cure a stenosis are angioplasty or the creation of an arterial bypass.

Aneurysm. It is a gradual dilation of an arterial segment over a typical time period of years. In this case, the arterial wall stretches and becomes thinner and weaker than normal arterial walls due to structural changes in the connective tissue. Consequently, untreated aneurysms can break causing severe hemorrhage. According to the aneurysm form, we can discern different typologies: saccular or fusiform. In particular, fusiform aneurysms are cylindrical dilations where the entire circumference of the artery is weakened; while saccular aneurysms are balloons-like bulges resulting from a weakening of one side of the artery wall. Saccular aneurysms can be caused by trauma or certain infections of the blood. Fusiform aneurysms are often complications of atherosclerosis, when local stenoses may lead to the release of vasoactive drugs that cause the artery to remodel. They can be located in any artery but are most commonly observed in the ascending and abdominal aorta or in cerebral arteries.

Chapter 3

Blood Flows in Arteries: Rigid Wall Models

Due to the progresses in computational mechanics techniques, in the last few decades several efforts have been dedicated towards the simulations of blood flows in arteries; we refer to [FQV⁺09] for an overview and an extensive bibliography. Modeling the cardiovascular system represents a challenging task due to the complex nature of the haemodynamic process and the need to provide results in a clinically reasonable time frame. Nevertheless, the potentiality of numerical simulations in the understanding of haemodynamic process both in the physiological and pathological conditions is high, since less invasive than *in vivo* investigations and potentially more accurate than *in vitro* studies.

The different levels of detail in the description of blood flows and of accuracy requirements lead to the development of a hierarchy of models. In general, the larger is the complexity of the model, the more the computational cost increases. For this reason, when only a global understanding of the arterial tree features is needed, *zero-dimensional models* are sufficient; otherwise, if a local detailed description of fluid dynamics is required, we need to consider *two- or three-dimensional models*. Specifically, a full simulation is required when the fluid phenomena are complex, such as in proximity of bifurcations, or in presence of pathologies such as aneurysms and stenoses.

When performing a local investigation, the selection of the appropriate model depends also on the arterial vessel considered, because of the different physical characteristics of blood in the vascular system as described in Chapter 2. E.g., the rheological behavior of the blood as a Newtonian fluid is a first approximation which can be adopted only for large and medium arteries and it is no more valid at the level of the arterioles, in which the dimension of the blood particles is of the same order of the diameter of the vessel. Moreover, the mechanical interaction between the blood flow and the vessel walls leads to consider *fluid-structure interaction models* which are computationally expensive, but able to properly represent the haemodynamic phenomena. Nevertheless, rigid wall models are sufficiently accurate for small and medium vessels, for which the wall displacement is considerably smaller than that of large vessels, whose deformation can reach up to a 10% of their radius.

In this chapter we describe the mathematical modeling of blood flows in vessels for two-dimensional problems, for which the computational domain represents a section of the vessel. We specifically consider a rigid wall model for a section of an artery, identifying the main quantities involved in the description of blood flow, including the system of PDEs that de-

scribes the blood flow, namely the *Navier-Stokes equations*. Moreover, in order to properly define the problem, suitable boundary conditions must be provided taking into account the pulsatile nature of the blood flow and the presence of the remaining part of the circulatory system.

For the numerical solution of the Navier-Stokes equations, we consider IGA in the framework of the Galerkin method for the semi-discrete spatial approximation and the generalized α -method [Whi99] to perform time discretization. The numerical stabilization of the standard Galerkin method of the Navier-Stokes equations is performed by means of the Variational Multiscale Method (VMS) for which we consider the formulation taking into account for the Large Eddy Simulation (VMS-LES) proposed in [BCC⁺07].

In Section 3.1 the Navier-Stokes equations are described and reported in dimensionless form. In Section 3.2 we describe the proper set of boundary conditions defining a well-posed problem under physiological conditions. In Section 3.3 we present the numerical approximation of the problem. In Section 3.4 we report and discuss some numerical results.

3.1 Mathematical modeling of blood flows

Since our investigation will focus on blood flows in large and medium sized vessels, we can assume for the fluid a Newtonian incompressible behavior. The main quantities involved in the description of blood flow are the *velocity* \mathbf{u} and the *pressure* P , both functions of time and space. In this section we recall the Navier-Stokes equations for an incompressible Newtonian viscous fluid with constant density, say ρ_f , in a bidimensional domain $\Omega \subseteq \mathbb{R}^2$ and in the time interval $(0, T)$. Firstly, we provide the dimensionless form of the Navier-Stokes equations, then the variational formulation, in view of their discretization. For more details on the existence, uniqueness and dependence of the solution from the data, we refer e.g. to [FQ⁺02, FQV⁺09].

3.1.1 The Navier-Stokes equations

The dynamic of fluids is described by the physical laws of mass and momentum conservation. In the hypothesis of constant density, the mass conservation property reduces to the *continuity equation* for an *incompressible* fluid, which reads:

$$\nabla \cdot \mathbf{u} = 0, \quad (3.1)$$

where $\mathbf{u} : \Omega \times (0, T) \rightarrow \mathbb{R}^2$ is the velocity of the fluid. In haemodynamics, blood is usually considered a constant density fluid with $\rho_f = 1.06 \text{ g/cm}^3$. The principle of conservation of the momentum leads to the following momentum equation:

$$\rho_f \frac{\partial \mathbf{u}}{\partial t} + \rho_f (\mathbf{u} \cdot \nabla) \mathbf{u} - \nabla \cdot \boldsymbol{\sigma}_f = \rho_f \mathbf{f}, \quad (3.2)$$

where the vector field $\mathbf{f} : \Omega \times (0, T) \rightarrow \mathbb{R}^2$ indicates the *body forces*, while $\boldsymbol{\sigma}_f$ is the second-order *Cauchy stress tensor*. Moreover, by means of the assumption that the blood behaves as a Newtonian incompressible fluid, a *constitutive law* relates the Cauchy stress tensor $\boldsymbol{\sigma}_f$ to the velocity field \mathbf{u} through the relation:

$$\boldsymbol{\sigma}_f = -PI + \mu_f (\nabla \mathbf{u} + \nabla \mathbf{u}^T) = -PI + 2\mu_f D(\mathbf{u}), \quad (3.3)$$

where P is the scalar function called *pressure* ($[P] = N/m^2$), μ_f is the fluid *dynamic viscosity* ($[\mu_f] = kg/ms$), while \mathbf{I} is the identity tensor and the tensor $D(\mathbf{u}) := \frac{(\nabla \mathbf{u} + \nabla \mathbf{u}^T)}{2}$ is the *strain tensor*. By substituting Eq. (3.3) in Eq. (3.2) and dividing by ρ_f , the ultimate form of the momentum equation for an incompressible Newtonian fluid is:

$$\frac{\partial \mathbf{u}}{\partial t} + (\mathbf{u} \cdot \nabla) \mathbf{u} + \nabla p - 2\nabla \cdot (\nu_f D(\mathbf{u})) = \mathbf{f}, \quad (3.4)$$

where we have introduced the scalar functions $p := \frac{P}{\rho_f}$, which is a *scaled pressure* ($[p] = m^2/s^2$), and $\nu_f := \frac{\mu_f}{\rho_f}$, the fluid *kinematic viscosity* ($[\nu_f] = m^2/s$).

As result, the Navier-Stokes equations that describe the motion of an incompressible Newtonian viscous fluid, with constant density ρ_f , reads:

$$\begin{cases} \frac{\partial \mathbf{u}}{\partial t} + (\mathbf{u} \cdot \nabla) \mathbf{u} + \nabla p - 2\nabla \cdot (\nu_f D(\mathbf{u})) = \mathbf{f} & \text{in } \Omega, t \in (0, T), \\ \nabla \cdot \mathbf{u} = 0 & \text{in } \Omega, t \in (0, T). \end{cases} \quad (3.5a) \quad (3.5b)$$

The problem described by the equations (3.5), in the unknown functions $\mathbf{u} = \mathbf{u}(\mathbf{x}, t)$ and $p = p(\mathbf{x}, t)$, must be completed by suitable initial and boundary conditions. The initial condition of the fluid velocity, provided by the function \mathbf{u}_0 , reads:

$$\mathbf{u}(\mathbf{x}, t = 0) = \mathbf{u}_0(\mathbf{x}) \quad \mathbf{x} \in \Omega, \quad (3.6)$$

Remark 3.1. *In haemodynamic applications for the initial condition we will consider $\mathbf{u}_0 = \mathbf{0}$. Despite the fact that we are using non physiological initial data, their effects on the numerical simulation can be considered negligible after a sufficiently long time of assessment (for example after a span of time of about two heartbeats).*

As for the boundary conditions, let $\Gamma_D, \Gamma_N \subseteq \partial\Omega$ be measurable subsets of $\partial\Omega$ such that $\overline{\Gamma_D \cup \Gamma_N} = \partial\Omega$ and $\overset{\circ}{\Gamma_D} \cap \overset{\circ}{\Gamma_N} = \emptyset$. We consider:

(N) *applied stresses* or *Neumann* boundary condition, i.e. given a vector field \mathbf{h} defined on Γ_N and denoting with \mathbf{n} the outward directed unit vector normal to Γ_N :

$$\boldsymbol{\sigma}_f \mathbf{n} = \mathbf{h} \quad \text{on } \Gamma_N; \quad (3.7)$$

(D) *prescribed velocity* or *Dirichlet* boundary condition, i.e. given a vector field \mathbf{g} defined on Γ_D :

$$\mathbf{u} = \mathbf{g} \quad \text{on } \Gamma_D. \quad (3.8)$$

If $\Gamma_D = \partial\Omega$, \mathbf{g} we need $\int_{\Gamma_D} \mathbf{g} \cdot \mathbf{n} = 0$, since \mathbf{u} satisfies (3.5b).

Remark 3.2. *In haemodynamic applications the vector field \mathbf{f} is usually set to zero; this hypothesis corresponds to consider negligible the effects of gravity.*

Remark 3.3. The term $(\mathbf{u} \cdot \nabla) \mathbf{u}$ in (3.5a), which describes the convective transport, is non-linear and quadratic in \mathbf{u} . When the fluid is highly viscous, this term may be neglected, since diffusion dominates the convection, yielding the so called Stokes equations:

$$\begin{cases} \frac{\partial \mathbf{u}}{\partial t} + \nabla p - 2\nabla \cdot (\nu_f D(\mathbf{u})) = \mathbf{f} & \text{in } \Omega, t \in (0, T), \\ \nabla \cdot \mathbf{u} = 0 & \text{in } \Omega, t \in (0, T), \end{cases} \quad (3.9a)$$

$$(3.9b)$$

endowed with suitable initial and boundary conditions.

3.1.2 The Navier-Stokes equations in dimensionless form

In order to provide the dimensionless form of the Navier-Stokes equations (3.5), we introduce a characteristic length of the domain, say L_0 , and a characteristic velocity, say V_0 . Typically, for the blood flow, L_0 is the vessel diameter, while V_0 is the average velocity. In such a way, we can provide the dimensionless space, time, pressure and velocity variables and body force, which we denote by the superscript $*$:

$$\mathbf{x}^* = \frac{\mathbf{x}}{L_0}, \quad t^* = t \frac{V_0}{L_0}, \quad p^* = \frac{p}{V_0^2}, \quad \mathbf{u}^* = \frac{\mathbf{u}}{V_0}, \quad \mathbf{f}^* := \frac{L_0}{V_0^2} \mathbf{f}. \quad (3.10)$$

Instead, the dimensionless differential operators, with respect to the independent variables, read:

$$\frac{\partial}{\partial t} = \frac{dt^*}{dt} \frac{\partial}{\partial t^*} = \frac{V_0}{L_0} \frac{\partial}{\partial t^*}, \quad \nabla = \frac{1}{L_0} \nabla^*, \quad D = \frac{1}{L_0} D^*. \quad (3.11)$$

In such a way, the momentum equation (3.5a) and the continuity equation (3.5b) in dimensionless form read, respectively:

$$\frac{V_0^2}{L_0} \frac{\partial \mathbf{u}^*}{\partial t^*} + \frac{V_0^2}{L_0} (\mathbf{u}^* \cdot \nabla^*) \mathbf{u}^* + \frac{V_0^2}{L_0} \nabla^* p^* - 2 \frac{V_0^2}{L_0} \nabla^* \cdot \left(\frac{\nu_f}{V_0 L_0} D^*(\mathbf{u}^*) \right) = \frac{V_0^2}{L_0} \mathbf{f}^*, \quad (3.12a)$$

$$\frac{V_0}{L_0} \nabla^* \cdot \mathbf{u}^* = 0, \quad (3.12b)$$

in the dimensionless physical domain $\Omega^* := \{\mathbf{x}^* \in \mathbb{R}^2 : \mathbf{x}^* = \frac{\mathbf{x}}{L_0}, \text{ with } \mathbf{x} \in \Omega\}$ and dimensionless time interval $(0, T^*) := \{t^* \in \mathbb{R} : t^* = t \frac{V_0}{L_0}, \text{ with } t \in (0, T)\}$. By multiplying Eq. (3.12) for L_0/V_0^2 , we identify the dimensionless parameter which describes the characteristic properties of the equation:

$$\mathbb{Re} = \frac{V_0 L_0}{\nu_f}, \quad (3.13)$$

which is the *Reynolds number*.

For the sake of simplicity, we will omit henceforth the superscript $*$ (unless when necessary). Moreover, we denote $\dot{\mathbf{u}} := \frac{\partial \mathbf{u}}{\partial t}$. In such a way the set of equations (3.5) in dimensionless form

reads:

$$\begin{cases} \dot{\mathbf{u}} + (\mathbf{u} \cdot \nabla) \mathbf{u} + \nabla p - 2\nabla \cdot \left(\frac{1}{\text{Re}} D(\mathbf{u}) \right) = \mathbf{f} & \text{in } \Omega, t \in (0, T), \\ \nabla \cdot \mathbf{u} = 0 & \text{in } \Omega, t \in (0, T). \\ \mathbf{u}(0) = \mathbf{u}_0 & \text{in } \Omega, \\ \boldsymbol{\sigma}_f \mathbf{n} = \mathbf{h} & \text{on } \Gamma_N, t \in (0, T), \\ \mathbf{u} = \mathbf{g} & \text{on } \Gamma_D, t \in (0, T), \end{cases} \quad \begin{array}{l} (3.14a) \\ (3.14b) \\ (3.14c) \\ (3.14d) \\ (3.14e) \end{array}$$

where the functions defining the initial and boundary conditions have been accordingly provided in dimensionless form.

Remark 3.4. *The Reynolds number measure the ratio of inertial forces with respect to viscous forces and it represents the parameter that allows to determine the transition between laminar and turbulent flow. The latter would typically manifest in some physiological conditions in the circulatory system and in pathological cases such as with stenotic vessels. Numerically, in order to capture the turbulence phenomena we may need to use the so-called turbulence models, such as VMS for Large Eddy Simulation [BCC⁺07, EH10, HS07, TMJ07, HMJ00].*

3.1.3 The Navier-Stokes equations in variational formulation

In view of the spatial approximation by means of the Galerkin method with IGA, we recall the variational formulation of the Navier-Stokes equations in dimensionless form given in Eq. (3.14) and completed by suitable initial and boundary conditions, as those described in Eqs. (3.6), (3.7) and (3.8), accordingly provided in dimensionless form.

We define the trial and test function spaces, respectively:

$$V_g := \left\{ \mathbf{v} \in [H^1(\Omega)]^2 : \mathbf{v}|_{\Gamma_D} = \mathbf{g} \right\}, \quad (3.15a)$$

$$V := \left\{ \boldsymbol{\varphi} \in [H^1(\Omega)]^2 : \boldsymbol{\varphi}|_{\Gamma_D} = \mathbf{0} \right\}, \quad (3.15b)$$

$$Q := L^2(\Omega).^1 \quad (3.15c)$$

We recast the Navier-Stokes equations in variational formulation by multiplying the momentum equation (3.14a) by a vector valued weighting function $\boldsymbol{\varphi} \in V$, integrating over the spatial domain and applying the Green's integration formula. Moreover, the continuity equation (3.14b) is multiplied by a scalar valued test function $q \in Q$ and integrated over the spatial domain. The variational formulation of the Navier-Stokes equations in *residual form* reads:

find, for all $t \in (0, T)$, $\mathbf{u}(t) \in V_g$ and $p(t) \in Q$ such that:

$$\begin{cases} B_M(\boldsymbol{\varphi}; \dot{\mathbf{u}}(t), \mathbf{u}(t), p(t)) = 0 & \forall \boldsymbol{\varphi} \in V, \\ B_C(\psi; \dot{\mathbf{u}}(t), \mathbf{u}(t), p(t)) = 0 & \forall \psi \in Q, \\ \mathbf{u}(0) = \mathbf{u}_0 & \text{in } \Omega, \end{cases} \quad \begin{array}{l} (3.16a) \\ (3.16b) \\ (3.16c) \end{array}$$

¹In the case in which we have a Dirichlet boundary conditions on the whole boundary, i.e. $\Gamma_D = \partial\Omega$, the pressure is determined up to a constant. We can impose the uniqueness of the solution e.g. by means of the zero-mean constraint. In such a case, the function space Q is defined as $Q := \left\{ \psi \in L^2(\Omega) : \int_{\Omega} \psi = 0 \right\}$.

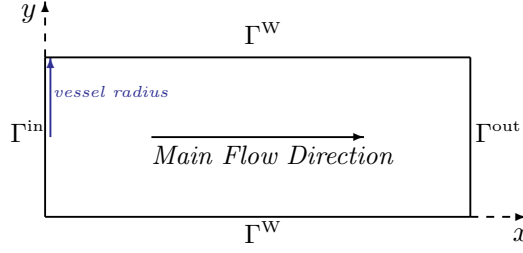


Figure 3.1: Two dimensional computational domain Ω for a vessel section of cylindrical shape. Boundary conditions set on Γ^W (wall boundary), Γ^{in} (inlet boundary) and Γ^{out} (outlet boundary).

where the residuals of the momentum and continuity equations are given by, respectively:

$$B_M(\varphi; \dot{\mathbf{u}}, \mathbf{u}, p) := m(\dot{\mathbf{u}}, \varphi) + a(\mathbf{u}, \varphi) + c(\mathbf{u}, \mathbf{u}, \varphi) + b(\varphi, p) - F(\varphi) - H(\varphi), \quad (3.17a)$$

$$B_C(\psi; \dot{\mathbf{u}}, \mathbf{u}, p) := b(\mathbf{u}, \psi), \quad (3.17b)$$

with the bilinear forms defined as $m(\dot{\mathbf{u}}, \varphi) := \int_{\Omega} \dot{\mathbf{u}} \cdot \varphi \, d\Omega$, $a(\mathbf{u}, \varphi) := \frac{2}{\text{Re}} \int_{\Omega} D(\mathbf{u}) : D(\varphi) \, d\Omega$ and $b(\varphi, p) := - \int_{\Omega} p \nabla \cdot \varphi \, d\Omega$; while the form $c(\cdot, \cdot, \cdot)$ is given by $c(\mathbf{v}, \mathbf{u}, \varphi) = \int_{\Omega} (\mathbf{v} \cdot \nabla) \mathbf{u} \cdot \varphi \, d\Omega$. Finally, the functionals are given by $F(\varphi) := \int_{\Omega} \mathbf{f} \cdot \varphi \, d\Omega$ and $H(\varphi) := \int_{\Gamma_N} \mathbf{h} \cdot \varphi \, d\Gamma$.

3.2 Boundary conditions for physiological flows

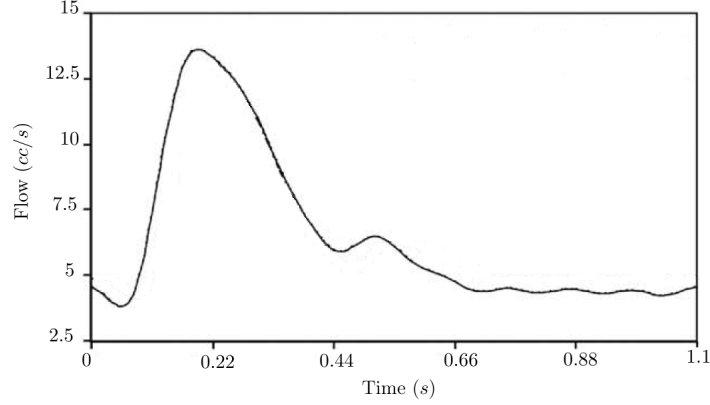
In modeling the blood flow we are interested in accounting for a part of the cardiovascular system without neglecting the effects of the downstream circulation. In this section we describe the boundary conditions formulating a physiologically-compatible two-dimensional model and a mathematically well-posed problem governed by Eqs. (3.14).

A first approximation of a section of a vessel can be considered a cylinder; thus, for a two-dimensional model, the computational domain reduces to a rectangle. An example of a two-dimensional computational domain is given in Figure 3.1. The upper and lower boundaries, say Γ^W , correspond to the walls surrounding the vessel. We impose on them homogeneous Dirichlet conditions ($\mathbf{g}^W = \mathbf{0}$), also called *no-slip condition*, responding to a *rigid wall model*. The boundary Γ^{in} represents the *inlet* boundary, while Γ^{out} the *outlet* boundary. A common practice, responding to physical considerations, is to prescribe a velocity profile on Γ^{in} , i.e. a Dirichlet condition (\mathbf{g}^{in}), while a suitable Neumann condition in the outlet section Γ^{out} , which represents the circulatory system. In such a way, we typically have $\Gamma_D = \Gamma^W \cup \Gamma^{\text{in}}$ and $\Gamma_N = \Gamma^{\text{out}}$. For more details and alternative formulations, we refer the interested reader to e.g. [VdVS11, Wom57, AADRF09, THZ98] and [BGH⁺09, VCFJT06].

3.2.1 The inlet condition: pulsatile flow

At the inlet boundary, we prescribe a pulsatile periodic flow mapped to a parabolic velocity profile, according to data provided in [FVCJT06]. We assume that the known function \mathbf{g}^{in} , defining the Dirichlet boundary condition (3.8) on Γ^{in} , assumes the form:

$$\mathbf{g}^{\text{in}} : \Gamma^{\text{in}} \times (0, T) \rightarrow \mathbb{R}^2 \quad \text{such that} \quad \mathbf{g}^{\text{in}}(\mathbf{x}, t) := \mathbf{v}^{\text{in}}(\mathbf{x})q(t), \quad (3.18)$$

Figure 3.2: Physiological flow $Q^{\text{in}}(t)$ (in cc/s) vs. time (in s).

with $\mathbf{v}^{\text{in}} : \Gamma^{\text{in}} \rightarrow \mathbb{R}^2$ a vectorial function and $q : (0, T) \rightarrow \mathbb{R}$ a scalar function. In particular, the velocity profile which we define belongs to the category of velocity profile approximations referred as the *assumed shape profile* [VdVS11]. In order to provide an explicit expression for Eq. (3.18), firstly we consider the dimensional setting in radial coordinates, then we move to the dimensionless form in Cartesian coordinates, assuming the invariance of the velocity with respect to the circumferential coordinate.

In Figure 3.2 we show a realistic volumetric flow rate profile $Q^{\text{in}}(t)$ at the inlet interface of a carotid artery with nominal radius $r_V = 0.3\text{cm}$ and period $T_{\text{HB}} = 1.1\text{s}$, where T_{HB} indicates the period of an *heartbeat*. By considering the definition of *volumetric flow rate*, which represents the volume of fluid passing through the inlet surface in a three-dimensional vessel, its expression is given by the integral of the velocity profile over the arterial cross section. In such a way, for every $t \in (0, T)$, we have:

$$Q^{\text{in}}(t) := \int_{\Gamma^{\text{in}}} \mathbf{g}^{\text{in}} \cdot \mathbf{n} \, d\Gamma = \int_0^{2\pi} \int_0^{r_V} \mathbf{v}^{\text{in}}(r) q(t) r \, dr \, d\theta = q(t) 2\pi \int_0^{r_V} \mathbf{v}^{\text{in}}(r) r \, dr, \quad (3.19)$$

for which we can define the dimensionless function in the temporal variable t as:

$$q : (0, T) \rightarrow \mathbb{R}, \quad q(t) := \frac{Q^{\text{in}}(t)}{2\pi \int_0^{r_V} \mathbf{v}^{\text{in}}(r) r \, dr}. \quad (3.20)$$

By imposing the constrain $q(\bar{t}) = 1$, with $\bar{t} := \arg \max_{t \in (0, T_{\text{HB}})} Q^{\text{in}}(t)$, we set:

$$\mathbf{v}^{\text{in}} : \Gamma^{\text{in}} \rightarrow \mathbb{R}^2, \quad \mathbf{v}^{\text{in}}(r) := \left(\frac{2Q_{\text{MAX}}^{\text{in}}}{\pi r_V^2} \left(1 - \frac{r^2}{r_V^2} \right), 0 \right), \quad (3.21)$$

where $Q_{\text{MAX}}^{\text{in}} := \max_{t \in (0, T_{\text{HB}})} Q^{\text{in}}(t)$. We operate the change of variables in Cartesian coordinates by setting $r = |y - r_V|$ and then we consider the dimensionless space, time and velocity variables given in Eqs. (3.10). In such a way, the inlet dimensionless condition for the physical (dimensionless) domain shown in Figure 3.1, reads:

$$\mathbf{g}^{\text{in}}(\mathbf{x}, t) = \mathbf{v}^{\text{in}}(\mathbf{x}) q(t) = 4y(-y + 1)q(t), \quad (3.22)$$

for $y \in (0, 1)$.

Remark 3.5. *In order to adapt this condition for vessels whose radius is smaller than the one for which the physiological flow rate is provided, we consider a suitable rescaling of the profile given in Figure 3.2.*

3.2.2 The outlet condition: the resistance condition

The blood flow in large and medium arteries is highly dependent on the outflow boundary conditions in ensuring realistic responses. This is due to the fact that pulse waves may be partially reflected by the downstream circulation at the outlet section of the artery, especially the pressure waves. In order to avoid spurious reflections of the pressure and flow, a geometrical multiscale approach can be adopted. In particular, we refer to a variant form of the classical *Resistance boundary condition* (see for instance [RMP⁺09, VdVS11]), which couples the model with zero-dimensional or *lumped* models. Specifically, we prescribe at the outlet boundary a Neumann condition similar to the one described in [BGH⁺09, BCHZ08].

On $\Gamma_N = \Gamma^{\text{out}}$ we consider the condition given in Eq. (3.7) decomposing the prescribed stress on the outlet face in its normal and tangential components as it follows:

$$\mathbf{h} := h_{\perp} \mathbf{n} + h_{\parallel} \mathbf{t}, \quad (3.23)$$

where \mathbf{n} is the outward directed unit vector normal to Γ^{out} and \mathbf{t} indicates the tangent vector. We set:

$$h_{\parallel} = 0, \quad (3.24a)$$

$$h_{\perp} = -(C_{\text{out}} Q_{\text{out}} + P_V). \quad (3.24b)$$

The coefficient C_{out} in Eq. (3.24b) is the *resistance constant* and it is a positive quantity (dimensionally, $[C_{\text{out}}] = \text{dyn} \cdot \text{s}/\text{cm}^5$). The values of this parameter can be obtained by *in vivo* measurements and vary with the vessel; we refer to [RMP⁺09] and [BGH⁺09] for physiological values. The term P_V allows to impose a physiologically realistic pressure in the vessel; dimensionally we set $P_V = 85 \text{ mmHg}$. Finally, Q_{out} refers to the flowrate through Γ^{out} , which we approximate by means of the following expression:

$$Q_{\text{out}} := \frac{\pi}{4} L_{\text{out}} \int_{\Gamma^{\text{out}}} \mathbf{u} \cdot \mathbf{n} \, d\Gamma, \quad (3.25)$$

where L_{out} is the diameter of the outlet face. The boundary condition in Eq. (3.23) is provided in its dimensionless form and imposed weakly in the variational formulation (3.16) by inserting it into the residual in Eq. (3.17a):

$$-\int_{\Gamma^{\text{out}}} \mathbf{h} \cdot \boldsymbol{\varphi} \, d\Gamma = \left(\int_{\Gamma^{\text{out}}} \mathbf{n} \cdot \boldsymbol{\varphi} \, d\Gamma \right) \left(C_{\text{out}}^* \int_{\Gamma^{\text{out}}} \mathbf{u} \cdot \mathbf{n} \, d\Gamma + p_V \right), \quad (3.26)$$

where the dimensionless constant C_{out}^* is given by $C_{\text{out}}^* := \frac{\pi}{4} C_{\text{out}} L_{\text{out}} \frac{L_0}{V_0 \rho_f}$, while $p_V = \frac{1}{V_0 \rho_f} P_V$, where L_0 and V_0 are the characteristic length and velocity introduced in Section 3.1.2, while ρ_f is the density fluid.

Remark 3.6. *Due to the fact that the imposition of a Neumann condition in the outlet section may cause instabilities in the presence of flow reversal, in [BGH⁺09] the condition of Eq. (3.23) is augmented by a term acting only in presence of reverse flows. Instead, we choose the basic form provided in [BCHZ08].*

3.3 The numerical approximation of the Navier-Stokes equations

In this section we present the numerical schemes for the solution of the Navier-Stokes equations (3.16). We provide the semi-discretized formulation in space based on the Galerkin method in the framework of NURBS-based IGA. For the numerical stabilization of the Navier-Stokes equations we consider the Variational Multiscale Method with turbulence modeling for the Large Eddy Simulation (VMS-LES) proposed in [BCC⁺07]. The time discretization is performed by means of the generalized α -method [Whi99, JWH00].

3.3.1 Spatial approximation by means of IGA

In order to provide the semi-discrete IGA-Galerkin formulation, as described in Chapter 1 for elliptic PDEs, for the spatial approximation of the Navier-Stokes equations (3.16) defined in the physical domain Ω , we first parametrize the computational domain Ω as a NURBS geometry. The space of NURBS functions in Ω , say \mathcal{V}^h , is given in Eq. (1.22). When considering NURBS-based IGA, we define the finite dimensional subspaces of the trial and test spaces given in Eq. (3.15) as subspaces of the space \mathcal{V}^h of NURBS. Specifically, we set $V^h := V \cap [\mathcal{V}^h]^2$, $Q^h := Q \cap \mathcal{V}^h$ and $V_g^h := V_g \cap [\mathcal{V}^h]^2$ (we refer to Example 1.11 for the case of non homogeneous essential boundary conditions). In such a way, the semi-discrete IGA-Galerkin formulation of problem (3.16) reads:

find, for all $t \in (0, T)$, $\mathbf{u}_h(t) \in V_g^h$ and $p_h(t) \in Q^h$ such that:

$$\begin{cases} B_M(\boldsymbol{\varphi}_h; \dot{\mathbf{u}}_h(t), \mathbf{u}_h(t), p_h(t)) = 0 & \forall \boldsymbol{\varphi}_h \in V^h, \\ B_C(\psi_h; \dot{\mathbf{u}}_h(t), \mathbf{u}_h(t), p_h(t)) = 0 & \forall \psi_h \in Q^h, \\ \mathbf{u}_h(0) = \mathbf{u}_0 & \text{in } \Omega, \end{cases} \quad \begin{aligned} (3.27a) \\ (3.27b) \\ (3.27c) \end{aligned}$$

where the respective residuals are given in Eqs. (3.17a) and (3.17b).

Remark 3.7. Due to the vectorial nature of functions in V_g^h or V^h , we group the basis functions by means of the canonical basis $\{\mathbf{e}_i\}_{i=1}^2$. In particular, let the dimension of V^h be $\dim V^h = N_{V^h}$, we define the basis functions as:

$$\mathcal{R}_A^1 := \begin{bmatrix} \mathcal{R}_A \\ 0 \end{bmatrix} = \mathcal{R}_A \mathbf{e}_1, \quad \mathcal{R}_A^2 := \begin{bmatrix} 0 \\ \mathcal{R}_A \end{bmatrix} = \mathcal{R}_A \mathbf{e}_2, \quad \forall A = 1, \dots, N_b, \quad \text{with } N_b := \frac{N_{V^h}}{2}.$$

In such way, we can consider separately the two components of the vectorial functions in V^h or V_g^h . In particular, the approximate solution of the unknown velocity field for each time $t \in (0, T)$ can be expressed in the form:

$$\mathbf{u}_h(t) = \sum_{i=1}^2 \sum_{A=1}^{N_b} u_{iA}(t) \mathcal{R}_A^i + \mathbf{g}_h(t), \quad (3.28)$$

where \mathbf{g}_h is the lifting function of the Dirichlet boundary data (eventually an approximation in the NURBS space), i.e. $\mathbf{g}_h|_{\Gamma_D} \approx \mathbf{g}$, this yields the assumption that $\{u_{iA}(t)\}_{A,i}$ are such that

$\sum_{i=1}^2 \sum_{A=1}^{N_b} u_{iA}(t) \mathcal{R}_A^i|_{\Gamma_D} = 0$. Moreover, the respective components are given by:

$$(\mathbf{u}_h)_1(t) = \sum_{A=1}^{N_b} u_{1A}(t) \mathcal{R}_A^1 + (\mathbf{g}_h)_1(t) \quad \text{and} \quad (\mathbf{u}_h)_2(t) = \sum_{A=1}^{N_b} u_{2A}(t) \mathcal{R}_A^2 + (\mathbf{g}_h)_2(t).$$

Under the assumption that the pressure and each velocity component are expressed in terms of the same (N_b) basis functions $\{\mathcal{R}_A\}_{A=1}^{N_b}$, if we consider the lexicographical reordering, the vectors of control variables for all $t \in (0, T)$, are:

$$\dot{\mathbf{U}}(t) = \left\{ \{u_{iA}(t)\}_{1 \leq A \leq N_b} \right\}_{i=1}^2, \quad \mathbf{U}(t) = \left\{ \{u_{iA}(t)\}_{1 \leq A \leq N_b} \right\}_{i=1}^2, \quad \mathbf{P}(t) = \{p_A(t)\}_{1 \leq A \leq N_b}. \quad (3.29)$$

In the theoretical development and in the computational setting, we consider the same basis functions for the velocity and the pressure spaces. It is well known that this couple of spaces does not satisfy the *Babuška-Brezzi condition* [Qua09, BF91], for which:

$$\text{there exists } \beta_0 > 0 \quad \text{such that} \quad \inf_{\psi_h \in Q^h} \sup_{\varphi_h \in V^h} \frac{b(\varphi_h, \psi_h)}{\|\psi_h\|_Q \|\varphi_h\|_V} \geq \beta_0, \quad (3.30)$$

leading to the presence of *spurious pressure modes*. In the framework of techniques used in FEA, several stabilized methods can be considered to overcome this issue, following the saddle-point nature of the continuous problem for the incompressible Navier-Stokes equations. A general study of stabilization techniques is presented in [BF91]; see also [CPGB07, JTM05, HW05, JW01, HFB86, FF92, TMJ07].

3.3.2 The Variational Multiscale method: stabilization and Large Eddy Simulation

The stabilized Galerkin formulation of the Navier-Stokes equations (3.16), proposed in [BCC⁺07] and presented here for NURBS-based IGA, is based on the Variational Multiscale formulation (VMS) for Large Eddy simulation (LES). The reason to use the VMS for the Navier-Stokes equations is multiple. Firstly, it has the role to provide a stable formulation in the sense of the inf-sup condition, then it controls the numerical instabilities arising in advection dominated regimes, i.e. for high Reynolds numbers. Finally, the VMS-LES provides a way to numerically model turbulence according to the Large Eddy simulation principles; the method is based on an a priori scales separation, contrarily to standard approaches which consider it a posteriori or by means of filters. The problem is decomposed into coarse and fine scales; an approximate analytical expression for the solution of the fine-scale equations is substituted into the coarse-scale equations, in order to obtain a closed system that can be solved numerically. The solution of the coarse-scale problem is assumed as the approximate solution of the Navier-Stokes equations. We briefly describe the significant steps that lead to the VMS-LES formulation, referring to [BCC⁺07] for a complete analysis.

Remark 3.8. *In the following, for simplicity, we assume that we have homogeneous Dirichlet boundary conditions for the Navier-Stokes equations, i.e. we impose in Eq. (3.8) $\Gamma_D = \partial\Omega$ and $\mathbf{g} = \mathbf{0}$. In such a way, the trial solution and the test spaces for the velocity are coincident,*

i.e. $V_g = V$. Moreover, by applying the Green's formula, the trilinear form $c(\cdot, \cdot, \cdot)$ in the momentum residual (3.17a), can be rewritten as:

$$c(\mathbf{v}, \mathbf{u}, \boldsymbol{\varphi}) = \int_{\Omega} (\mathbf{v} \cdot \nabla) \mathbf{u} \cdot \boldsymbol{\varphi} \, d\Omega = \int_{\Omega} \nabla \cdot (\mathbf{v} \otimes \mathbf{u}) \cdot \boldsymbol{\varphi} \, d\Omega = - \int_{\Omega} \nabla \boldsymbol{\varphi} : (\mathbf{v} \otimes \mathbf{u}) \, d\Omega. \quad (3.31)$$

Remark 3.9. In order to make the notation consistent with the one used in [BCC⁺07], in this section we will refer to the arguments of the residuals in Eqs. (3.17) as (\mathbf{u}, p) , instead of $(\dot{\mathbf{u}}, \mathbf{u}, p)$. This choice is possible since the relation between $\dot{\mathbf{u}}$ and \mathbf{u} is known.

Decomposition into fine and coarse scales

Given the test spaces V and Q associated to the Navier-Stokes equations (3.16) with homogeneous Dirichlet boundary conditions on $\Gamma_D = \partial\Omega$, we define the space $\mathcal{S} := V \times Q$ and decompose it into the direct sum of a finite dimensional (*coarse-scale*) subspace $\bar{\mathcal{S}} = \bar{V} \times \bar{Q}$ and a (*fine-scale*) subspace $\tilde{\mathcal{S}} = \tilde{V} \times \tilde{Q}$, such that:

$$\mathcal{S} = \bar{\mathcal{S}} \oplus \tilde{\mathcal{S}}. \quad (3.32)$$

In order to define the decomposition of each element in \mathcal{S} , say $\mathbf{s} := (\mathbf{u}, p)$, into a unique pair of elements $(\bar{\mathbf{u}}, \bar{p}) = \bar{\mathbf{s}} \in \bar{\mathcal{S}}$ (*coarse-scale* component), and $(\tilde{\mathbf{u}}, \tilde{p}) = \tilde{\mathbf{s}} \in \tilde{\mathcal{S}}$ (*fine-scale* component), we introduce a projector operator $\mathbb{P} : \mathcal{S} \rightarrow \bar{\mathcal{S}} : \mathbf{s} \mapsto \bar{\mathbf{s}}$. Once \mathbb{P} is chosen, the direct sum of Eq. (3.32) is well defined and we can write each element in \mathcal{S} as $\mathbf{s} = \bar{\mathbf{s}} + \tilde{\mathbf{s}}$. By considering the decomposition of the test functions into their coarse- and fine-scale components $(\boldsymbol{\varphi}, \psi) = (\bar{\boldsymbol{\varphi}}, \bar{\psi}) + (\tilde{\boldsymbol{\varphi}}, \tilde{\psi})$, we can use the linearity of the momentum and continuum residuals to write the problem (3.16) in the form:

find, for all $t \in (0, T)$, $\mathbf{s}(t) = (\mathbf{u}(t), p(t)) \in \mathcal{S}$ such that, respectively:

$$\begin{cases} B_M(\bar{\boldsymbol{\varphi}}; (\mathbf{u}(t), p(t))) + B_M(\tilde{\boldsymbol{\varphi}}; (\mathbf{u}(t), p(t))) = 0 & \forall \bar{\boldsymbol{\varphi}} \in \bar{\mathcal{S}}, \tilde{\boldsymbol{\varphi}} \in \tilde{\mathcal{S}}, \\ B_C(\bar{\psi}; (\mathbf{u}(t), p(t))) + B_C(\tilde{\psi}; (\mathbf{u}(t), p(t))) = 0 & \forall \bar{\psi} \in \bar{\mathcal{S}}, \tilde{\psi} \in \tilde{\mathcal{S}}, \\ \mathbf{u}(0) = \mathbf{u}_0 & \text{in } \Omega. \end{cases} \quad (3.33a) \quad (3.33b) \quad (3.33c)$$

For the sake of simplicity, since we deal with the spatial decomposition, henceforth we will leave implicit the initial condition of Eq. (3.33c) and the temporal dependence of the solution (\mathbf{u}, p) . Starting from problem (3.33), we can decompose the Navier-Stokes equations into the coupled coarse-scale (3.34a) and fine-scale (3.34b) problems (by assuming that each of the terms in Eq. (3.33) are zero independently from the others), which are respectively defined by the equations:

$$\begin{cases} B_M(\bar{\boldsymbol{\varphi}}; (\mathbf{u}, p)) = 0 & \forall \bar{\boldsymbol{\varphi}} \in \bar{\mathcal{S}}, \\ B_C(\bar{\psi}; (\mathbf{u}, p)) = 0 & \forall \bar{\psi} \in \bar{\mathcal{S}}; \end{cases} \quad (3.34a)$$

$$\begin{cases} B_M(\tilde{\boldsymbol{\varphi}}; (\mathbf{u}, p)) = 0 & \forall \tilde{\boldsymbol{\varphi}} \in \tilde{\mathcal{S}}, \\ B_C(\tilde{\psi}; (\mathbf{u}, p)) = 0 & \forall \tilde{\psi} \in \tilde{\mathcal{S}}; \end{cases} \quad (3.34b)$$

We express Eq. (3.34a) as a *finite*-dimensional system for the coarse-scale component of the solution, depending parametrically on the fine-scale component. Likewise, Eq. (3.34b) can be rewritten as an *infinite*-dimensional system for the fine-scale component of the solution, depending parametrically on the coarse-scale component. With this aim, we firstly observe

that, once fixed the test functions, say $(\boldsymbol{\varphi}, \psi)$, we can interpret the residual of the continuity equation of Eq. (3.17b) as a linear functional in (\mathbf{u}, p) ; moreover we can decompose the residual of the momentum equation into the sum of a linear functional in (\mathbf{u}, p) , say $B_{M,1}$, a bilinear form in (\mathbf{u}, p) , say $B_{M,2}$, which are respectively given by:

$$B_{M,1}(\boldsymbol{\varphi}; (\mathbf{u}, p)) := m(\dot{\mathbf{u}}, \boldsymbol{\varphi}) + a(\mathbf{u}, \boldsymbol{\varphi}) + b(\boldsymbol{\varphi}, p), \quad (3.35a)$$

$$B_{M,2}(\boldsymbol{\varphi}; (\mathbf{u}, p), (\mathbf{u}, p)) := c(\mathbf{u}, \mathbf{u}, \boldsymbol{\varphi}), \quad (3.35b)$$

and a constant $F(\boldsymbol{\varphi})$ in (\mathbf{u}, p) . This results in:

$$B_M(\boldsymbol{\varphi}; (\mathbf{u}, p)) = B_{M,1}(\boldsymbol{\varphi}; (\mathbf{u}, p)) + B_{M,2}(\boldsymbol{\varphi}; (\mathbf{u}, p), (\mathbf{u}, p)) + F(\boldsymbol{\varphi}) \quad (3.36)$$

where we have used the same notation for the forms and functional defining the residual of the momentum equation of Eq. (3.17a). In such a way, by considering the decomposition of the unknown $\mathbf{s} = (\mathbf{u}, p) \in \mathcal{S}$ in its coarse- and fine-components, i.e. $\mathbf{s} = \bar{\mathbf{s}} + \tilde{\mathbf{s}}$, the residuals of the coarse- and fine-scale problems can be rewritten as it follows:

$$B_M(\bar{\boldsymbol{\varphi}}; \bar{\mathbf{s}} + \tilde{\mathbf{s}}) = B_{M,1}(\bar{\boldsymbol{\varphi}}; \bar{\mathbf{s}}) + B_{M,1}(\bar{\boldsymbol{\varphi}}; \tilde{\mathbf{s}}) + B_{M,2}(\bar{\boldsymbol{\varphi}}; \bar{\mathbf{s}}, \bar{\mathbf{s}}) \quad (3.37a)$$

$$+ B_{M,2}(\bar{\boldsymbol{\varphi}}; \bar{\mathbf{s}}, \tilde{\mathbf{s}}) + B_{M,2}(\bar{\boldsymbol{\varphi}}; \tilde{\mathbf{s}}, \bar{\mathbf{s}}) + B_{M,2}(\bar{\boldsymbol{\varphi}}; \tilde{\mathbf{s}}, \tilde{\mathbf{s}}) + F(\bar{\boldsymbol{\varphi}}),$$

$$B_C(\bar{\psi}; \bar{\mathbf{s}} + \tilde{\mathbf{s}}) = B_C(\bar{\psi}; \bar{\mathbf{s}}) + B_C(\bar{\psi}; \tilde{\mathbf{s}}), \quad (3.37b)$$

$$B_M(\tilde{\boldsymbol{\varphi}}; \bar{\mathbf{s}} + \tilde{\mathbf{s}}) = B_{M,1}(\tilde{\boldsymbol{\varphi}}; \bar{\mathbf{s}}) + B_{M,1}(\tilde{\boldsymbol{\varphi}}; \tilde{\mathbf{s}}) + B_{M,2}(\tilde{\boldsymbol{\varphi}}; \bar{\mathbf{s}}, \bar{\mathbf{s}}) \quad (3.37c)$$

$$+ B_{M,2}(\tilde{\boldsymbol{\varphi}}; \bar{\mathbf{s}}, \tilde{\mathbf{s}}) + B_{M,2}(\tilde{\boldsymbol{\varphi}}; \tilde{\mathbf{s}}, \bar{\mathbf{s}}) + B_{M,2}(\tilde{\boldsymbol{\varphi}}; \tilde{\mathbf{s}}, \tilde{\mathbf{s}}) + F(\tilde{\boldsymbol{\varphi}}),$$

$$B_C(\tilde{\psi}; \bar{\mathbf{s}} + \tilde{\mathbf{s}}) = B_C(\tilde{\psi}; \bar{\mathbf{s}}) + B_C(\tilde{\psi}; \tilde{\mathbf{s}}). \quad (3.37d)$$

Remark 3.10. In Eq. (3.37a) the term $B_{M,2}(\bar{\boldsymbol{\varphi}}; \bar{\mathbf{s}}, \tilde{\mathbf{s}}) + B_{M,2}(\bar{\boldsymbol{\varphi}}; \tilde{\mathbf{s}}, \bar{\mathbf{s}})$ is called cross-stress term, while we refer to $B_{M,2}(\bar{\boldsymbol{\varphi}}; \tilde{\mathbf{s}}, \tilde{\mathbf{s}})$ as the Reynolds stress term.

Firstly, we consider the fine-scale problem (3.34b) in which the coarse-scale component of the unknown $\bar{\mathbf{s}}$ is considered as a parameter entering the equations. In such a way, the problem (3.34b) reads:

find $\tilde{\mathbf{s}} \in \tilde{\mathcal{S}}$ such that:

$$\begin{cases} B_{M,\bar{\mathbf{s}}}(\tilde{\boldsymbol{\varphi}}; \tilde{\mathbf{s}}) + B_{M,2}(\tilde{\boldsymbol{\varphi}}; \tilde{\mathbf{s}}, \tilde{\mathbf{s}}) = \langle \tilde{\boldsymbol{\varphi}}, Res_M(\bar{\mathbf{s}}) \rangle_{\tilde{V}, \tilde{V}'}, & \forall \tilde{\boldsymbol{\varphi}} \in \tilde{\mathcal{S}}, \\ B_{C,\bar{\mathbf{s}}}(\tilde{\psi}; \tilde{\mathbf{s}}) = \langle \tilde{\psi}, Res_C(\bar{\mathbf{s}}) \rangle_{\tilde{Q}, \tilde{Q}'}, & \forall \tilde{\psi} \in \tilde{\mathcal{S}}, \end{cases} \quad (3.38a)$$

$$\quad (3.38b)$$

where each term in Eq. (3.38) is defined according to [BCC⁺07] as:

$$B_{M,\bar{\mathbf{s}}}(\tilde{\boldsymbol{\varphi}}; \tilde{\mathbf{s}}) := B_{M,1}(\tilde{\boldsymbol{\varphi}}; \tilde{\mathbf{s}}) + B_{M,2}(\tilde{\boldsymbol{\varphi}}; \bar{\mathbf{s}}, \tilde{\mathbf{s}}) + B_{M,2}(\tilde{\boldsymbol{\varphi}}; \tilde{\mathbf{s}}, \bar{\mathbf{s}}), \quad (3.39a)$$

$$\langle \tilde{\boldsymbol{\varphi}}, Res_M(\bar{\mathbf{s}}) \rangle_{\tilde{V}, \tilde{V}'} = -(F(\tilde{\boldsymbol{\varphi}}) + B_{M,1}(\tilde{\boldsymbol{\varphi}}; \bar{\mathbf{s}}) + B_{M,2}(\tilde{\boldsymbol{\varphi}}; \bar{\mathbf{s}}, \bar{\mathbf{s}})), \quad (3.39b)$$

$$B_{C,\bar{\mathbf{s}}}(\tilde{\psi}; \tilde{\mathbf{s}}) := B_C(\tilde{\psi}; \tilde{\mathbf{s}}), \quad (3.39c)$$

$$\langle \tilde{\psi}, Res_C(\bar{\mathbf{s}}) \rangle_{\tilde{Q}, \tilde{Q}'} := -B_C(\tilde{\psi}; \bar{\mathbf{s}}). \quad (3.39d)$$

Specifically, the forms $B_{M,\bar{\mathbf{s}}}(\cdot; \tilde{\mathbf{s}})$ and $B_{C,\bar{\mathbf{s}}}(\cdot; \tilde{\mathbf{s}})$ are linear in $\tilde{\mathbf{s}}$, while $B_{M,2}(\cdot; \bar{\mathbf{s}}, \tilde{\mathbf{s}})$ is bilinear in $\tilde{\mathbf{s}}$. Moreover, the source terms are expressed in terms of the functionals $Res_M(\bar{\mathbf{s}}) \in \tilde{V}'$ and $Res_C(\bar{\mathbf{s}}) \in \tilde{Q}'$, which can be view as the corresponding coarse-scale residuals *lifted* to the dual of the corresponding fine-scale spaces \tilde{V}' , \tilde{Q}' , and which define the following coarse-scale residual into $\tilde{\mathcal{S}}'$:

$$Res(\bar{\mathbf{s}}) := \begin{bmatrix} Res_M(\bar{\mathbf{s}}) \\ Res_C(\bar{\mathbf{s}}) \end{bmatrix}. \quad (3.40)$$

The solution $\tilde{\mathbf{s}}$ of problem (3.38) can be formally written in terms of $Res(\bar{\mathbf{s}})$ and $\bar{\mathbf{s}}$. It is expected that the larger the space $\bar{\mathcal{S}}$ is chosen, the better is the approximation of \mathbf{s} by means of $\bar{\mathbf{s}}$, thus the smaller are the component $\tilde{\mathbf{s}}$ and the coarse scale residual $Res(\bar{\mathbf{s}})$ into the dual space $\bar{\mathcal{S}}'$. With the additional hypothesis that $\tilde{\mathbf{s}}$ is zero if $Res(\bar{\mathbf{s}})$ is zero, the following perturbation series expansion of $\tilde{\mathbf{s}}$ in terms of $Res(\bar{\mathbf{s}})$ can be considered:

$$\tilde{\mathbf{s}} = \sum_{k=1}^{\infty} \varsigma^k \tilde{\mathbf{s}}_k, \quad (3.41)$$

where $\varsigma := \|Res(\bar{\mathbf{s}})\|_{\bar{\mathcal{S}}'}$. We substitute Eq. (3.41) into Eqs. (3.38) and we use a recurrence formula to group coefficients of the powers of ς coming from the expansion of the bilinear form in $\tilde{\mathbf{s}}$ $B_{M,2}(\cdot; \tilde{\mathbf{s}}, \tilde{\mathbf{s}})$. By equating like coefficients of the powers of ς in the full expansion of the Eqs. (3.38), we obtain a sequence of coupled linear variational problems, each defined by the same (linear) operator in $\tilde{\mathbf{s}}_k$ that can be formally inverted through a *fine-scale Green's operator*.

Since in practice, neither the sum of an infinite number of terms nor the exact determination of the fine-scale Green's operator are possible, the serie in Eq. (3.41) is truncated at the first order and reads:

$$\tilde{\mathbf{s}} = \varsigma \tilde{\mathbf{s}}_1, \quad (3.42)$$

with $\tilde{\mathbf{s}}_1$ the solution of the first variational problem approximated as:

$$\tilde{\mathbf{s}}_1 = -\tau \frac{Res(\bar{\mathbf{s}})}{\|Res(\bar{\mathbf{s}})\|_{\bar{\mathcal{S}}'}}, \quad (3.43)$$

where τ is an approximation of the fine-scale Green's operator. In such a way, we obtain an approximated form for $\tilde{\mathbf{s}}$ in terms of $\bar{\mathbf{s}}$ which can be used into the finite dimensional problem (3.34a) to close the system, whose unknown is the coarse-scale component $\bar{\mathbf{s}}$.

Remark 3.11. *Following [BCC⁺07], we consider the coarse-scaled solution $\bar{\mathbf{s}}$ as the numerical approximation of $\mathbf{s} = (\mathbf{u}, p)$. As usual, a dual aim moves to the choice of a convenient dimension for $\bar{\mathcal{S}}$: the larger is the finite dimensional space $\bar{\mathcal{S}}$, the better is the approximation of (\mathbf{u}, p) by means of $(\bar{\mathbf{u}}, \bar{p})$, but at the expense of the computational effort.*

Implementation and resulting semi-discrete formulation

In the framework of the Galerkin-IGA method, we define the finite-dimensional subspaces $\bar{V} \subseteq V$ and $\bar{Q} \subseteq Q$ in terms of the NURBS basis functions which represent the computational domain. Specifically, given the space of NURBS basis functions in Ω , say \mathcal{V}^h , we define $\bar{V} := V \cap [\mathcal{V}^h]^2$ and $\bar{Q} := Q \cap \mathcal{V}^h$.

Remark 3.12. *In order to explicit the dependence from the mesh parameter h , as done in Section 3.3.1, we denote $V^h := \bar{V}$ and $Q^h := \bar{Q}$; similarly every function belonging to $\bar{V}, \bar{Q}, \bar{\mathcal{S}}$ will be written with the superscript h .*

In such a way the coarse-scale problem (3.37) reads:

find, for all $t \in (0, T)$, $\mathbf{s}_h(t) = (\mathbf{u}_h(t), p_h(t)) \in V^h \times Q^h$ such that

$$\begin{cases} B_M(\varphi_h; \mathbf{s}_h(t) + \tilde{\mathbf{s}}(t)) = 0 & \forall \varphi_h \in V^h, \\ B_C(\psi_h; \mathbf{s}_h(t) + \tilde{\mathbf{s}}(t)) = 0 & \forall \psi_h \in Q^h, \\ \mathbf{u}_h(0) = \mathbf{u}_0 & \text{in } \Omega, \end{cases} \quad (3.44)$$

where the residuals of the momentum and continuity equation are defined in Eqs. (3.37a) and (3.37b). The explicit expression for $\tilde{\mathbf{s}} = (\tilde{\mathbf{u}}, \tilde{p})$, in the assumptions made in Eqs. (3.42) and (3.43), reads:

$$\tilde{\mathbf{u}} = \tau_M \text{Res}_M(\mathbf{s}_h), \quad (3.45a)$$

$$\tilde{p} = \tau_C \text{Res}_C(\mathbf{s}_h), \quad (3.45b)$$

where the discrete coarse scale residuals (Res_M , Res_C) and the discrete approximation of the operators \mathcal{L}_{ad}^{-1} and $\nabla \cdot \mathcal{L}_{ad}^{-1} \nabla$ (respectively, τ_M , τ_C) are given by:

$$\text{Res}_M(\mathbf{s}_h) = \text{Res}_M(\mathbf{u}_h, p_h) := \frac{\partial \mathbf{u}_h}{\partial t} + (\mathbf{u}_h \cdot \nabla) \mathbf{u}_h + \nabla p_h - \frac{2}{\text{Re}} \nabla \cdot (D(\mathbf{u}_h)) - \mathbf{f}, \quad (3.46a)$$

$$\text{Res}_C(\mathbf{s}_h) = \text{Res}_C(\mathbf{u}_h, p_h) := \nabla \cdot \mathbf{u}_h, \quad (3.46b)$$

$$\tau_M := \left[\frac{4}{\Delta t^2} + \mathbf{u}_h \cdot \mathbf{G} \mathbf{u}_h + C_I \frac{1}{\text{Re}^2} \mathbf{G} : \mathbf{G} \right]^{\frac{1}{2}}, \quad (3.46c)$$

$$\tau_C := \frac{1}{\tau_M \mathbf{g} \cdot \mathbf{g}}, \quad (3.46d)$$

with \mathbf{G} , defined component wise as $G_{i,j} := \sum_{k=1}^2 \frac{\partial \eta_k}{\partial x_i} \frac{\partial \eta_k}{\partial x_j}$ for $i, j = 1, 2$, the covariant metric tensor related to the geometrical mapping from the physical to the parametric coordinates, while $g_i := \sum_{k=1}^2 \frac{\partial \eta_k}{\partial x_i}$, for $i = 1, 2$. For square meshes $\mathbf{G} = \frac{1}{h^2} I$ and $\mathbf{g} \cdot \mathbf{g} = \frac{1}{h^2}$, with h the mesh size. The positive constant C_I derives from an element-wise inverse estimate; it is independent from the mesh size, but depends on the degree p of the basis functions, in particular it is set as $C_I := 60 \cdot 2^{p-2}$, according to [Whi99]. The term Δt refers to the time step, which appears into the definition of Eq. (3.46c), even if we have not already introduced the time discretization.

Remark 3.13. *The stabilization parameters τ_M and τ_C may degenerate for $\Delta t \rightarrow 0$ for fixed values of the mesh size h , velocity and Reynolds number. This issue can be resolved by setting the dimensionless time step:*

$$\Delta t = \chi \frac{h_l}{V_0}, \quad (3.47)$$

where h_l and V_0 are the characteristic dimensionless mesh size and velocity; χ is a selected coefficient which we set equal to 0.5. In Figure 3.3 it is shown the dependency of the stabilization parameters τ_M and τ_C on Δt for fixed values of $\|\mathbf{u}_h\|_{L^\infty(\Omega)} = 1$, $\text{Re} = 278$ (3.3a) or $\text{Re} = 1500$ (3.3b); we consider $p = 2$ and three different meshes with sizes $h_1 = 2^{-3}$, $h_2 = 2^{-4}$ and $h_3 = 2^{-5}$.

The problem (3.44) in spatial semi-discretized form, resulting from the VMS-LES formulation, can be viewed as an augmented stabilized form of the IGA-Galerkin formulation (3.27). In particular, considering the Navier-Stokes equations (3.16), completed by suitable boundary conditions, its stabilized semi-discrete formulation in the framework of the variational multi-scale method reads:

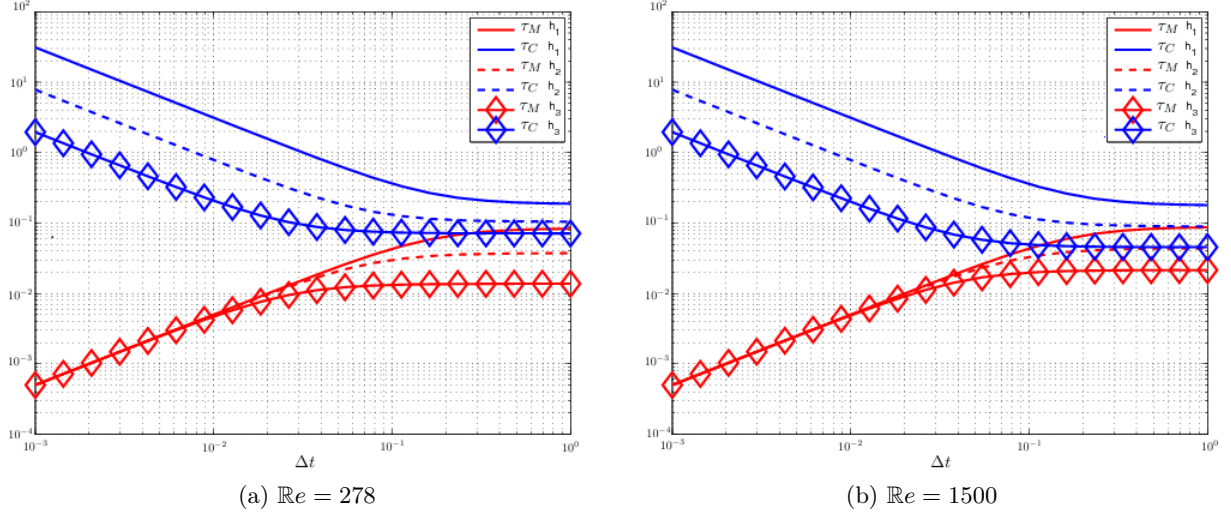


Figure 3.3: Stabilization parameters τ_M and τ_C vs. Δt for $\text{Re} = 278$ (3.3a) and $\text{Re} = 1500$ (3.3b) for different mesh sizes.

find, for all $t \in (0, T)$, $\mathbf{u}_h(t) \in V_g^h$ and $p_h(t) \in Q^h$ such that:

$$\begin{cases} B_M^{VMS-LES}(\varphi_h; \dot{\mathbf{u}}_h(t), \mathbf{u}_h(t), p_h(t)) = 0 & \forall \varphi_h \in V^h, \\ B_C^{VMS-LES}(\psi_h; \dot{\mathbf{u}}_h(t), \mathbf{u}_h(t), p_h(t)) = 0 & \forall \psi_h \in Q^h, \\ \mathbf{u}_h(0) = \mathbf{u}_0 & \text{in } \Omega, \end{cases} \quad \begin{matrix} (3.48a) \\ (3.48b) \\ (3.48c) \end{matrix}$$

where the *augmented* residuals are given element wise over the computational mesh by, respectively:

$$B_M^{VMS-LES}(\varphi_h; \dot{\mathbf{u}}_h, \mathbf{u}_h, p_h) := B_M(\varphi_h; \dot{\mathbf{u}}_h, \mathbf{u}_h, p_h) \quad (3.49a)$$

$$\begin{aligned} & + \sum_{K \in \mathcal{K}_h} [(\mathbf{u}_h \cdot \nabla \varphi_h, \tau_M \text{Res}_M(\mathbf{u}_h, p_h))_{L^2(K)} \\ & \quad + (\nabla \cdot \varphi_h, \tau_C \nabla \cdot \mathbf{u}_h)_{L^2(K)} \\ & \quad + (\mathbf{u}_h \cdot \nabla \varphi_h^T, \tau_M \text{Res}_M(\mathbf{u}_h, p_h))_{L^2(K)} \\ & \quad - (\nabla \varphi_h, \tau_M \text{Res}_M(\mathbf{u}_h, p_h) \otimes \tau_M \text{Res}_M(\mathbf{u}_h, p_h))_{L^2(K)}], \end{aligned}$$

$$B_C^{VMS-LES}(\psi_h; \dot{\mathbf{u}}_h, \mathbf{u}_h, p_h) := B_C(\psi_h; \dot{\mathbf{u}}_h, \mathbf{u}_h, p_h) \quad (3.49b)$$

$$+ \sum_{K \in \mathcal{K}_h} (\nabla \psi_h, \tau_M \text{Res}_M(\mathbf{u}_h, p_h))_{L^2(K)}.$$

Remark 3.14. The additional terms appearing in Eqs. (3.49) can be compared to classical stabilization terms, such as SUPG. Specifically, the classical SUPG stabilization consider only the first two terms in Eq. (3.49a) and Eq. (3.49b) and we will refer to this formulation as VMS-SUPG. The additional terms in Eq. (3.49a) (the last ones) are an half of the cross-stress and the Reynolds-stress terms due to the LES modeling.

3.3.3 Time discretization: the generalized- α method

The choice to refer to the generalized- α method [JWH00, Whi99] as time discretization scheme for the semi-discretized problem (3.49) is due to its capability in controlling the numerical dissipation, without compromising accuracy. The amount of desired high frequencies dissipation is taken into account by the parameter $\rho_\infty \in [0, 1]$ (see for instance [Hug00]), which is the spectral radius of the amplification matrix of the discretized problem as the time step tends to infinity. Once fixed, the parameters, say $\alpha_m, \alpha_f, \delta \in [0, 1]$, which define the generalized- α method, can be defined in terms of ρ_∞ according to considerations of accuracy and stability. In [Whi99] it is shown that second order accuracy can be achieved provided that:

$$\delta = \frac{1}{2} + \alpha_m - \alpha_f, \quad (3.50)$$

while unconditional stability if

$$\alpha_m \geq \alpha_f \geq \frac{1}{2}. \quad (3.51)$$

Moreover, low-frequency dissipation is minimized, with respect to a given level of high-frequency dissipation, by choosing:

$$\alpha_m = \frac{1}{2} \left(\frac{3 - \rho_\infty}{1 + \rho_\infty} \right), \quad \alpha_f = \frac{1}{1 + \rho_\infty}. \quad (3.52)$$

Remark 3.15. We set the parameter ρ_∞ to a default value of $\rho_\infty = 0.5$, a compromise between the zero dissipation case ($\rho_\infty = 1$) and the maximal dissipation ($\rho_\infty = 0$). This choice was performed also in [BCC⁺07], where it is shown to be effective even in turbulence simulations. We refer to [JWH00] for a discussion about the choice of ρ_∞ .

In order to apply the generalized- α method to the semi-discretized stabilized Navier-Stokes equations (3.48), we define the *discrete residuals* as the continuous residuals evaluated in the basis functions of the spaces V^h and Q^h , i.e.:

$$\mathbf{R}_M(\dot{\mathbf{u}}_h(t), \mathbf{u}_h(t), p_h(t)) := \left\{ \left\{ B_M^{VMS-LES}(\mathcal{R}_A^i; \dot{\mathbf{u}}_h(t), \mathbf{u}_h(t), p_h(t)) \right\}_{1 \leq A \leq N_b} \right\}_{i=1}^2, \quad (3.53a)$$

$$\mathbf{R}_C(\dot{\mathbf{u}}_h(t), \mathbf{u}_h(t), p_h(t)) := \left\{ B_C^{VMS-LES}(\mathcal{R}_A; \dot{\mathbf{u}}_h(t), \mathbf{u}_h(t), p_h(t)) \right\}_{1 \leq A \leq N_b}, \quad (3.53b)$$

where $B_M^{VMS-LES}$ and $B_C^{VMS-LES}$ are respectively given in Eqs. (3.48a) and (3.48b).

The discretization of the time interval $(0, T)$, is performed by means of a *discrete time vector* $\{t_n\}_{n=0}^{N_t}$, subdividing $(0, T)$ in a set of N_t time intervals of size Δt . For the sake of simplicity, in the vectors of control variables of Eq. (3.29) we replace t_n with the subscript n .

Remark 3.16. We recall that, when using the *VMS-LES augmented form*, we set Δt as in Eq. (3.47), by taking into account Remark 3.13.

The generalized- α algorithm reads: at each time step t_n , given $\dot{\mathbf{U}}_n, \mathbf{U}_n, \mathbf{P}_n$, find $\dot{\mathbf{U}}_{n+1}$,

\mathbf{U}_{n+1} , $\dot{\mathbf{U}}_{n+\alpha_m}$, $\mathbf{U}_{n+\alpha_f}$, \mathbf{P}_{n+1} such that:

$$\mathbf{R}_M \left(\dot{\mathbf{U}}_{n+\alpha_m}, \mathbf{U}_{n+\alpha_f}, \mathbf{P}_{n+1} \right) = 0, \quad (3.54a)$$

$$\mathbf{R}_C \left(\dot{\mathbf{U}}_{n+\alpha_m}, \mathbf{U}_{n+\alpha_f}, \mathbf{P}_{n+1} \right) = 0, \quad (3.54b)$$

$$\mathbf{U}_{n+1} = \mathbf{U}_n + \Delta t \dot{\mathbf{U}}_n + \delta \Delta t \left(\dot{\mathbf{U}}_{n+1} - \dot{\mathbf{U}}_n \right), \quad (3.54c)$$

$$\dot{\mathbf{U}}_{n+\alpha_m} = \dot{\mathbf{U}}_n + \alpha_m \left(\dot{\mathbf{U}}_{n+1} - \dot{\mathbf{U}}_n \right), \quad (3.54d)$$

$$\mathbf{U}_{n+\alpha_f} = \mathbf{U}_n + \alpha_f \left(\mathbf{U}_{n+1} - \mathbf{U}_n \right). \quad (3.54e)$$

In particular, Eq. (3.54a) and Eq. (3.54b) are, respectively, the momentum and continuity vectors of the discrete residuals with velocity and acceleration evaluated at the intermediate times $t_{n+\alpha_f} = t_n + \alpha_f(t_{n+1} - t_n)$ and $t_{n+\alpha_m} = t_n + \alpha_m(t_{n+1} - t_n)$, while the pressure at t_{n+1} .

Remark 3.17. *The algorithm considers $\dot{\mathbf{U}}(t)$ and $\mathbf{U}(t)$ as independent variables.*

In order to deal with the nonlinearity of the system of equations (3.54) we use the *Newton method* [QSS07], by coupling the method with a *predictor-multicorrector algorithm*, as done in [BCC⁺07, Whi99].

Predictor stage

According to [BCC⁺07, Whi99] we set:

$$\dot{\mathbf{U}}_{n+1,(0)} = \begin{cases} \dot{\mathbf{g}}_h(t_{n+1}) & \text{on } \Gamma_D, \\ \left(\frac{\delta - 1}{\delta} \right) \dot{\mathbf{U}}_n & \text{otherwise;} \end{cases} \quad (3.55a)$$

$$\mathbf{U}_{n+1,(0)} = \begin{cases} \mathbf{g}_h(t_{n+1}) & \text{on } \Gamma_D, \\ \mathbf{U}_n & \text{otherwise;} \end{cases} \quad (3.55b)$$

$$\mathbf{P}_{n+1,(0)} = \mathbf{P}_n. \quad (3.55c)$$

Multi-corrector stage

The following steps are repeated for $l = 1, 2, \dots, l_{\max}$:

STEP 1 Set:

$$\dot{\mathbf{U}}_{n+\alpha_m,(l)} = \dot{\mathbf{U}}_n + \alpha_m \left(\dot{\mathbf{U}}_{n+1,(l-1)} - \dot{\mathbf{U}}_n \right), \quad (3.56a)$$

$$\mathbf{U}_{n+\alpha_f,(l)} = \mathbf{U}_n + \alpha_f \left(\mathbf{U}_{n+1,(l-1)} - \mathbf{U}_n \right), \quad (3.56b)$$

$$\mathbf{P}_{n+1,(l)} = \mathbf{P}_{n+1,(l-1)}. \quad (3.56c)$$

STEP 2 The discrete residuals are assembled:

$$\mathbf{R}_{M,(l)} := \mathbf{R}_M \left(\dot{\mathbf{U}}_{n+\alpha_m,(l)}, \mathbf{U}_{n+\alpha_f,(l)}, \mathbf{P}_{n+1,(l)} \right), \quad (3.57a)$$

$$\mathbf{R}_{C,(l)} := \mathbf{R}_C \left(\dot{\mathbf{U}}_{n+\alpha_m,(l)}, \mathbf{U}_{n+\alpha_f,(l)}, \mathbf{P}_{n+1,(l)} \right). \quad (3.57b)$$

STEP 3 Given a prescribed tolerance tol_α , check the following condition on the relative norm of the residual vectors:

$$\frac{\sqrt{\|\mathbf{R}_{M,(l)}\|_2^2 + \|\mathbf{R}_{C,(l)}\|_2^2}}{\sqrt{\|\mathbf{R}_{M,(0)}\|_2^2 + \|\mathbf{R}_{C,(0)}\|_2^2}} < tol_\alpha; \quad (3.58)$$

If the condition (3.58) is satisfied, the control variables at time step t_{n+1} are set to:

$$\dot{\mathbf{U}}_{n+1} = \dot{\mathbf{U}}_{n+1,(l-1)}, \quad \mathbf{U}_{n+1} = \mathbf{U}_{n+1,(l-1)}, \quad \mathbf{P}_{n+1} = \mathbf{P}_{n+1,(l-1)}, \quad (3.59)$$

and the algorithm terminates,

otherwise we assemble the consistent tangent matrix of the nonlinear system, written as a block matrix:

$$\mathbf{K} = \begin{bmatrix} \mathbf{K}_{Cp} & \mathbf{K}_{C\dot{\mathbf{u}}} \\ \mathbf{K}_{Mp} & \mathbf{K}_{M\dot{\mathbf{u}}} \end{bmatrix}, \quad (3.60)$$

where:

$$\mathbf{K}_{Cp} := \frac{\partial \mathbf{R}_C(\dot{\mathbf{U}}_{n+\alpha_m}, \mathbf{U}_{n+\alpha_f}, \mathbf{P}_{n+1})}{\partial \mathbf{P}_{n+1}}, \quad (3.61a)$$

$$\mathbf{K}_{C\dot{\mathbf{u}}} := \frac{\partial \mathbf{R}_C(\dot{\mathbf{U}}_{n+\alpha_m}, \mathbf{U}_{n+\alpha_f}, \mathbf{P}_{n+1})}{\partial \dot{\mathbf{U}}_{n+1}} \quad (3.61b)$$

$$= \alpha_m \frac{\partial \mathbf{R}_C(\dot{\mathbf{U}}_{n+\alpha_m}, \mathbf{U}_{n+\alpha_f}, \mathbf{P}_{n+1})}{\partial \dot{\mathbf{U}}_{n+\alpha_m}} + \alpha_f \delta \Delta t \frac{\partial \mathbf{R}_C(\dot{\mathbf{U}}_{n+\alpha_m}, \mathbf{U}_{n+\alpha_f}, \mathbf{P}_{n+1})}{\partial \mathbf{U}_{n+\alpha_f}},$$

$$\mathbf{K}_{Mp} := \frac{\partial \mathbf{R}_M(\dot{\mathbf{U}}_{n+\alpha_m}, \mathbf{U}_{n+\alpha_f}, \mathbf{P}_{n+1})}{\partial \mathbf{P}_{n+1}}, \quad (3.61c)$$

$$\begin{aligned} \mathbf{K}_{M\dot{\mathbf{u}}} &:= \frac{\partial \mathbf{R}_M(\dot{\mathbf{U}}_{n+\alpha_m}, \mathbf{U}_{n+\alpha_f}, \mathbf{P}_{n+1})}{\partial \dot{\mathbf{U}}_{n+1}} \quad (3.61d) \\ &= \alpha_m \frac{\partial \mathbf{R}_M(\dot{\mathbf{U}}_{n+\alpha_m}, \mathbf{U}_{n+\alpha_f}, \mathbf{P}_{n+1})}{\partial \dot{\mathbf{U}}_{n+\alpha_m}} + \alpha_f \delta \Delta t \frac{\partial \mathbf{R}_M(\dot{\mathbf{U}}_{n+\alpha_m}, \mathbf{U}_{n+\alpha_f}, \mathbf{P}_{n+1})}{\partial \mathbf{U}_{n+\alpha_f}}. \end{aligned}$$

STEP 4 Solve the following liner system:

$$\begin{bmatrix} \mathbf{K}_{Cp} & \mathbf{K}_{C\dot{\mathbf{u}}} \\ \mathbf{K}_{Mp} & \mathbf{K}_{M\dot{\mathbf{u}}} \end{bmatrix} \begin{bmatrix} \Delta \mathbf{P}_{n+1,(l)} \\ \Delta \dot{\mathbf{U}}_{n+1,(l)} \end{bmatrix} = - \begin{bmatrix} \mathbf{R}_{C,(l)} \\ \mathbf{R}_{M,(l)} \end{bmatrix}. \quad (3.62)$$

STEP 5 The iterates are updated as:

$$\dot{\mathbf{U}}_{n+1,(l)} = \dot{\mathbf{U}}_{n+1,(l-1)} + \Delta \dot{\mathbf{U}}_{n+1,(l)}, \quad (3.63a)$$

$$\mathbf{U}_{n+1,(l)} = \mathbf{U}_{n+1,(l-1)} + \delta \Delta t \Delta \dot{\mathbf{U}}_{n+1,(l)}, \quad (3.63b)$$

$$\mathbf{P}_{n+1,(l)} = \mathbf{P}_{n+1,(l-1)} + \Delta \mathbf{P}_{n+1,(l)}. \quad (3.63c)$$

Then we return to **STEP 1**.

Remark 3.18. At **STEP 3** we are using a Newton's linearization of the residual with respect to $\dot{\mathbf{u}}$ to improve the current values of the vectors variables by solving the system in Eq. (3.62) in the unknown vector $\dot{\mathbf{U}}$.

Firstly we do not consider in the tangent matrix the terms corresponding to the differential of the diffusion

Remark 3.19. *We do not provide explicit expressions for the matrices and residual vectors which define the system in Eq. (3.62), but we point out that following strategies have been adopted in order to simplify the implementation. Firstly, we do not consider into the formulation of the tangent matrix the terms corresponding to the differentiation of the stabilization parameters, τ_M and τ_C given respectively in Eq. (3.46c) and (3.46c). Moreover, the contribution of the discretized terms relative to the resistance boundary condition of Eq. (3.26) is taken into account only in the residual vectors $\mathbf{R}_{C,(l)}$, $\mathbf{R}_{M,(l)}$, yielding an inexact form of the tangent system in Eq. (3.62), but only limited to the contribution associated to Γ^{out} .*

3.4 Numerical results

In this section we provide numerical results for blood flows with rigid wall models. In particular, we take into account vessels with stenosis and a domain describing an aneurysm. Although the computational domains considered refers to idealized configurations, they highlight the capability of IGA in representing smooth geometries, as the ones provided by in-vivo investigations. We discuss the VMS-LES stabilization in Section 3.3.2, then we consider the importance of imposing the resistance boundary condition, described in Section 3.2.2, to obtain more realistic responses with respect to an homogeneous Neumann boundary condition. In the examples considered, except when otherwise specified, the nominal radius of the vessels is set to $r_V = 0.15\text{cm}$ and the profile of the inlet velocity is the one described in Section 3.2.1, with a default value for the maximum flow rate set to $\max_{t \in (0, T_{HB})} Q^{in}(t) = 1.237\text{cm}^3/\text{s} = 0.1237\text{cc}/\text{s}$.

Moreover, the blood is considered a Newtonian fluid with constant density $\rho_f = 1.06\text{g}/\text{cm}^3$ and dynamic viscosity $\mu_f = 4 \cdot 10^{-2}\text{g}/(\text{cm} \cdot \text{s})$. The simulations were performed for a period corresponding to three heartbeats ($3T_{HB}$); the results shown correspond to the last heartbeat, in order to allow sufficient time for the flow to adopt from the initial condition.

3.4.1 Asymmetric and axisymmetric stenosis: a comparison between VMS stabilizations

We consider an asymmetric stenosed vessel with length equal to 2.4cm . We consider a reduction of the area in the stenosed region of the 50%, yielding the resulting radius in the central section of the stenosis, distant 0.75cm from the inlet face, to be equal to 0.075cm . The resulting domain $\Omega \subseteq \mathbb{R}^2$ is exactly represented by means of globally \mathcal{C}^1 -continuous NURBS basis functions of degree $p = 2$; the mesh is constituted by $N_{el} = 128 \times 32$ elements; according to condition in Eq. (3.47) the dimensionless time step is set to $\Delta t = 0.03125$, corresponding to a dimensional time step equal to $\Delta t = 2.68 \cdot 10^{-4}\text{s}$. The dimensionless resistance constant C_{out}^* used in the resistance boundary condition of Eq. (3.26), is set to $C_{out}^* = 0.3085$ by considering a resistance constant $C_{out} = 162\text{dyn} \cdot \text{s}/\text{cm}^5$, while the reference pressure is fixed to a default value of $P_V = 85\text{mmHg}$ (valid for all the simulations). The geometrical data ($L_0 = 0.3\text{cm}$), the choice on the value for the maximum flow rate, which yields a characteristic velocity of $V_0 = 35\text{cm}/\text{s}$, and the values characterizing the fluid, are such that, for this problem, the Reynolds number is $\text{Re} = 278$.

The pulsatile nature of the flow and the narrowing of the vessel cause a periodic generation of vortices. This can be seen in Figure 3.4, where we report the streamlines of the velocity at

different times in the flow cycle which cover a period equal to the heartbeat $T_{\text{HB}} = 1.1s$. In Figure 3.5 we show the magnitude of the velocity field at the corresponding times, rescaling the color map at each time step in order to show the minimum and maximum values obtained. As expected, we can see that the velocity yields its global maximum at the time corresponding to the peak flow in the central section of the stenosis.

In order to study the behavior of the stabilization based on the VMS-LES method, described in Section 3.3.2, we compare the solution with that obtained from the VMS-SUPG stabilization, neglecting the LES terms (see Remark 3.14). By considering Figures 3.6 and 3.7 we deduce that, even for the small value of the Reynolds number considered and being the flow substantially laminar, the solution is sensible to the use of the LES terms. Specifically, in Figure 3.6 we show the corresponding velocity field obtained by using the VMS-SUPG stabilization, rescaled accordingly with the values obtained with the VMS-LES one. Moreover, we plot at significant time steps the velocity fields with the VMS-LES and VMS-SUPG stabilizations. The same study is performed comparing the vorticity in Figure 3.7. In this case the difference of the magnitude of the vorticity has its maximum values in the proximity of the walls in the region beyond the stenosis and in the middle of the sectional area corresponding to the presence of vortexes. The relative difference of the value of the vorticity in the latter region for the two stabilizations is about the 1 – 2%.

We perform the same study starting from the same pathological configuration of an axisymmetric stenosis with a maximum reduction of the area of the vessel of the 50% at a distal section from the inlet face located at about the 22% of the total length equal to 12cm. For this simulation we set the vessel radius to $r_V = 0.3cm$ and the maximum flow rate to $\max_{t \in (0, T_{\text{HB}})} Q^{\text{in}}(t) = 13.7cm^3/s$. The domain is represented by means of globally \mathcal{C}^1 -continuous NURBS basis functions of degree $p = 2$; the mesh is constituted by $N_{el} = 320 \times 32$ elements and the dimensional time step is set to $\Delta t = 3.875 \cdot 10^{-4}s$. In such a way, the Reynolds number is $Re = 1500$. In this case the flow is substantially laminar and periodic, but we observe in Figure 3.8 that the two VMS models lead to noticeable differences in the vorticity. In particular, the deviation of the vorticity value is about of the order of the 5% in the region in which the vortexes develop. In Figure 3.9 we show the streamlines of the velocity at the same time, corresponding to $t = 0.0465s$.

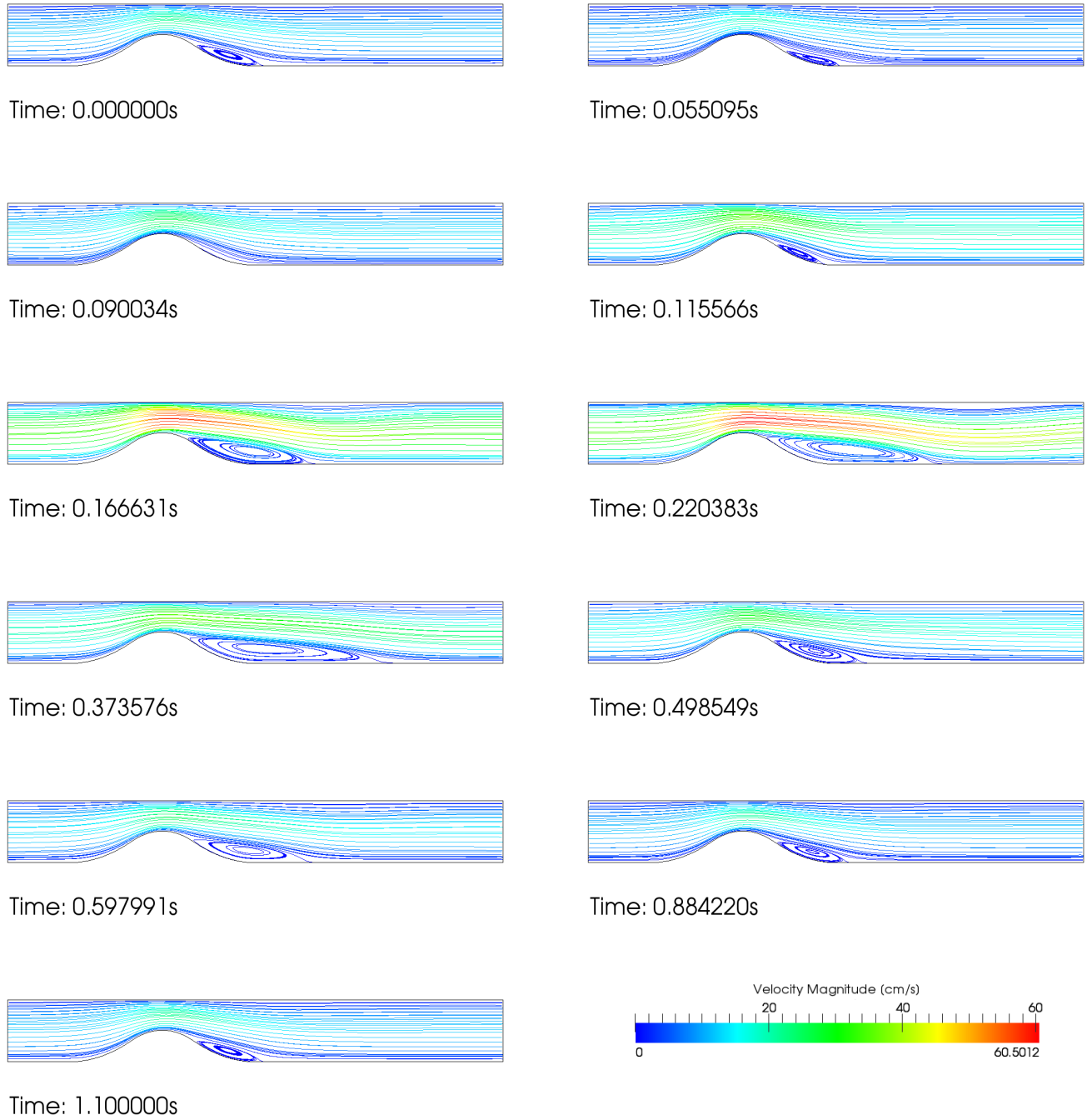


Figure 3.4: Streamlines for the asymmetric stenosis at different times in the cardiac cycle. Streamlines are colored according to the velocity magnitude, $Re = 278$.

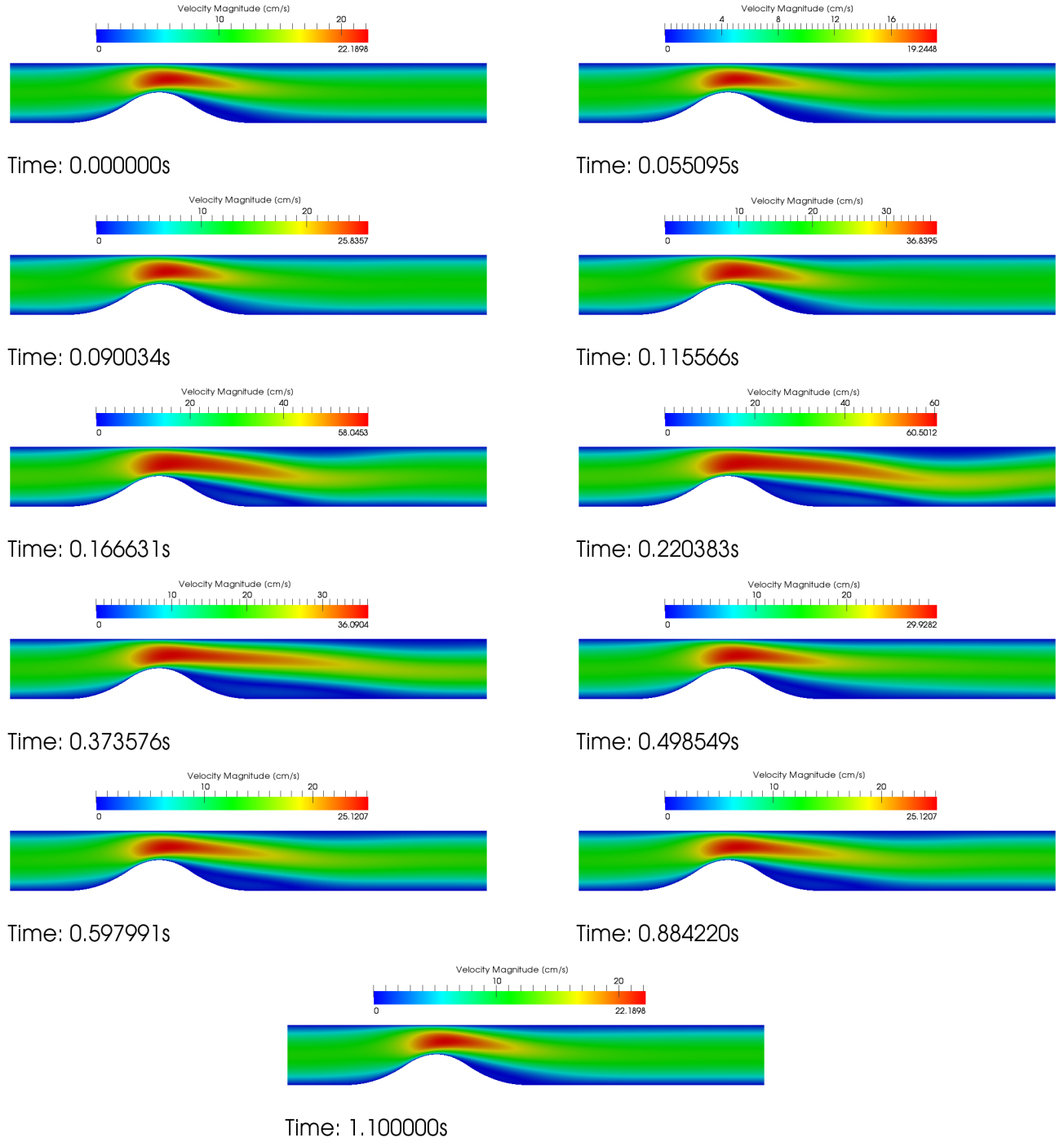


Figure 3.5: Velocity magnitude (in cm/s) for the asymmetric stenosis, colormap rescaled at each time step.

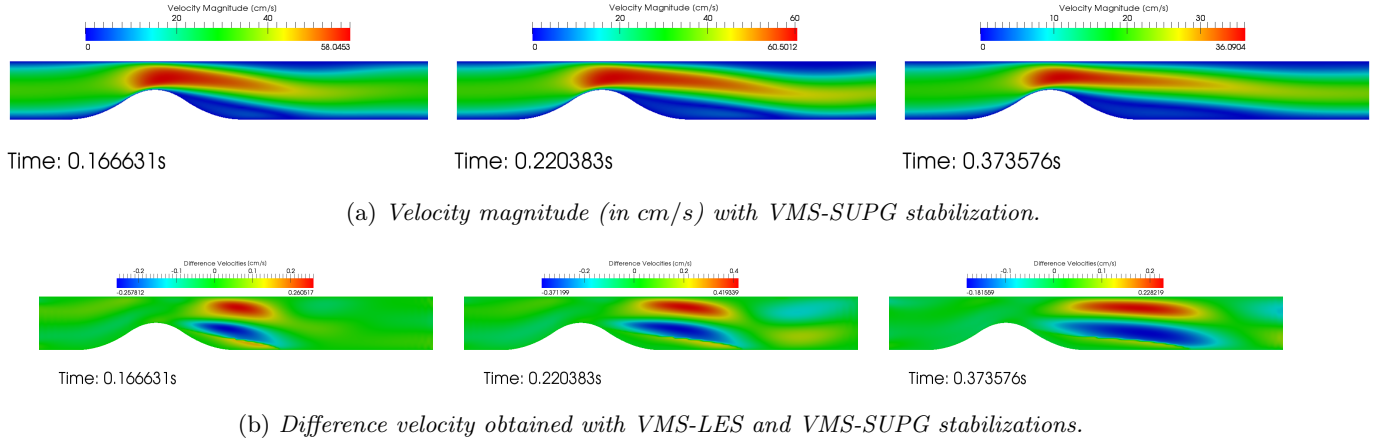


Figure 3.6: Velocity magnitude (in cm/s) for the asymmetric stenosis considering VMS-SUPG stabilization; difference of the velocity magnitude for the VMS-LES and VMS-SUPG stabilizations, $Re = 278$.

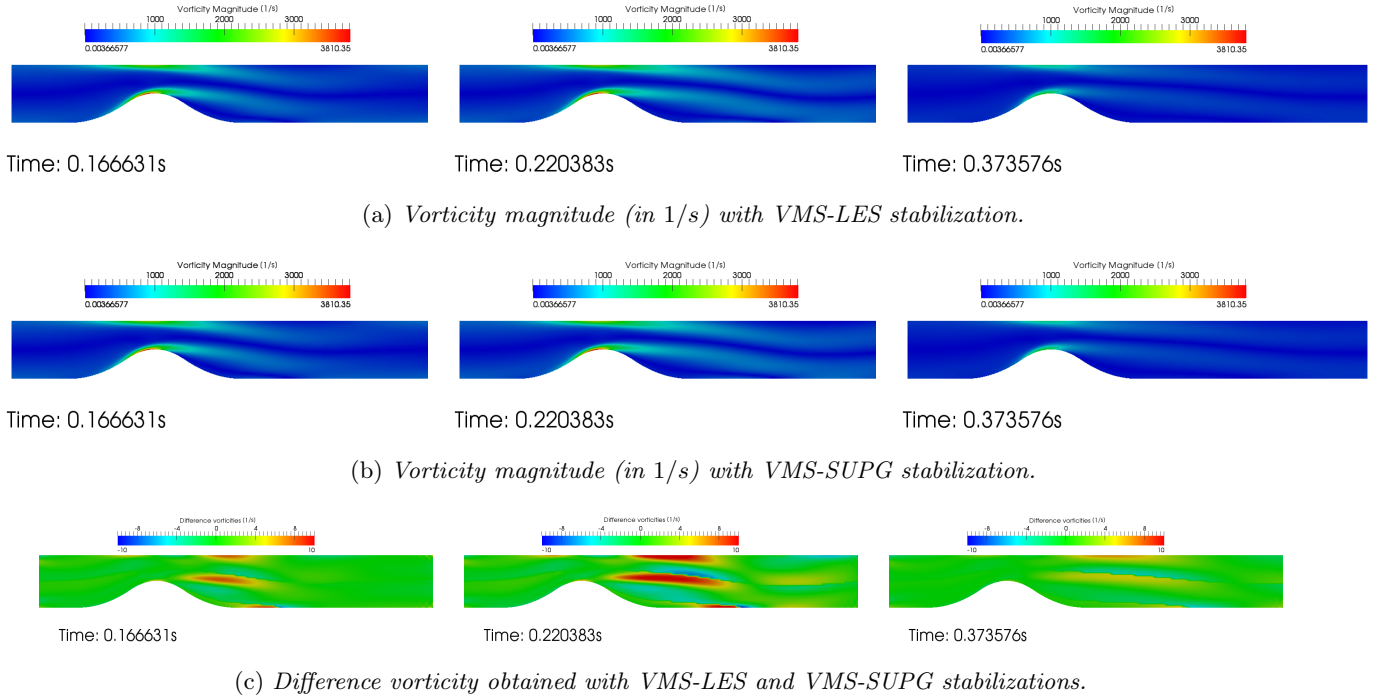


Figure 3.7: Vorticity magnitude (in $1/s$) for the asymmetric stenosis considering VMS-SUPG stabilization; difference of the vorticity magnitude for the VMS-LES and VMS-SUPG stabilizations, $Re = 278$.

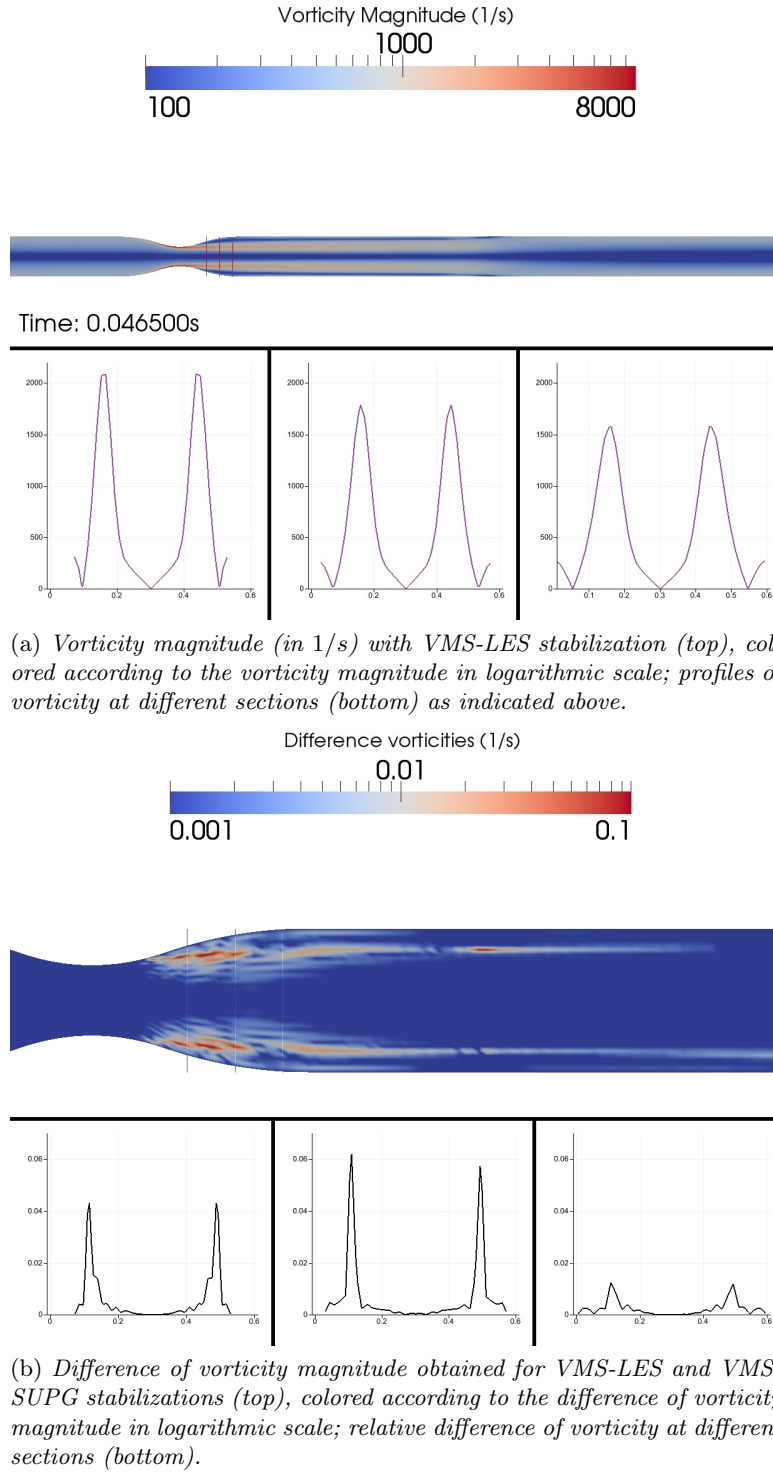


Figure 3.8: Vorticity magnitude (in 1/s) for the axisymmetric stenosis considering VMS-LES stabilization and difference of the vorticity for VMS-LES and VMS-SUPG stabilizations. Data relative to time $t = 0.046s$, $\mathbb{R}e = 1500$.

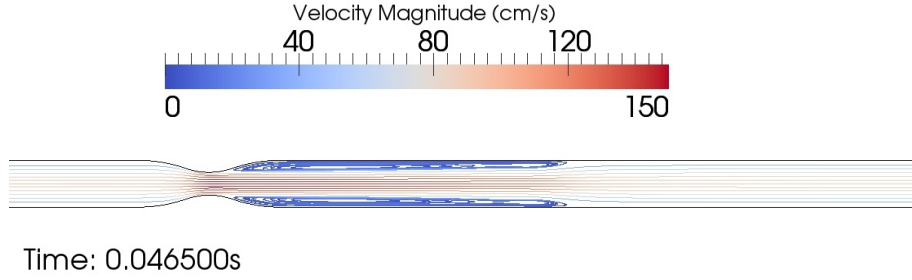


Figure 3.9: Streamlines for the axisymmetric stenosis colored according to the velocity magnitude, time $t = 0.046s$, $\mathbb{R}e = 1500$.

3.4.2 Symmetric stenosis: a comparison between boundary conditions

We consider a pathological configuration represented by an axisymmetric stenosis at a distal section from the inlet face of about $0.75cm$. The stenosis induces a reduction of the area of the 75% in a vessel of length $2.4cm$. The domain $\Omega \subseteq \mathbb{R}^2$, in which the problem is defined, is represented by means of globally \mathcal{C}^1 -continuous NURBS basis functions of degree $p = 2$; the mesh is constituted by $N_{el} = 128 \times 32$ elements; according to condition in Eq. (3.47) the dimensionless time step is set to $\Delta t = 0.03125$, corresponding to a dimensional time step equal to $\Delta t = 2.68 \cdot 10^{-4}s$. The values of the parameter defining the method are the same as in Section 3.4.1, yielding a Reynolds number equals to $\mathbb{R}e = 278$. In Figure 3.10 we report the streamlines of the flow at different phases in the pulse cycle which cover a period equals to the heartbeat $T_{HB} = 1.1s$. Both the restriction of the vessel and the pulsatile nature of the flow generate complex vorticious structures in the vessel. The number of vortexes tends to increase when using the resistance condition in Eq. (3.26). In particular, it increases in the systolic phase up to a maximum of 5 at the peak of the heart pulse, when the velocity attains its maximum value. We can notice that the flow is non-axisymmetric, contrary to the one that occurs in case of an homogeneous Neumann boundary condition at the outlet. In Figure 4.3 we compare the streamlines at the distal region obtained by using different kind of boundary conditions, the resistance and homogeneous Neumann boundary conditions. We also plot the component u_y of the velocity field. We observe that the result obtained with the resistance boundary condition is more realistic, since it allows to reduce the reflection of the pressure waves from the outlet. As observed e.g. in [VCFJT06], the choice of the boundary condition has a significant impact on the velocity and pressure fields.

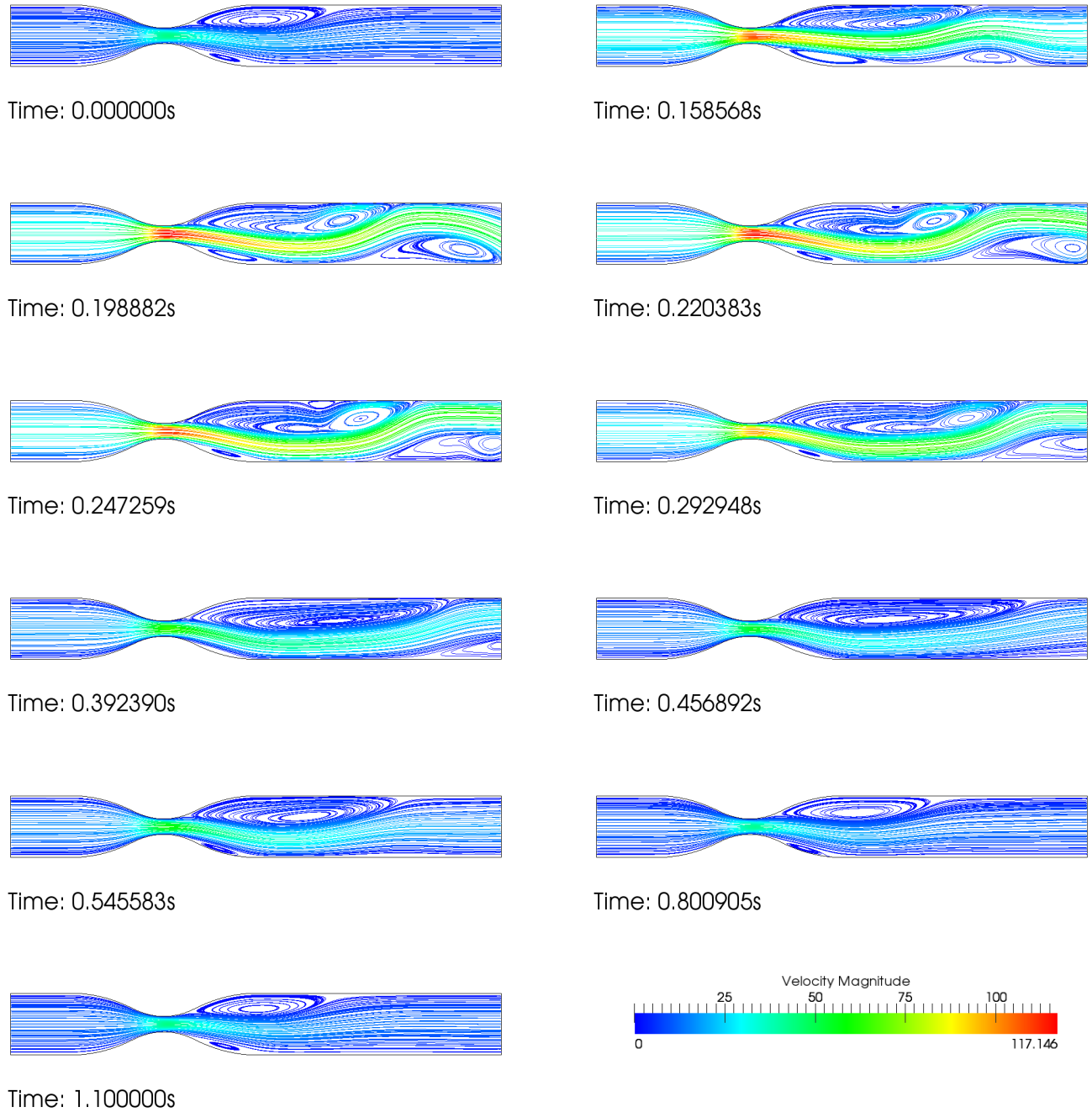
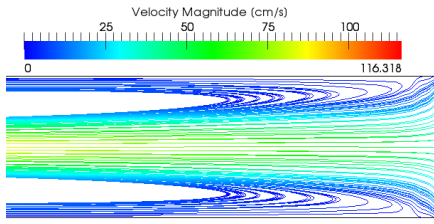
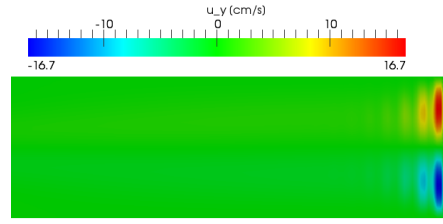


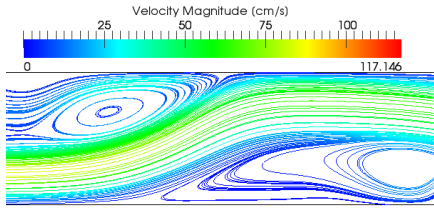
Figure 3.10: Streamlines for the symmetric stenosis at different times in the cardiac cycle. Streamlines are colored according to the velocity magnitude, $Re = 278$.



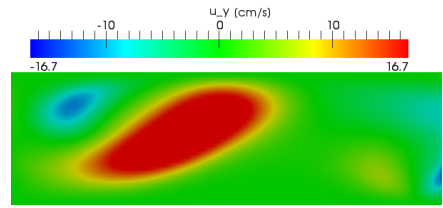
Time: 0.220383s



Time: 0.220383s

(a) *Streamlines and component u_y of the velocity with homogeneous Neumann BCs.*

Time: 0.220383s



Time: 0.220383s

(b) *Streamlines and component u_y of the velocity with resistance BCs.*

Figure 3.11: Comparison between homogeneous Neumann boundary conditions and resistance boundary conditions imposed on the outlet interface for the symmetric stenosis and $\text{Re} = 278$. Solutions in the distal region at the peak flow time.

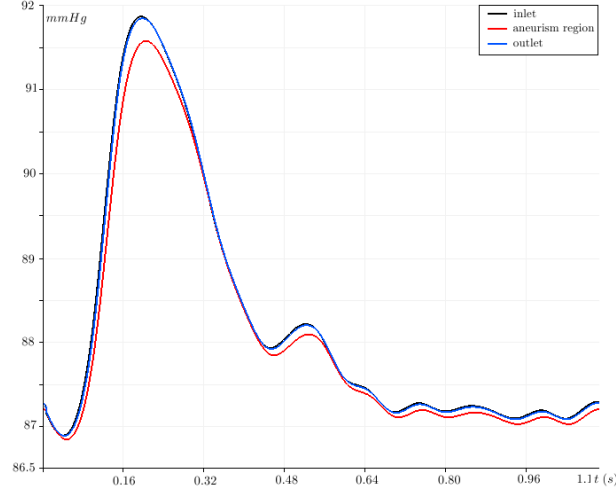


Figure 3.12: Evolution of the pressure in time (s) sampled in three points at the inlet (black) and outlet (blue) boundaries and corresponding to the aneurism region, for $\mathbb{R}e = 278$.

3.4.3 Artery with an Aneurysm

In this section we present the solution obtained for an idealized aneurysm, which occurs in a curved vessel. By means of IGA we are able to provide an exact representation of this geometry, using basis functions of degree $p = 2$ and global continuity \mathcal{C}^1 . The mesh is constituted by $N_{el} = 99 \times 32$ elements; and the resulting dimensionless time step, according to condition (3.47), is $\Delta t = 0.037037$, with corresponding dimensional time step $\Delta t = 3.18 \cdot 10^{-4} s$. The dimensionless resistance constant for this specific problem is set to $C_{out}^* = 5.046$ corresponding to resistance constant $C_{out} = 2500 dyn \cdot s / cm^5$, an higher value with respect to the one considered in the previous sections. As in Sections 3.4.1 and 3.4.1, the data characterizing the geometry and the choice of the maximum flow rate value yield a Reynolds number equal to $\mathbb{R}e = 278$. In Figure 3.13 we report the streamlines of the velocity at different times in the heartbeat period in order to show the development of vortexes. We observe that the flow maintains laminar behavior with vortexes developing in the aneurysm. Their maximum number is 3, corresponding to the peak of the flow. In particular, throughout the deceleration phase we can observe a quite stable flow presenting only a vortex in the aneurysm region. In Figure 3.12 we plot the pressure curves during the cardiac cycle in three different points in the domain. The results are in good agreement with those reported in [VCFJT06], even if different geometries are considered.

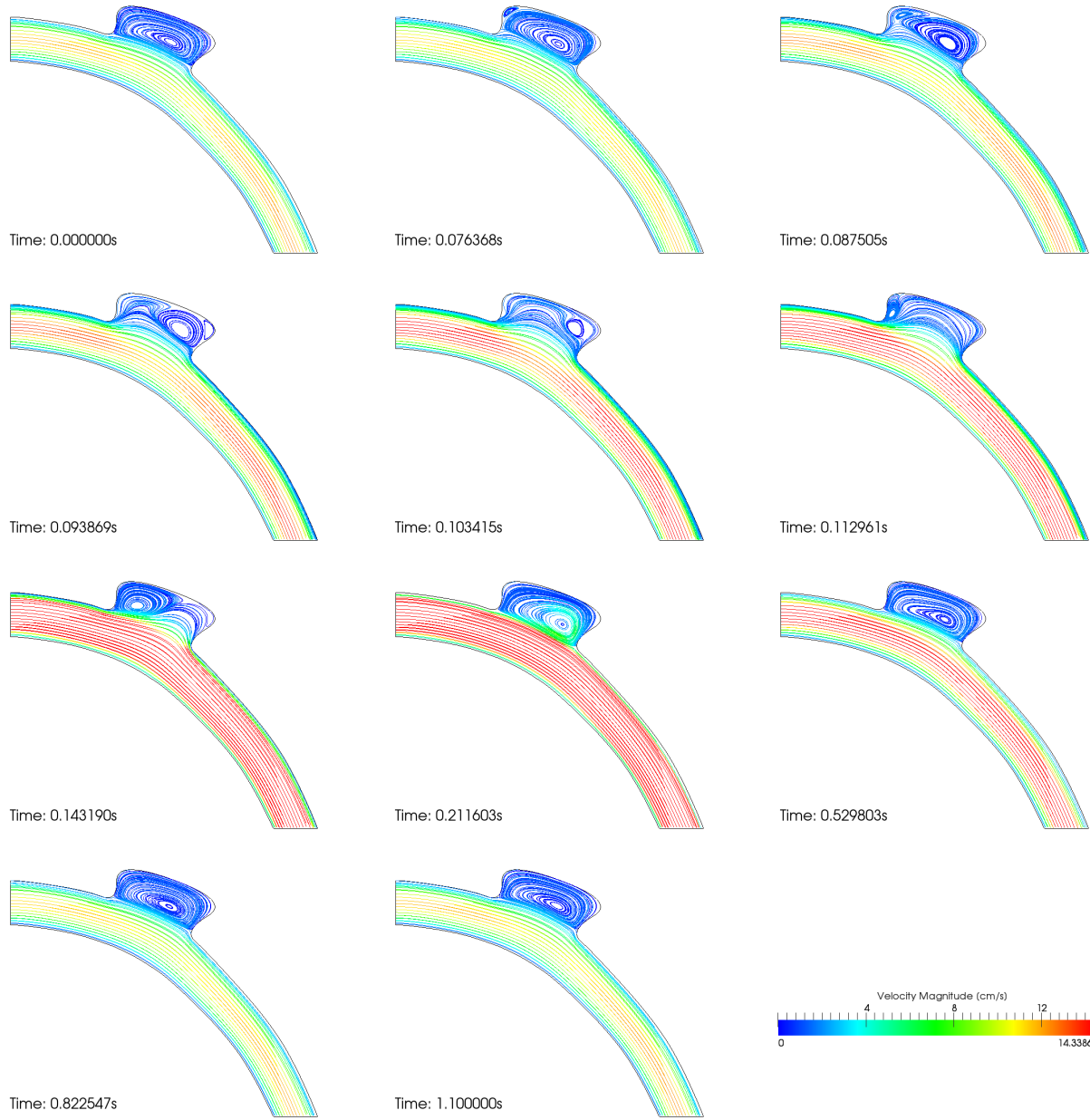


Figure 3.13: Streamlines for the aneurysm at different times in the cardiac cycle. Streamlines are colored according to the velocity magnitude, $Re = 278$.

Chapter 4

Isogeometric Analysis for Reduced Fluid-Structure Interaction Models

In haemodynamic applications a deep understanding of the Fluid-Structure Interaction (FSI) mechanisms is a key factor to describe the vascular dynamics in medium-large vessels, where the deformation of the walls assumes relevant values. In addition, the large part of the arterial diseases and pathologies can be properly studied only if the mechanical response of the vessel walls to the pulsatile nature of blood flow is taken into account. This is due to the fact that a rigid wall approximation is able to capture only the main features of the flow field, but precluding e.g. the study of the pressure propagation phenomena. Nevertheless, accounting for a detailed description of the compliance of the arterial walls gives rise to challenging mathematical and numerical problems.

Mathematically, FSI models couple the fluid problem, describing the blood flow, and a structural problem, representing the deformation of the wall. From the numerical point of view, usually, the two major classes of methods considered are referred to as *staggered* or *monolithic* approaches [NV09, BCHZ08]. The former looks for separated and sequential solutions of the fluid and structural subproblems once per time step by means of suitable existing fluid and structure solvers and then combines the solutions with a coupling condition, which is in general not exactly satisfied. Their simplicity has the drawback that the resulting numerical scheme may be unstable in haemodynamics, because of the high added mass effect. The monolithic approach considers a unique fluid-structure solver by treating implicitly the coupling condition which is exactly satisfied. In this case, the numerical schemes are stable, but the computational cost associated to their numerical solution is relevant. Moreover, the resulting system of equations is highly nonlinear even if the vessel wall mechanics is described by means of simple linearly elastic PDEs.

The most common approaches are those related to an *Arbitrary Lagrangian Eulerian* (ALE) formulation, which considers the fluid problem defined in a domain Ω_t varying in time. Significant progresses have been achieved within this formulation both in the context of FEA [FQV⁺09, NV09, BvG⁺12, vTG⁺06] and IGA [BCHZ08, BGH⁺09]; however, the update of the moving computational domain makes the model computationally expensive.

In order to respond to a reduction of the computational costs for haemodynamics FSI, a new formulation, called *coupled momentum method for fluid-solid interaction problems* (CMM-FSI), was proposed by Figueroa et al. in [FVCJT06]. This method couples the solid and the fluid problems in the variational formulation, embedding the wall model into the fluid

problem as a *generalized Robin boundary condition*, as done e.g. in [NV09], but keeping the fluid domain fixed. This results in a fully coupled, reduced monolithic approach with a limited computational effort due to the identification between the degrees of freedom of the vessel wall and those of the fluid velocity.

Starting from [FVCJT06], we consider a reduced FSI model formulated as generalized Navier-Stokes equations in a fixed domain. The problem is expressed only in terms of the primitive variables of the fluid problem, i.e. the velocity \mathbf{u} and the pressure P , by means of a *kinematic condition* (continuity of velocities) and through an approximation of the wall displacement, say $\boldsymbol{\eta}$, in terms of the fluid velocity and acceleration fields. The mechanical response of the wall enters the fluid problem as a boundary condition [NV09] thanks to the *dynamic condition* (balancing of contact forces) and the thin wall approximation. In this work, we consider the *linear elastic Koiter shell model* for the arterial walls, as done e.g. in [vTG⁺06], however, contrarily to [vTG⁺06], we consider the complete linear Koiter shell model without neglecting the bending terms which involves high order derivatives. Indeed, our numerical simulations are based on IGA, for which the standard Galerkin formulation can be used, as pointed out in Chapter 1 and Appendix A.

In Section 4.1 we present the linear elastic Koiter shell model for the description of the wall mechanics. In Section 4.2 the coupled momentum method is described; we derive the dimensionless variational formulation of the reduced FSI problem resulting from the models considered and the coupling conditions. Then, we briefly describe the numerical approximation of the reduced model. Finally, in Section 4.3, we present some numerical results by comparing different choices on the parameters which characterize the method.

4.1 Mathematical modeling of artery walls

When dealing with FSI problems, the complex physiological structure of the arterial wall in medium and large vessels (see Chapter 2) requires to resort to reduced structural models to reduce the computational cost, even if only an average description of the mechanical response of the wall is provided. The first assumption, see e.g. [FVCJT06, NV09, BvG⁺12, vTG⁺06], is a thin wall approximation, which allow to identify the solid domain with the boundary of the fluid domain. Further simplifications involve the nature of the material constituting the walls, which are assumed to be homogeneous, isotropic and incompressible, despite they are in fact anisotropic and heterogeneous. By means of these hypotheses we can consider the so called *shell models* which are more computationally convenient than the ones describing the behavior of each layer constituting the wall [Hol06]. Specifically, we refer to the *linear Koiter shell model*, whose equations have been demonstrated to be asymptotically equivalent to three-dimensional problems for thin elastic shells, see e.g. the references quoted in [Cia05].

In this section we recall the main concepts connected to the differential geometry of surfaces with a brief presentation notationally oriented. We derive the Koiter shell equations for a geometry in cylindrical coordinates, representing a cylindrical ring whose radius is a function of the longitudinal coordinate. Moreover, since we are in the hypothesis that the *Kirchhoff-Love kinematic condition* holds, the terms in the equations do not depend on the circumferential coordinate θ and the axial symmetry allows to eventually consider a one-dimensional model. For further details on differential geometry applied to the elastic theory, in particular the mathematical analysis and formulation of the linear Koiter shell equations, we refer the interested reader to e.g. [Cia05].

4.1.1 Differential geometry: preliminaries

In the hypothesis that the wall thickness, say h_s , is small enough, an elastic shell can be defined referring to its middle surface, say Γ^s , described by a two-dimensional manifold with boundary. For the sake of simplicity, we will consider henceforth the Einstein's convention for which repeated indexes are summed. In particular Greek letters refers to indexes assuming values in the set $\{1, 2\}$, whereas Latin indexes in $\{1, 2, 3\}$.

Let $\omega \subseteq \mathbb{R}^2$, be a connected subset which defines a two-dimensional manifold with standard differentiable structure whose local coordinates are denoted by (ξ_1, ξ_2) . Moreover, let $\psi : \omega \rightarrow \Gamma^s \subseteq \mathbb{R}^3$ be an injective *regular* mapping defining a two-dimensional manifold with boundary by introducing a local system of curvilinear coordinates whose covariant basis vectors are given by:

$$\mathbf{a}_\alpha = \frac{\partial \psi}{\partial \xi_\alpha}, \text{ for } \alpha = 1, 2, \quad \mathbf{a}_3 = \frac{\mathbf{a}_1 \times \mathbf{a}_2}{\|\mathbf{a}_1 \times \mathbf{a}_2\|}, \quad (4.1)$$

where \times denotes the exterior product, while $\|\cdot\|$ is the euclidean norm. By using the assumption that ψ is regular, the two vectors $\mathbf{a}_1(\xi_1, \xi_2), \mathbf{a}_2(\xi_1, \xi_2)$ are linearly independent in all the points $(\xi_1, \xi_2) \in \omega$ and ψ is an injective immersion of ω in Γ^s . The two vectors $\mathbf{a}_1(\xi_1, \xi_2), \mathbf{a}_2(\xi_1, \xi_2)$ define the tangent plane to the surface Γ^s in (ξ_1, ξ_2) , while $\mathbf{a}_3(\xi_1, \xi_2)$ is the normal unit to the tangent plane in (ξ_1, ξ_2) . The contravariant basis vectors $\{\mathbf{a}^i\}_{i=1}^3$ are defined by means of the relation:

$$\mathbf{a}^i \cdot \mathbf{a}_j = \delta_{i,j}, \text{ for } i, j = 1, 2, 3, \quad (4.2)$$

with $\delta_{i,j}$ the Kronecker symbol. Therefore, the covariant and contravariant components of the *first fundamental form* of the surface are given by:

$$a_{\alpha\beta} = \mathbf{a}_\alpha \cdot \mathbf{a}_\beta, \quad a^{\alpha\beta} = \mathbf{a}^\alpha \cdot \mathbf{a}^\beta = a_{\alpha\beta}^{-1}, \text{ for } \alpha, \beta = 1, 2, \quad (4.3)$$

and the covariant and mixed component of the *second fundamental form* respectively by:

$$b_{\alpha\beta} = \mathbf{a}_3 \cdot \frac{\partial \mathbf{a}_\beta}{\partial \xi_\alpha} = -\mathbf{a}_\alpha \cdot \frac{\partial \mathbf{a}_3}{\partial \xi_\beta}, \quad b_\alpha^\beta = a^{\beta\sigma} b_{\sigma\alpha}, \text{ for } \alpha, \beta = 1, 2. \quad (4.4)$$

An arbitrary vector field, say $\boldsymbol{\eta}$, defined on Γ^s , can be represented in covariant components $\eta_i : \omega \rightarrow \mathbb{R}$, i.e. $\boldsymbol{\eta}(\psi(\xi_1, \xi_2)) = \eta_i(\xi_1, \xi_2) \mathbf{a}^i(\xi_1, \xi_2)$, and its surface covariant derivatives are expressed as:

$$\eta_{\beta|\alpha} = \frac{\partial \eta_\beta}{\partial \xi_\alpha} - \Gamma_{\alpha\beta}^\sigma \eta_\sigma \text{ for } \alpha, \beta = 1, 2, \quad (4.5)$$

in terms of the *Christoffel symbols of the first and second kind*:

$$\Gamma_{\alpha\beta\tau} = \frac{\partial \mathbf{a}_\beta}{\partial \xi_\alpha} \cdot \mathbf{a}_\tau, \quad \Gamma_{\alpha\beta}^\sigma = a^{\sigma\tau} \Gamma_{\alpha\beta\tau} = \frac{\partial \mathbf{a}_\beta}{\partial \xi_\alpha} \cdot \mathbf{a}^\sigma, \text{ for } \alpha, \beta, \sigma = 1, 2. \quad (4.6)$$

Now, let $\Omega := \omega \times \left[-\frac{h_s}{2}, \frac{h_s}{2}\right] \subseteq \mathbb{R}^3$, then, if h_s is small enough (see [Cia05]), we can define a *shell* whose middle surface is Γ^s and thickness h_s by means of the mapping:

$$\Psi : \Omega \rightarrow \Omega^s \subseteq \mathbb{R}^3, \quad \Psi(\xi_1, \xi_2, \xi_3) := \psi(\xi_1, \xi_2) + \xi_3 \mathbf{a}_3(\xi_1, \xi_2). \quad (4.7)$$

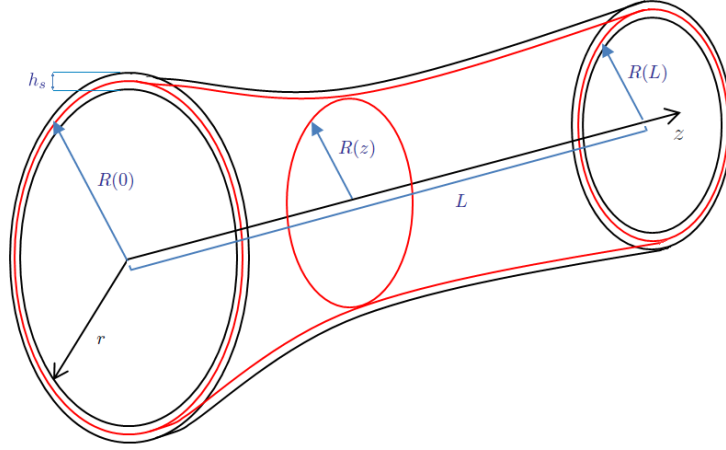


Figure 4.1: Example 4.1: shell of thickness h_s and middle surface represented by a cylindrical ring with $R = R(z)$.

Example 4.1 (Cylindrical ring with $R = R(z)$). Let us consider the shell given in Figure 4.1 of thickness h_s and middle surface Γ^s (in red). The surface Γ^s can be parametrized by the mapping:

$$\psi : \omega \subseteq \mathbb{R}^2 \rightarrow \Gamma^s \subseteq \mathbb{R}^3, \quad \psi(\theta, z) := (R(z) \cos \theta, R(z) \sin \theta, z)^T, \quad (4.8)$$

where $\omega := \{(\theta, z) : \theta \in [0, 2\pi), z \in [0, L]\}$ and $R : [0, L] \rightarrow \mathbb{R}^2$ is a smooth function. It represents a cylindrical ring aligned along the canonical base vector z , whose length is equal to L and radius is a function of the longitudinal coordinate, i.e. $R := R(z)$. For the sake of simplicity, we denote henceforth with the superscript $'$ the derivative of different quantities with respect to the longitudinal coordinate z . The covariant basis is then given by:

$$\mathbf{a}_1 = \frac{\partial \psi}{\partial \xi_1} = \begin{bmatrix} -R(z) \sin \theta \\ R(z) \cos \theta \\ 0 \end{bmatrix}, \quad \mathbf{a}_2 = \frac{\partial \psi}{\partial \xi_2} = \begin{bmatrix} R'(z) \cos \theta \\ R'(z) \sin \theta \\ 1 \end{bmatrix}, \quad \mathbf{a}_3 = \frac{1}{\sqrt{1 + (R'(z))^2}} \begin{bmatrix} \cos \theta \\ \sin \theta \\ -R'(z) \end{bmatrix}. \quad (4.9)$$

Therefore, the first and second fundamental forms are:

$$a_{\alpha\beta} = \begin{bmatrix} (R(z))^2 & 0 \\ 0 & (R'(z))^2 + 1 \end{bmatrix}, \quad b_{\alpha\beta} = \frac{1}{\sqrt{1 + (R'(z))^2}} \begin{bmatrix} -R(z) & 0 \\ 0 & R''(z) \end{bmatrix}; \quad (4.10)$$

this yields:

$$a^{\alpha\beta} = \begin{bmatrix} \frac{1}{(R(z))^2} & 0 \\ 0 & \frac{1}{1 + (R'(z))^2} \end{bmatrix}, \quad b_\alpha^\beta = \frac{1}{\sqrt{1 + (R'(z))^2}} \begin{bmatrix} -\frac{1}{R(z)} & 0 \\ 0 & \frac{R''(z)}{1 + (R'(z))^2} \end{bmatrix}. \quad (4.11)$$

Moreover, we explicit the Christoffel symbols of the second kind, which are given by:

$$\begin{aligned} \Gamma_{11}^1 = \Gamma_{21}^2 = 0, \quad \Gamma_{11}^2 &= -\frac{R(z)R'(z)}{1 + (R'(z))^2}, \quad \Gamma_{21}^1 = \frac{R'(z)}{R(z)}, \\ \Gamma_{22}^1 = \Gamma_{12}^2 = 0, \quad \Gamma_{12}^1 &= \frac{R'(z)}{R(z)}, \quad \Gamma_{22}^2 = \frac{R'(z)R''(z)}{1 + (R'(z))^2}. \end{aligned} \quad (4.12)$$

According to Eq. (4.7), the shell represented in Figure 4.1 can be parametrized by the mapping:

$$\Psi(\theta, z, \xi_3) := \begin{bmatrix} \left(R(z) + \frac{\xi_3}{\sqrt{1 + (R'(z))^2}} \right) \cos \theta \\ \left(R(z) + \frac{\xi_3}{\sqrt{1 + (R'(z))^2}} \right) \sin \theta \\ \left(z - \frac{\xi_3 R'(z)}{\sqrt{1 + (R'(z))^2}} \right) \end{bmatrix}.$$

◇

4.1.2 The linear Koiter shell model

In general, shell theories are based on some kinematic assumptions that relate the displacement of the points located in a material line orthogonal to the middle surface to the corresponding point on the middle surface. In particular, under the *Kirchhoff-Love kinematic condition*, for which any point of such material lines remains on the normal of the deformed middle surface after the deformation and preserve its distance from it, we can express the displacement field of the shell uniquely in terms of the displacement of the mid surface. Moreover, the external loads on the shell faces are reduced to equivalent loads acting in the middle surface. The *linear Koiter shell model* considers an additional assumption for which the state of the stress inside the shell is planar and parallel to the mid surface. For the sake of simplicity, the PDEs governing the dynamic of the shell are provided in their variational formulation.

Let Ω^s be a linearly elastic shell, whose thickness h_s is sufficiently small and denote by Γ^s its middle surface. Moreover, let λ, μ the two *Lamé constants* characterizing the material, or equivalently, the corresponding *Young's modulus* E and *Poisson ratio* ν :

$$\lambda = \frac{E\nu}{(1+\nu)(1-2\nu)}, \quad \mu = \frac{E}{2(1+\nu)}. \quad (4.13)$$

The weak formulation of the linear Koiter shell equations [Cia05] is expressed in terms of the contravariant components of the shell elasticity tensor and of the covariant components of the linearized metric and curvature changes of the surface. Specifically, the elasticity tensor reads component wise:

$$E^{\alpha\beta\sigma\tau} = \frac{4\lambda\mu}{\mu + 2\lambda} a^{\alpha\beta} a^{\sigma\tau} + 2\mu(a^{\alpha\sigma} a^{\beta\tau} + a^{\alpha\tau} a^{\beta\sigma}), \quad (4.14)$$

or equivalently, by means of the relation (4.13):

$$E^{\alpha\beta\sigma\tau} = \frac{2E\nu}{1-\nu^2} a^{\alpha\beta} a^{\sigma\tau} + \frac{E}{1+\nu} (a^{\alpha\sigma} a^{\beta\tau} + a^{\alpha\tau} a^{\beta\sigma}). \quad (4.15)$$

The latter are defined as the linear part with respect to the vectorial field $\boldsymbol{\eta}$, of the associated covariant change of metric tensor and change of curvature tensor; they are given by, respectively:

$$\gamma_{\alpha\beta}(\boldsymbol{\eta}) = \frac{1}{2} (\eta_{\alpha|\beta} + \eta_{\beta|\alpha}) - b_{\alpha\beta} \eta_3, \quad (4.16a)$$

$$\rho_{\alpha\beta}(\boldsymbol{\eta}) = \eta_{3|\alpha\beta} - b_{\alpha}^{\sigma} b_{\sigma\beta} \eta_3 + b_{\alpha}^{\sigma} \eta_{\sigma|\beta} + b_{\beta}^{\tau} \eta_{\tau|\alpha} + b_{\beta}^{\tau} |_{\alpha} \eta_{\tau}, \quad (4.16b)$$

where η_i , for $i = 1, 2, 3$, are the covariant components of $\boldsymbol{\eta}$, the covariant derivatives $\eta_{\alpha|\beta}$ are given in Eq. (4.5), while $\eta_{3|\alpha\beta}$ and $b_\beta^\tau|_\alpha \eta_\tau$ are defined as:

$$\eta_{3|\alpha\beta} := \partial_{\alpha\beta}\eta_3 - \Gamma_{\alpha\beta}^\sigma \partial_\sigma \eta_3 \quad \text{and} \quad b_\beta^\tau|_\alpha \eta_\tau := \partial_\alpha b_\beta^\tau + \Gamma_{\alpha\sigma}^\tau b_\beta^\sigma - \Gamma_{\alpha\beta}^\sigma b_\sigma^\tau. \quad (4.17)$$

We introduce the following function space:

$$V := \left\{ \boldsymbol{\eta} \in H^1(\omega) \times H^1(\omega) \times H^2(\omega) : \eta_i|_{\gamma_0} = 0 \text{ for } i = 1, 2, 3, \text{ and } \frac{\partial \eta_3}{\partial n}|_{\gamma_0} = 0 \right\}, \quad (4.18)$$

where $\gamma_0 \subseteq \partial\omega$ denotes the subset of the boundary in which essential homogeneous boundary conditions are imposed and $\frac{\partial \cdot}{\partial n}$ is the outer normal derivative operator along $\partial\omega$. Then, the variational formulation of the linear Koiter shell model for a shell Ω^s with volume shell density ρ_s , which is clamped along γ_0 and whose motion takes place in the interval time $(0, T)$, reads:

find, for all $t \in (0, T)$, $\boldsymbol{\eta}(t) \in V$ such that:

$$\begin{aligned} \int_\omega h_s \rho_s \frac{\partial^2 \boldsymbol{\eta}}{\partial t^2} \cdot \boldsymbol{\zeta} J d\xi_1 d\xi_2 + \int_\omega \frac{h_s}{2} E^{\alpha\beta\sigma\tau} \gamma_{\alpha\beta}(\boldsymbol{\eta}) \gamma_{\sigma\tau}(\boldsymbol{\zeta}) J d\xi_1 d\xi_2 \\ + \int_\omega \frac{h_s^3}{24} E^{\alpha\beta\sigma\tau} \rho_{\sigma\tau}(\boldsymbol{\eta}) \rho_{\alpha\beta}(\boldsymbol{\zeta}) J d\xi_1 d\xi_2 = \int_\omega \boldsymbol{t}^s \cdot \boldsymbol{\zeta} J d\xi_1 d\xi_2 \quad \forall \boldsymbol{\zeta} \in V, \end{aligned} \quad (4.19)$$

where $(J d\xi_1 d\xi_2)$ is the area element along Γ^s , with $J := \sqrt{\det(a_{\alpha\beta})}$; whereas \boldsymbol{t}^s is the surface force acting on the shell. Moreover, the problem (4.19) must be completed by suitable initial conditions for the displacement field of the form:

$$\boldsymbol{\eta}(t=0) = \boldsymbol{\eta}_0 \quad \text{and} \quad \frac{\partial \boldsymbol{\eta}}{\partial t}(t=0) = \bar{\boldsymbol{\eta}}_0. \quad (4.20)$$

Remark 4.1. *The weak formulation of the linear Koiter shell accounts for both the membrane (or stretching) and the bending (or flexural) terms, the former being related to the linearized change of metric tensor and the latter to the change of curvature tensor. Alternative formulations for the shell model derived from the Koiter shell equations (4.19) are given in [NV09], even if the bending terms are neglected (however a contribution due to a prestress tensor is added to the linear terms). Further modifications of the specific linear elastic cylindrical Koiter shell model (see Example 4.2) are provided in [BuG⁺12, vTG⁺06], where the model is extended in order to account for a viscoelastic response of the shell.*

Remark 4.2. *We refer to [Cia05] for the equivalent (in the sense of distribution) strong form of the linear Koiter shell problem (4.19).*

Example. 4.1 (Cylindrical ring with $R = R(z)$). For the shell defined in Example 4.1, let $\boldsymbol{\eta} \in V$ be a vector field, describing the displacement of the middle surface Γ^s and whose covariant components are respectively denoted by $\eta_\theta := \eta_1$, $\eta_z := \eta_2$ and $\eta_r := \eta_3$, according to the system of cylindrical coordinates introduced. Moreover, by means of the assumption of axial symmetry of the geometry, the problem (4.19) is completely independent from the circumferential coordinate θ , provided that \boldsymbol{t}^s is suitably chosen. This leads to consider the problem (4.19) to be expressed only in the variables (η_z, η_r) , which represent the *longitudinal displacement* and the radial displacement, respectively. In such a way, the function space V of Eq. (4.18), in which the problem (4.19) is defined, is given by:

$$V = \{(\eta_z, \eta_r) \in H^1(0, L) \times H^2(0, L) : \eta_z|_{\gamma_0} = 0, \eta_r|_{\gamma_0} = 0 \text{ and } \eta_r'|_{\gamma_0} = 0\}, \quad (4.21)$$

with $\gamma_0 \subseteq \{0, L\}$. If the shell is clamped, it means that $\gamma_0 \equiv \{0, L\}$ and on the corresponding boundary defined by $\gamma_0 \times \left(-\frac{h_s}{2}, \frac{h_s}{2}\right)$ essential homogeneous boundary conditions are prescribed.

The covariant components of the linearized change of metric tensor and change of curvature tensor associated with $\boldsymbol{\eta}$ can be computed by means of Eq. (4.16) and they are respectively given by:

$$\begin{aligned} \gamma_{11}(\boldsymbol{\eta}) &= \frac{R(z)R'(z)}{1 + (R'(z))^2} \eta_z + \frac{R(z)}{\sqrt{1 + (R'(z))^2}} \eta_r, \quad \gamma_{12}(\boldsymbol{\eta}) = \gamma_{21}(\boldsymbol{\eta}) = 0, \\ \gamma_{22}(\boldsymbol{\eta}) &= \eta'_z - \frac{R'(z)R''(z)}{1 + (R'(z))^2} \eta_z - \frac{R''(z)}{\sqrt{1 + (R'(z))^2}} \eta_r, \\ \rho_{11}(\boldsymbol{\eta}) &= \frac{1}{1 + (R'(z))^2} (R(z)R'(z)\eta'_r - \eta_r) + \frac{R(z)R'(z)}{(1 + (R'(z))^2)^{3/2}} \left(-\frac{1}{R(z)} + \frac{R''(z)}{1 + (R'(z))^2}\right) \eta_z, \\ \rho_{12}(\boldsymbol{\eta}) &= \rho_{21}(\boldsymbol{\eta}) = 0, \\ \rho_{22}(\boldsymbol{\eta}) &= \eta''_r - \frac{R'(z)R''(z)}{1 + (R'(z))^2} \eta'_r - \frac{R''(z)}{\sqrt{1 + (R'(z))^2}} \eta_r + \frac{R''(z)}{(1 + (R'(z))^2)^{3/2}} \left(\eta'_z - \frac{R'(z)R''(z)}{1 + (R'(z))^2} \eta_z\right) \\ &\quad + \frac{1}{2(1 + (R'(z))^2)^{5/2}} (2R'''(z)(1 + (R'(z))^2) - 3R''(z)) \eta_z. \end{aligned} \tag{4.22a}$$

$$\tag{4.22b}$$

Moreover, the controvariant components of the shell elasticity tensor, expressed in terms of the Young's modulus E and the Poisson ratio ν , are null except the following components:

$$\begin{aligned} E^{1111} &= \frac{2E}{1 - \nu^2} \frac{1}{(R(z))^4}, \quad E^{1122} = E^{2211} = \frac{2E\nu}{1 - \nu^2} \frac{1}{(R(z))^2} \frac{1}{(1 + (R'(z))^2)}, \\ E^{2222} &= \frac{2E}{1 - \nu^2} \frac{1}{(1 + (R'(z))^2)^2}. \end{aligned} \tag{4.23}$$

By substituting the expressions of Eq. (4.22) and Eq. (4.23) into Eq. (4.19), we have the explicit form of the PDEs defining the Koiter shell model for the given geometry. \diamond

Example 4.2. The linear elastic cylindrical Koiter shell model, considered e.g. in [BvG⁺12, vTG⁺06] (where terms representing a viscoelastic behavior are added), can be deduced from Example 4.1, considering a constant radius, say R . This yields the following well known model, defined on the function space V of Eq. (4.21):

find, for all $t \in (0, T)$, $\boldsymbol{\eta}(t) = (\eta_z(t), \eta_r(t)) \in V$ such that:

$$\begin{aligned} h_s \rho_s \int_0^L \frac{\partial^2 \boldsymbol{\eta}}{\partial t^2} \cdot \boldsymbol{\zeta} dz &+ h_s \int_0^L \left(\frac{E\nu}{1 - \nu^2} \left(\eta'_z + \frac{1}{R} \eta_r \right) \left(\zeta'_z + \frac{1}{R} \zeta_r \right) + \frac{E}{1 + \nu} \left(\eta'_z \zeta'_z + \frac{1}{R^2} \eta_r \zeta_r \right) \right) dz \\ &+ \frac{h_s^3}{12} \int_0^L \left(\frac{E\nu}{1 - \nu^2} \left(\eta''_r - \frac{1}{R^2} \eta_r \right) \left(\zeta''_r - \frac{1}{R^2} \zeta_r \right) + \frac{E}{1 + \nu} \left(\eta''_r \zeta''_r + \frac{1}{R^4} \eta_r \zeta_r \right) \right) dz \\ &= \int_0^L \mathbf{t}^s \cdot \boldsymbol{\zeta} dz \quad \forall \boldsymbol{\zeta} \in V. \end{aligned} \tag{4.24}$$

\diamond

Example 4.3. An additional simplification consist in assuming that the structure deforms only in the normal direction to the middle surface; this assumption is widely adopted in the vascular dynamic modeling, see for instance [NV09]. This hypothesis leads to neglect all the terms involving the covariant components η_1, η_2 of the displacement field, i.e. $\boldsymbol{\eta} = (0, 0, \eta_3)$. The resulting function space V of Eq. (4.18), reduces to the following:

$$V := \left\{ \eta \in H^2(\omega) : \eta|_{\gamma_0} = 0 \text{ and } \frac{\partial \eta}{\partial n}|_{\gamma_0} = 0 \right\}, \quad (4.25)$$

while the covariant change of metric tensor and change of curvature tensor respectively, are given by:

$$\gamma_{\alpha\beta}(\boldsymbol{\eta}) = -b_{\alpha\beta}\eta_3, \quad (4.26a)$$

$$\rho_{\alpha\beta}(\boldsymbol{\eta}) = \partial_{\alpha\beta}\eta_3 - \Gamma_{\alpha\beta}^\sigma \partial_\sigma \eta_3 - b_\alpha^\sigma b_{\sigma\beta} \eta_3. \quad (4.26b)$$

In the specific case of the clamped cylindrical shell in Example 4.2, the function space is $V = \{\eta \in H^2(0, L) : \eta(0) = \eta(L) = 0 \text{ and } \eta'(0) = \eta'(L) = 0\}$ and problem (4.19) with only normal (radial) displacement reads:

find, for all $t \in (0, T)$, $\eta_r(t) \in V$ such that:

$$\begin{aligned} h_s \rho_s \int_0^L \frac{\partial^2 \eta_r}{\partial t^2} \zeta dz + h_s \int_0^L \left(\frac{E}{1-\nu^2} \frac{1}{R^2} \eta_r \zeta \right) dz \\ + \frac{h_s^3}{12} \int_0^L \left(\frac{E\nu}{1-\nu^2} \left(\eta_r'' - \frac{1}{R^2} \eta_r \right) \left(\zeta'' - \frac{1}{R^2} \zeta \right) + \frac{E}{1+\nu} \left(\eta_r'' \zeta'' + \frac{1}{R^4} \eta_r \zeta \right) \right) dz \\ = \int_0^L t_r^f \zeta dz \quad \forall \zeta \in V. \end{aligned} \quad (4.27)$$

◇

Remark 4.3. We observe that the bending terms in the resulting linear elastic Koiter shell model involve high order derivatives. Usually, shell models based on the linear Koiter shell equations (4.19) account only for the membrane terms, as done e.g. [vTG⁺06, NV09]. This choice is motivated by considering that these high order terms are relatively small with respect to the membrane terms. Nevertheless, in [vTG⁺06], it is highlighted the lack of analytical results proving the well-posedness of FSI problems whose structural problem does not include higher-order derivative terms corresponding to bending or viscoelastic behavior.

Remark 4.4. The linear elastic Koiter shell model described by the PDEs (4.19) is a two-dimensional model for the vessel wall applicable to three-dimensional FSI problems. In order to obtain a model which describes the mechanical response of the wall in case of two-dimensional models for the fluid, we need to reduce to a one-dimensional model for the structure by considering a section of the given surface, corresponding to the one selected for the domain of the fluid. In this case additional coupling conditions must be imposed in order to close the resulting system of equations. Nevertheless, one-dimensional models constitute a simple way to describe the dynamic of the shell in case of axial symmetric geometries as the ones described in the examples of this section. Consider, e.g., the linear elastic Koiter shell model in Example 4.1. The invariance with respect to the circumferential coordinate θ allows to consider the problem for a selected angle $\tilde{\theta}$, thus defined on a domain $\tilde{\Gamma}^s$ whose coordinates considered are only the radial and the axial ones. By symmetry, the solution can be extended to the domain defined in

correspondence of the coordinate $\tilde{\theta}_1 = \tilde{\theta} + \pi$. In such a way we can obtain a one-dimensional model for a section in correspondence of a diameter of the shell, without resorting to additional coupling conditions (being these constituted by the symmetry).

4.2 The reduced Fluid-Structure Interaction model

In this section we present a reduced FSI model in the framework of the coupled momentum method [FVCJT06]. We describe the procedure leading to the formulation of the coupled problem in the form of generalized Navier-Stokes equations (3.16) in the primitive variables describing the fluid flow (\mathbf{u}, p) , without the need to introduce additional degrees of freedom representing the displacement of the wall $(\boldsymbol{\eta})$. Since we consider the linear elastic Koiter shell model of Section 4.1, we obtain a different formulation with respect to [FVCJT06, NV09]; in particular, this leads to the choice of different function spaces and the presence of high order terms on the boundary. For three-dimensional models, the problem is fully coupled, instead for two-dimensional models we need to take into account Remark 4.4 and consider axial symmetric geometries. The resulting coupled problem (for the specific case of a two-dimensional model of a cylindrical vessel) is provided in its dimensionless form, according to the process of Section 3.1.2. Finally, we consider the numerical approximation of the generalized Navier-Stokes equations by means of IGA for the spatial approximation.

4.2.1 The Coupled Momentum method

In large and medium vessels, blood flows can be modeled as the flow of an incompressible, Newtonian viscous fluid (see Section 3.1). Thus, the motion of the fluid in the computational domain, say Ω^f , can be described by means of the Navier-Stokes equations (3.5). In order to formulate a well posed problem, Eq. (3.5) must be completed by suitable initial conditions, for which we consider Remark 3.1, and boundary conditions. As for the latter, on the *inlet* boundary Γ^{in} and on the *outlet* boundary Γ^{out} we consider the same set of boundary conditions described in Section 3.2 (eventually extended to the three-dimensional model case, without performing any reduction). Nevertheless, the *no-slip* boundary condition, prescribed on the part of the boundary corresponding to the interface with the vessel wall Γ^w , is replaced by imposing a normal stress (a traction), say \mathbf{t}^f , i.e. $\boldsymbol{\sigma}_f \mathbf{n} = \mathbf{t}^f$ on Γ^w .

We briefly recall the dimensional form of the Navier-Stokes equations defined in the domain Ω^f with this set of boundary conditions for the general case of domains $\Omega^f \subseteq \mathbb{R}^d$, for $d = 2, 3$, corresponding to two-dimensional and three-dimensional fluid problems. By following the notation introduced in Chapter 3, let \mathbf{u} be the fluid velocity and P the pressure, whereas we denote by ρ_f the density fluid so that we can distinguish it from the density of the wall, indicated by ρ_s . Moreover, let \mathbf{g}^{in} and \mathbf{h} be the dimensional vector fields representing respectively the inlet and outlet condition of Section 3.2 and \mathbf{u}_0 the initial velocity field. We consider the notation μ_f and ν_f for indicating the dynamic and kinematic viscosity of the fluid. The problem describing the blood flow in the time interval $(0, T)$ reads (for $d=2,3$):

find $\mathbf{u} : \Omega^f \times (0, T) \rightarrow \mathbb{R}^d$ and $P : \Omega^f \times (0, T) \rightarrow \mathbb{R}$ such that:

$$\left\{ \begin{array}{ll} \rho_f \frac{\partial \mathbf{u}(t)}{\partial t} + \rho_f (\mathbf{u}(t) \cdot \nabla) \mathbf{u}(t) - \nabla \cdot \boldsymbol{\sigma}_f(\mathbf{u}(t), P(t)) = \mathbf{f} & \text{in } \Omega^f, t \in (0, T), \quad (4.28a) \\ \nabla \cdot \mathbf{u}(t) = 0 & \text{in } \Omega^f, t \in (0, T), \quad (4.28b) \\ \mathbf{u}(t=0) = \mathbf{u}_0 & \text{in } \Omega^f, \quad (4.28c) \\ \mathbf{u}(t) = \mathbf{g}^{\text{in}} & \text{on } \Gamma^{\text{in}}, t \in (0, T), \quad (4.28d) \\ \boldsymbol{\sigma}_f(\mathbf{u}(t), P(t)) \mathbf{n} = \mathbf{h} & \text{on } \Gamma^{\text{out}}, t \in (0, T), \quad (4.28e) \\ \boldsymbol{\sigma}_f(\mathbf{u}(t), P(t)) \mathbf{n} = \mathbf{t}^f & \text{on } \Gamma^{\text{w}}, t \in (0, T), \quad (4.28f) \end{array} \right.$$

where $\boldsymbol{\sigma}_f(\mathbf{u}, P) = -PI + 2\mu_f D(\mathbf{u})$ is the Cauchy stress tensor, with $D(\mathbf{u}) = \frac{(\nabla \mathbf{u} + \nabla \mathbf{u}^T)}{2}$ the strain rate tensor.

The vector field \mathbf{t}^f is not yet specified and it will be determined by the coupling between the fluid and the structural problems. Specifically, the two conditions that allow to perform the coupling are the so called *kinematic condition*, which requires the continuity of the fluid and the structural velocities at the interface Γ^{w} , i.e.:

$$\frac{\partial \boldsymbol{\eta}}{\partial t} \Big|_{\Gamma^{\text{w}}} = \mathbf{u} \Big|_{\Gamma^{\text{w}}}, \quad (4.29)$$

and the *dynamic condition*, that imposes the balance of contact forces at the interface, for which the contact force of the fluid represented by \mathbf{t}^f is equal and opposite to the contact force of the wall, say \mathbf{t}^s :

$$\mathbf{t}^f = -\mathbf{t}^s, \text{ on } \Gamma^{\text{w}}. \quad (4.30)$$

We assume for the structure a thin wall approximation and we choose as constitutive model the linear Koiter shell model described in Section 4.1.2. In such a way, in case of three-dimensional models, we can close the fluid problem (4.28) since the fluid boundary Γ^{w} coincides with the domain Γ^s in which the structural problem (4.19) is defined; this yields $\Gamma^{\text{w}} \equiv \Gamma^s$. Moreover, the vector field \mathbf{t}^s of Eq. (4.30) corresponds to the one of Eq. (4.19). Instead, according to Remark 4.4, in order to not increase the computational cost, for two-dimensional models we restrict to the case of axial symmetric geometries and the coupled FSI problem follows as well.

In [FVCJT06, NV09], since a membrane model is assumed for the structure, the spatial differentiability requirements as for the trial and test spaces of the fluid and solid problems are the same. In such a case, the coupling is performed at the variational level by considering the standard variational formulation for the fluid problem and embedding the structure equation into the fluid problem as boundary condition. Instead, in our case, a membrane-bending model leads to define suitable trial and test spaces for the respective weak formulations in order to obtain the same spatial differentiability requirement for all the components of the unknowns. In particular we impose an higher spatial differentiability requirement as we will describe in next section.

The resulting problem is defined in the unknowns $\boldsymbol{\eta}$ (wall displacement), \mathbf{u} (fluid velocity) and P (fluid pressure). With the aim of reducing the computational costs, a strong coupling between the degrees of freedom of the vector fields describing the displacement and the velocity can be performed. As a consequence, the problem is written only in terms of the primitive variables related to the fluid problem (\mathbf{u}, P) . Moreover, it is possible to maintain fixed the computational domain for the fluid problem, being the degrees of freedom of the

velocity field on Γ^w enhanced with an additional contribution due to the wall. The structure (surface) displacement is obtained by means of a consistent time integration of the velocity and acceleration. Specifically, by using the coupling condition of Eq. (4.29), we replace $\boldsymbol{\eta}$ by a vector field, say \mathbf{d} , expressed in terms of the fluid velocity \mathbf{u} and acceleration, say $\dot{\mathbf{u}}$, and given by:

$$\mathbf{d} : \Gamma^w \times (0, T) \rightarrow \mathbb{R}^d, \quad \mathbf{d}(t) := \boldsymbol{\eta}(t_0) + \Delta t \mathbf{u}(t_0) + \frac{\Delta t^2}{2} [(1 - 2\beta)\ddot{\mathbf{u}}(t_0) + 2\beta\ddot{\mathbf{u}}(t)]. \quad (4.31)$$

Remark 4.5. *Even if we have not already performed the discretization in time, we express the approximation \mathbf{d} by involving the time step $\Delta t := t - t_0$. We underline that the same strategy has been adopted in the discrete formulation of the VMS-LES of Section 3.3.2.*

The approximation of Eq. (4.31) is performed in the framework of the *Newmark algorithm* [Hug00] in order to be consistent with the time integration scheme used, i.e. the generalized- α method of Section 3.3.3. The Newmark method is formulated for second order differential equations in time in the general form $a\ddot{w}(t) + b\dot{w}(t) + cw(t) = d$ for which, at the discrete level we consider:

$$w_{n+1} = w_n + \Delta t \dot{w}_n + \frac{\Delta t^2}{2} [(1 - 2\beta)\ddot{w}_n + 2\beta\ddot{w}_{n+1}], \quad (4.32a)$$

$$\dot{w}_{n+1} = \dot{w}_n + \Delta t [(1 - \delta)\ddot{w}_n + \delta\ddot{w}_{n+1}]. \quad (4.32b)$$

The algorithm of Eq. (4.32) is unconditionally stable if the parameters δ and β satisfy the following relation, see for instance [Hug00]:

$$2\beta \geq \delta \geq \frac{1}{2}. \quad (4.33)$$

By recognizing that Eq. (4.32a) corresponds to Eq. (4.31) and Eq. (4.32b) to the updating of the velocities of Eq. (3.54c) in the generalized- α method, we can assure an unconditional stable approximation provided that the parameter β in Eq. (4.31) is related to the parameter δ , also used in the generalized- α method, through the condition of Eq. (4.33). In particular, following Eqs. (3.50) and (3.52), we can write δ as a function of the amount of high frequency dissipation $\rho_\infty \in [0, 1]$, as $\delta = \frac{1}{1 + \rho_\infty}$. Therefore, $\delta \in \left[\frac{1}{2}, 1\right]$ and the unconditional stability condition is satisfied for all the choices of the parameter $\beta \in \left[\frac{1}{4}, 1\right]$ satisfying Eq. (4.33).

Remark 4.6. *By considering the kinematic condition of Eq. (4.29) and the expression of $\mathbf{u}(t_0)$ in terms of $\dot{\mathbf{u}}(t_0)$ and $\ddot{\mathbf{u}}(t_0)$ in Eq. (4.32b), the approximation provided in Eq. (4.31) yields that the continuity of velocities is satisfied up to a term of the first order in $t - t_0$. This follows by:*

$$\dot{\mathbf{d}}(t) - \mathbf{u}(t) = (t - t_0)\delta(-\ddot{\mathbf{u}}(t) + \ddot{\mathbf{u}}(t_0)) + \frac{(t - t_0)^2}{2} ((1 - 2\beta)\ddot{\mathbf{u}}(t_0) + 2\beta\ddot{\mathbf{u}}(t)).$$

4.2.2 The reduced FSI problem: variational formulation and dimensionless form

Let us start by considering the general case of a three-dimensional FSI model. The complete FSI problem consists in solving the fluid problem (4.28) in the domain Ω^f , with the boundary

condition of Eq. (4.28f) provided by the structural problem. In particular, we consider a clamped shell, i.e., by using the same notation introduced in Section (4.1.2), the portion of the boundary γ_0 in which essential boundary conditions are imposed for the structural problem coincide with $\gamma_0 \equiv \partial\omega$ and we denote by $\Gamma_0 := \psi(\gamma_0)$. In order to obtain a strongly coupled problem at the variational level, we consider the strong form of the fluid problem (4.28) and of the structural problem, see Remark 4.2, and we multiply Eq. (4.28a) and Eq. (4.28b), defining the fluid problem, and the governing equations the structural problem, by respectively the test functions $\boldsymbol{\varphi}$, ψ and $\boldsymbol{\zeta}$. According to the coupling condition of Eq. (4.29) we require that $\boldsymbol{\varphi}|_{\Gamma^w} = \boldsymbol{\zeta}$. We then integrate over the respective computational domains and apply the Green's formula to obtain the variational formulations of each problem. By means of the dynamic condition of Eq. (4.30) and the constrain on the test functions $\boldsymbol{\varphi}$ and $\boldsymbol{\zeta}$, we obtain the following equality:

$$-\int_{\Gamma^w} \mathbf{t}^f \cdot \boldsymbol{\varphi} \, d\Gamma = \int_{\omega} \mathbf{t}^s \cdot \boldsymbol{\zeta} \, J d\xi_1 d\xi_2. \quad (4.34)$$

Moreover, we impose the same spatial differentiability requirement for all the components of the functions belonging to the trial and test spaces relative to the unknown velocity field. Therefore, since we are using the complete linear Koiter shell model without neglecting the bending terms which involve fourth order derivatives, the trial and test function spaces will be defined by functions whose components are in the space $H^2(\Omega)$. In such a way, the embedding process of the structural problem into the fluid problem by means of Eq. (4.34) results in a generalized form of the Navier-Stokes equations in variational formulation, with trial and test function spaces defined by:

$$V_g = \left\{ \boldsymbol{\varphi} \in \left[H^2(\Omega^f) \right]^3 : \boldsymbol{\varphi}|_{\Gamma^{\text{in}}} = \mathbf{g}^{\text{in}}, \boldsymbol{\varphi}|_{\Gamma_0} = \mathbf{0} \text{ and } \frac{\partial \boldsymbol{\varphi}}{\partial n}|_{\Gamma_0} = \mathbf{0} \right\}, \quad (4.35a)$$

$$V = \left\{ \boldsymbol{\varphi} \in \left[H^2(\Omega^f) \right]^3 : \boldsymbol{\varphi}|_{\Gamma^{\text{in}}} = \mathbf{0}, \boldsymbol{\varphi}|_{\Gamma_0} = \mathbf{0} \text{ and } \frac{\partial \boldsymbol{\varphi}}{\partial n}|_{\Gamma_0} = \mathbf{0} \right\}, \quad (4.35b)$$

$$Q := L^2(\Omega^f). \quad (4.35c)$$

We now repeat these steps in the case of two-dimensional models whose computational domain is defined by an axial symmetric geometry. For the sake of illustration, we consider the case in which the geometry of the vessel is approximated by a cylinder, but the generalization to the case of Example 4.1 is straightforward.

Let us assume that the artery posses a cylindrical shape with length L and radius R and consider a section along a diameter. The computational domain, centered with respect to the axis of symmetry consists of a structure describing the deformable wall Ω^s which delimits the domain Ω^f where the fluid motion takes place. By assuming a thin wall approximation and identifying the middle surface Γ^s with the fluid interface, the corresponding domains in which the fluid problem and the structural problem reads: $\Omega^f := \{(x, y) : x \in (0, L) \text{ and } y \in (-R, R)\}$, whose boundary is $\partial\Omega^f = \Gamma^{\text{in}} \cup \Gamma^{\text{out}} \cup \Gamma^w$ with $\Gamma^{\text{in}} := \{0\} \times (-R, R)$, $\Gamma^{\text{out}} := \{L\} \times (-R, R)$, $\Gamma^w := [0, L] \times \{-R, R\}$, and $\Gamma^s := \{(x, y) : x \in (0, L) \text{ and } y \in \{-R, R\}\}$, with boundary $\Gamma^0 := \{(x, y) : x \in \{0, L\} \text{ and } y \in \{-R, R\}\}$.

Moreover, the computational domain Ω in which the reduced FSI problem is defined coincides with the fluid domain, i.e. $\Omega \equiv \Omega^f$. In the framework of the three-dimensional model, we derive the weak formulation of the fluid and structural problems imposing the higher spatial

differentiability requirement. In such a way, the fluid problem reads:

find, for all $t \in (0, T)$, $\mathbf{u}(t) \in V_g^f$ and $p(t) \in Q$ such that:

$$\left\{ \begin{array}{l} \int_{\Omega^f} \rho_f \frac{\partial \mathbf{u}(t)}{\partial t} \cdot \boldsymbol{\varphi} \, d\Omega + \int_{\Omega^f} \rho_f (\mathbf{u}(t) \cdot \nabla) \mathbf{u}(t) \cdot \boldsymbol{\varphi} \, d\Omega + \int_{\Omega^f} 2\mu_f D(\mathbf{u}(t)) : D(\boldsymbol{\varphi}) \, d\Omega \\ - \int_{\Omega^f} P(t) \nabla \cdot \boldsymbol{\varphi} \, d\Omega - \int_{\Omega^f} \mathbf{f} \cdot \boldsymbol{\varphi} \, d\Omega - \int_{\Gamma^{\text{out}}} \mathbf{h} \cdot \boldsymbol{\varphi} \, d\Gamma - \int_{\Gamma^{\text{w}}} \mathbf{t}^f \cdot \boldsymbol{\varphi} \, d\Gamma = 0 \quad \forall \boldsymbol{\varphi} \in V^f, \\ \int_{\Omega^f} (\nabla \cdot \mathbf{u}(t)) \psi \, d\Omega = 0 \end{array} \right. \quad \forall \psi \in Q, \quad (4.36a)$$

where the trial and test function spaces are defined as: $V_g^f := \left\{ \mathbf{v} \in [H^2(\Omega)]^2 : \mathbf{v}|_{\Gamma^{\text{in}}} = \mathbf{g}^{\text{in}} \right\}$, $V^f := \left\{ \boldsymbol{\varphi} \in [H^2(\Omega)]^2 : \boldsymbol{\varphi}|_{\Gamma^{\text{in}}} = \mathbf{0} \right\}$ and $Q := L^2(\Omega)$. The structural problem reads:

find, for all $t \in (0, T)$, $\boldsymbol{\eta}(t) \in V^s$ such that:

$$\begin{aligned} & h_s \rho_s \int_{\Gamma^s} \frac{\partial^2 \boldsymbol{\eta}(t)}{\partial t^2} \cdot \boldsymbol{\zeta} \, d\Gamma \\ & + h_s \int_{\Gamma^s} \left(\frac{E\nu}{1-\nu^2} \left(\eta'_x(t) + \frac{1}{R} \eta_y(t) \right) \left(\zeta'_x + \frac{1}{R} \zeta_y \right) + \frac{E}{1+\nu} \left(\eta'_x(t) \zeta'_x + \frac{1}{R^2} \eta_y(t) \zeta_y \right) \right) d\Gamma \\ & + \frac{h_s^3}{12} \int_{\Gamma^s} \left(\frac{E\nu}{1-\nu^2} \left(\eta''_y(t) - \frac{1}{R^2} \eta_y(t) \right) \left(\zeta''_y - \frac{1}{R^2} \zeta_y \right) + \frac{E}{1+\nu} \left(\eta''_y(t) \zeta''_y + \frac{1}{R^4} \eta_y(t) \zeta_y \right) \right) d\Gamma \\ & - \int_{\Gamma^s} \mathbf{t}^s \cdot \boldsymbol{\zeta} \, d\Gamma = 0 \end{aligned} \quad \forall \boldsymbol{\zeta} \in V^s,$$

where the function space V^s is given by: $V^s := \left\{ (\eta_x, \eta_y) \in H^2(\Gamma^s) : \eta_x|_{\gamma_0} = 0, \eta_y|_{\gamma_0} = 0 \text{ and } \eta'_y|_{\gamma_0} = 0 \right\}$ and we have denoted by means of the superscript $'$ the differentiation with respect to x .

By means of the the kinematic condition of Eq. (4.30) and the specific choice of the fluid-structure test functions, which satisfy $\boldsymbol{\varphi}|_{\Gamma^{\text{w}}} = \boldsymbol{\zeta}$, we obtain the relation:

$$- \int_{\Gamma^{\text{w}}} \mathbf{t}^f \cdot \boldsymbol{\varphi} \, d\Gamma = \int_{\Gamma^s} \mathbf{t}^s \cdot \boldsymbol{\zeta} \, d\Gamma. \quad (4.37)$$

Thus, by using the approximation \mathbf{d} of $\boldsymbol{\eta}$ and the kinematic coupling condition $\mathbf{u} = \frac{\partial \boldsymbol{\eta}}{\partial t}$ on $\Gamma^{\text{w}} \equiv \Gamma^s$ and defining the following trial and test spaces:

$$V_g = \left\{ \boldsymbol{\varphi} \in [H^2(\Omega)]^2 : \boldsymbol{\varphi}|_{\Gamma^{\text{in}}} = \mathbf{g}^{\text{in}}, \boldsymbol{\varphi}|_{\Gamma_0} = \mathbf{0} \text{ and } \partial_z \boldsymbol{\varphi}|_{\Gamma_0} = \mathbf{0} \right\}, \quad (4.38a)$$

$$V = \left\{ \boldsymbol{\varphi} \in [H^2(\Omega)]^2 \text{ such that } \boldsymbol{\varphi}|_{\Gamma^{\text{in}}} = \mathbf{0}, \boldsymbol{\varphi}|_{\Gamma_0} = \mathbf{0} \text{ and } \partial_z \boldsymbol{\varphi}|_{\Gamma_0} = \mathbf{0} \right\}, \quad (4.38b)$$

$$Q := L^2(\Omega^f). \quad (4.38c)$$

the reduced FSI problem in terms of the primitive variables (\mathbf{u}, P) of the fluid problem, reads:

find, for all $t \in (0, T)$, $\mathbf{u}(t) \in V_g$ and $P(t) \in Q$ such that:

$$\left\{ \begin{aligned} & \int_{\Omega_f} \rho_f \frac{\partial \mathbf{u}(t)}{\partial t} \cdot \boldsymbol{\varphi} \, d\Omega + \int_{\Omega_f} \rho_f (\mathbf{u}(t) \cdot \nabla) \mathbf{u}(t) \cdot \boldsymbol{\varphi} \, d\Omega + \int_{\Omega_f} 2\mu_f D(\mathbf{u}(t)) : D(\boldsymbol{\varphi}) \, d\Omega \\ & - \int_{\Omega_f} P(t) \nabla \cdot \boldsymbol{\varphi} \, d\Omega - \int_{\Omega_f} \mathbf{f} \cdot \boldsymbol{\varphi} \, d\Omega - \int_{\Gamma^{\text{out}}} \mathbf{h} \cdot \boldsymbol{\varphi} \, d\Gamma + h_s \rho_s \int_{\Gamma^{\text{w}}} \frac{\partial \mathbf{u}(t)}{\partial t} \cdot \boldsymbol{\varphi} \, d\Gamma \\ & + h_s \int_{\Gamma^{\text{w}}} \left(\frac{E\nu}{1-\nu^2} \left(d'_x(t) + \frac{1}{R} d_y(t) \right) \left(\varphi'_x + \frac{1}{R} \varphi_y \right) + \frac{E}{1+\nu} \left(d'_x(t) \varphi'_x + \frac{1}{R^2} d_y(t) \varphi_y \right) \right) d\Gamma \\ & + \frac{h_s^3}{12} \int_{\Gamma^{\text{w}}} \left(\frac{E\nu}{1-\nu^2} \left(d''_y(t) - \frac{1}{R^2} d_y(t) \right) \left(\varphi''_y - \frac{1}{R^2} \varphi_y \right) + \frac{E}{1+\nu} \left(d''_y(t) \varphi''_y + \frac{1}{R^4} d_y(t) \varphi_y \right) \right) d\Gamma \\ & = 0 \quad \forall \boldsymbol{\varphi} \in V, \\ & \int_{\Omega_f} (\nabla \cdot \mathbf{u}(t)) \psi \, d\Omega = 0 \quad \forall \psi \in Q, \quad (4.39b) \\ & \mathbf{u}(t=0) = \mathbf{u}_0 \quad \text{in } \Omega, \quad (4.39c) \\ & \boldsymbol{\eta}(t=0) = \boldsymbol{\eta}_0 \quad \text{on } \Gamma^{\text{w}}. \quad (4.39d) \end{aligned} \right. \quad (4.39a)$$

Remark 4.7. For the numerical simulations we will set $\mathbf{u}(t=0) = \mathbf{0}$ and $\boldsymbol{\eta}(t=0) = \mathbf{0}$, for which the considerations in Remark 3.1 still hold. Moreover, since we have expressed the reduced FSI problem (4.39) only in terms of \mathbf{u} and P by means of the approximation \mathbf{d} of $\boldsymbol{\eta}$, the initial condition (4.39d) is expressed in terms of $\boldsymbol{\eta}$, since initializes the approximation \mathbf{d} of $\boldsymbol{\eta}$.

We proceed by deriving the dimensionless form of the reduced FSI problem (4.39), starting from its variational formulation. The scaling factors for the variables of the problem (4.39) are chosen equal to the ones used to perform the derivation of the Navier-Stokes equations describing the blood flow for a rigid-wall model in dimensionless form, see Section 3.1.2. Specifically, we refer to Eqs. (3.10) and (3.11) to define the dimensionless variables and differential operators. In particular, we can observe that the function \mathbf{d} is dimensionally a length, since it is an approximation of the displacement field $\boldsymbol{\eta}$. This yields:

$$\begin{aligned} \mathbf{d}^* &= \frac{\mathbf{d}}{L_0} = \frac{1}{L_0} \left(L_0 \boldsymbol{\eta}_0^* + \Delta t^* T_0 V_0 \mathbf{u}_0^* + \frac{(\Delta t^*)^2 T_0^2}{2} \left[(1-2\beta) \frac{V_0^2}{L_0} \frac{\partial \mathbf{u}_0^*}{\partial t^*} + 2\beta \frac{V_0^2}{L_0} \frac{\partial \mathbf{u}^*}{\partial t^*} \right] \right) \\ &= \boldsymbol{\eta}_0^* + \Delta t^* \mathbf{u}_0^* + \frac{(\Delta t^*)^2}{2} \left[(1-2\beta) \frac{\partial \mathbf{u}_0^*}{\partial t^*} + 2\beta \frac{\partial \mathbf{u}^*}{\partial t^*} \right], \end{aligned} \quad (4.40)$$

where for the sake of simplicity, $\boldsymbol{\eta}_0^*$ indicates $\boldsymbol{\eta}_0^* := \boldsymbol{\eta}^*(t_0^*)$ and analogously for $\mathbf{u}_0^* := \mathbf{u}^*(t_0^*)$.

We rescale all the terms of Eq. (4.39) by the fluid density ρ_f , then we follow the same steps of Section 3.1.2 by substituting the dimensional quantities with their dimensionless counterpart. In such a way, the coefficients multiplying the integrals over Γ^{w} relative to the structural part of the problem, can be provided in their dimensionless form by means of the following expressions:

$$\rho_s^* := \frac{\rho_s}{\rho_f}, \quad h_s^* := \frac{h_s}{L_0}, \quad E^* := \frac{E}{\rho_f V_0^2}, \quad R^* = \frac{R}{L_0}. \quad (4.41)$$

In particular, we can observe that, in the specific case of constant radius, $R^* = 1/2$. Finally, we multiply all terms by the coefficient $\frac{1}{V_0^2 L_0}$ and we obtain the dimensionless form of the

reduced FSI problem in variational formulation defined in the dimensionless computational domain $\Omega^* := \Omega/L_0$. For the sake of simplicity, we will omit henceforth the superscript $*$ and we denote by V_g, V, Q the respective spaces in Eq. (4.38) of functions defined in dimensionless variables. Moreover, by denoting with p the rescaled dimensionless pressure, $\dot{\mathbf{u}} := \frac{\partial \mathbf{u}}{\partial t}$ the dimensionless acceleration field and \mathbf{f} the dimensionless source term relative to the fluid problem, the reduced FSI problem in residual form reads:

find, for all $t \in (0, T)$, $\mathbf{u}(t) \in V_g$ and $p(t) \in Q$ such that:

$$\begin{cases} \bar{B}_M(\boldsymbol{\varphi}; \dot{\mathbf{u}}(t), \mathbf{u}(t), p(t)) = 0 & \forall \boldsymbol{\varphi} \in V, \\ \bar{B}_C(\psi; \dot{\mathbf{u}}(t), \mathbf{u}(t), p(t)) = 0 & \forall \psi \in Q, \\ \mathbf{u}(t=0) = \mathbf{u}_0 & \text{in } \Omega, \\ \boldsymbol{\eta}(t=0) = \boldsymbol{\eta}_0 & \text{in } \Omega. \end{cases} \quad \begin{aligned} (4.42a) \\ (4.42b) \\ (4.42c) \\ (4.42d) \end{aligned}$$

where the residuals of the momentum and continuity equations of the generalized Navier-Stokes equations (4.42) are given respectively, by:

$$\begin{aligned} \bar{B}_M(\boldsymbol{\varphi}; \dot{\mathbf{u}}, \mathbf{u}, p) := & m(\dot{\mathbf{u}}, \boldsymbol{\varphi}) + a(\mathbf{u}, \boldsymbol{\varphi}) + c(\mathbf{u}, \mathbf{u}, \boldsymbol{\varphi}) + b(\boldsymbol{\varphi}, p) - F(\boldsymbol{\varphi}) - H(\boldsymbol{\varphi}) \\ & + m_s(\dot{\mathbf{u}}, \boldsymbol{\varphi}) + H_s^{\text{mem}}(\mathbf{u}, \boldsymbol{\varphi}) + H_s^{\text{ben}}(\mathbf{u}, \boldsymbol{\varphi}) \end{aligned} \quad (4.43a)$$

$$\bar{B}_C(\psi; \dot{\mathbf{u}}, \mathbf{u}, p) := b(\mathbf{u}, \psi), \quad (4.43b)$$

with the forms and functionals relative to the fluid part of the reduced FSI problem defined as in Section 3.1.3, for which we briefly recall that the bilinear forms are given by $m(\dot{\mathbf{u}}, \boldsymbol{\varphi}) := \int_{\Omega} \dot{\mathbf{u}} \cdot \boldsymbol{\varphi} \, d\Omega$, $a(\mathbf{u}, \boldsymbol{\varphi}) := \frac{2}{\text{Re}} \int_{\Omega} D(\mathbf{u}) : D(\boldsymbol{\varphi}) \, d\Omega$ and $b(\boldsymbol{\varphi}, p) := - \int_{\Omega} p \nabla \cdot \boldsymbol{\varphi} \, d\Omega$; while the form $c(\cdot, \cdot, \cdot)$ is given by $c(\mathbf{v}, \mathbf{u}, \boldsymbol{\varphi}) = \int_{\Omega} (\mathbf{v} \cdot \nabla) \mathbf{u} \cdot \boldsymbol{\varphi} \, d\Omega$ and the functionals are $F(\boldsymbol{\varphi}) := \int_{\Omega} \mathbf{f} \cdot \boldsymbol{\varphi} \, d\Omega$ and $H(\boldsymbol{\varphi}) := \int_{\Gamma_N} \mathbf{h} \cdot \boldsymbol{\varphi} \, d\Gamma$. Moreover, we have introduced the bilinear form:

$$m_s(\dot{\mathbf{u}}, \boldsymbol{\varphi}) := h_s \rho_s \int_{\Gamma^W} \dot{\mathbf{u}} \cdot \boldsymbol{\varphi} \, d\Gamma, \quad (4.44a)$$

$$H_s^{\text{mem}}(\mathbf{u}, \boldsymbol{\varphi}) := h_s \int_{\Gamma^W} \left(\frac{E\nu}{1-\nu^2} (d'_x + 2d_y) (\varphi'_x + 2\varphi_y) + \frac{E}{1+\nu} (d'_x \varphi'_x + 4d_y \varphi_y) \right) d\Gamma, \quad (4.44b)$$

$$H_s^{\text{ben}}(\mathbf{u}, \boldsymbol{\varphi}) := \frac{h_s^3}{12} \int_{\Gamma^W} \left(\frac{E\nu}{1-\nu^2} (d''_y - 4d_y) (\varphi''_y - 4\varphi_y) + \frac{E}{1+\nu} (d''_y \varphi''_y + 16d_y \varphi_y) \right) d\Gamma, \quad (4.44c)$$

where Eq. (4.44a) denote the added mass effect due to the structural part; whereas Eqs. (4.44b) refer to the membrane and bending terms of the structural equations embedded as boundary data.

Remark 4.8. *If we compare the variational formulation of the Navier-Stokes equations (3.17) describing the blood flow and of the generalized Navier-Stokes equations (4.43) derived from the strong coupling between the fluid and structure problems, we observe that the main difference relies on the definition of the trial and test function spaces, respectively in Eq. (3.15) and Eq. (4.38), other than the presence of the generalized boundary conditions on Γ^W . We underline that the higher differentiability requirement is due to the choice on the structural model;*

however it is possible to adopt different models which does not require this level of regularity; see for instance [FVCJT06, NV09].

4.2.3 Numerical approximation: IGA and generalized- α method

Since the reduced FSI problem (4.43) is formulated as a generalized Navier-Stokes equations in the unknowns \mathbf{u} and p , in order to perform its numerical approximation we can use the same methods adopted for the fluid problem in a rigid wall model illustrated in Section 3.3. In particular, the semi-discretized formulation in space is based on the Galerkin method in the framework of NURBS-based IGA, as explained in Section 3.3.1. We consider the stabilization based on the variational multiscale method for large eddy simulation (VMS-LES) of [BCC⁺07] and described in Section 3.3.2. We observe that the stabilization considered is not affected by the boundary terms appearing in the generalized Navier-Stokes equations. In such a way, the semi-discretized problem reads as in Eq. (3.48), where the finite dimensional subspaces $V_g^h \subseteq V_g$, $V^h \subseteq V$ and $Q^h \subseteq Q$ of the respective trial and test spaces of Eq. (4.38), are defined as subspaces of the space \mathcal{V}^h of NURBS on the computational domain Ω , as previously. Moreover, considering the spatial differentiability requirements on the spaces V_g and V of Eq. (4.38), the numerical approximation by means of IGA allows to use a standard Galerkin formulation for the semi-discretization in space of the high order derivatives involved in the generalized boundary condition introduced by the coupling (see Remark 1.12). It is sufficient to require that the *NURBS* basis functions defining \mathcal{V}^h are, at least, globally \mathcal{C}^1 -continuous in Ω .

The time integration scheme used is the generalized- α method and the choice to formulate the reduced FSI problem (4.43) in the unknowns (\mathbf{u}, p) , allows to use the standard generalized- α method of Section 3.3.3. We highlight that the same strategies described in Remark 3.19 are adopted to simplify the implementation. In addition, we implement the resistance boundary condition in an explicit way. This choice does not lead to a degradation on the global accuracy, as we will see in Section 4.3 when comparing the results for the implicit or explicit implementation of this term.

4.3 Numerical results

In this section we presents some numerical results for the reduced FSI method solved by means of IGA in a two-dimensional cylindrical geometry. Firstly, we compare the results obtained with the rigid-wall and the reduced FSI model. Then, we analyze the behavior of the reduced model for different values of the parameters considered. In particular, we compare the solutions obtained for the same material property when changing the value of the resistance constant C_{out} , relative to the resistance boundary condition (see Section 3.2.2); then, we consider a case of different elastic response of the wall, supposed to be less rigid. Finally, we analyze the contribution of the longitudinal displacement by comparing the model with the linear elastic Koiter shell model with only radial displacement (4.27).

All the numerical simulations are performed by using a mesh of $N_{el} = 160 \times 16$ elements for a dimensional time step $\Delta t = 3.875 \cdot 10^{-4} s$. The geometry is represented by NURBS basis functions of degree $p = 2$, in such a way that they are globally \mathcal{C}^1 -continuous, as required by the reduced FSI model.

The values reported in Table 4.1 are used in the simulation of a reference configuration and correspond to physiological values for a common carotid artery section; we refer e.g.

Table 4.1: Fluid and structural physical and geometrical parameters for the axisymmetric cylindrical artery.

Parameter	Value	Parameter	Value
Length	$L = 12cm$	Radius	$R_0 = 0.3cm$
Maximum flow rate(inlet BC)	$Q_{MAX}^{in} = 13.7cm^3/s$	Resistance constant	$C_{out} = 5300dyn \cdot s/cm^5$
Fluid density	$\rho_f = 1.055g/cm^3$	Fluid dynamic viscosity	$\mu_f = 0.04cm^2/s$
Wall thickness	$h_s = 0.06cm$	Wall density	$\rho_s = 1.055g/cm^3$
Young's Modulus	$E = 4 \cdot 10^6 dyn/cm^2$	Poisson ratio	$\nu = 0.5$

to [BvG⁺12] and [FVCJT06, BGH⁺09]. In particular, the elastic characteristics of the vessel walls are described by the Poisson ratio $\nu = 0.5$ and the Young's modulus $E = 4 \cdot 10^6 dyn/cm^2$. Moreover, the resulting Reynolds Number is $\mathbb{Re} = 1534$. Each simulation is performed for a period corresponding to three heartbeats ($3T_{HB}$, with $T_{HB} = 1.1s$) and the results reported refer to the last heartbeat. If not otherwise specified, we sample the data shown in two sections, which we will denote by S_1 and S_2 , located respectively at $d_1 = 0.9cm$ and $d_2 = 11.1cm$ from the inlet.

4.3.1 A comparison between rigid wall and reduced FSI models

We study the results obtained by using a rigid wall model and the reduced FSI model described in Section 4.2. The main quantities which highlight the differences between the choice of one model instead of the other are the pressure and the flow. We analyze them in Figure 4.2.

The pressure curves refer to the middle point of section S_1 and S_2 , respectively, and we can observe that the ones referring to the rigid wall model present an higher peak pressure value especially in proximity of the inlet section. Moreover, the absolute minimum and maximum values of the pressure assumed all along the vessel section and for all the heartbeat period yield an higher pressure drop for a rigid wall model, as reported in literature [FVCJT06] and experienced in physiological flow with stiffer vessels. As for the flow curves, as expected, by the inlet condition prescribed (see Section 3.2.1) the two curves overlap in the section S_1 closest to the inlet. The differences are noticeable when considering the flow in the section S_2 , proximal to the outlet. The curve relative to the rigid wall model overlaps the profiles of section S_1 as it is expected for an incompressible fluid in a rigid domain [FVCJT06], while the one relative to the reduced FSI model shows a modest phase lag between sections S_1 and S_2 . Lastly, an additional term of comparison are the streamlines for the solutions of the two models. We have selected an instant at the beginning of the heartbeat in order to show the different behavior of the streamlines in a section at the middle off the geometry considered. It is noticeable in Figure 4.3 that, while in the case of rigid wall, the streamlines does not show any curvature and appear to be exactly parallel to the wall, the streamlines of the solution of the reduced FSI problem show a different pattern due to the interaction of the fluid with the wall.

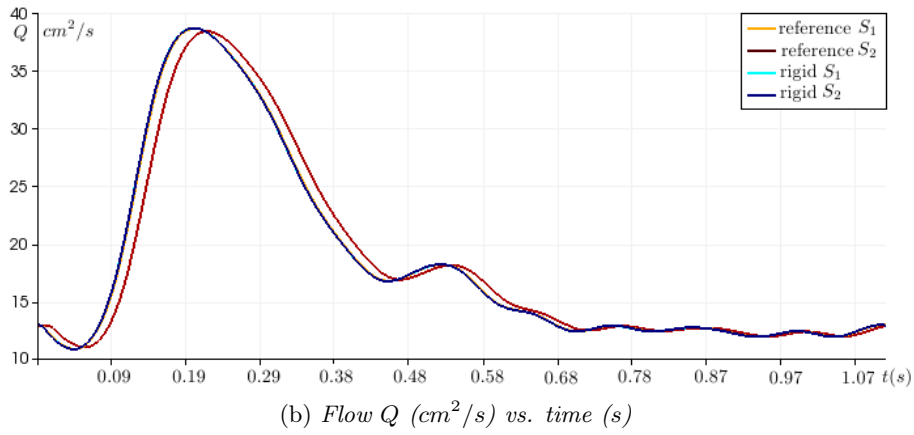
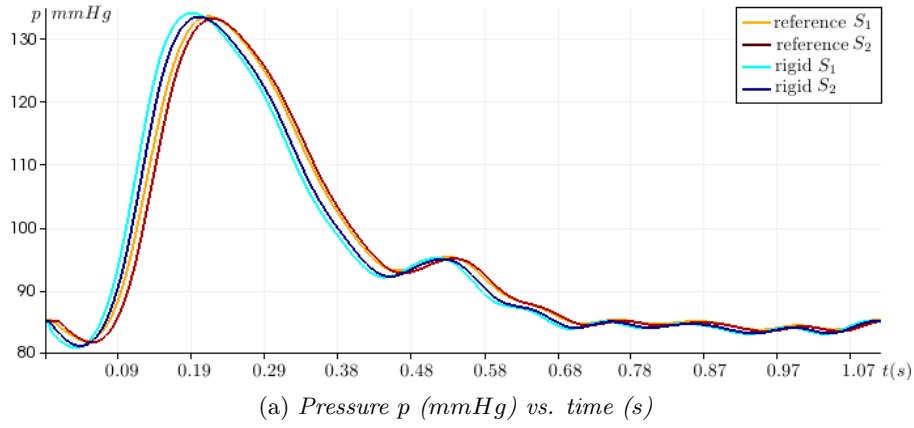
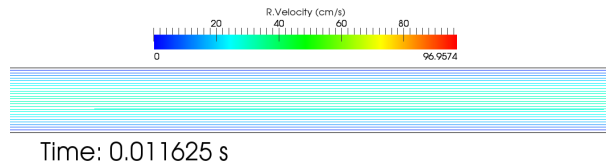
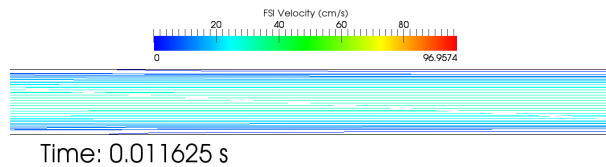


Figure 4.2: Comparison between rigid (blue colors) and reduced FSI (red colors) models: pressure and flow vs. time, respectively in a middle point of sections S_1 and S_2 and in through sections S_1 (clear) and S_2 (dark). In legend, *reference* and *rigid* refer respectively to the rigid model and to the reduced FSI model.



(a) Streamlines for the rigid model.



(b) Streamlines for the reduced FSI model.

Figure 4.3: Comparison between rigid and reduced FSI models: streamlines at $t = 0.0116$ in a region distal 7cm from the inlet interface.

4.3.2 The reference configuration

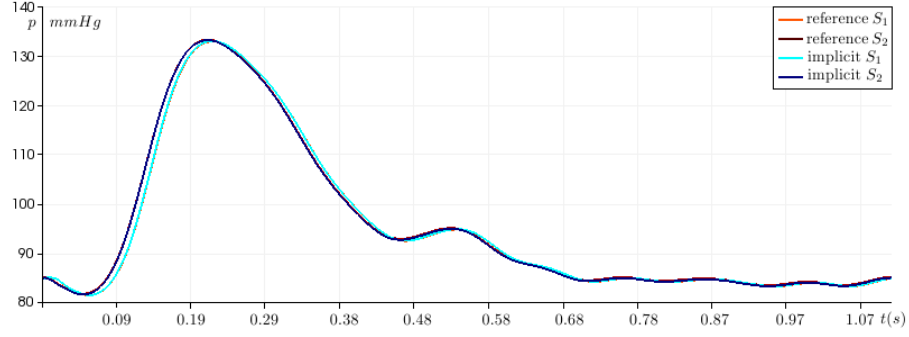
In this section we discuss the numerical results obtained with the reduced FSI model for the geometrical and physical data collected in Table 4.1.

We first consider in Figure 4.4 the pressure and flow curves in sections S_1 and S_2 . We can observe that in both the graphs there is a complete overlapping between the solutions obtained by implementing the resistance condition explicitly or implicitly. By implementing the resistance condition in an explicit way, the contribution of the discretized terms relative to this boundary condition enters the tangent system of the generalized-*alpha* method only in the residual vectors. Contrary, in the case in which we consider an implicit scheme, we have to add to the tangent matrix complicated terms or to resort to an inexact form of the tangent system (limited to the contribute on Γ^{out}). Since we obtained weak differences between the two strategies, we have chosen to implement it in a explicit way. The profile relative to the pressure wave can be compared with the one reported in [BvG⁺12] which corresponds to a physiological pressure curve.

As for the flow, we can see a phase lag between the one relative to the section S_1 in proximity of the inlet boundary and to the section S_2 in proximity of the outlet. Moreover in Figure 4.4 we show the displacement of the wall relative to the considered sections. In cyan we plot the displacement of the top wall relative to S_1 during the complete heartbeat period, while in green the one relative to S_2 . Once more we can observe a complete overlapping between the solutions obtained with an implicit or explicit method. The complete analysis of the solution relative to the displacement field during an heartbeat period is performed in Figure 4.5, considering both for the components of the displacement and the total displacement, the relative displacement with respect to the values at the beginning of the heartbeat, i.e $\boldsymbol{\eta} - \boldsymbol{\eta}(t = 0)$. We consider the displacement relative to three points of the wall located respectively at the top wall of sections S_1 , S_2 and of a section located at the middle of the vessel. We can see that the longitudinal displacement computed by means of the linear Koiter shell model show a behavior different from the one of the work [BvG⁺12] in which are considered also viscoelastic effects, but not the bending terms. In particular, considering the mid point of the arterial vessel the shape is nearly the same, but we obtain a minimum which is much more higher than the one provided by [BvG⁺12], where $\min_{t \in (0, T_{\text{HB}})} \eta_x \approx -0.1 \text{mm}$ while in our case $\min_{t \in (0, T_{\text{HB}})} \eta_x \approx -0.045 \text{mm}$. Nevertheless, the total longitudinal displacement that we obtain ($\max_{t \in (0, T_{\text{HB}})} \eta_x(t) - \min_{t \in (0, T_{\text{HB}})} \eta_x(t) = 0.07 \text{mm}$) is included in the range of values obtained by experimental studies, as reported in [BvG⁺12]. We can observe in Figure 4.5c that the contribution to the total displacement is determined in large part by the radial displacement; we will discuss later the choice of a linear Koiter shell model considering only the radial displacement in Section 4.3.4.

In Figures 4.6, 4.7, 4.8 we collect the solutions obtained at different times during the heartbeat period, in particular, we refer to $t = 0.0116 \text{s}$, in which the wall velocity reaches its maximum value, to the time corresponding to the peak systole and finally to the mid-diastolic phase. For all of them we sample the pressure along the centerline, the longitudinal and radial displacements of the upper wall boundary and the spatial distribution for the fluid and wall velocities. In particular, in order to highlight the behavior of the wall velocity we have represented it by means of arrays. We can observe that the maximum value of the wall velocity during the total heartbeat period is not attained at the peak systole, but rather at $t = 0.0116 \text{s}$, more over, it does not determine the maximum displacement of the wall. We

obtain the maximum displacement at the time corresponding to the peak systole in which the direction of the wall velocity vectors is normal to the wall. By means of the approximation formula (4.31), for which we consider a default value of $\beta = 1.0$, it results that the contribution of the acceleration term is not negligible. When considering the profiles of each component of the displacement, we can see that their shape does not undergo noticeable changes at all the times considered, but their mean absolute values is sensibly different during the peak systole. The presence of the boundary layers for the radial displacement close to the inlet and outlet sections is explained by the use of homogeneous essential boundary conditions for the wall model, we refer to [BvG⁺12] for more details. In particular, the oscillations that normally would appear are reduced by the bending terms involved in the model.



(a) Pressure (mmHg) vs. time (s)

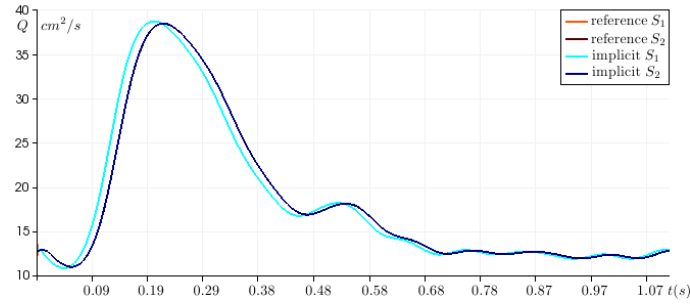
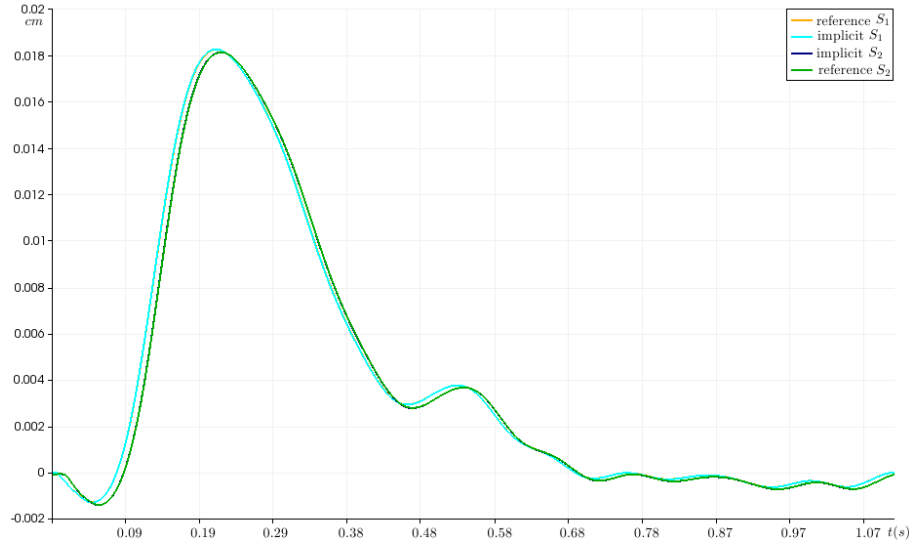
(b) Flow Q (cm^2/s) vs. time (s)(c) Displacement magnitude $\eta - \eta(t=0)$ (cm) vs. time (s)

Figure 4.4: Comparison between implicit (blue colors) and explicit (red colors) schemes for the resistance condition: pressure, flow and total displacement vs. time, at sections S_1 (clear) and S_2 (dark).

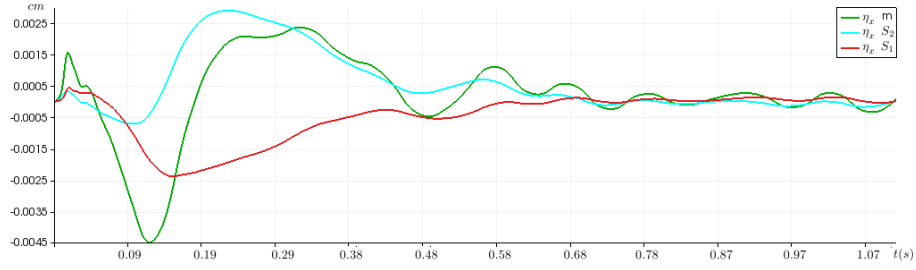
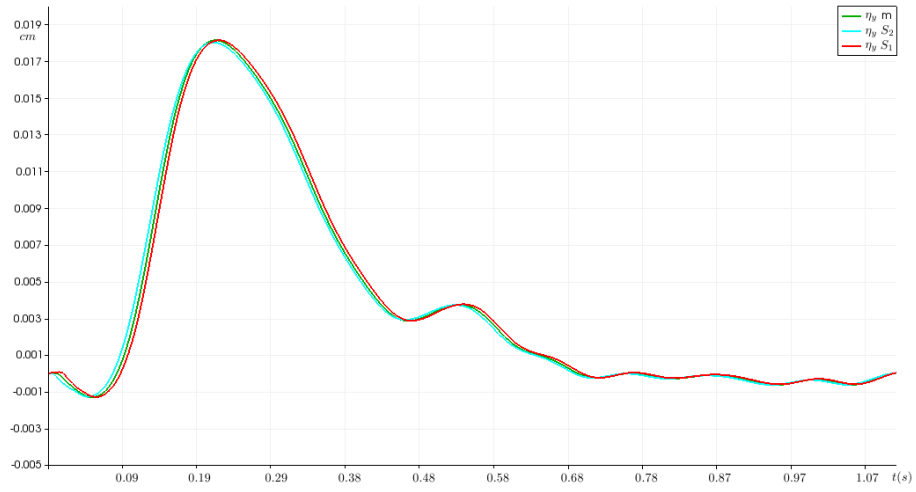
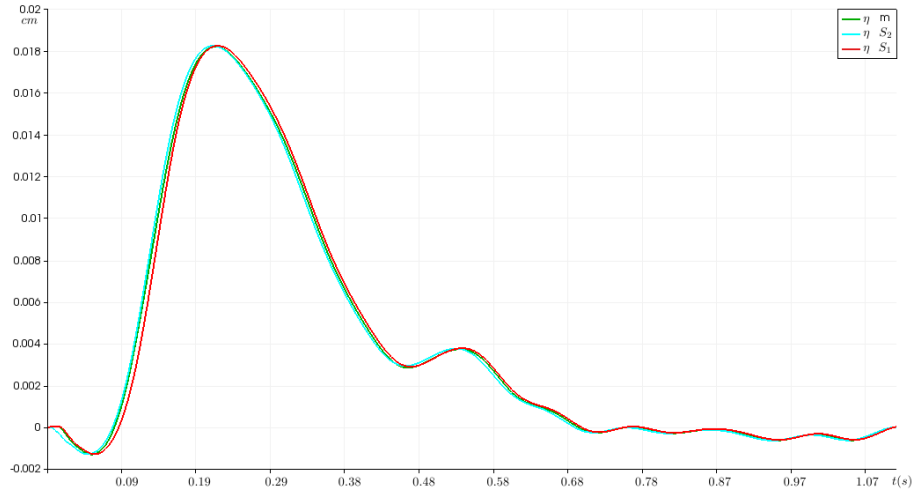
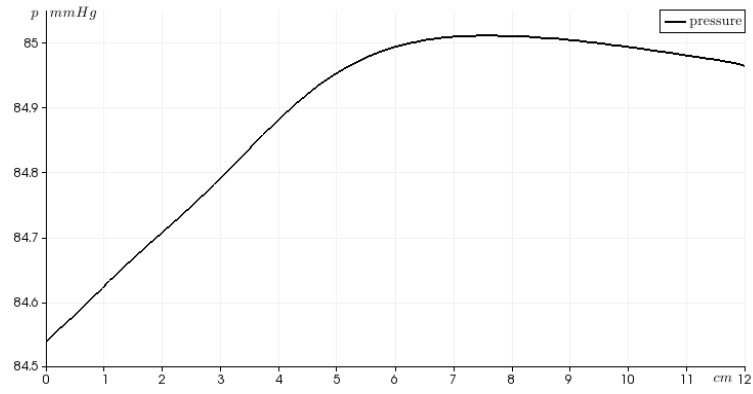
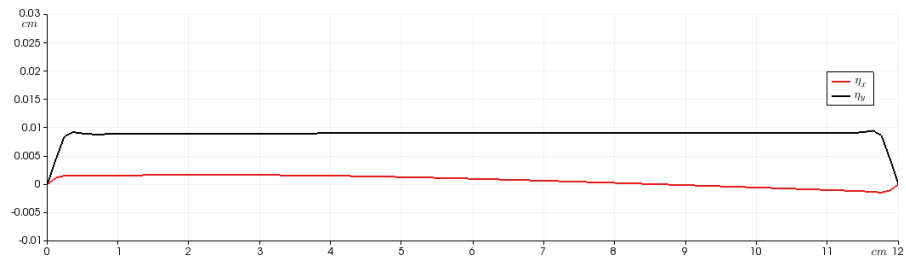
(a) Longitudinal displacement $\eta_x - \eta_x(t=0)$ (cm) vs. time (s)(b) Radial displacement $\eta_y - \eta_y(t=0)$ (cm) vs. time (s)(c) Displacement magnitude $\eta - \eta(t=0)$ (cm) vs. time (s)

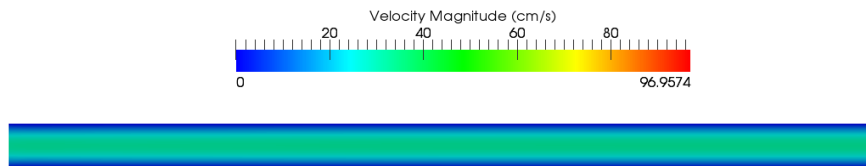
Figure 4.5: Analysis of the displacement field during an heartbeat period for the reference configuration at the sections S_1 (red), S_2 (cyan) and at a section distal 10cm from the inlet interface (green).



(a) Pressure (mmHg) vs. longitudinal coordinate (cm), along the centerline

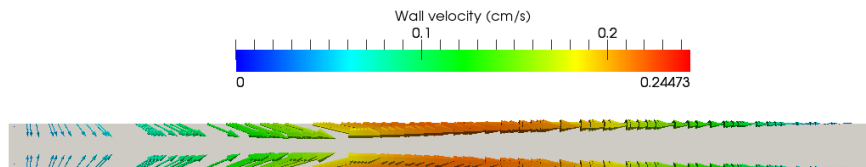


(b) Components displacement η_x (red) and η_y (black) vs. longitudinal coordinate (cm)



Time: 0.011625 s

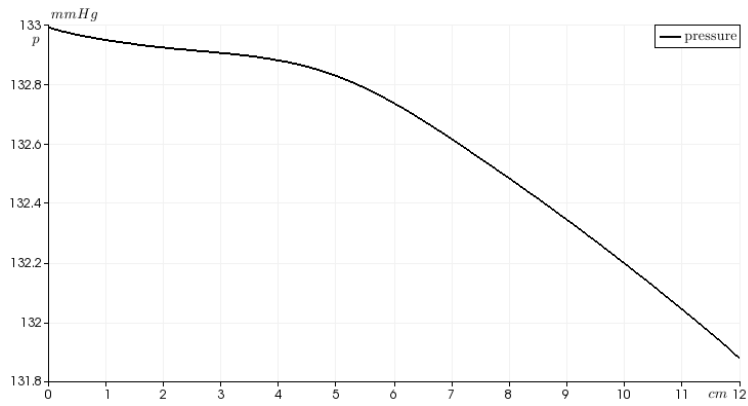
(c) Fluid velocity magnitude (cm/s)



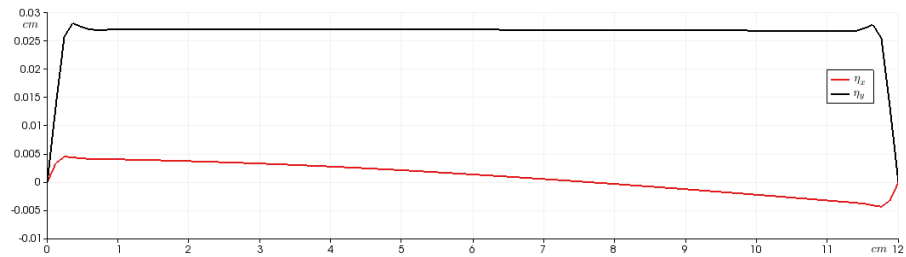
Time: 0.011625 s

(d) Wall velocity (cm/s)

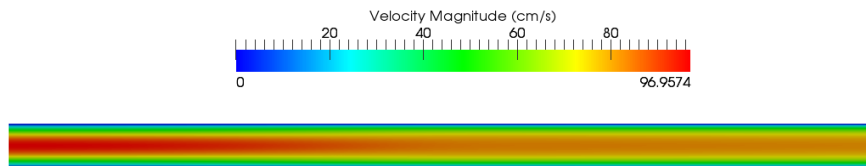
Figure 4.6: Solutions for the reference configuration at time $t = 0.011625$.



(a) Pressure (mmHg) vs. longitudinal coordinate (cm), along the centerline

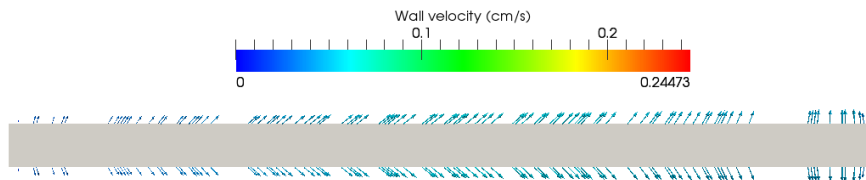


(b) Components displacement η_x (red) and η_y (black) vs. longitudinal coordinate (cm)



Time: 0.203437 s

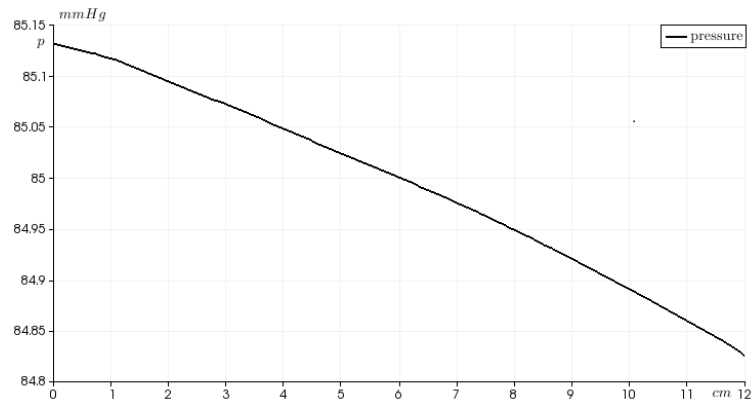
(c) Fluid velocity magnitude (cm/s)



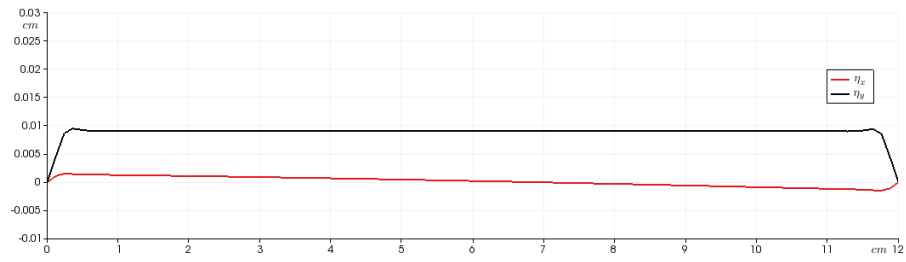
Time: 0.203437 s

(d) Wall velocity (cm/s)

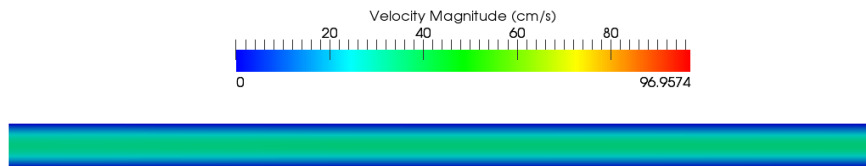
Figure 4.7: Solutions for the reference configuration at the peak systole.



(a) Pressure (mmHg) vs. longitudinal coordinate (cm), along the centerline

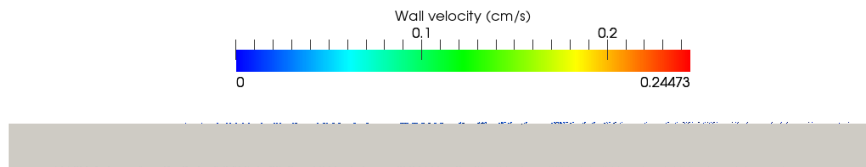


(b) Components displacement η_x (red) and η_y (black) vs. longitudinal coordinate (cm)



Time: 0.751750 s

(c) Fluid velocity magnitude (cm/s)



Time: 0.751750 s

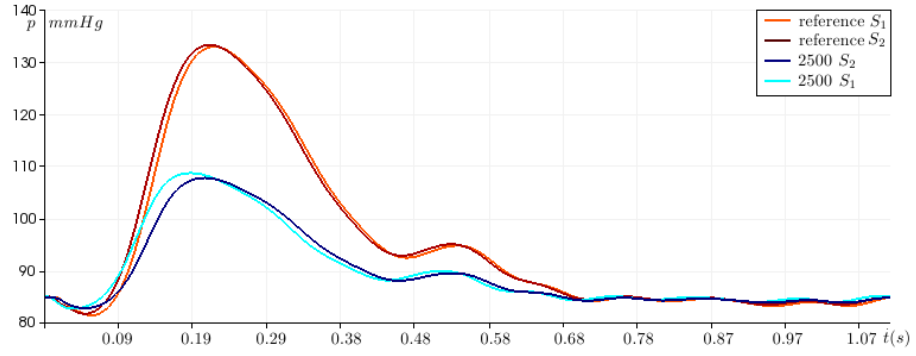
(d) Wall velocity (cm/s)

Figure 4.8: Solutions for the reference configuration in the mean diastolic phase.

4.3.3 A comparison between different parameters

In this section we study the sensibility of the model to some of the parameters used in the simulations. Firstly, we address the choice of the resistance boundary condition (Section 3.2.2). As reference value we set $C_{\text{out}} = 5300 \text{ dyn} \cdot \text{s/cm}^5$ and we compare the solutions with values $C_{\text{out}} = 2500 \text{ dyn} \cdot \text{s/cm}^5$ in Figure 4.9 and $C_{\text{out}} = 10000 \text{ dyn} \cdot \text{s/cm}^5$ in Figure 4.10. In both the cases we consider the pressure and flow curves and the total displacement in the sections S_1 and S_2 . We analyze the flow rate, for which we can observe that there are not significant differences, apart from the increase in the phase lag according to the use of an higher parameter for the resistance constant. The differences are more discernible when considering the plots of the pressure and the total displacement, for which we can observe significant differences with respect to the case $C_{\text{out}} = 5300 \text{ dyn} \cdot \text{s/cm}^5$ responding to physiological data. Nevertheless, as expected an higher value for the resistance condition yield a reduction of the spurious reflection at the outlet. Furthermore, the pressure drop ($p_{\text{max}} - p_{\text{min}}$) is higher with higher values of C_{out} . The total displacement is quite unrealistic for the value $C_{\text{out}} = 10000 \text{ dyn} \cdot \text{s/cm}^5$, since it corresponds to a 17% of the radius, while for $C_{\text{out}} = 5300 \text{ dyn} \cdot \text{s/cm}^5$ we obtain the physiological value of the 9.6% of the radius, lastly in the case of $C_{\text{out}} = 2500 \text{ dyn} \cdot \text{s/cm}^5$ we have a total displacement equal to 4.67% of the radius.

As expected, the model is also sensible to the values for the Young's modulus. In particular, we compare the solution obtained with the reference configuration with the one in which the wall is considered less rigid. In particular, we set the value of the Young's modulus $E = 2 \cdot 10^6 \text{ dyn/cm}^2$ as in [BvG⁺12]. This value is close to the physiological one, but we notice in Figure 4.11 the sensitivity of the model to the elastic behavior of the wall, which in this case shows a total displacement of the 18.5% of the radius compared with the 9.6% previously considered. Moreover, noticeable differences are shown in the flow curves in Figure 4.11b where, as expected, it is highlighted the increase in the phase lag in case of lower Young's modulus.



(a) Pressure (mmHg) vs. time (s)

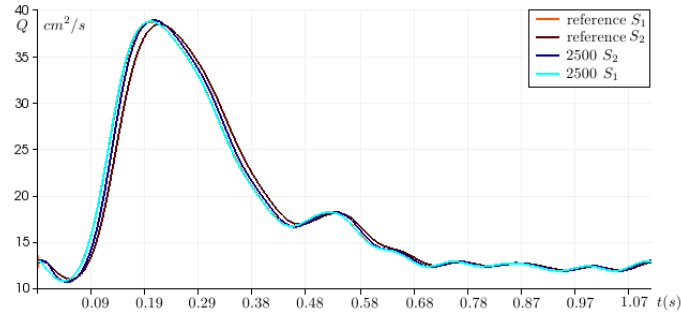
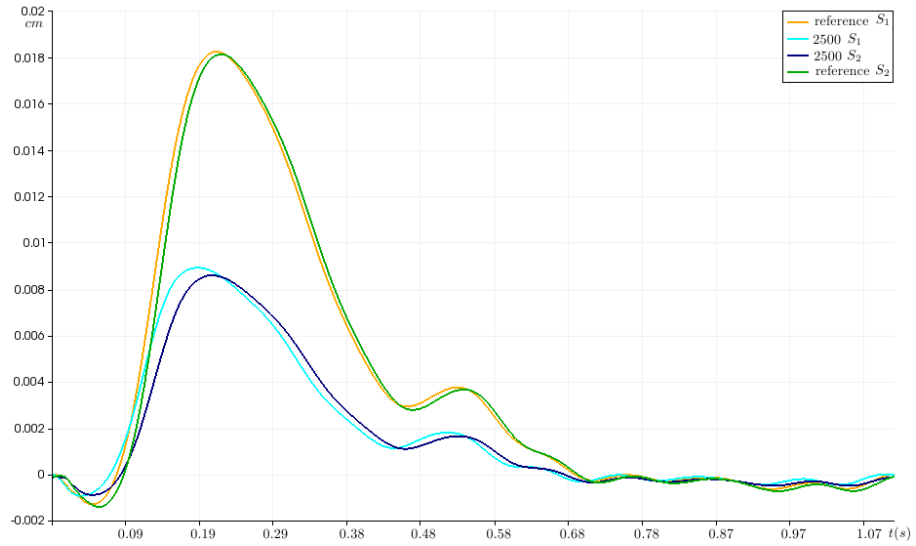
(b) Flow Q (cm^2/s) vs. time (s)(c) Displacement magnitude $\eta - \eta(t = 0)$ (cm) vs. time (s)

Figure 4.9: Comparison between $C_{\text{out}} = 5300 \text{ dyn} \cdot \text{s}/\text{cm}^5$ (red colors) and $C_{\text{out}} = 2500 \text{ dyn} \cdot \text{s}/\text{cm}^5$ (blue colors): pressure and flow vs. time, respectively in a middle point of sections S_1 and S_2 and in through sections S_1 (clear) and S_2 (dark). Total displacement magnitude at the sections S_1 and S_2 . In legend, *reference* and *2500* refer respectively to $C_{\text{out}} = 5300 \text{ dyn} \cdot \text{s}/\text{cm}^5$ and $C_{\text{out}} = 2500 \text{ dyn} \cdot \text{s}/\text{cm}^5$.

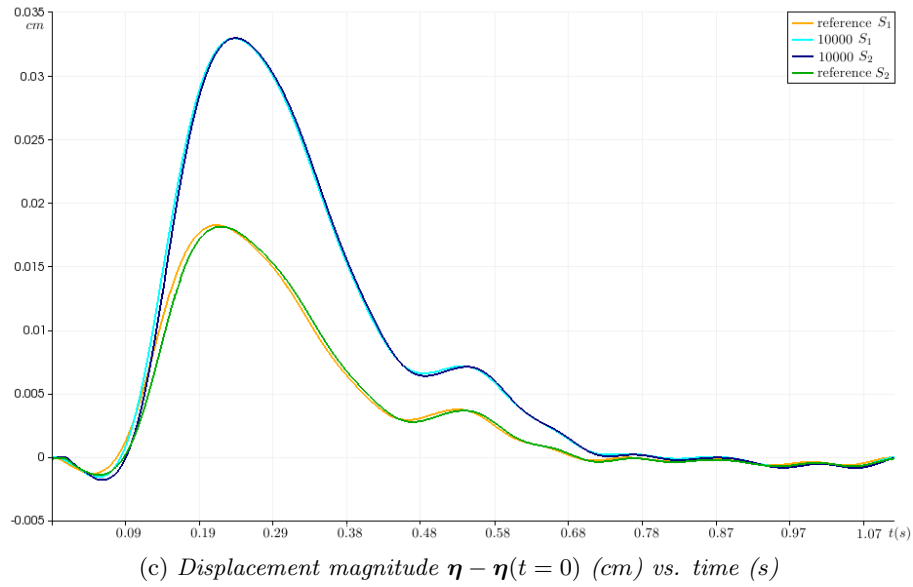
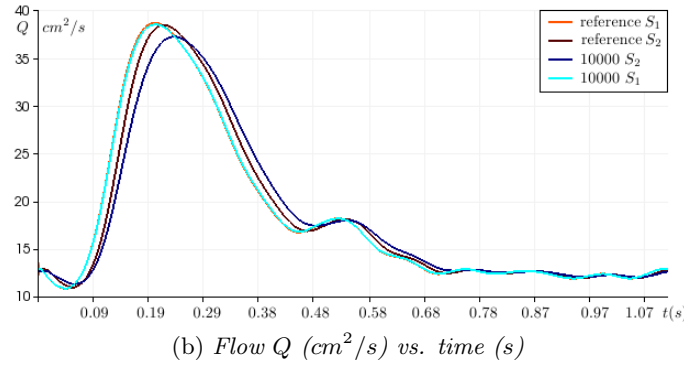
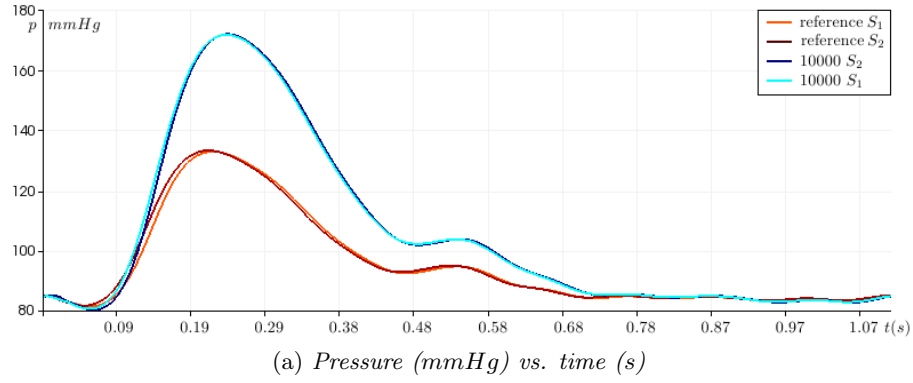


Figure 4.10: Comparison between $C_{\text{out}} = 5300 \text{ dyn} \cdot \text{s}/\text{cm}^5$ (red colors) and $C_{\text{out}} = 10000 \text{ dyn} \cdot \text{s}/\text{cm}^5$ (blue colors): pressure and flow vs. time, respectively in a middle point of sections S_1 and S_2 and in through sections S_1 (clear) and S_2 (dark). Total displacement magnitude at the sections S_1 and S_2 . In legend, *reference* and *10000* refer respectively to $C_{\text{out}} = 5300 \text{ dyn} \cdot \text{s}/\text{cm}^5$ and $C_{\text{out}} = 10000 \text{ dyn} \cdot \text{s}/\text{cm}^5$.

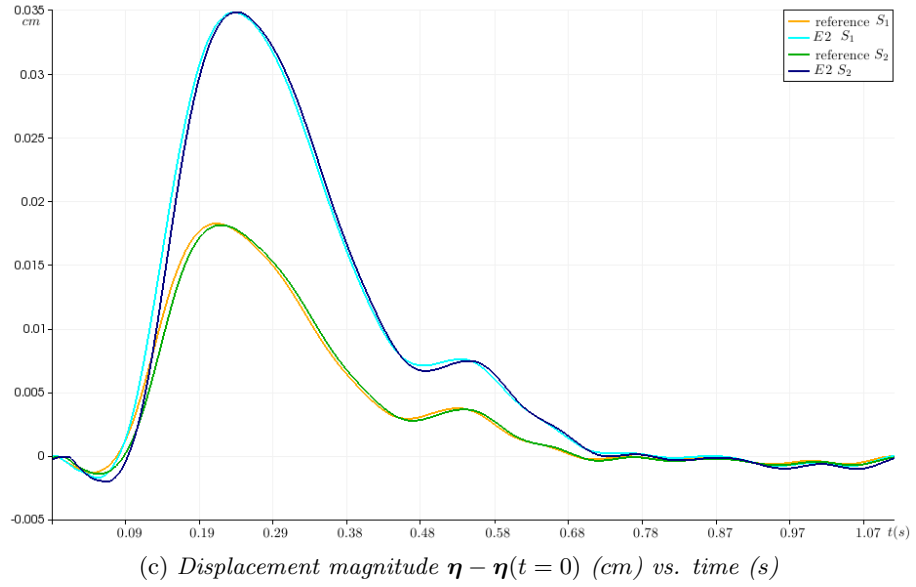
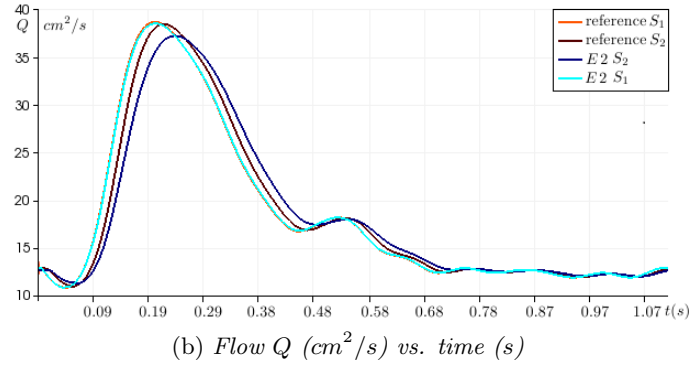
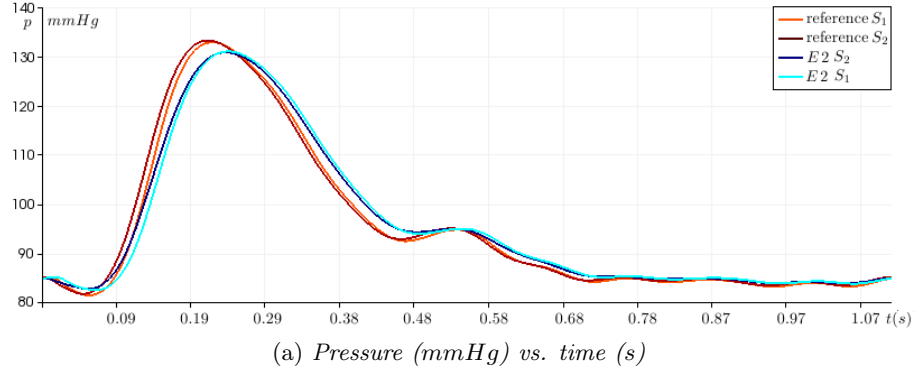


Figure 4.11: Comparison between $E = 4 \cdot 10^6 \text{ dyn/cm}^2$ (red colors) and $E = 2 \cdot 10^6 \text{ dyn/cm}^2$ (blue colors): pressure and flow vs. time, respectively in a middle point of sections S_1 and S_2 and in through sections S_1 (clear) and S_2 (dark). Total displacement magnitude at the sections S_1 and S_2 . In legend, *reference* and *E2* refer respectively to $E = 4 \cdot 10^6 \text{ dyn/cm}^2$ and $E = 2 \cdot 10^6 \text{ dyn/cm}^2$.

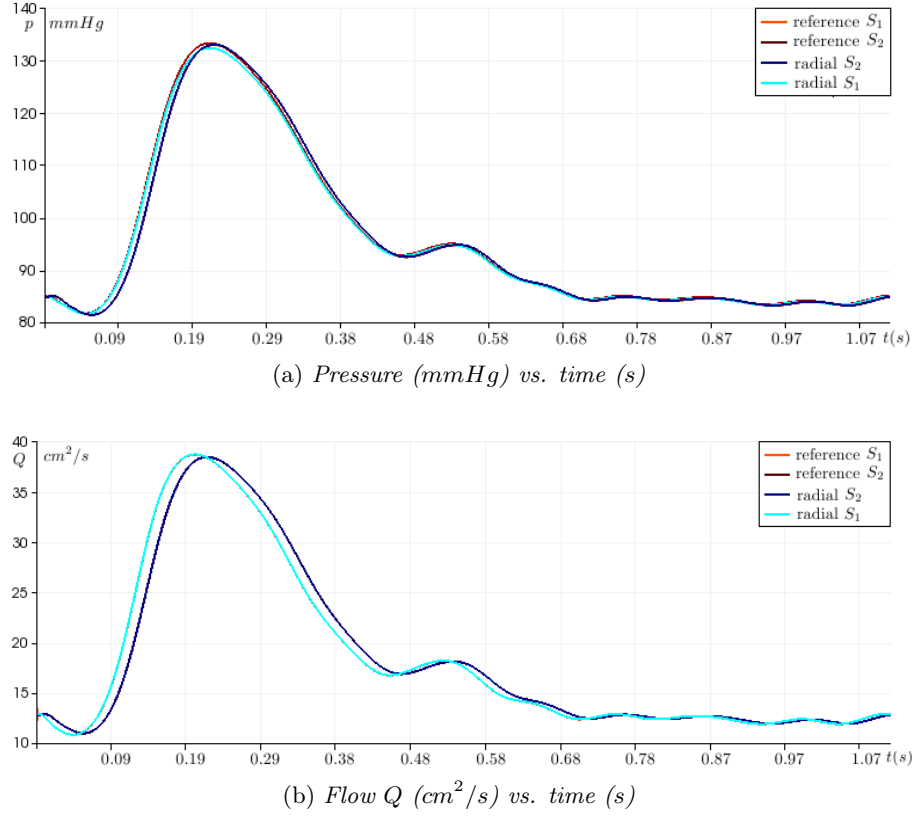


Figure 4.12: Comparison between simplified linear Koiter shell model (blue colors) with respect to the full model (red colors): pressure and flow vs. time, respectively in a middle point of sections S_1 and S_2 and in through sections S_1 (clear) and S_2 (dark). In legend, *reference* and *radial* refer respectively to the full model and to the simplified model (radial displacement).

4.3.4 Numerical simulation with the linear Koiter shell model with radial displacement

We consider the simplified linear Koiter shell model of Eq. (4.27) with respect to the full model of Eq. (4.24), as it is described in Example 4.3. In particular, for the simplified model this case we assume that the structure deforms only in the normal direction to the middle surface, i.e. we report only radial displacement. The relative contribution of the longitudinal displacement leads to minimal differences between the two models. In particular, in Figure 4.12 we report the pressure and flow plots vs. time in sections S_1 and S_2 , which shows good agreement between the two models. Moreover, in Figure 4.13 we analyze both the total displacement for each section S_1 and S_2 and the components of the relative displacement in section S_1 where we can observe that there is a minimal difference (2% of the total displacement for the full model). This results shows and justifies the fact that in vascular dynamics is widely accepted the assumption of main radial displacement of the wall.

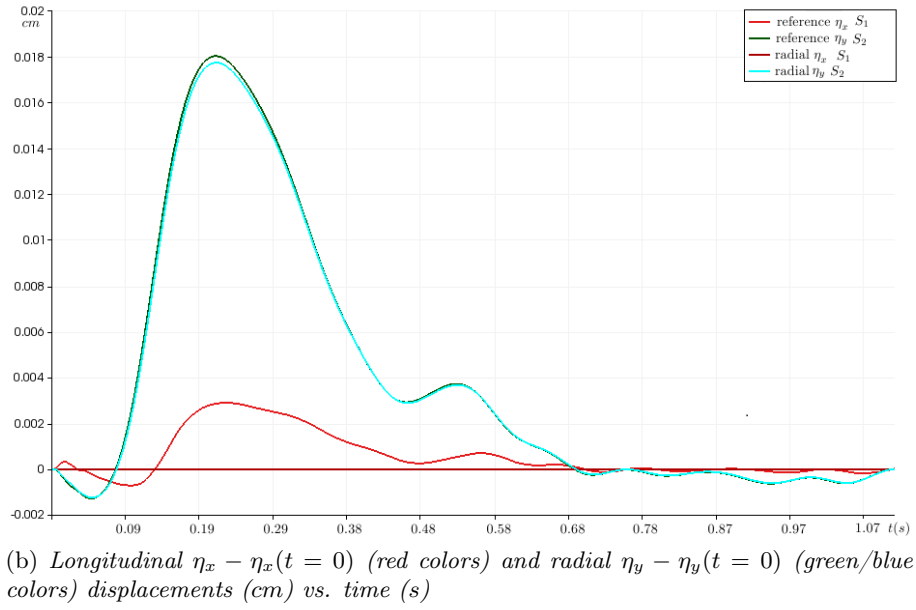
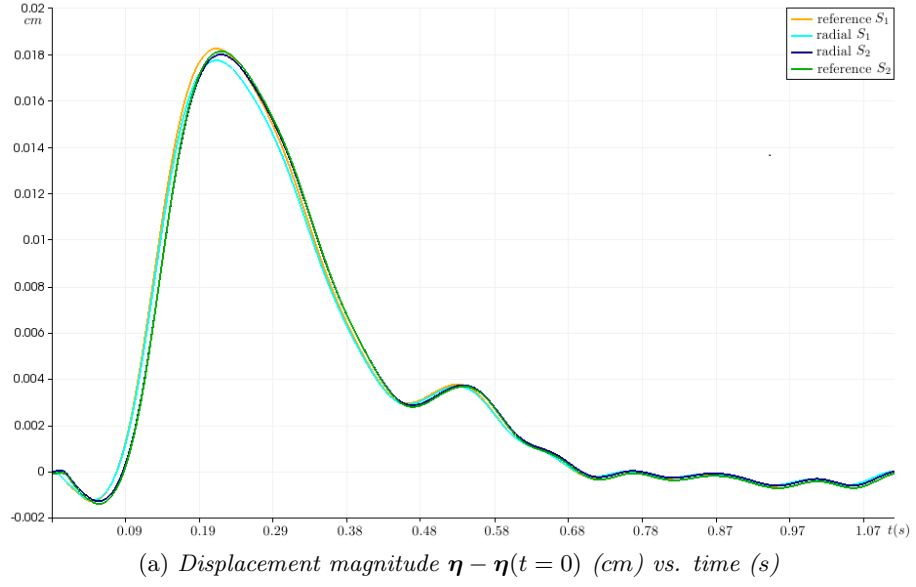


Figure 4.13: Comparison between simplified linear Koiter shell model with respect to the full model: total displacement magnitude and components at the sections S_1 (clear) and S_2 (dark). In legend, *reference* and *radial* refer respectively to the full model and to the simplified model (radial displacement).

Conclusions

In this thesis we have dealt with the numerical approximation of a reduced Fluid-Structure Interaction (FSI) problem in haemodynamic applications by means of Isogeometric Analysis (IGA).

In the first part, we investigated some aspects of IGA [CHB09], starting with a discussion on the representation of geometries by means of Non-Uniform Rational B-Splines (NURBS) [PT97]. IGA has been considered in the framework of the Galerkin method for the numerical approximation of Partial Differential Equations (PDEs) [CHB09], specifically for high order PDEs. Moreover, extending the results obtained in [BBadVC⁺06], we provided an a priori error estimate under h -refinement for the NURBS-based IGA approximation of high order scalar elliptic PDEs. In particular, we focused on the derivation of the errors in lower order norms by means of the *Aubin-Nietsche's argument* [Ode00, SF73]. The numerical examples provided, confirmed the theoretical results and highlighted some of the advantages of IGA compared to Finite Element Analysis (FEA). These include the possibility of an exact geometrical representation [CHB05], an higher level of accuracy, simplified and enriched refinement procedures [CHR07], and globally smoother basis functions with compact support for the analysis.

The improvements provided by IGA with respect to FEA in terms of both accuracy and efficiency, led to consider the method for haemodynamic applications [BCHZ08].

Firstly, we considered the simulation of blood flows in two-dimensional rigid arteries. The Navier-Stokes equations have been used to represent blood flows, with a proper set of boundary conditions [VdVS11, BGH⁺09]. For the numerical solution of the Navier-Stokes equations we have considered IGA in the framework of the Galerkin method for the spatial approximation and the generalized- α method to perform the discretization in time. The standard Galerkin method has been stabilized by means of the Variational Multiscale method accounting for Large Eddy Simulation [BCC⁺07]. Numerical examples of pathological conditions in idealized geometries have been reported and discussed.

Rigid wall models, which neglect the deformability of the arterial vessels, preclude the connect study of the blood flows, especially in large arteries, whose walls undergo sensible deformations. In order to account for the compliance of the vessel, FSI models must be used. In haemodynamics, FSI models describe the mechanical interaction between the blood flow and the response of the arterial wall to the deformation by coupling the Navier-Stokes equations with structural models. The complexity and the elevated computational cost in the numerical approximation of FSI problems, led to consider a reduced FSI model. Based on a thin wall approximation, a shell model has been adopted to describe the arterial wall similarly to [FQV⁺09]. Specifically, we have considered a linear elastic Koiter shell model for axisymmetric geometries [Cia05], capable to capture both radial and longitudinal displacements.

A further level of reduction may be introduced by coupling at the variational level the fluid and structural problems [FVCJT06, NV09] by means of the kinematic and dynamic

conditions [vTG⁺06], thus resulting in the embedding of the structural problem into the fluid one as a generalized boundary condition. In the framework of [FVCJT06], the strong coupling between the degrees of freedom relative to the wall displacement and to the fluid velocity on the boundary, led us to numerically solve the resulting generalized Navier-Stokes equations only in terms of the primitive variables velocity and pressure, in a fixed computational domain. Usually, for the structure only a membrane model is considered [FVCJT06, NV09]; instead, we took into account in this formulation also the bending terms, which involve high order derivatives. The choice to use IGA for the numerical approximation has turned out to be crucial when solving the resulting generalized Navier-Stokes equations, since high order terms are involved. Moreover, the exact geometrical representation of smooth geometries constitutes a peculiarity of IGA that reveals its efficiency in dealing with patient-specific geometries. Even if we considered only two-dimensional geometries, the procedure based on IGA revealed very efficient. We obtained that the computational cost is comparable to rigid wall models. Moreover, the implementation does not require significant efforts once a solver for the Navier-Stokes equations is available. Although the methodology discussed was presented in detail for two-dimensional problems (for which it is required to assume axisymmetric geometries unless considering additional conditions) the same approach can be eventually applied to three-dimensional geometries.

Further extensions of this work may involve the choice of the structural model. First of all, additional terms can be considered in the structural problem in order to include viscoelastic effects [BvG⁺12, vTG⁺06]; thin structural models can be also investigated [Hol06]. Further developments are represented by the analysis of different boundary conditions for the fluid in combination with the reduced FSI model, including Womersley profiles at the inlet [Wom57, AADRF09, THZ98] and impedance condition at the outlet [FVCJT06]. Finally, a rigorous mathematical analysis of the reduced FSI model may be investigated. Specifically, further work is required in order to provide stability results for this formulation.

APPENDICES

Appendix A

Isogeometric Analysis for Navier-Stokes Equations in Stream Function Formulation

We consider the numerical approximation of the Navier-Stokes equations in stream function formulation, for which the equations are recast in a fourth order nonlinear problem in terms of a scalar function called *stream function*. One of the advantages of this formulation is the fact that, at least in two-dimensional problems, we can considerably reduce the size of the discrete system obtained with the Galerkin method with respect to the one corresponding to the Navier-Stokes equations in primitive variables. Moreover, the stream function formulation yields a stable problem in the standard Galerkin formulation, which at the discrete level, requires basis functions at least \mathcal{C}^1 -continuous. This requirement can be satisfied by using NURBS-based IGA (see Remark 1.12). Specifically, we consider the solution of a benchmark problem, i.e. the Lid-driven cavity problem for different values of the Reynolds number, for which we compare the numerical results with those available in literature, in particular in [GGS82].

A.1 The Navier-Stokes equations in stream function formulation

We consider the Navier-Stokes equations governing the flow of an incompressible fluid in a domain $\Omega \subseteq \mathbb{R}^2$ for the time interval $(0, T)$ in terms of the dimensionless primitive variables, i.e. the velocity and the pressure fields (\mathbf{u}, p) (see Section 3.1.2). In order to deduce the stream function formulation, we start from the variational formulation of the problem complemented with Dirichlet and Neumann boundary conditions, imposed respectively on the subsets $\Gamma_D, \Gamma_N \subseteq \partial\Omega$ (see Eq. (3.16)). By using the same notation introduced in Section 3.1.2, in particular referring to the function spaces V_g, V, Q of Eqs. (3.15), the problem reads:

find, for all $t \in (0, T)$, $\mathbf{u}(t) \in V_g, p(t) \in Q$ such that:

$$\begin{cases} m(\dot{\mathbf{u}}(t), \boldsymbol{\varphi}) + a(\mathbf{u}(t), \boldsymbol{\varphi}) + c(\mathbf{u}(t), \mathbf{u}(t), \boldsymbol{\varphi}) + b(\boldsymbol{\varphi}, p(t)) = F(\boldsymbol{\varphi}) + H(\boldsymbol{\varphi}) & \forall \boldsymbol{\varphi} \in V, \text{ (A.1a)} \\ b(\mathbf{u}(t), \psi) = 0 & \forall \psi \in Q, \text{ (A.1b)} \\ \mathbf{u}(0) = \mathbf{u}_0 & \text{in } \Omega, \text{ (A.1c)} \end{cases}$$

where $m(\dot{\mathbf{u}}, \boldsymbol{\varphi}) := \int_{\Omega} \dot{\mathbf{u}} \cdot \boldsymbol{\varphi} \, d\Omega$, $a(\mathbf{u}, \boldsymbol{\varphi}) := \frac{2}{\mathbb{R}e} \int_{\Omega} D(\mathbf{u}) : D(\boldsymbol{\varphi}) \, d\Omega$, $b(\boldsymbol{\varphi}, p) := - \int_{\Omega} p \nabla \cdot \boldsymbol{\varphi} \, d\Omega$ and $c(\mathbf{v}, \mathbf{u}, \boldsymbol{\varphi}) := \int_{\Omega} (\mathbf{v} \cdot \nabla) \mathbf{u} \cdot \boldsymbol{\varphi} \, d\Omega$; while $F(\boldsymbol{\varphi}) := \int_{\Omega} \mathbf{f} \cdot \boldsymbol{\varphi} \, d\Omega$ and $H(\boldsymbol{\varphi}) := \int_{\Gamma_N} \mathbf{h} \cdot \boldsymbol{\varphi} \, d\Gamma$; moreover $D(\mathbf{u}) := \frac{(\nabla \mathbf{u} + \nabla \mathbf{u}^T)}{2}$ is the strain rate tensor.

We introduce the spaces of divergence-free functions, subsets of the respective spaces V_g and V , defined as:

$$W_g := \{\mathbf{u} \in V_g : \nabla \cdot \mathbf{u} = 0\} \subseteq V_g, \quad (\text{A.2a})$$

$$W := \{\boldsymbol{\varphi} \in V : \nabla \cdot \boldsymbol{\varphi} = 0\} \subseteq V. \quad (\text{A.2b})$$

A function $\mathbf{u} \in V_g$, solution of the problem (A.1), is also a solution of the following problem:
find, for all $t \in (0, T)$, $\mathbf{u}(t) \in W_g$ such that:

$$\begin{cases} m(\dot{\mathbf{u}}(t), \boldsymbol{\varphi}) + a(\mathbf{u}(t), \boldsymbol{\varphi}) + c(\mathbf{u}(t), \mathbf{u}(t), \boldsymbol{\varphi}) = F(\boldsymbol{\varphi}) + H(\boldsymbol{\varphi}) & \forall \boldsymbol{\varphi} \in W, \\ \mathbf{u}(0) = \mathbf{u}_0 & \text{in } \Omega. \end{cases} \quad (\text{A.3a})$$

$$\quad (\text{A.3b})$$

Moreover, we consider over the space of scalar functions $H^2(\Omega)$ the equivalence relation \sim defined by the following:

$$\text{for all } v, w \in H^2(\Omega) : \quad v \sim w \text{ if and only if } w - v \in \mathbb{R}, \quad (\text{A.4})$$

whose equivalence classes are denoted by $[\cdot]_{\sim}$. The resulting quotient space of scalar functions in $H^2(\Omega)$ identified up to a constant, is given by:

$$X := \{[v]_{\sim} : v \in H^2(\Omega)\}, \quad (\text{A.5})$$

and we identify each element of X with its equivalence class, i.e. $v \in X$ means $v \in [v]_{\sim}$, with $[v]_{\sim} \in X$. In the additional hypothesis that Ω is a simply connected two-dimensional domain, given $\boldsymbol{\varphi} \in W$ there exists a unique $w \in X$ such that:

$$\boldsymbol{\varphi} = \mathbf{curl} w, \quad (\text{A.6})$$

where the partial differential operator \mathbf{curl} is defined as:

$$\mathbf{curl} : X \rightarrow [H^1(\Omega)]^2, \quad \mathbf{curl} w := \left(\frac{\partial w}{\partial y}, -\frac{\partial w}{\partial x} \right), \quad (\text{A.7})$$

see for reference [ABadVB⁺07, GR79]. In particular, the operator \mathbf{curl} provides an isomorphism between the spaces W_g , W and the following spaces defined as, respectively:

$$\Phi_g := \{v \in X : \mathbf{curl} v|_{\Gamma_D} = \mathbf{g}\}, \quad (\text{A.8a})$$

$$\Phi := \{w \in X : \mathbf{curl} w|_{\Gamma_D} = \mathbf{0}\}. \quad (\text{A.8b})$$

In such a way, we can recast the Navier-Stokes problem (A.3) in a problem whose unknown is the scalar function $v \in \Phi_g$, called *stream function*, and it reads:

find, for all $t \in (0, T)$, $v(t) \in \Phi_g$ such that:

$$\begin{cases} \bar{m}(\dot{v}(t), w) + \bar{a}(v(t), w) + \bar{c}(v(t), v(t), w) = \bar{F}(w) + \bar{H}(w) & \forall w \in \Phi, \\ v(0) = v_0 & \text{in } \Omega, \end{cases} \quad (\text{A.9a})$$

$$\quad (\text{A.9b})$$

where the forms and the functionals in Eq. (A.9) are defined as:

$$\bar{m}(\dot{v}, w) := \int_{\Omega} \frac{\partial \dot{v}}{\partial y} \frac{\partial w}{\partial y} d\Omega + \int_{\Omega} \frac{\partial \dot{v}}{\partial x} \frac{\partial w}{\partial x} d\Omega \quad (\text{A.10a})$$

$$\bar{a}(v, w) := \frac{2}{\mathbb{R}e} \int_{\Omega} \left(2 \frac{\partial^2 v}{\partial x y} \frac{\partial^2 w}{\partial x y} + \frac{1}{2} \left(\frac{\partial^2 v}{\partial y^2} - \frac{\partial^2 v}{\partial x^2} \right) \left(\frac{\partial^2 w}{\partial y^2} - \frac{\partial^2 w}{\partial x^2} \right) \right) d\Omega, \quad (\text{A.10b})$$

$$\bar{c}(v, v, w) := \int_{\Omega} \left(\left(\frac{\partial v}{\partial y} \frac{\partial^2 v}{\partial x y} - \frac{\partial v}{\partial x} \frac{\partial^2 v}{\partial y^2} \right) \frac{\partial w}{\partial y} - \left(-\frac{\partial v}{\partial y} \frac{\partial^2 v}{\partial x^2} + \frac{\partial v}{\partial x} \frac{\partial^2 v}{\partial x y} \right) \frac{\partial w}{\partial x} \right) d\Omega, \quad (\text{A.10c})$$

$$\bar{F}(w) := \int_{\Omega} \left(f_x \frac{\partial w}{\partial y} - f_y \frac{\partial w}{\partial x} \right) d\Omega, \quad (\text{A.10d})$$

$$\bar{H}(w) := \int_{\Gamma_N} \left(h_x \frac{\partial w}{\partial y} - h_y \frac{\partial w}{\partial x} \right) d\Gamma, \quad (\text{A.10e})$$

with $\mathbf{f} = (f_x, f_y)$ and $\mathbf{h} = (h_x, h_y)$; the initial condition is such that $\mathbf{curl} v_0 = \mathbf{u}_0$. The problem (A.9) is the *stream function formulation* for the Navier-Stokes equations (A.1) and it is a time dependent fourth order nonlinear PDE. By construction, the \mathbf{curl} of the scalar field v solution of the problem (A.9) returns the velocity field \mathbf{u} , solution of the problem (A.3) which is, by definition, divergence free. The pressure field, appearing in problem (A.1) can be obtained by solving a second order PDE depending on the stream function v , see e.g. [GR79].

Remark A.1. *By definition of the spaces Φ_g and Φ in Eq. (A.8), the scalar field $v \in \Phi_g$ solution of the problem (A.9) is not a scalar function, but a class of equivalence of functions determined up to a constant. We enforce the uniqueness of the solution of the problem (A.9) in a classical sense by imposing a value in a point in the domain. Moreover, we recast the essential boundary condition $\mathbf{curl} v|_{\Gamma_D} = \mathbf{g}$ in the form of essential boundary conditions for fourth order PDEs, i.e. given $d_1, d_2 : \Gamma_D \rightarrow \mathbb{R}$, $v|_{\Gamma_D} = d_1$, $\nabla v \cdot \mathbf{n}|_{\Gamma_D} = d_2$. In particular, by means of the relation between the two solutions, i.e. $\mathbf{curl} v = \mathbf{u}$, a Dirichlet boundary condition $\mathbf{u}|_{\Gamma_D} = \mathbf{g} = (g_x, g_y)$ yields a condition of the form $\nabla v \cdot \mathbf{n}|_{\Gamma_D} = (-g_y, g_x) \cdot \mathbf{n}$; while the former boundary condition $v|_{\Gamma_D} = d_1$ can be deduced by means of the constraint for the uniqueness, which imposes a value for v in a point in the domain Ω , and the Fundamental Theorem of Calculus. For the sake of simplicity, we provide the Galerkin formulation of the problem (A.9) in terms of functions in Φ and Φ_g , postponing the issue of the uniqueness of the solution in the classical sense to the specific Lid-driven cavity problem.*

A.1.1 Numerical approximation: Isogeometric Analysis

In order to find the numerical approximated solution of the problem (A.9), we provide the semi-discretized spatial formulation by means of the IGA-Galerkin method presented in Section 1.2. Moreover we use the generalized- α method [Whi99, JWH00] for scalar problems for the approximation in time.

Let the two-dimensional computational domain Ω be represented by a NURBS geometry. We consider the finite dimensional space of NURBS in the physical domain, say \mathcal{V}^h , given in Eq. (1.22) and we define the finite dimensional subspaces of the trial and test function spaces of Eq. (A.8) as the NURBS spaces given respectively by $\Phi^h := \Phi \cap \mathcal{V}^h$ and $\Phi_g^h := \Phi_g \cap \mathcal{V}^h$, with $N_s := \dim \Phi^h$. In this manner, the IGA-Galerkin approximation of the problem (A.9) reads:

find, for all $t \in (0, T)$, $v_h(t) \in \Phi_g^h$ such that:

$$\begin{cases} \bar{m}(\dot{v}_h(t), w_h) + \bar{a}(v_h(t), w_h) + \bar{c}(v_h(t), v_h(t), w_h) = \bar{F}(w_h) + \bar{H}(w_h) & \forall w_h \in \Phi^h, \text{ (A.11a)} \\ \mathbf{curl} v_h(0) = \mathbf{u}_0 & \text{in } \Omega, \text{ (A.11b)} \end{cases}$$

where the forms and the functionals are given in Eq. (A.10). By the notation of Chapter 1, we introduce the vectors of control variables for all $t \in (0, T)$ for the *function* v_h and its time derivative \dot{v}_h , given by:

$$\dot{\mathbf{V}}(t) = \{\dot{v}_i(t)\}_{i=1}^{N_s} \quad \text{and} \quad \mathbf{V}(t) = \{v_i(t)\}_{i=1}^{N_s}. \quad (\text{A.12})$$

Moreover, we rewrite Eq. (A.11a) in residual form as:

find, for all $t \in (0, T)$, $v_h(t) \in \Phi_g^h$ such that:

$$\begin{cases} B_h(w_h, \dot{v}_h(t), v_h(t)) = 0 & \forall w_h \in \Phi^h, \text{ (A.13a)} \\ \mathbf{curl} v_h(0) = \mathbf{u}_0 & \text{in } \Omega, \text{ (A.13b)} \end{cases}$$

with $B_h(w_h, \dot{v}_h, v_h) := \bar{m}(\dot{v}_h(t), w_h) + \bar{a}(v_h(t), w_h) + \bar{c}(v_h(t), v_h(t), w_h) - \bar{F}(w_h) - \bar{H}(w_h)$ and we define the vector of discrete residuals whose components are the residuals $B_h(\cdot, \dot{v}_h, v_h)$ evaluated in the NURBS basis function for the function space Φ^h , say \mathcal{R}_i , for $i = 1, \dots, N_s$, i.e.:

$$\mathbf{R}(\dot{v}_h(t), v_h(t)) := \{B_h(\mathcal{R}_i; \dot{v}_h(t), v_h(t))\}_{i=1}^{N_s}. \quad (\text{A.14})$$

In this manner, we can perform the discretization in time by means of the generalized- α method for scalar problems, for which we refer to [Whi99, JWH00]. We introduce a *discrete time vector* $\{t_n\}_{n=0}^{N_t}$, subdividing $(0, T)$ in a set of N_t time intervals of size $\Delta t_n = t_{n+1} - t_n$. For the sake of simplicity, in the vectors of control variables of Eq. (A.12) we replace t_n with the subscript n . The generalized- α algorithm reads: at time step t_n , given $\dot{\mathbf{V}}_n, \mathbf{V}_n$, find $\dot{\mathbf{V}}_{n+1}, \mathbf{V}_{n+1}, \dot{\mathbf{V}}_{n+\alpha_m}, \mathbf{V}_{n+\alpha_f}$ such that:

$$\mathbf{R}(\dot{\mathbf{V}}_{n+\alpha_m}, \mathbf{V}_{n+\alpha_f}) = 0, \quad (\text{A.15a})$$

$$\mathbf{V}_{n+1} = \mathbf{V}_n + \Delta t_n \dot{\mathbf{V}}_n + \delta \Delta t_n (\dot{\mathbf{V}}_{n+1} - \dot{\mathbf{V}}_n), \quad (\text{A.15b})$$

$$\dot{\mathbf{V}}_{n+\alpha_m} = \dot{\mathbf{V}}_n + \alpha_m (\dot{\mathbf{V}}_{n+1} - \dot{\mathbf{V}}_n), \quad (\text{A.15c})$$

$$\mathbf{V}_{n+\alpha_f} = \mathbf{V}_n + \alpha_f (\mathbf{V}_{n+1} - \mathbf{V}_n), \quad (\text{A.15d})$$

where the parameters $\alpha_m, \alpha_f, \delta \in [0, 1]$, defining the generalized- α method, are chosen on the basis of accuracy and stability considerations as in Eqs. (3.50) and (3.52). We deal with the nonlinearity of the system of equations (A.15) in the framework of the case of the generalized- α algorithm for vector-scalar problems, see Section 3.3.3, coupling the method with a *predictor-multicorrector algorithm*.

A.2 Numerical results: the Lid-driven cavity problem

We consider the Navier-Stokes problem (A.9) in stream function formulation to solve the

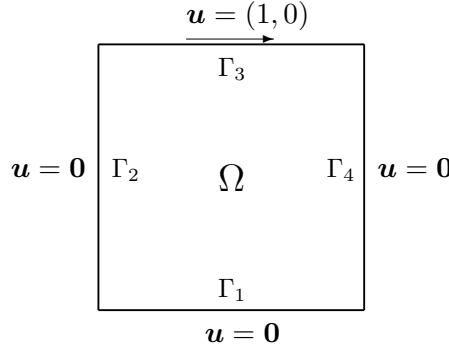


Figure A.1: Lid-driven cavity problem: problem setting and data. $\Omega = (0, 1)^2$, $\Gamma_D = \partial\Omega$.

benchmark *Lid-driven cavity problem* for different values of the Reynolds number, specifically $\text{Re} = 100, 400, 1000, 5000$. In Figure A.1 we report the data relative to the problem defined in the domain $\Omega = (0, 1)^2$ in terms of the unknown velocity field \mathbf{u} . By recalling Remark A.1, we impose the uniqueness of the solution v of problem (A.9) in a classical sense, by imposing that $v(0, 0, t) = 0$ for all $t \in (0, T)$. In such a way, the boundary conditions for the Navier-Stokes equations in stream function formulation reads: $v|_{\partial\Omega} = 0$, $\nabla v \cdot \mathbf{n}|_{\Gamma_3} = 1$ and $\nabla v \cdot \mathbf{n}|_{\Gamma_i} = 0$ for $i = 1, 2, 4$.

We represent the computational domain $\Omega = (0, 1)^2$ of Figure A.1 by means of \mathcal{C}^1 -continuous B-Splines basis functions of degree $p = 2$, on uniform meshes with $N_{el} = (2^8)^2$ elements. We set the time step Δt , for the time approximation with the generalized- α method, to a default value of $\Delta t = 0.1$. The initial condition for the stream function is set to $v(0) = 0$.

For each value of the Reynolds number considered, $\text{Re} = 100, 400, 1000, 5000$, we compare the solutions obtained, at the steady state, with the data in [GGS82]. In Figures A.2, A.3, A.4, A.6 a comparison is performed in terms of the streamlines, vorticity contour lines and the positions of the vortexes centers with respect to [GGS82]. The values of the stream function and the vorticity contour lines are the ones used in [GGS82] and reported in Table A.2. Moreover, for $\text{Re} = 5000$ we show in Figure A.5 the evolution of the streamlines from the initial condition to the steady state. In Table A.1 we compare with [GGS82] the positions of the vortexes centers and the corresponding values that the stream function v assumes. The notation is the same reported in [GGS82]; in particular, as for the vortexes the letters B, L, and R denote the bottom, left, and right corners respectively. As reported in literature, the number of regions in which the vortexes develop increases for higher values of the Reynolds number, specifically in the corners of the domain. E.g. for $\text{Re} = 5000$, we can observe in Figure A.6 that two secondary vortexes in the bottom corners and a third vortex in the upper right corner appear with respect to lower Reynolds numbers. When the Reynolds number increases the centers of the primary and the secondary vortexes move towards the center of the domain. Furthermore, we can also notice that the larger is Re , the slower is the convergence to the steady state. We can conclude that the results obtained by using IGA are in good agreement with the results available in literature, even in the case of high Reynolds Numbers.

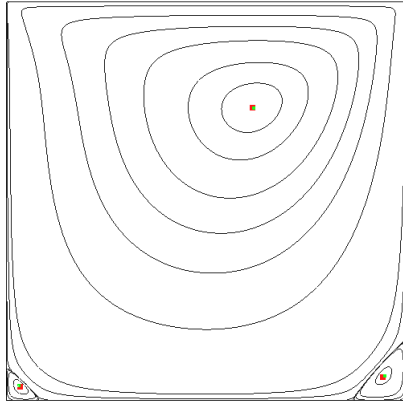
Table A.1: Vortex centers: numerical results compared with [GGS82].

vortex	property	$\mathbb{R}e = 100$		$\mathbb{R}e = 400$	
		result	[GGS82]	result	[GGS82]
Primary	v_{\min}	-0.1035	-0.103423	-0.1140	-0.113909
	x -coordinate	0.6150	0.6172	0.5550	0.5547
	y -coordinate	0.7350	0.7344	0.6050	0.6055
First BL	v_{\max}	$1.7690 \cdot 10^{-6}$	$1.74877 \cdot 10^{-6}$	$1.4224 \cdot 10^{-5}$	$1.41951 \cdot 10^{-5}$
	x -coordinate	0.0341	0.0313	0.0512	0.0508
	y -coordinate	0.0346	0.0391	0.0472	0.0469
First BR	v_{\max}	$1.2604 \cdot 10^{-5}$	$1.25374 \cdot 10^{-5}$	$6.4301 \cdot 10^{-4}$	$6.42352 \cdot 10^{-4}$
	x -coordinate	0.9400	0.9453	0.8850	0.8906
	y -coordinate	0.0600	0.0625	0.1200	0.1250

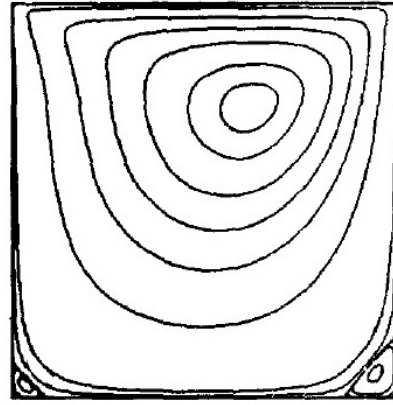
vortex	property	$\mathbb{R}e = 1000$		$\mathbb{R}e = 5000$	
		result	[GGS82]	result	[GGS82]
Primary	v_{\min}	-0.1185	-0.117929	-0.1121	-0.118966
	x -coordinate	0.5300	0.5313	0.5050	0.5117
	y -coordinate	0.5650	0.5625	0.5200	0.5352
First T	v_{\max}	—	—	$1.2301 \cdot 10^{-3}$	$1.454641 \cdot 10^{-3}$
	x -coordinate	—	—	0.0625	0.0625
	y -coordinate	—	—	0.9102	0.9102
First BL	v_{\max}	$2.2969 \cdot 10^{-4}$	$2.31129 \cdot 10^{-4}$	$1.34379 \cdot 10^{-3}$	$1.36119 \cdot 10^{-3}$
	x -coordinate	0.0834	0.0859	0.0730	0.0703
	y -coordinate	0.0777	0.0781	0.1360	0.1367
First BR	v_{\max}	0.0017	$1.75102 \cdot 10^{-3}$	$2.61468 \cdot 10^{-3}$	$3.08358 \cdot 10^{-3}$
	x -coordinate	0.8650	0.8594	0.8200	0.8086
	y -coordinate	0.1100	0.1094	0.0750	0.0742
Second BL	v_{\max}	—	—	$-1.05856 \cdot 10^{-7}$	$-7.08860 \cdot 10^{-8}$
	x -coordinate	—	—	0.0085	0.0117
	y -coordinate	—	—	0.0078	0.0078
Second BR	v_{\max}	$-1.36433 \cdot 10^{-8}$	$-9.31929 \cdot 10^{-8}$	$-7.21597 \cdot 10^{-7}$	$-1.43226 \cdot 10^{-6}$
	x -coordinate	0.9930	0.9922	0.985	0.9805
	y -coordinate	0.0070	0.0078	0.0160	0.0195

Table A.2: Values for the contour lines of the stream-function and the vorticity.

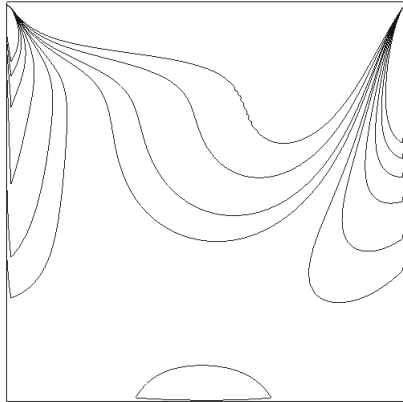
Contour lines		
<i>Stream function</i>		<i>Vorticity</i>
$-1.0 \cdot 10^{-10}$	-0.1175	-3.0
$-1.0 \cdot 10^{-7}$	$1.0 \cdot 10^{-8}$	-2.0
$-1.0 \cdot 10^{-5}$	$1.0 \cdot 10^{-7}$	-1.0
$-1.0 \cdot 10^{-4}$	$1.0 \cdot 10^{-6}$	-0.5
$-1.0 \cdot 10^{-2}$	$1.0 \cdot 10^{-5}$	0
$-3.0 \cdot 10^{-2}$	$5.0 \cdot 10^{-5}$	0.5
$-5.0 \cdot 10^{-2}$	$1.0 \cdot 10^{-4}$	1.0
$-7.0 \cdot 10^{-2}$	$2.5 \cdot 10^{-4}$	2.0
$-9.0 \cdot 10^{-2}$	$5.0 \cdot 10^{-4}$	3.0
$-1.0 \cdot 10^{-1}$	$1.0 \cdot 10^{-3}$	4.0
-0.11	$1.5 \cdot 10^{-3}$	5.0
-0.115	$3.0 \cdot 10^{-3}$	



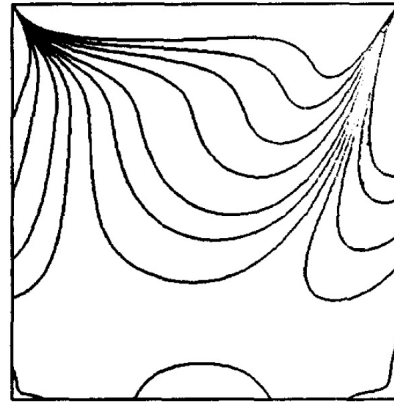
(a) Streamlines and position of vortex centers.



(b) Streamlines in [GGS82].



(c) Vorticity contour lines.



(d) Vorticity contours in [GGS82].

Figure A.2: Lid-driven cavity problem, $\text{Re} = 100$: comparison of the results (steady state reached at $t = 16$) with [GGS82]. Computed vortexes centers (■) compared with those in [GGS82] (■).

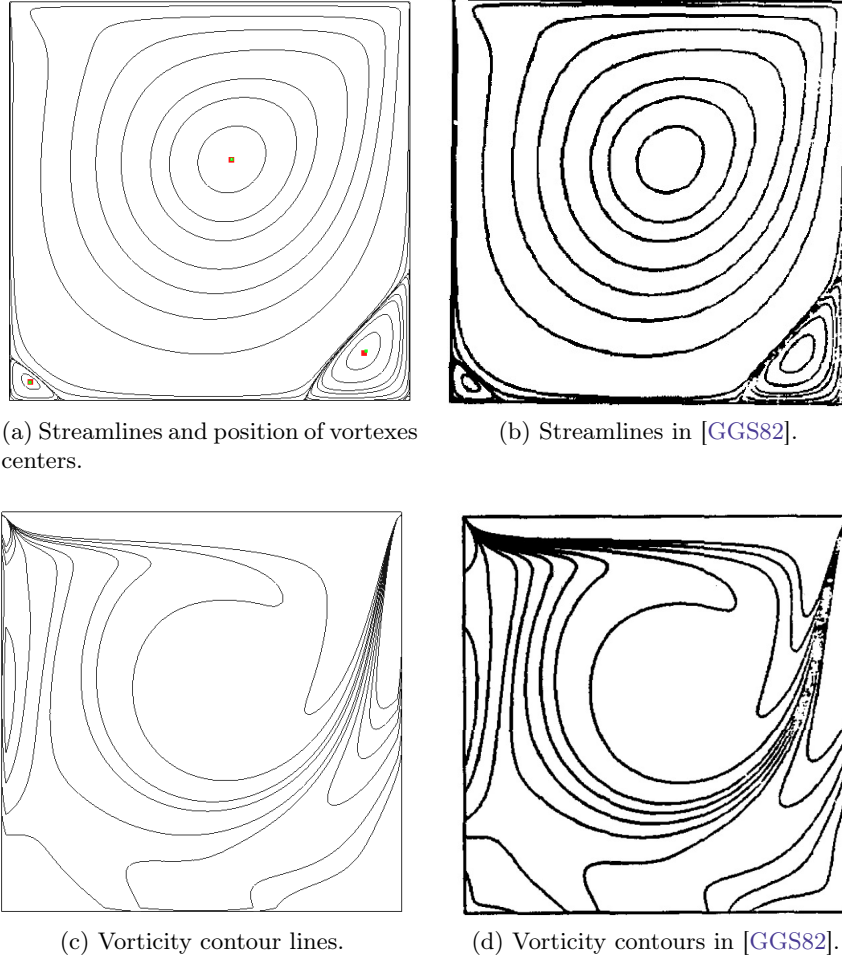
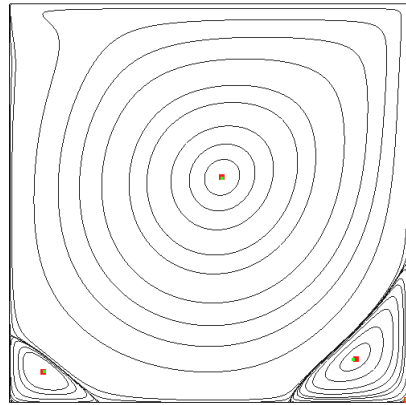
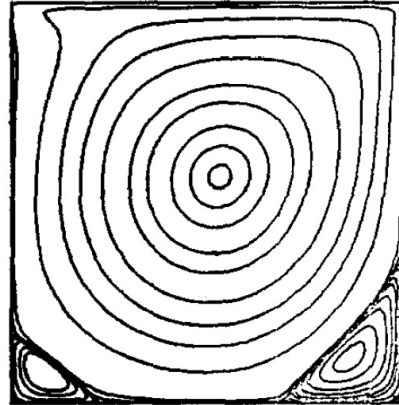


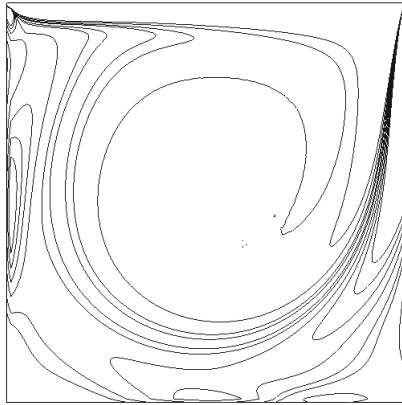
Figure A.3: Lid-driven cavity problem, $\text{Re} = 400$: comparison of the results (steady state reached at $t = 40$) with [GGS82]. Computed vortexes centers (■) compared with those in [GGS82] (■).



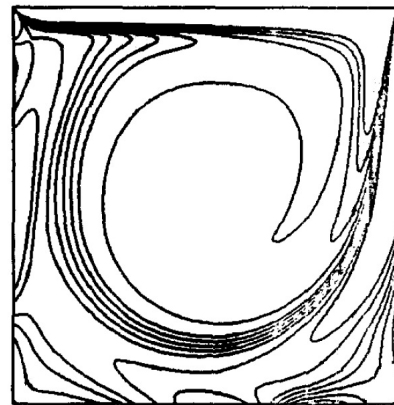
(a) Streamlines and position of vortex centers.



(b) Streamlines in [GGS82].



(c) Vorticity contour lines.



(d) Vorticity contours in [GGS82].

Figure A.4: Lid-driven cavity problem, $Re = 1000$: comparison of the results (steady state reached at $t = 40$) with [GGS82]. Computed vortex centers (■) compared with those in [GGS82] (■).

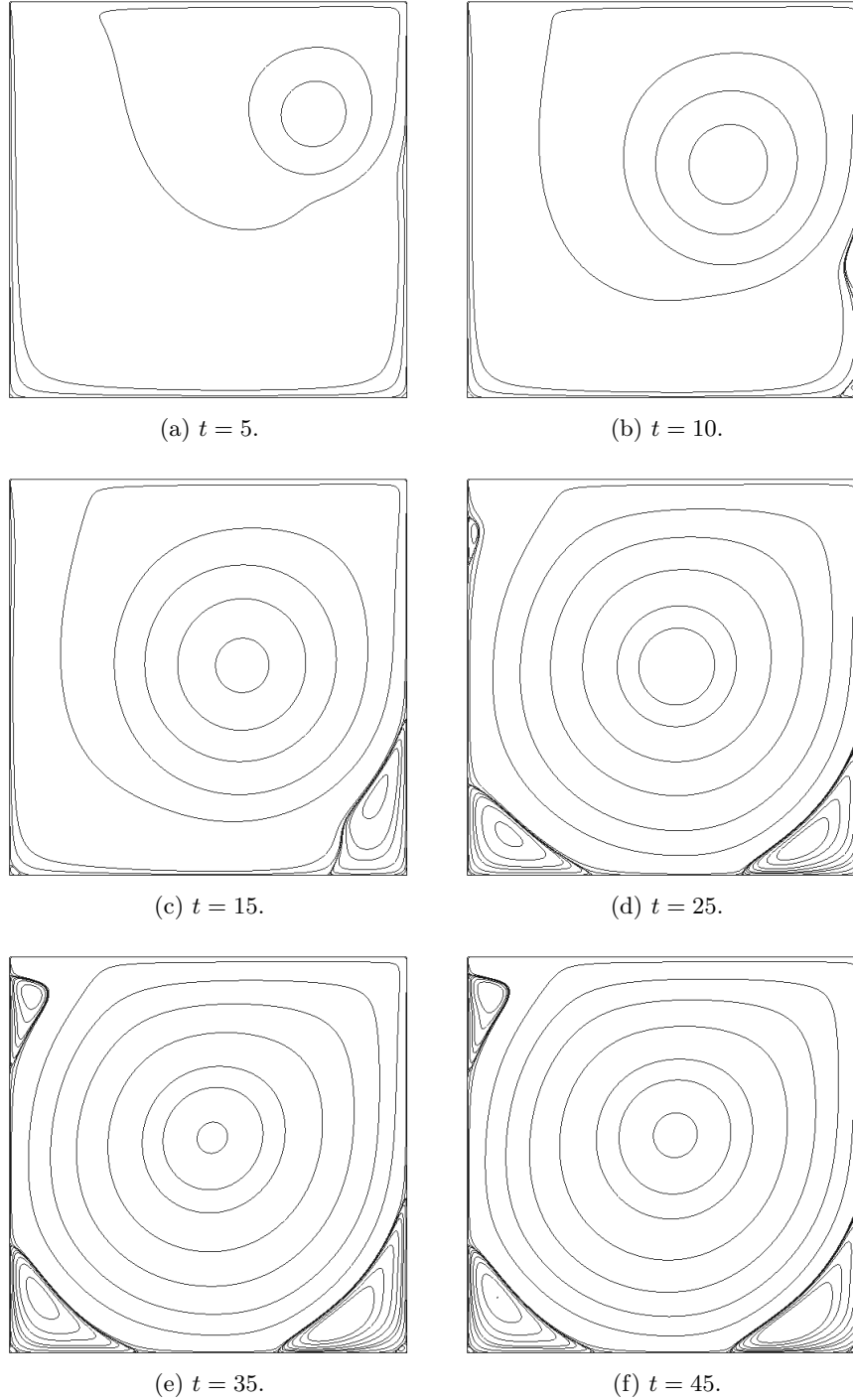
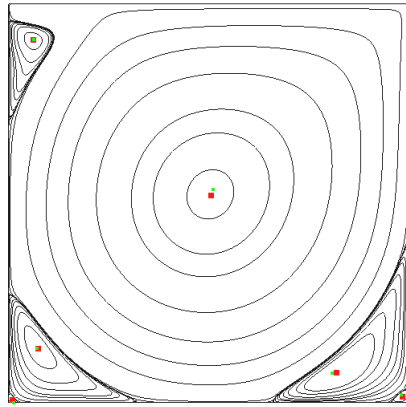
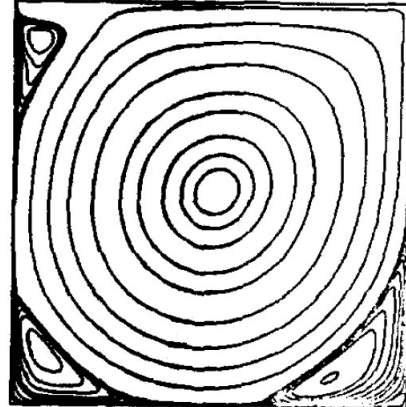


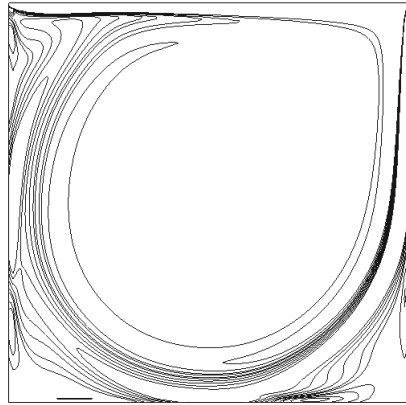
Figure A.5: Lid-driven cavity problem, $\text{Re} = 5000$: streamlines at different time steps.



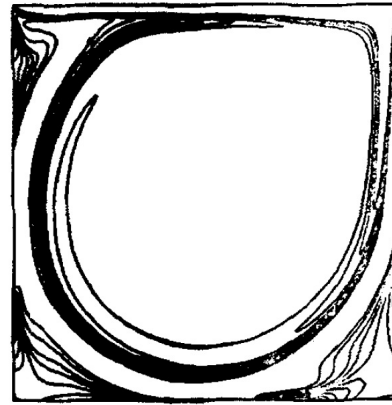
(a) Streamlines and position of vortex centers.



(b) Streamlines in [GGS82].



(c) Vorticity contour lines.



(d) Vorticity contours in [GGS82].

Figure A.6: Lid-driven cavity problem, $Re = 5000$: comparison of the results (steady state reached at $t = 50$) with [GGS82]. Computed vortexes centers (■) compared with those in [GGS82] (■).

Appendix B

Imposition of Essential Boundary Conditions for High Order PDEs

We discuss the strong imposition of essential boundary conditions for high order PDEs solved by means of the Galerkin method in the framework of NURBS-based IGA. In particular, we consider the imposition of the boundary condition on the normal gradient of the solution stemming from a fourth order partial differential operator. We consider a method based on the explicit formula for derivatives of multivariate NURBS basis functions for which a system of equations involving a subset of the control variables needs to be solved. The general case for higher order partial differential operators can be obtained straightforwardly; we only mention the case of homogeneous essential boundary conditions imposed on the whole boundary domain for the trilaplacian operator (see Example 1.14). An alternative approach can be found in [LDE⁺12], where a periodic *Bézier extraction operator* is introduced to enforce the strong imposition of periodic boundary conditions. The technique that we propose, even if computationally more expensive, allows the strong imposition of essential boundary conditions that are not necessarily neither homogeneous nor periodic.

B.1 Strong imposition for fourth order PDEs

When considering a fourth order partial differential operator, e.g. the bilaplacian operator (see Example 1.13), which defines a scalar boundary value problem in a domain Ω for the unknown u , the essential boundary conditions are of the following type:

$$u|_{\Gamma_{Ess}} = g_1, \quad \nabla u \cdot \mathbf{n}|_{\Gamma_{Ess}} = g_2, \quad (\text{B.1})$$

for some functions $g_1, g_2 : \Gamma_{Ess} \rightarrow \mathbb{R}$, where $\Gamma_{Ess} \subseteq \partial\Omega$ denotes the subset of the boundary in which we impose the essential boundary conditions and \mathbf{n} is the outward directed unit vector normal to Γ_{Ess} . For the sake of simplicity we consider the case in which $\Gamma_{Ess} \equiv \partial\Omega$.

Let the domain Ω be parametrized as a NURBS geometry for which the NURBS basis functions are built starting from open knot vectors. Specifically, we assume that Ω is a NURBS surface represented by means of the geometrical mapping \mathbf{x} of Eq. (1.18), which is defined in the parametric domain $\hat{\Omega} = [0, 1]^2$ and assumed to be invertible. By recalling the notation introduced in Chapter 1, we denote the knot vectors in each parametric direction $\alpha = 1, 2$ as $\Xi_\alpha = \{\xi_1^\alpha, \xi_2^\alpha, \dots, \xi_{n_\alpha+p_\alpha+1}^\alpha\}$, which define in the parametric domain the corresponding univariate B-Splines basis functions of degree p_α , say $\{N_{i_\alpha}^\alpha\}_{i_\alpha=1}^{n_\alpha}$ in Eq. (1.1). By introducing

the set of multi-indexes $I = \{\mathbf{i} = (i_1, i_2) : 0 \leq i_\alpha \leq n_\alpha, \alpha = 1, 2\}$, we assign a set of weights $\omega = \{\omega_{\mathbf{i}}\}_{\mathbf{i} \in I}$ which defines the weighting function W of Eq. (1.14) and the bivariate NURBS basis $\{R_{\mathbf{i}}\}_{\mathbf{i} \in I}$ of Eq. (1.15) in the parametric domain; while $\{\mathcal{R}_{\mathbf{i}}\}_{\mathbf{i} \in I}$ are the basis functions in the physical space Ω of equation Eq. (1.22).

Let u_h be a function in the space of NURBS in the physical domain \mathcal{V}^h given in Eq. (1.22); we assume that u_h is the approximated solution of the fourth order PDE obtained by means of the IGA-Galerkin method. Moreover, following Eq. (1.24), we write $u_h = \sum_{\mathbf{i} \in I} \mathcal{R}_{\mathbf{i}} d_{\mathbf{i}}$, where

$\{d_{\mathbf{i}}\}_{\mathbf{i} \in I}$ is the set of control variables. In order to impose the essential boundary conditions, it is convenient to use the relation between the approximated solution u_h defined in the physical domain Ω and its corresponding function, say \hat{u}_h of Eq. (1.23), defined in the parametric domain $\hat{\Omega}$. Specifically, this relation is determined by the geometrical mapping and given by:

$$u_h = \hat{u}_h \circ \mathbf{x}^{-1} \quad \text{or equivalently} \quad \hat{u}_h = u_h \circ \mathbf{x}. \quad (\text{B.2})$$

Moreover, we introduce an extension of the boundary data in the space of NURBS, say $g_{1,h}$ and $g_{2,h}$, respectively given by:

$$g_{1,h} : \Omega \rightarrow \mathbb{R}, \quad g_{1,h} := \sum_{\mathbf{i} \in I} \mathcal{R}_{\mathbf{i}} g_{\mathbf{i}}^1 \quad \text{and} \quad g_{2,h} : \Omega \rightarrow \mathbb{R}, \quad g_{2,h} := \sum_{\mathbf{i} \in I} \mathcal{R}_{\mathbf{i}} g_{\mathbf{i}}^2, \quad (\text{B.3})$$

with $\{g_{\mathbf{i}}^1\}_{\mathbf{i} \in I}$ and $\{g_{\mathbf{i}}^2\}_{\mathbf{i} \in I}$ the corresponding sets of control variables.

By means of the end-point interpolation property (see Section 1.1.5) and Eq. (B.2), we perform the strong imposition of the boundary condition $u_h|_{\partial\Omega} = g_{1,h}$ identifying the control variables of $g_{1,h}$ and of u_h whose indexes are in the set $K_1 := \{\mathbf{i} = (i_1, i_2) \in I : i_1 = 1, \text{ or } i_1 = n_1, \text{ or } i_2 = 1, \text{ or } i_2 = n_2\} \subseteq I$.

The imposition of the boundary condition on the normal gradient of the solution $\nabla u_h \cdot \mathbf{n}|_{\partial\Omega} = g_{2,h}$ is not any longer straightforward; specifically, in order to recast the condition in terms of the solution \hat{u}_h in the parametric domain, we use both the chain rule and Eq. (B.2), for which:

$$\nabla u_h = \left[T^{-T} \hat{\nabla} \hat{u}_h \right] \circ \mathbf{x}^{-1}, \quad (\text{B.4})$$

where we denote by $\hat{\nabla}$ the gradient operator with respect to the parametric coordinates. Moreover, we use the relation between the outward directed unit normal vectors to the boundaries in the physical domain, denoted by \mathbf{n} , and in the parametric domain, say $\hat{\mathbf{n}}$, given by:

$$\mathbf{n} = J T^{-T} \hat{\mathbf{n}}, \quad (\text{B.5})$$

where T is the deformation tensor of the geometrical mapping of Eq. (1.4) and J is the Jacobian of the mapping of Eq. (1.20). In particular, Eq. (B.4) and Eq. (B.5) yield:

$$g_{2,h} \circ \mathbf{x}^{-1}|_{\partial\hat{\Omega}} = J \nabla \hat{u}_h^T (T^T T)^{-1} \hat{\mathbf{n}}|_{\partial\hat{\Omega}}. \quad (\text{B.6})$$

In the framework of the strong imposition of the boundary condition $u_h|_{\partial\Omega} = g_{1,h}$, from Eq. (B.6), we can establish a system of relations between a subset of the control variables of u_h and of $g_{2,h}$. With this aim, we use the definition of derivative of NURBS basis functions, given in Eq. (1.12), and the fact that bivariate open knot NURBS basis functions are used. Specifically, we are interested in computing:

$$\frac{\partial \hat{u}_h}{\partial \eta_1}(\xi_1^1, \cdot), \quad \frac{\partial \hat{u}_h}{\partial \eta_1}(\xi_{n_1+p_1+1}^1, \cdot), \quad \frac{\partial \hat{u}_h}{\partial \eta_2}(\cdot, \xi_1^2), \quad \frac{\partial \hat{u}_h}{\partial \eta_2}(\cdot, \xi_{n_2+p_2+1}^2).$$

We take as example the first of the above derivatives, for which we have:

$$\begin{aligned} \frac{\partial \hat{u}_h}{\partial \eta_1}(\xi_1^1, \eta_2) &= \sum_{\mathbf{i} \in I} d_{\mathbf{i}} \frac{\partial R_{\mathbf{i}}}{\partial \eta_1}(\xi_1^1, \eta_2) \\ &= \frac{1}{W(\xi_1^1, \eta_2)} \frac{\partial N_2^1}{\partial \eta_1}(\xi_1) \sum_{j=1}^{n_2} N_j^2(\eta_2) \left(\omega_{(2,j)} d_{(2,j)} - \omega_{(1,j)} d_{(1,j)} \frac{\sum_{l=1}^{n_2} N_l^2(\eta_2) \omega_{(2,l)}}{W(\xi_1^1, \eta_2)} \right). \end{aligned} \quad (\text{B.7})$$

Remark B.1. By means of the imposition of the essential boundary condition $u_h|_{\partial\Omega} = g_{1,h}$, we find the control variables $\{d_{(1,j)}\}_{j=1}^{n_2}$, $d_{(2,1)}$ and $d_{(2,n_2)}$; while, in this particular case, the set of unknowns is represented by the control variables $\{d_{(2,j)}\}_{j=2}^{n_2-1}$.

By collecting in the right hand side of Eq. (B.7) the *known terms* we obtain the relation:

$$\begin{aligned} \sum_{j=2}^{n_2-1} N_j^2(\eta_2) d_{(2,j)} \omega_{(2,j)} &= \frac{\partial \hat{u}_h}{\partial \eta_1}(\xi_1^1, \eta_2) W(\xi_1^1, \eta_2) \left(\frac{\partial N_2^1}{\partial \eta_1}(\xi_1) \right)^{-1} \\ &\quad + \sum_{j=1}^{n_2} \frac{N_j^2(\eta_2) d_{(1,j)} \omega_{(1,j)}}{W(\xi_1^1, \eta_2)} \left(\sum_{l=1}^{n_2} N_l^2(\eta_2) \omega_{(2,l)} \right) \\ &\quad - N_1^2(\eta_2) d_{(2,1)} \omega_{(2,1)} - N_{n_2}^2(\eta_2) d_{(2,n_2)} \omega_{(2,n_2)}, \end{aligned} \quad (\text{B.8})$$

which leads to the solution of an interpolation problem. In particular, we enforce Eq. (B.8) in $n_2 - 2$ points equally spaced in the parametric domain restricted to the second parametric direction, i.e. in $\{\bar{\eta}_j^2\}_{j=2}^{n_2-1}$, with $\bar{\eta}_j^2 := \frac{j-1}{n_2-1}$.

The same method is implemented for the other derivatives, leading to the solution of linear systems in the unknown control variables $\{d_{(2,j)}\}_{j=2}^{n_2-1}$, $\{d_{(n_1-1,j)}\}_{j=2}^{n_2-1}$, $\{d_{(j,2)}\}_{j=2}^{n_1-1}$ and $\{d_{(j,n_2-1)}\}_{j=2}^{n_1-1}$, respectively.

Remark B.2. The method can be extended to the strong imposition of essential boundary conditions in case of partial differential operators of order higher than four. E.g., let us consider the PDE defined by the trilaplacian operator of Eq. (1.41a) and completed by homogeneous essential boundary conditions on the whole boundary. Moreover, let u_h be the approximated solution obtained by means of the IGA-Galerkin method, whose control variables are denoted by $\{d_{\mathbf{i}}\}_{\mathbf{i} \in I}$. By means of the end-point interpolation property and Eq. (B.2) the imposition of the boundary condition $u_h|_{\partial\Omega} = 0$ of Eq. (1.41b) consists in setting to zero the control variables whose indexes are in the set $K_1 := \{\mathbf{i} = (i_1, i_2) \in I : i_1 = 1, \text{ or } i_1 = n_1, \text{ or } i_2 = 1, \text{ or } i_2 = n_2\} \subseteq I$, i.e. $\{d_j = 0\}_{j \in K_1}$. By means of this constrain, to perform the imposition of the boundary condition $(\nabla u \cdot \mathbf{n})|_{\partial\Omega} = 0$ of Eq. (1.41c) the method yields $\{d_j = 0\}_{j \in K_2}$, with $K_2 := \{\mathbf{i} = (i_1, i_2) \in I : i_1 = 2, \text{ or } i_1 = n_1 - 1, \text{ or } i_2 = 2, \text{ or } i_2 = n_2 - 1\} \subseteq I$. Finally, in order to satisfy the essential boundary condition $\Delta u_h|_{\partial\Omega} = 0$ in Eq. (1.41d), analogous considerations on the second order derivatives of NURBS basis functions and the relation:

$$\Delta u = \frac{1}{J} \hat{\nabla} \left[J(T^T T)^{-1} \hat{\nabla} \hat{u} \right] \circ \mathbf{x}^{-1},$$

lead to impose $\{d_j = 0\}_{j \in K_3}$, with $K_3 := \{\mathbf{i} = (i_1, i_2) \in I : i_1 = 3, \text{ or } i_1 = n_1 - 2, \text{ or } i_2 = 3, \text{ or } i_2 = n_2 - 2\} \subseteq I$.

Bibliography

- [AADRF09] D. Abi-Abdallah, A. Drochon, V. Robin, and O. Fokapu. Pulsed magnetohydrodynamic blood flow in a rigid vessel under physiological pressure gradient. *Computer Methods in Biomechanics and Biomedical Engineering*, **12**:445–458, 2009.
- [ABadVB⁺07] F. Auricchio, L. Beirão da Veiga, F. Buffa, C. Lovadina, A. Reali, and G. Sangalli. A fully locking-free isogeometric approach for plane linear elasticity problems: a stream function formulation. *Computer Methods in Applied Mechanics and Engineering*, **197**:160–172, 2007.
- [AF07] R.A. Adams and J.J.F. Fournier. *Sobolev Spaces*. Academic Press, New York, 2007.
- [AQV02] F. Auteri, L. Quartapelle, and L. Vigeveno. Accurate $\omega - \psi$ spectral solution of the singular driven cavity problem. *Journal of Computational Physics*, **180**:597–615, 2002.
- [BadVBRs10] L. Beirão da Veiga, A. Buffa, J. Rivas, and G. Sangalli. Some estimates for h - p - k -refinement in Isogeometric Analysis. *Numerische Mathematik*, **118**:271–305, 2010.
- [BBadVC⁺06] Y. Bazilevs, L. Beirão da Veiga, J.A. Cottrell, T.J.R. Hughes, and G. Sangalli. Isogeometric Analysis: Approximation, stability, and error estimates for h -refined meshes. *Mathematical Models and Methods in Applied Sciences*, **16**:1031–1090, 2006.
- [BCC⁺07] Y. Bazilevs, V.M. Calo, J.A. Cottrell, T.J.R. Hughes, A. Reali, and G. Scovazzi. Variational multiscale residual-based turbulence modeling for large eddy simulation of incompressible flows. *Computer Methods in Applied Mechanics and Engineering*, **197**:173–201, 2007.
- [BCC⁺10] Y. Bazilevs, V.M. Calo, J.A. Cottrell, J.A. Evans, T.J.R. Hughes, S. Lipton, M.A. Scott, and T.W. Sederberg. Isogeometric Analysis using T-splines. *Computer Methods in Applied Mechanics and Engineering*, **199**:229–263, 2010.
- [BCHZ08] Y. Bazilevs, V.M. Calo, T.J.R. Hughes, and Y. Zhang. Isogeometric fluid-structure interaction: theory, algorithms and computations. *Computer Mechanics*, **43**:3–37, 2008.
- [BF91] F. Brezzi and M. Fortin. *Mixed and Hybrid Finite Element Methods*. Springer-Verlag, New York, 1991.

- [BGH⁺09] Y. Bazilevs, J.R. Gohean, T.J.R. Hughes, R.D. Moser, and Y. Zhang. Patient-specific isogeometric fluid-structure interaction analysis of thoracic aortic blood flow due to implantation of the Jarvik 2000 left ventricular assist device. *Computer Methods in Applied Mechanics and Engineering*, **198**:3534–3550, 2009.
- [BH07] Y. Bazilevs and T.J.R. Hughes. Weak imposition of Dirichlet boundary conditions in fluid mechanics. *Computers and Fluids*, **36**:12–26, 2007.
- [BS06] C.-H. Bruneau and M. Saad. The 2D lid-driven cavity problem revisited. *Computers and Fluids*, **35**:326–348, 2006.
- [BvG⁺12] M. Bukač, S. Čanić, R. Glowinski, J. Tambača, and A. Quaini. Fluid-structure interaction in blood flow capturing non-zero longitudinal structure displacement. *Journal of Computational Physics*, 2012. doi: <http://dx.doi.org/10.1016/j.jcp.2012.08.033>.
- [BW97] J. Bonet and R.D. Wood. *Nonlinear Continuum Mechanics for Finite Element Analysis*. Cambridge University Press, New York, 1997.
- [CH93] J. Chung and G.M. Hulbert. A time integration algorithm for structural dynamics with improved numerical dissipation: the generalized- α method. *Journal of Applied Mechanics*, **60**:371–375, 1993.
- [CHB05] J.A. Cottrell, T.J.R. Hughes, and Y. Bazilevs. Isogeometric analysis: CAD, finite elements, NURBS, exact geometry and mesh refinement. *Computer Methods in Applied Mechanics and Engineering*, **194**:4135–4195, 2005.
- [CHB09] J.A. Cottrell, T.J.R. Hughes, and Y. Bazilevs. *Isogeometric Analysis: Toward Integration of CAD and FEA*. John Wiley & Sons, Chichester, UK, 2009.
- [CHR07] J.A. Cottrell, T.J.R. Hughes, and A. Reali. Studies of refinement and continuity in isogeometric structural analysis. *Computer Methods in Applied Mechanics and Engineering*, **196**:4160–4183, 2007.
- [Cia05] P.G. Ciarlet. *An Introduction to Differential Geometry with Applications to Elasticity*. Springer, Netherlands, 2005. Reprinted from *Journal of Elasticity*, **78–79**, 2005.
- [CPGB07] R. Codina, J. Principe, O. Guash, and S. Badia. Time dependent subscales in the stabilized finite element approximation of incompressible flow problems. *Computer Methods in Applied Mechanics and Engineering*, **196**:2413–2430, 2007.
- [DBH12] L. Dedè, M.J. Borden, and T.J.R. Hughes. Isogeometric Analysis for topology optimization with a phase field model. *Archives of Computational Methods in Engineering*, **19**:427–465, 2012.
- [dFRV11] C. de Falco, A. Reali, and R. Vázquez. GeoPDEs: a research tool for Isogeometric Analysis of PDEs. *Advances in Engineering Software*, **42**:1020–1034, 2011.

- [Dis03] M. Discacciati. *Gâteaux and Fréchet derivatives*. EPFL, Lausanne, 2003. Lecture Notes.
- [EBBH09] J.A. Evans, Y. Bazilevs, I. Babuška, and T.J.R. Hughes. n -widths, sup-infs, and optimality ratios for the k -version of the isogeometric finite element method. *Computer Methods in Applied Mechanics and Engineering*, **198**:1726–1741, 2009.
- [EH10] J.A. Evans and T.J.R. Hughes. Variational multiscale analysis: a new link between flux correction, total variation, and constrained optimization. *ICES Report, Institute for Computational Engineering and Sciences, The University of Texas at Austin*, 10–35, 2010.
- [EH12a] J.A. Evans and T.J.R. Hughes. Isogeometric divergence-conforming B-splines for the steady Navier-Stokes equations. *ICES Report, Institute for Computational Engineering and Sciences, The University of Texas at Austin*, 12–15, 2012.
- [EH12b] J.A. Evans and T.J.R. Hughes. Isogeometric divergence-conforming B-Splines for the unsteady Navier–Stokes equations. *ICES Report, Institute for Computational Engineering and Sciences, The University of Texas at Austin*, 12–16, 2012.
- [FF92] L.P. Franca and S.L. Frey. Stabilized finite element methods: II. The incompressible Navier-Stokes equations. *Computer Methods in Applied Mechanics and Engineering*, **99**:209–233, 1992.
- [Fio00] S. Fiocca. *Fondamenti di anatomia e fisiologia umana*. Sorbona, Naples, 2000.
- [FQ⁺02] L. Formaggia, A. Quarteroni, et al. In: Mathematical modeling and numerical simulation of the cardiovascular system, *Modelling of Living Systems*. Elsevier, Handbook of Numerical Analysis Series, 2002. N.Ayache eds.
- [FQV⁺09] L. Formaggia, A. Quarteroni, A. Veneziani, et al. *Cardiovascular Mathematics: Modeling and simulation of the circulatory system*. Modeling, Simulation and Applications. Springer, Milan, 2009.
- [FVCJT06] C.A. Figueroa, I.E. Vignon-Clementel, T.J.R. Jansen, K.E. and Hughes, and C.A. Taylor. A coupled momentum method for modeling blood flow in three-dimensional deformable arteries. *Computer Methods in Applied Mechanics and Engineering*, **195**:5685–5706, 2006.
- [GGS82] U. Ghia, K.N. Ghia, and C.T. Shin. High-Re solutions for incompressible flow using the Navier–Stokes equations and a multigrid method. *Journal of Computational Physics*, **48**:387–411, 1982.
- [GP12] T. Gordini and L. Pantieri. *L’arte di scrivere con L^AT_EX*. 2008-2012.
- [GQ07] J.L. Guermond and L. Quartapelle. Finite Element solutions of unsteady viscous flows past multiple airfoils. *15th International Conference on Numerical Methods in Fluid Dynamics*, pages 566–571, 2007.

- [GR79] V. Girault and P.A. Raviart. *Finite element approximation of the Navier-Stokes equations*. Springer-Verlag, Berlin-New York, 1979.
- [HE10] T.J.R. Hughes and J.A. Evans. Isogeometric Analysis. *ICES Report, Institute for Computational Engineering and Sciences, The University of Texas at Austin*, 10–18, 2010.
- [HFB86] T.J.R. Hughes, L.P. Franca, and M. Balestra. A new finite element formulation for computational fluid dynamics. V. Circumventing the Babuška-Brezzi condition: a stable Petrov-Galerkin formulation of the Stokes problem accommodating equal-order interpolations. *Computer Methods in Applied Mechanics and Engineering*, **59**:85–99, 1986.
- [HMJ00] T.J.R. Hughes, L. Mazzei, and K.E. Jansen. Large Eddy Simulation and the variational multiscale method. *Computing and Visualization in Science*, **3**:47–59, 2000.
- [HNF⁺99] D.W. Holdsworth, C.J.D. Norley, R. Frayne, D.A. Steinman, and B.K. Rutt. Characterization of common carotid artery blood-flow waveforms in normal subjects. *Physiological Measurements*, **20**:219–240, 1999.
- [Hol06] G.A. Holzapfel. Determination of material models for arterial walls from uniaxial extension tests and histological structure. *Journal of Theoretical Biology*, **238**:290–302, 2006.
- [HRS10] T.J.R. Hughes, A. Reali, and G. Sangalli. Efficient quadrature for NURBS-based isogeometric analysis. *Computer Methods in Applied Mechanics and Engineering*, **199**:301–313, 2010.
- [HS07] T.J.R. Hughes and G. Sangalli. Variational Multiscale Analysis: the fine-scale Greens function, projection, optimization, localization, and stabilized methods. *SIAM Journal on Numerical Analysis*, **45**:539–557, 2007.
- [Hug00] T.J.R. Hughes. *The Finite Element Method: Linear Static and Dynamic Finite Element Analysis*. Dover Publications, Mineola, New York, 2000.
- [HW05] T.J.R. Hughes and G.N. Wells. Conservation properties for the Galerkin and stabilised forms of the advectiondiffusion and incompressible Navier-Stokes equations. *Computer Methods in Applied Mechanics and Engineering*, **194**:1141–1159, 2005.
- [JTM05] K.E. Jansen and A.E. Tejada-Martínez. On the interaction between dynamic model dissipation and numerical dissipation due to streamline upwind/Petrov-Galerkin stabilization. *Computer Methods in Applied Mechanics and Engineering*, **194**:1225–1248, 2005.
- [JW01] K.E. Jansen and Whiting. A stabilized finite element method for the incompressible NavierStokes equations using a hierarchical basis. *International Journal for Numerical Methods in Fluids*, **35**:93–116, 2001.

- [JWH00] K.E. Jansen, C.H. Whiting, and G.M. Hulbert. A generalized- α method for integrating the filtered Navier–Stokes equations with a stabilized finite element method. *Computer Methods in Applied Mechanics and Engineering*, **190**:305–319, 2000.
- [Koi70] W.T. Koiter. On the mathematical foundations of shell theory. *Proceedings of the international congress on mathematics*, **3**:123–130, 1970.
- [LDE⁺12] J. Liu, L. Dedè, J.A. Evans, M.J. Borden, and T.J.R. Hughes. Isogeometric Analysis of the advective Cahn–Hilliard equation: spinodal decomposition under shear flow. *ICES Report, Institute for Computational Engineering and Sciences, The University of Texas at Austin*, 12–12, 2012.
- [LEB⁺10] S. Lipton, J.A. Evans, Y. Bazilevs, T. Elguedj, and T.J.R. Hughes. Robustness of isogeometric structural discretizations under severe mesh distortion. *Computer Methods in Applied Mechanics and Engineering*, **199**:357–373, 2010.
- [LTM98] P. Le Tallec and J. Mouro. Fluid structure interaction with large structural displacements. *Computer Methods in Applied Mechanics and Engineering*, **190**:3039–3067, 1998.
- [NV09] F. Nobile and C. Vergara. An effective Fluid-Structure Interaction formulation for vascular dynamics by generalized Robin conditions. *SIAM Journal on Scientific Computing*, **30**:731–763, 2009.
- [Ode00] J.T. Oden. *Advanced Theory of Finite Elements: an Introduction to the Mathematical Foundation of the Finite Element Method*. Texas Institute for Computational and Applied Mathematics, The University of Texas at Austin, 2000. Lecture Notes.
- [Pol05] M. Polner. *Galerkin Least-Squares stabilization operators for the Navier-Stokes equations*. PhD thesis, University of Twente, 2005.
- [PT97] L. Piegl and W. Tiller. *The NURBS Book*. Springer–Verlag, New York, 1997.
- [QSS07] A. Quarteroni, R. Sacco, and F. Saleri. *Numerical Mathematics*. Springer–Verlag, New York, 2007.
- [Qua93] L. Quartapelle. Numerical solution of the incompressible Navier-Stokes equations. *International series of numerical mathematics*, **48**, 1993.
- [Qua09] A. Quarteroni. *Numerical Models for Differential Problems*. Springer–Verlag, Milan, 2009.
- [RMP⁺09] P. Reymond, F. Merenda, F. Perren, D. Rufenacht, and N. Stergiopoulos. Validation of a one-dimensional model of the systemic arterial tree. *American Journal Physiological Heart Circulation Physiology*, **297**:H208–H222, 2009.
- [SC06] C.M. Shearer and C.E.S. Cesnik. Modified generalized- α method for integrating governing equations of very flexible aircraft. *47th AIAA/ASME/ASCE/AHS/ASC Structures, Structural Dynamics, and Materials Conference*, pages 1–21, 2006.

- [SDS⁺12] D. Schillinger, L. Dedè, M.A. Scott, J.A. Evans, M.J. Borden, E. Rank, and T.J.R. Hughes. An Isogeometric Design-through-analysis methodology based on adaptive hierarchical refinement of NURBS, immersed boundary methods, and T-spline CAD surfaces. *Computer Methods in Applied Mechanics and Engineering*, 2012.
- [SF73] G. Strang and G. Fix. *An Analysis of the Finite Element Method*. Wellesley–Cambridge Press, Englewood Cliffs, N.J., 1973.
- [SK83] R. Schreiber and H.B. Keller. Spurious solutions in driven cavity calculations. *Journal of Computational Physics*, **49**:165–172, 1983.
- [THZ98] C.A. Taylor, T.J.R. Hughes, and C.K. Zarins. Finite element modeling of blood flow in arteries. *Computer Methods in Applied Mechanics and Engineering*, **158**:155–196, 1998.
- [TMJ07] A.E. Tejada-Martínez and K.E. Jansen. Variational multiscale residual-based turbulence modeling for large eddy simulation of incompressible flows. *Computer Methods in Applied Mechanics and Engineering*, **197**:173–201, 2007.
- [V⁺08] U. Veronesi et al. *Salute per tutti*. R.C.S. Libri S.p.a., Milan, 2008.
- [VCFJT06] I.E. Vignon-Clementel, C.A. Figueroa, K.E. Jansen, and C.A. Taylor. Outflow boundary conditions for three-dimensional finite element modeling of blood flow and pressure in arteries. *Computer Methods in Applied Mechanics and Engineering*, **195**:3776–3796, 2006.
- [VdVS11] F.N. Van de Vosse and N. Stergiopulos. Pulse wave propagation in the arterial tree. *Annual Review of Fluid Mechanics*, **43**:467–499, 2011.
- [VF03] S.S. Varghese and S.H. Frankel. Numerical modeling of pulsatile turbulent flow in stenotic vessels. *Journal of Biomechanical Engineering*, **125**:445–460, 2003.
- [vTG⁺06] S. Čanić, J. Tambača, G. Guidoboni, A. Mikelić, C.J. Hartley, and D. Rosenstrauch. Modeling viscoelastic behavior of arterial walls and their interaction with pulsatile blood flow. *SIAM Journal on Applied Mathematics*, **67**:164–193, 2006.
- [WF07] L. Waite and J. Fine. *Applied Biofluid Mechanics*. McGraw-Hill, 2007.
- [WFC08] W.A. Wall, M.A. Frenzel, and C. Cyron. Isogeometric structural shape optimization. *Computer Methods in Applied Mechanics and Engineering*, **197**:2976–2988, 2008.
- [Whi99] C.H. Whiting. Stabilized Finite Element methods for fluid dynamics using a hierarchical basis. Master’s thesis, Rensselaer Polytechnic Institute Troy, New York, 1999.
- [Wom57] J.R. Womersley. Oscillatory flow in arteries: the constrained elastic tube as a model of arterial flow and pulse transmission. *Physics in Medicine and Biology*, **2**, 1957.

- [WSN05] N. Westerhof, N. Stergiopulos, and M.I.M. Noble. *Snapshots of Hemodynamics, An Aid for Clinical Research and Graduate Education*. Springer-Verlag, New York, 2005.

Acknowledgements

Al termine di questo lavoro vorrei ringraziare tutte le persone che ne hanno reso possibile la realizzazione.

In primo luogo il Prof. S.Serra Capizzano, che mi ha sempre sostenuto nell'intraprendere questo percorso, e il Prof. A.Quarteroni, per avermi offerto la possibilità di inserirmi nel suo gruppo di ricerca. Mi rivolgo ad entrambi con profonda gratitudine per l'attenzione e il tempo dedicatomi nonostante i molteplici impegni. In ultimo, il Dr.Ing. Luca Dedè per aver seguito passo a passo il mio lavoro e per il contributo nello sviluppo della tesi.

Grazie a Davide, per avermi aiutato i primi giorni nell'installare codice e librerie; a Cristiano e Paolo per i suggerimenti tecnici; I would like to thank Toni, for taking an interest in the results obtained.

La mia riconoscenza va alla mia famiglia, per avermi offerto questa possibilità e avermi sostenuto per tutta la sua durata, nonostante le vicende travagliate e le corse. Un grazie speciale è rivolto al mio consolatore di sempre.

Je voudrais aussi remercier M.me Claudine, pour sa hospitalité et gentillesse, et le petit ange qui s'appelle Céline Graph, pour son aide le premier jour à Lausanne.

Grazie a tutte le persone che mi hanno seguito e aiutato a distanza, quali Silvia, Amanda e il Prof. Donatelli, e a tutte coloro che mi hanno regalato la loro vicinanza. Di queste ultime fa parte tutto il gruppo di ricerca dell'EPFL, tra cui, in particolare, Matteo, per avermi ascoltato sempre ed avermi incoraggiato a schiudermi dal mio guscio, Gianluigi, per le opportunità e i consigli, Francesca, per un sorriso in ogni momento. A Luca, nonostante le tensioni degli ultimi tempi, grazie per le camminate che si sono trasformate in corse contro il tempo. Grazie ai miei colleghi di ufficio, a Paolo, per la sua disponibilità e la capacità di mettermi sempre a mio agio con la mitica frase "fai come ti senti", and Aymen, thanks for your gentleness, humor and advices. Anche a tutti gli altri ragazzi e ragazze, un grazie per i momenti passati in compagnia e le esperienze vissute insieme.

